1-1-2013

Investigation of Three-Way (TWC), Lean NOx Trap (LNT) and Selective Catalytic Reduction (SCR) Catalysts For Control of NOx Emissions from Lean-Burn Engines

Christopher Dominic DiGiulio
University of South Carolina

INVESTIGATION OF THREE-WAY (TWC), LEAN NO_X TRAP (LNT) AND SELECTIVE CATALYTIC REDUCTION (SCR) CATALYSTS FOR CONTROL OF NO_X EMISSIONS FROM LEAN-BURN ENGINES

by

Christopher D. DiGiulio

Bachelor of Science
University of Oklahoma, 2008

Submitted in Partial Fulfillment of the Requirements

For the Degree of Doctor of Philosophy in

Chemical Engineering

College of Engineering and Computing

University of South Carolina

2013

Accepted by:

Dr. Michael D. Amiridis, Major Professor

Dr. Oleg S. Alexeev, Committee Member

Dr. A. Jochen Lauterbach, Committee Member

Dr. Donna A. Chen, Committee Member

Dr. Todd J. Toops, Committee Member

Dr. John W. Weidner, Chemical Engineering Department Chair

Dr. Lacy K. Ford, Vice Provost and Dean of Graduate Studies

DEDICATION

TO MY WIFE RACHEL…

THIS IS BUT ONE CHAPTER IN THE REST OF OUR LIVES TOGETHER

LOVE ALWAYS,

CHRIS

ACKNOWLEDGEMENTS

First and foremost, I would like to acknowledge my advisor Dr. Michael Amiridis, who made all of this possible. I would like to thank him for accepting me into his group, even though he had already made commitments to other students. I would like to thank him for allowing me the freedom to pursue my own ideas and avenues of research. I would like to thank him for making time for me, even though he has an exceptionally busy schedule and for inviting me into his home to share a holiday meal with his family. Lastly, I would like to thank him for his invaluable insight and perspective. He is someone that I could never predict, but who always offered the best advice. I learned something every time we met. I hope that as I continue to grow in my career and as a person, I develop the long-sighted perspective that he so clearly possesses.

I would like to acknowledge Dr. Oleg Alexeev for all of his time and support, especially when I first arrived in Dr. Amiridis' research group. He, more than anyone, deserves the credit for teaching me the proper way to design equipment and perform experiments. Dr. Alexeev's un-compromising principles in pursuit of the truth taught me to be patient and focus on performing scientifically valid experiments, even when I desperately needed to make progress.

I would like to acknowledge Dr. John Monnier for the integral role he played in shaping my education. I am sincerely thankful, that instead of retiring, Dr. Monnier's love for catalysis brought him to the University of South Carolina to a lab with no windows across the hall from mine. He became a resource that any student would be lucky to have. I would to like thank him

for welcoming my questions, even when they were not related to his area of emphasis, and for allowing me to use his equipment. I would also like to thank him for allowing me to work on one of his projects and challenging me to learn and advance my education every time we spoke. Most importantly, I would like to thank Dr. Monnier for all of the advice he provided me and all of the stories he shared. They will stay with me forever.

I would like to acknowledge Dr. Donna Chen for her overt excitement and charisma for the field of Surface Science, but also for her love of education and the pursuit of knowledge in general. I would like to thank her for being such an exceptional teacher and for helping guide my research, especially during the early stages. She is easily one of my favorite professors.

I would like to acknowledge Dr. Lauterbach for allowing me to become a de facto member in his research group and attend weekly meetings to learn from him and his other students. I would also like to thank him for the critical role he played in re-directing my dissertation research. Lastly, I would also like to thank him for offering his time, equipment and expertise in pursuit of my research goals.

I would like to acknowledge Dr. Toops, Dr. James Parks II, Dr. Jae-Soon Choi, Dr. Miyoung Kim and Josh Phil for accepting me into the group at Oak Ridge National lab and for the integral role they all played in helping me complete my dissertation research. Under their guidance, my view of automotive catalysis matured from a very specific examination of NSR catalysts into a much more comprehensive perspective of the entire field. I would specifically like to thank Dr. Miyoung Kim for her patience and time when teaching me how to operate the bench reactor at ORNL. I would like to thank Josh Pihl for helping me when I had experimental difficulties and for all of the work he did behind the scenes to make sure that my efforts were not in vain. I would like to thank Dr. Jae-Soon Choi for volunteering time on his reactor and for

being understanding when things were accidentally broken. I would like to thank Dr. James Parks II for approving my inclusion into the group and for all of the advice he provided from an engines perspective. Lastly, I would like to thank Dr. Todd Toops for mentoring me while at ORNL and for becoming yet another valued professional advisor and joining my PhD committee.

In summary, I am sincerely thankful for having the opportunity to interact and learn from so many skilled and successful professionals. I feel that my experience has not been typical and that I am truly lucky to have worked with all of you. I am also thankful that while you all were exceptional mentors and teachers, to me, you feel more like my close friends.

Additionally, I would like to thank all of the administrative/technical staff that helped along the way, specifically: Marcia Rowen, Loretta Hardcastle, Vernon Dorrell, Brian Loggans, Chuck Holland and Pam Olszewski. Thank you all.

Funding from the National Science Foundation and the Department of Energy, which made all of this research possible – and therefore my PhD possible, was also immensely appreciated.

Lastly, I would like to acknowledge my family, especially my parents, for their love and support and for encouraging me to reach for my dreams and providing me with the tools to achieve my goals. Thank you for always emphasizing the value of education, even when I was too immature to listen. Now, begrudgingly following your advice has made all the difference in the world. I will never be able to truly repay you for the difference you have made. All I can say is:

Thank you,

Chris

ABSTRACT

Lean-burn gasoline engines are approximately 10% more fuel efficient than conventional, stoichiometric-burn ones. Although relatively modest, if implemented across the entire U.S. automotive fleet, this improvement in fuel economy could have far-reaching implications on the amount of gasoline imported in the country on an annual basis. However, the development of a cost-effective catalytic converter catalyst capable of meeting emission regulations for lean-burn vehicles still represents a major technical challenge. Currently, lean NO_X trap (LNT) and selective catalytic reduction (SCR) catalysts are used for this purpose, but both systems suffer from significant drawbacks. For example, LNT catalysts generally require high platinum group metal (PGM) loadings and are highly susceptible to sulfur poisoning. SCR catalysts require a costly urea-dosing system for delivery of urea as the reducing agent into the exhaust stream, as well as a secondary "fuel" tank for on-board storage of urea.

LNT catalysts are typically favored for smaller gasoline engines and are designed for periodic operation in lean and rich environments. NO_X is stored on the LNT system during a longer (e.g., 60 – 120 s) lean period and rapidly reduced during a much shorter (e.g., 1- 5 s) rich period. The mechanism for NO_X storage is fairly well understood, but the NO_X reduction mechanism is still the subject of considerable debate. Lean/rich cycling monitored by *in situ* Fourier Transform infrared spectroscopy (FTIR) confirmed the presence of surface isocyanate (NCO) species during reduction. Quantification of the FTIR results confirmed that surface NCO species could account for as much as 30% of the N_2 formed during the rich period. Hydrolysis of the NCO species to NH_3 in the presence of water vapor could also play a significant role. The

effect of the lean/rich cycle timing on NH_3 formation over a commercial LNT catalyst was also considered. At low temperatures, both the release and reduction of stored NO_X was kinetically limited and longer rich periods favored increased NO_X conversion and NH_3 formation. At elevated temperatures, the opposite was true and shorter rich periods favored increased NO_X conversion and NH_3 formation. The effects of cycle timing were most pronounced in the 250 – 400 °C temperature range, where optimization of the cycle timing could potentially decrease the PGM requirements of the LNT, especially in a coupled LNT-SCR system.

SCR catalysts are typically favored for heavy-duty applications, but General Motors (GM) recently developed a urea-less, passive-NH_3, three way catalyst SCR approach (TWC-SCR) for lean-gasoline vehicles. This TWC-SCR approach also relies on lean/rich cycling, but in this case NH_3 is intentionally formed over a TWC during rich periods and stored on a downstream SCR catalyst. The stored NH_3 is then used during a subsequent lean period to reduce lean-NO_X. NH_3 generation over TWCs under steady and cycling conditions was investigated. The temperature, catalytic formulation and reductant concentration all affected NH_3 formation. Storage of NH_3 on the downstream SCR catalyst was also considered. At low temperatures, the selective reduction of NO_X by stored NH_3 was favored over a Cu-zeolite SCR catalyst. Above 350 °C, NH_3 oxidation was favored over NO_X reduction. Recent bench reactor screening using a two-reactor, bench-core reactor configuration demonstrated the viability of the TWC-SCR configuration and NO_X conversions exceeding 98% were measured.

TABLE OF CONTENTS

LIST OF TABLES

LIST OF FIGURES

CHAPTER 1. INTRODUCTION, MOTIVATION, LITERATURE REVIEW AND REAL SYSTEMS

1.1 INTRODUCTION

Lean-burn gasoline engines have attracted the attention of automobile manufactures because operation in an oxygen-rich (i.e., lean) environment leads to higher engine efficiency, which translates into better fuel economy and lower emissions of CO_2. For example, Heck and Farrauto [1] reported that lean-burn engines could achieve engine efficiencies 20 – 30% higher than conventional ones. However, the three-way catalysts (TWCs) commonly employed for removal of emissions from stoichiometric-burn engines cannot reduce NO_X in the presence of excess O_2, which stimulated significant research activity into the development of new catalytic converter catalysts for application in lean-burn engine exhaust systems.

Selective catalytic reduction by hydrocarbons (HC-SCR) and ammonia (NH_3-SCR) were suggested as promising solutions. Initially, HC-SCR catalysts were the most attractive solution because the hydrocarbon reductants necessary for NO_X reduction were already available on the vehicle (as gasoline) and a urea/NH_3 storage tank would not need to added, filled or maintained for this catalyst to be commercially implemented [2,3]. Unfortunately, HC-SCR catalysts generally suffer from poor activity in a narrow temperature range, poor thermal stability and especially poor hydrothermal stability [2–5]. Therefore, NH_3-SCR catalysts seemed to be the better alternative at the time because they had already been implemented for stationary sources and a considerable amount of information regarding these catalytic systems was known [2–

4,6,7]. However, NH_3-SCR catalysts for mobile sources requires on-board storage of NH_3/urea, which can limit the practicality of this system, especially for smaller passenger cars [2–4,6].

In the mid 1990's, researchers at Toyota introduced an innovative solution to compete with HC-SCR and NH_3-SCR catalysts, which they referred to as, NO_X storage and reduction (NSR) catalysts [8]. These catalysts were designed to function in periodic lean/rich environments. In this case, NO_X was stored during lean phases and then reduced to N_2 by intermittent rich periods. Early NSR catalysts were capable of NO_X conversions as high as 90%, but were highly susceptible to sulfur poisoning and required ultra-low sulfur fuels for commercial implementation [8].

The following literature review summarizes the general operation features, reaction mechanisms and the highlights the function of each catalytic component present on NO_X storage and reduction catalysts. A brief review of real-world catalytic converter systems and how NSR catalysts fit into this larger framework is also discussed.

1.2 MOTIVATION AND SIGNIFICANCE

In the 1970s, the Clean Air Act was passed by Congress to improve air quality in the United States. This gave the Environmental Protection Agency (EPA) the authority to write and enforce regulations regarding criteria pollutants [9]. Currently, six criteria pollutants are regulated by the EPA and include: ground level ozone, particulate matter, carbon monoxide, nitrogen oxides, sulfur dioxide and lead. In 2006, mobile sources were responsible for approximately 35% of volatile organic compounds (VOCs), 58% of NO_X and 78% of CO emitted into the atmosphere. VOCs contain known carcinogens (e.g., benzene) and can additionally react with NO_X in the presence of sunlight to form ground level ozone - an eye and throat irritant that can potentially cause respiratory tract problems and/or lung damage [10,11].

Similarly, nitrogen dioxide (NO_2) contributes to acid rain and smog formation and is also a respiratory irritant. Carbon monoxide (CO) exposure can lead to reduced mental alertness, heart attacks, cardiovascular diseases, impaired fetal development and death [11].

Since automobiles account for a significant portion of the criteria pollutants released, the EPA has steadily implemented more and more stringent regulations to minimize the amount of toxic pollutants emitted by automobiles each year, as shown in Fig. 1, with mandated emission decreases for approaching 2 orders of magnitude (by 2004) in comparison to an uncontrolled vehicle operating in 1968. This triggered a massive search for catalytic materials in the 1970s capable of operating under harsh emission environments. In response, so called three way catalysts (TWCs) were developed and typical formulations consisted of Pt-Rh bimetallic particles deposited on a CeO_2 modified Al_2O_3 support. TWCs are capable of simultaneously oxidizing carbon monoxide and hydrocarbons to CO_2 and H_2O and reducing NO_X to N_2, but only when operated in a very narrow regime near stoichiometric conditions (air-to-fuel ratio $\approx$ 14.67:1), as shown in Fig. 2.

More recently, a 2007 assessment report generated by the Intergovernmental Panel on Climate Change (IPCC) stated warming of the climate to be, “unequivocal, as evident from observations regarding increases in global air and ocean temperatures, widespread melting of snow and ice and rising global sea levels” [12]. Anthropogenic greenhouse gases (GHG) were attributed to the observed changes in global climate. In April of 2007, the Supreme Court concluded that greenhouse gases meet the clean air definition of an air pollutant, which gave the EPA authority to regulate greenhouse gas emissions. On April 1, 2010 the EPA and the National Highway Traffic Safety Administration (NHTSA) finalized a rule that harmonized greenhouse gas emissions and fuel economy standards for light-duty vehicles for model years 2012 through

2016 [13]. The regulation requires an estimated combined average of 250 g CO_2/mi, which is equivalent to 35.5 mi/gal if met through fuel economy improvements alone.

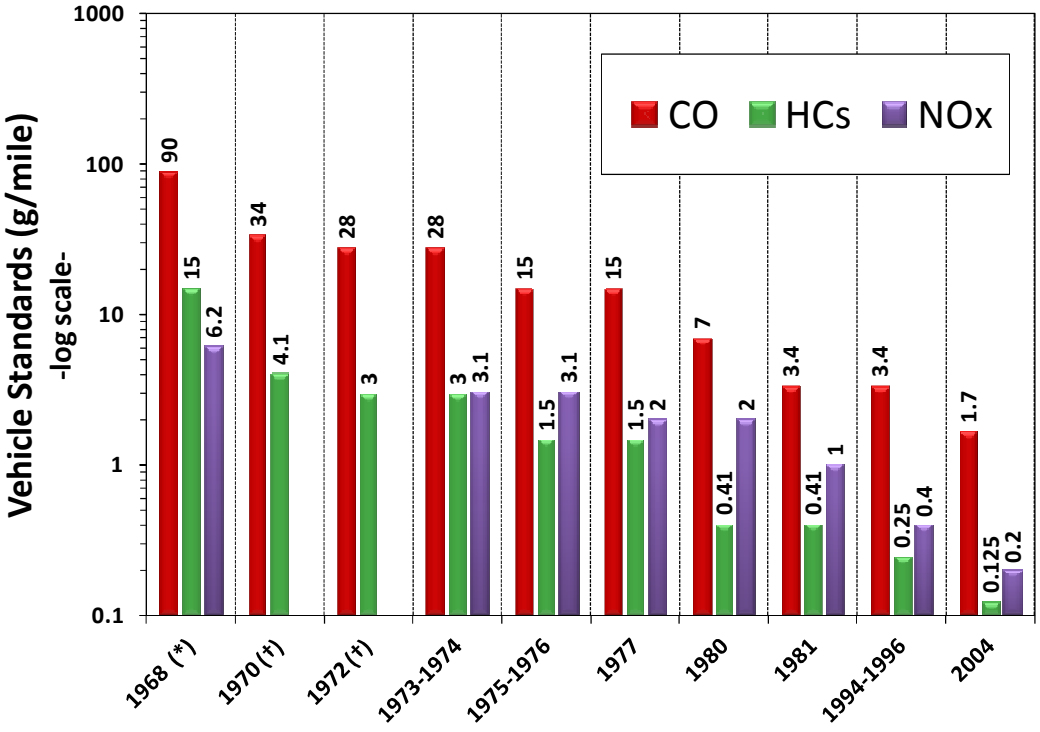

Figure 1. Progression of emissions standards in the US for light-duty, gasoline fueled vehicles, recreated from Faiz et al. [14], where (*) represents uncontrolled emissions from a 1968 light-duty vehicle and (†) denotes that no NO_X regulations were in place from 1970 to 1972.

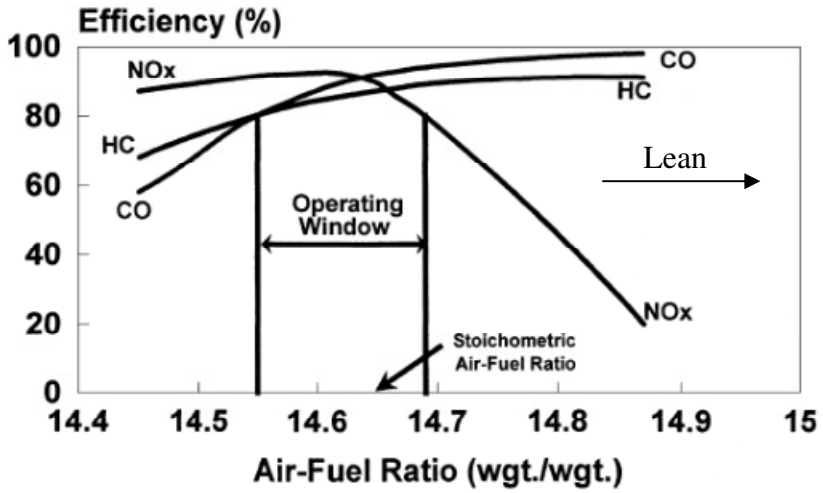

Figure 2. Conversion efficiency of CO, NO_X and HCs over a TWC, Farrauto and Heck [15].

As previously mentioned, one obvious way to increase the fuel efficiency of the internal combustion engine and decrease CO_2 emissions is to run the engine lean. If you examine Fig. 2 however, it becomes clear that the traditionally used TWC-only systems (1970s – present) will not be able to remove NO_X under these conditions. Thus, additional catalytic technologies in combination with the TWC need to be implemented in order to meet the emission regulations shown in Fig. 1.

1.3 Literature Review

The primary focus of this dissertation was on NO_X Storage and reduction catalysts (i.e, Chapters 2 and 3), so an in-depth review of these materials is warranted. Following the literature review, real-world catalytic converter systems are discussed, only some of which include an NSR catalyst.

1.3.1 General Features of NO_X Storage and Reduction Catalysts

As previously discussed, NO_X storage and reduction catalysts are designed for periodic operation in lean and rich environments from 100 to 400 °C, but the optimum temperature is approximately 350 °C [3]. Commercial NSR formulations are based on a $Pt/Ba/Al_2O_3$ catalyst promoted using Rh and/or CeO_2. The platinum loading typically varies from 1 to 2.5 wt %, while the Ba loading usually ranges from 8 to 30 wt %. The Rh loading is always substantially lower than the Pt loading, but CeO_2 loadings can be quite high and may even exceed the Ba loadings. Typical exhaust gas concentrations for NSR cycling conducted in laboratory investigations are shown in Table 1.

The lean period duration typically ranges from 60 to 120 s, while the rich period only lasts 1 to 5 s [16–20]. A short rich period is a necessary feature of NSR catalyst operation because longer rich periods would result in a more substantial fuel penalty and negate the benefits of lean-burn operation. Fig. 3 provides a simplified schematic of the NSR surface chemistry (Fig. 3A) and the expected NO_X reactor profile (Fig. 3B) obtained during cycling. As shown in Fig. 3A, NO is oxidized to NO_2 over precious metals during the lean period. The NO_2 then spills over onto the storage component and is stored in the form of a nitrite/nitrate [21,22]. During rich periods, the nitrates are reduced to N_2, but N_2O and NH_3 can also be produced. While the mechanism for NO_X storage is widely accepted, the mechanism for reduction of stored nitrates is still unclear and seems to be dependent on the reductant [23,24]. Hydrocarbons (HCs), CO and H_2 were included as possible reductants in Fig. 3A, but H_2 is commonly cited to be the most effective reductant during laboratory investigations. Generally, the activity for reductants is as follows: $H_2 \geq CO > C_3H_6 >> C_3H_8$, where CO and H_2 have been reported to show similar activity if H_2O is included in the feed [25–28]. In Fig. 3B, NO_X storage is indicated by an outlet

NO_X concentration lower than the inlet NO_X concentration. As storage elapses, the storage component becomes saturated with NO_X and the outlet NO_X concentration eventually approaches the inlet concentration. At this point, the rich period begins and the NO_X concentration drops considerably. During the rich period, the stored NO_X is reduced to N_2 and the storage component is regenerated. After the storage component has been regenerated, the reductant is removed from the feed and storage resumes.

In some investigations H_2O has been reported to increase the activity of CO as a reductant [28], but Epling et al. [29] reported that addition of H_2O and CO_2 negatively influenced storage capacity of NSR catalysts. H_2O was proposed to interact with hydroxyl groups on Al_2O_3 and render these sites incapable of NO_X storage. CO_2 and NO_2 were proposed to compete for the same storage sites on BaO. Since CO_2 and H_2O will always be present in actual engine exhausts, it is critical to understand how these species interact with the catalyst surface. SO_2 exposure results in irreversible adsorption during typical reaction conditions and prolonged exposure can lead to complete loss of the NSR activity [30].

In summary, NO_X storage and reduction catalysts are designed for periodic operated in 60 s lean, 5 s rich periods. The optimum temperature is approximately 350 °C. H_2 and CO are the best reducing agents and storage occurs most readily for feeds containing NO + O_2 or NO_2. Both H_2O and CO_2 can be detrimental to storage capacity, but the effect is reversible. SO_2, on the other hand, can completely deactivate the catalyst.

Table 1†. Typical Operating Conditions for NSR Catalysts.

	NO	O_2	C_3H_6	CO	H_20	CO_2	N_2/He
Rich	0.07%	0.60%	0.2%	0.50%	10%	14.50%	bal
Lean	0.70%	4.00%	0.80%	0.10%	10%	12.70%	bal

†Reproduced from Takahashi et al. [8].

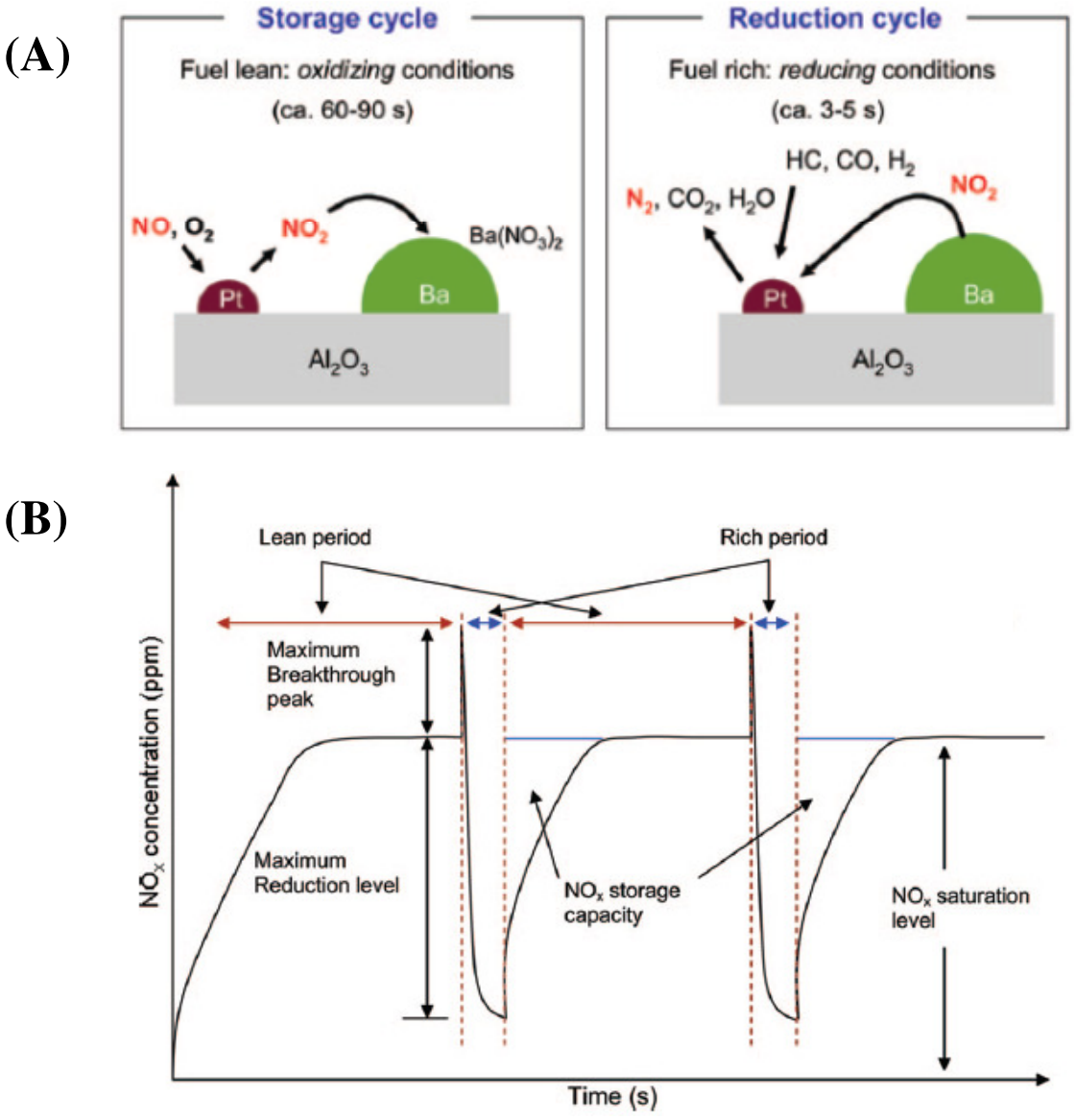

Figure 3. (A) Schematic showing proposed surface chemistry and timing occurring during storage/reduction, (B) Corresponding reactor profiles obtained during storage/reduction, Roy and Baiker [4].

1.3.2 THE MECHANISM OF NO_X STORAGE AND REDUCTION

1.3.2.1 NO_X STORAGE

Many investigations have been performed in an attempt to understand the mechanism for NO_X storage [21,22,27,31–38]. Initially, Bogner et al. [38] proposed that storage occurred as nitrites, where oxidation of NO to NO_2 over Pt was necessary before storage could occur. However, Sedlmair et al. [31] observed storage in the form of nitrites and nitrates when a $Pt/Ba/Al_2O_3$ catalyst was exposed to mixtures of NO and O_2 and reported that the amount of surface nitrites on Ba reached a maximum at 18 min and declined thereafter. This led the authors to conclude that nitrites were intermediates in the formation of nitrates. Several other authors have also suggested the formation of nitrites to be an intermediary step [21,22,33,39]. Alternatively, Prinetto et al. [40] proposed that storage of NO_2, which was not promoted by Pt, occurred through a disproportionation reaction that led to a stored nitrate and release of gas phase NO. Other researchers have also reported storage via this mechanism [38,41], but Cant and Patterson [32] reported an initial, short-lived phase involving storage of NO_2 without the evolution of gas phase NO. Again, this observation supports the intermediacy of nitrites, as more clearly seen for disproportionation reaction mechanism as shown in Eqns. 1, 2 and 3 [4].

$$BaO + NO_2(g) \rightarrow BaO - NO_2 \quad (1)$$

$$BaO - NO_2 \rightarrow BaO_2 + NO(g) \quad (2)$$

$$BaO_2 + 2NO_2(g) \rightarrow Ba(NO_3)_2 \quad (3)$$

In a later study, Forzatti et al. concluded that NO_X storage could occur via two routes, as shown in Fig. 4 [42]. The "nitrite" route (A) involves oxidation of NO on Pt sites and subsequent storage as nitrites on neighboring Ba sites, which can later be oxidized to nitrates.

The "nitrate" route (B), also known as the disproportionation route, proceeds through oxidation of NO to NO_2 on Pt and subsequent storage on neighboring Ba sites as nitrates with the evolution of gas phase NO. Under typical reactions conditions, the nitrite route was expected to be the dominant route for NO_X storage.

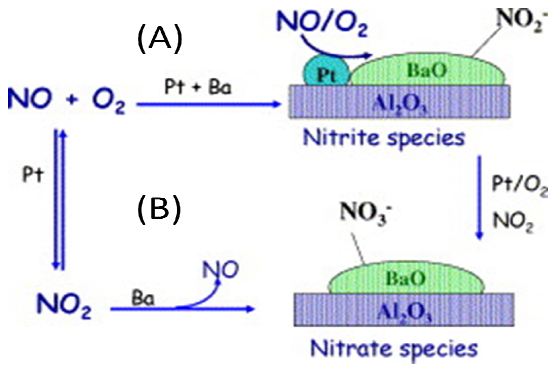

Figure 4. Mechanism of NO storage in the presence of oxygen, where (A) represents the "nitrite" route and (B) represents the "nitrate" route, Forzatti et al. [42]

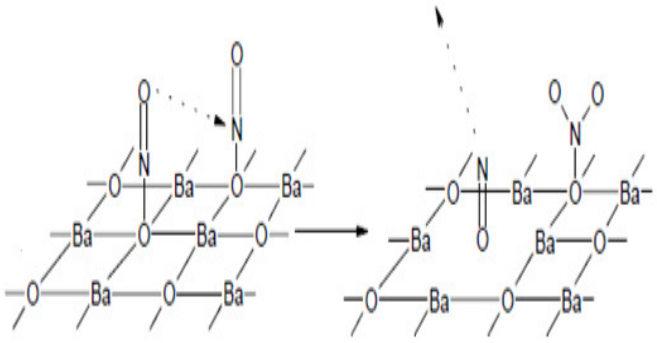

Figure 5. Mechanism of NO_X storage in the absence of oxygen, Fanson et al. [43].

Fanson et al. [43] proposed a different mechanism involving the direct adsorption of NO on BaO as a surface nitrite, which was subsequently oxidized by another adsorbed nitrite species to a monodentate nitrate, as shown in Fig. 5. The oxidation of NO to NO_2 over Pt did not appear

to be a critical step in this work because the authors observed significant storage even in the absence of oxygen. They cited the primary role of Pt to be adsorption of gas phase O_2, which then spills onto nearby BaO sites. This conclusion contradicts other studies, which assert that the primary method of storage occurs through interaction of NO_2 with BaO [38,41,44–46].

Recently another adsorption mechanism has been discussed involving co-adsorption or cooperative adsorption of nitrite-nitrate pairs on BaO [47–54]. Several theoretical studies have predicted the formation of nitrite-nitrate pairs on MgO and BaO [47,53,54] and Yi et al. [49] experimentally confirmed the presence of these nitrite-nitrate pairs on a thick BaO model surface upon admission of NO_2 at 90 K. In a later work, Yi and coworkers [48] suggested the simultaneous monotonic increase and saturation of peaks at 1240 and 1300-1500cm^{-1} to be indicative of nitrite-nitrate ion pairs when BaO films were exposed to NO_2 at 300 K. Alternatively, Desikusumastuti et al. [51] observed the formation of nitrites followed by nitrates when BaO was exposed to NO_2 at 100 K, but simultaneous formation of nitrites and nitrates at 300 K. They proposed a cooperative mechanism that operates at low temperatures that switches to a non-cooperative mechanism at higher temperatures. In summary, these mechanistic pathways have been developed to describe NO_X adsorption on BaO and the operating mechanism could largely be dependent on the source of NO_X available, the Ba loading and the temperature of exposure.

Considering that oxidation of NO to NO_2 has been reported as a key step in the storage mechanism, it is worth mentioning that two kinetic models have been proposed for NO oxidation on Pt. Olsson et al. [55] proposed a Langmuir-Hinshelwood model and observed that adding BaO to the support decreased the rate of NO oxidation. The basic nature of BaO was used to explain this observation, where BaO may donate electron density to the platinum. A more

electron rich Pt surface would then be expected to favor the formation of oxides [55–57]. Crocoll et al. [58] proposed Eley-Rideal kinetics and O_2 dissociatively adsorbed on the surface of Pt, while gas phase NO reacted with O_{ads} to form NO_2. A negative order was observed with respect to NO_2, which implied that NO_2 inhibited oxidation of NO. Oxidation of Pt^0 to $Pt^{+\delta}$ by NO_2 has previously been reported [56]. Interestingly, both kinetic reports mentioned deactivation due to formation of oxides.

1.3.2.2 REDUCTION

The reduction mechanism for stored NO_X has not been investigated nearly as thoroughly as the storage mechanism, possibly because the duration of the rich period makes it much more difficult to investigate [16]. For example, Nova et al. previously reported that the possible mechanisms for the reduction of NO_X in a rich environment are fairly well established from research on TWCs, but the mechanism for NO_X release from the storage component is still open to debate [59,60]. Currently multiple release mechanisms have been proposed including: 1.) thermal release enabled by heat generated from oxidation of reductants, 2.) a decrease in gas phase oxygen, which destabilizes stored nitrates due a shift in the storage equilibrium, 3.) spillover and reduction of NO_2 on Pt sites, 4.) establishment of a net reducing environment that decreases the stability of nitrates, 5.) direct reaction of the reductant (or activated reductant molecule spilled over from Pt) with stored nitrates [59–62]. Nova et al. [60] concluded that the main mechanism for decomposition of stored nitrates did not proceed via thermal decomposition, but instead proceeded through one of the following pathways: 1.) activation of H_2 on Pt site, followed by spillover of the H_2 onto the alumina support and migration towards a nitrate adspecies, which is then either decomposed to gas-phase NO_X that re-adsorbs on Pt to be reduced or directly reduced on the support 2.) surface diffusion of NO_X adspecies toward reduced Pt and

subsequent reduction. Further reports by Nova and coworkers [23,63,64] favor the two-step reduction mechanism involving activation of H_2 on a Pt site, followed by spillover onto the alumina support and surface diffusion towards the nitrate adspecies, which are then decomposed to NO_X and released into the gas phase. These species are then further reduced over Pt sites to form NH_3. The NH_3 can then react with stored nitrates to produce N_2. Mulla et al. [65] also predicted the formation of NH_3 as an intermediate, when H_2 was used as the reductant. If CO was used as the reductant, in the absence of water, the mechanism was proposed to proceed via cyanate/isocyanate species that react with nitrates to produce N_2 [24,64]. In the presence of water, the cyanate/isocyanate species could be hydrolyzed to form NH_3, which would then reduce stored NO_X, as previously discussed. Lastly, CO and water mixtures could undergo the water gas shift (WGS) reaction to produce hydrogen, where H_2 would then reduce nitrates via the already described mechanism. Kumar et al. performed isotopic labeling experiments and again concluded that NH_3 was an important intermediate in the reduction of stored NO_X [66]. The reduction of NO_X by hydrogen can be summarized according to Fig. 6, where path 1 is direct reduction of NO_X to N_2, path 2 is reduction of NO_X to ammonia, path 3 is reduction of stored NO_X by ammonia, path 4 is oxidation of NH_3 to N_2, and path 5 is decomposition of NH_3 to N_2 [67]. However, the reduction of NO_X by CO, CH_4, C_3H_6, C_3H_8 and other small hydrocarbons has not been investigated nearly as thoroughly, but the direct reduction by CO and hydrocarbons and indirect reduction via steam reforming and water gas shift have been suggested [4].

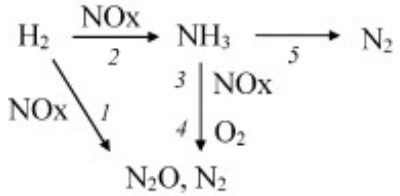

Figure 6. Possible reaction pathways for the reduction of stored NO_X by H_2, Clayton et al. [67].

1.3.2.3 THE EFFECT OF THE PT-BAO INTERFACE

One factor known to influence both the mechanism for storage and reduction of NO_X is the Pt-BaO interface and several different types of storage sites have been mentioned in the literature [21,29,68–70]. Mahzoul et al. [46] initially proposed two types of Pt sites, one close to barium, which was responsible for the storage of nitrates, and one far from barium responsible for the oxidation of NO to NO_2. In a later study, Cant et al. [68] observed a five-fold increase in the NO_X storage-reduction rate for a $Pt/BaO/Al_2O_3$ over a physical mixture of Pt/SiO_2 and BaO/Al_2O_3 when a system comprising a Pt/SiO_2 catalyst, solely for oxidation of NO to NO_2, was placed upstream of a Ba/Al_2O_3. The authors concluded that co-loading of both Pt and Ba was essential for efficient NO_X storage and reduction. Lindholm et al. [69] attributed the idea of different storage sites to one of several possibilities including: 1.) aluminum and barium storage sites, 2.) surface and bulk barium sites, and 3.) barium close and far from the noble metal. Bhatia et al. [70] also defined two different storage sites in their modeling efforts of the NSR process. "Fast" sites corresponded to a location close to the Pt/BaO interface – where storage was most likely to occur according to the nitrite route shown in Fig. 4. "Slow" sites represented storage in locations far from the Pt/BaO interface – where storage was most likely occurring according to the nitrate route described in Fig. 4. Sakamoto et al. [71] demonstrated using a thin film of BaO on a Si (100) that NO_X adsorbed more readily near the Pt/BaO interface. The decomposition of $Ba(NO_3)_2$ was also suggested to occur most rapidly near the Pt/BaO interface. The authors suggested that this preferential adsorption explained observations by others in the literature that only 20% of the NSR catalyst is utilized [72]. Recently, Kumar and coworkers [66] used isotopic labeling studies to investigate storage near-to and far-from the Pt/Ba interface.

Fig. 7 summarizes their results, where (a) is a pristine surface, (b) is after exposure to NO, (c) is after NO-^{15}NO isotopic exchange, and (d) is after reduction. Notice that the authors have only shown significant reduction near the Pt/BaO interface, whereas the rest of the surface remains partially saturated with NO_X. Lastly, many groups have stressed the importance of the Pt/Ba interface for optimization of both the storage and reduction cycles in NSR catalysts [8,21,29,46,73,74].

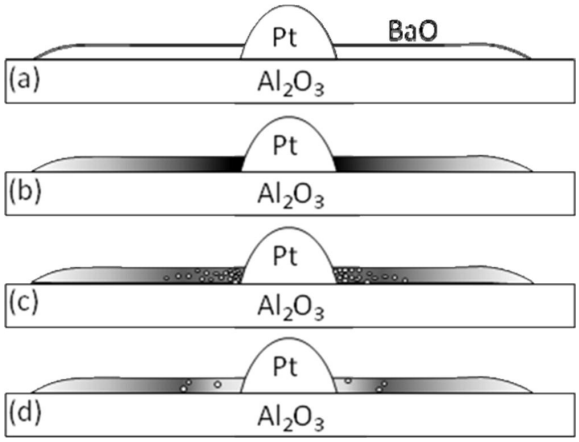

Figure 7. Schematic of NO_X storage (shaded), $^{15}NO_X$ isotopic exchange (dots) and reduction on a $Pt/BaO/Al_2O_3$ catalyst where (a) A pristine surface, (b) After NO_X storage, (c) After $^{15}NO_X$ exchange and (d) After reduction, Kumar et al. [66].

1.3.3 Important Catalyst Components

NO_X storage and reduction catalysts are usually comprised of the following constituents: 1.) a noble metal, which provides both NO oxidation and reduction activity, 2.) a storage component, which mainly provides NO_X storage capacity, but may also act as a promoter for other reactions (e.g. Ba has been suggested as a promoter for the water gas shift reaction [75], 3.) a support, which provides a high surface area substrate on which the storage component and

noble metal are dispersed. Additionally, a variety of promoters have been investigated to increase the thermal stability of the support or stabilize precious metal dispersion, increase sulfur tolerance, enhance storage capacity and improve reduction efficiency or selectivity. The following sub sections summarize the compounds used and their currently proposed/accepted role in the NO_X storage and reduction catalytic system.

1.3.3.1 NOBLE METALS

The impact of noble metals on NSR activity can be divided into four main subdivisions including: 1.) oxidation of NO to NO_2, 2.) reduction of stored NO_X to N_2 and 3.) resistance to sulfur tolerance. In the following subsections, each of these issues will be addressed regarding the specific metals commonly used in NSR catalysts.

PLATINUM

Pt has been extensively used in automotive catalysis because it is an excellent oxidation catalyst [7]. Therefore, it should not be surprising that Pt is the most commonly used noble metal in NSR catalysts. As mentioned, the loading typically varies from 1-2.5 wt % with a dispersion ranging from 3 to 80% [76–81]. For NSR catalysts, one of the most important aspects of Pt is its ability to oxidize NO to NO_2. Clayton et al. [77] reported that conversion of NO to NO_2 reached a maximum between 270 to 330°C, where the catalyst with 20 % dispersion of Pt was most active, followed by 50 % dispersion, 8 % dispersion and lastly, 3 % dispersion. This is in agreement with a study by Kim et al. [82] where smaller Pt particles were reported to offer better NO_X storage activity. However, Lee et al. [83] determined that a sample with 4% dispersion had a turn over frequency (TOF) 100 times greater than a sample with 82% dispersion, which is also in agreement with other reports in the literature [84]. This led Xue et al. [84] and others to propose that NO oxidation over Pt was a structure sensitive reaction since

NO oxidation occurred more readily over larger particles [83]. Olsson and Fridell [56] similarly argued that smaller Pt particles were less active for NO oxidation, but argued the difference was due to increased susceptibility of oxidation. XPS measurements conducted on Pt/Al_2O_3 and $Pt/Ba/Al_2O_3$ samples confirmed the presence of both PtO and PtO_2 phases, but the $Pt/Ba/Al_2O_3$ catalyst generally formed more PtO_2 than Pt/Al_2O_3. The authors explained the increased formation of Pt oxides on Pt/Al_2O_3 using the electrophilic nature of the alumina support, where Pt was expected to donate electron density to the Al_2O_3 support. To form Pt oxide, Pt must be able to transfer electrons to the oxygen, but when Pt is supported on an electrophilic support electron donation from the Pt to the support suppresses formation of Pt oxides [57]. The basic nature of BaO influences Pt in the opposite way and higher amounts of Pt oxides were observed.

When a Pt/Al_2O_3 and $Pt/BaO/Al_2O_3$ catalyst were exposed to pulses of NO in the absence of oxygen during temporal analysis of products (TAP) experiments, both NO decomposition and adsorption/storage were observed [85]. NO decomposition was proposed to occur through Reactions 4 – 10. Over the reduced Pt catalyst, the first pulses of NO produced nearly stoichiometric amounts of N_2, but as the number of pulses increased, oxygen accumulated on the surface and inhibited NO bond scission. As the surface become more crowded, N_2O was observed. The N_2O yield reached a maximum at the same time as breakthrough of NO was observed. Over $Pt/Ba/Al_2O_3$, NO breakthrough was delayed because storage and decomposition could occur simultaneously. Under these conditions, storage could occur either through spillover of oxygen from Pt onto the Ba, where a BaO_2 site could then directly react with gas phase NO, or direct formation of NO_2 over the Pt, which then reacts with BaO.

$$NO + Pt \leftrightarrow NO - Pt \quad 4$$

$$NO - Pt \leftrightarrow N - Pt + O - Pt \quad (5)$$

$$2N - Pt \leftrightarrow N_2(g) + 2Pt \quad (6)$$

$$2NO - Pt \leftrightarrow N_2O(g) + Pt + O - Pt \quad (7)$$

$$NO - Pt + N - Pt \leftrightarrow NO_2(g) + 2Pt \quad (8)$$

$$NO - Pt + O - Pt \leftrightarrow NO_2(g) + 2Pt \quad (9)$$

$$O - Pt + O - Pt \leftrightarrow O_2(g) + 2Pt \quad (10)$$

Anderson et al. [86] observed a dramatic increase in NO_X storage for $Pt/Ba/Al_2O_3$ over Ba/Al_2O_3, which further supported the crucial role of Pt in NSR catalyst formulations. Pt has also been reported to catalyze the transition from Ba nitrites to Ba nitrates [22,86]. Schmitz et al. [87] determined that NO oxidation over Pt was influenced by the following factors (in order of importance): support > pretreatment > loading > calcination atmosphere > calcination temperature > precursor salt. The reduction of NO on Pt does not seem to be nearly as dependent on particle size, but could be related to the strength of the Pt–NO bond or could also be structure sensitive, as is the case for Pd and Rh [83,84,88–92].

As demonstrated by Fridell et al. [62], Pt also plays an important role in the reduction of stored NO_X. For example when BaO/Al_2O_3 was cycled between lean and rich periods, no appreciable NO_X storage was observed during lean periods and only minor NO_X reduction occurred during rich phases. A $Pt\text{-}Rh/Al_2O_3$ catalyst was able to completely reduce NO_X during rich phases, but no NO_X storage was observed during lean periods. Su et al. [22] also reported that Pt was necessary for activation of hydrocarbons. Currently, NO reduction over Pt is explained by one of two mechanisms including: (1) NO decomposition on reduced Pt sites, where the main role of the reductant is to scavenge surface oxygen from Pt and keep the Pt in a

reduced state so the NO dissociation can occur, or (2) the direct reaction between released NO_X and adsorbed reductants on Pt sites [5,60,93]. In a series of publications, Abdulhamid et al. [25–27] demonstrated that Pt was an effective metal for reduction of stored NO_X using H_2 and CO for temperatures between 250°C and 350°C. C_3H_6 was reported to be somewhat less efficient and C_3H_8 showed no NO_X reduction capability. Although CO was initially an effective reductant, the authors reported deterioration of the reduction efficiency with increased cycling. Lower temperatures also reduced the reduction efficiency for CO. The observed loss was attributed to either poisoning of Pt by strongly adsorbed CO or through the formation of isocyanate species on alumina or barium in the Pt/BaO interfacial region, which would prevent NO_X spillover from the storage component to the precious metal. The authors attributed CO accumulation on the surface Pt sites to be the main cause of deactivation from 150 to 250°C due to the high heat of adsorption of CO on Pt. However an FTIR band at 2117 cm^{-1} (assigned to a cyanide species on Pt) was observed and was stable under both lean and rich conditions, which was assigned to a stable cyanide species that blocked NO_X spillover from the storage sites to Pt.

The location of Pt, synthetic route, method of deposition and type of precursor used also affect the catalytic performance [76,80,81,94–96]. Elizundia et al. [81] reported that deposition of the Ba precursor before the Pt precursor led to a more active catalyst. In their case, preparation of a 1.3%Pt-15.7%Ba/Al_2O_3 (w/w) sample was accomplished using sequential wet impregnations of tetraammineplatinum nitrite [$Pt(NH_3)_4(NO_2)_2$] and barium acetate [$Ba(CH_3COO)_2$]. After each impregnation, samples were dried and then calcined at 650°C for 4 h. The dispersion of Pt ranged from 0.6 – 5.5%. The authors attributed the increased catalytic activity of samples where Ba had been impregnated first to increased Pt/Ba interfacial contact. Lindholm et al. [95] reported higher storage capacity and reduction efficiency for samples where

Pt was deposited before Ba. Preparation of monolithic 3%Pt/20.7%Ba/Al_2O_3 samples was accomplished using incipient wetness impregnation of platinum nitrite, $Pt(NH_3)_4(NO_2)_2$, and dip coating of barium nitrate, $Ba(NO_3)_2$. After each impregnation, samples were dried at 80°C for 12 h and then calcined at 550°C for 2 h. The dispersion of Pt ranged from 18 – 25%. Lindholm et al. [95] hypothesized that the higher activity of Al/Pt/Ba was caused by better dispersion of Ba on the support, which led to better interfacial contact between Pt and Ba. Interestingly, both Elizundia et al. [81] and Lindholm et al. [95] linked the catalytic activity to the degree of contact between Pt and Ba, but observed opposite results in terms of impregnation order. Dawody et al. [94] compared samples prepared from hexachloroplatinic acid [$H_2Pt(Cl)_6$], tetraammineplatinum hydroxide [$Pt(NH_3)_4(OH)_2$], diammineplatinum nitrite [$Pt(NH_3)_2(NO_2)_2$] and platinum nitrate [$Pt(NO_3)_2$] and found that samples derived from platinum nitrate were the most active for NO_X storage and reduction followed by tetraammineplatinum hydroxide. The resulting dispersions and activity differences were explained by electrostatic interactions and/or ion and ligand exchange between the Pt complex and the BaO/$BaCO_3$/Al_2O_3 support. Pereda-Ayo et al. [96] similarly reported that tetraammineplatinum hydroxide to be a better Pt precursor than hexachloroplatinic acid when used for synthesis of NSR materials. Buchel et al. [97] synthesized NSR catalysts using the flame spray pyrolysis method [98,99], with Pt selectively on Al_2O_3 or $BaCO_3$ and found that Pt located on Al_2O_3 exhibited better NO oxidation activity, but Pt located on Ba showed greater reduction activity. Above 350 °C, the location of Pt insignificantly influenced storage and reduction.

Pt, like Ba, is susceptible to sulfur poisoning and the formation of Pt sulfides, which could block potential NO oxidation sites, have been observed [35,36,100–102]. Sedlmair et al. reported a higher reduction temperature for Pt during TPR after the catalyst had been sulfided

and hypothesized that decreased activity during cycling might be explained by the higher Pt reduction temperatures [36]. Amberntsson et al. [103–106] alternatively reported an increase in NO oxidation activity for Pt-containing catalysts after exposure to SO_2, which they explained by reaction of Pt-O with SO_2 to form sulfites and sulfates. The sulfided Pt was hypothesized to remain in a reduced state during NO oxidation, which explained the higher activity. Fridell et al. [106] also proposed that exposure to SO_2 leads to sintering of the Pt particles, which enhanced the oxidation activity because larger particle were less likely to be oxidized and also exhibited higher TOFs. This rational was explained in a previous work by Olsson et al. linking dispersion and the presence of BaO to differences in flow reactor studies [56], Pt with a higher dispersion or in the presence of BaO was more likely to be oxidized, which then decreased NO oxidation activity. During lean conditions, Pt has been reported to catalyze the oxidation of SO_2 to SO_3, which facilitates the formation of bulk $BaSO_4$ [107], but Su et al. [22] observed nearly-identical spectra after $SO_2 + O_2$ exposure for a Ba/Al_2O_3 and $Pt/BaO/Al_2O_3$ catalyst and concluded that Pt did not play a significant role during poisoning by SO_2. During rich conditions, Pt can also form Pt-S bonds, as observed by Kim et al. and others [35,108]. The formation of BaS has also been reported [109,110]. During subsequent lean periods, Pt-S and BaS species could be re-oxidized to form bulk/surface barium and aluminum sulfates [35,36]. Re-oxidation of reduced sulfur compounds is thought to preferentially poison sites near the Pt/BaO interface [35,36,71,102,111].

PALLADIUM

In recent publications, Pd has been suggested as a viable alternative to Pt for NSR catalysts because of its high activity during both lean and rich periods and its ability to activate saturated hydrocarbons [25,27,112,113]. Facile interconversion between Pd^{2+} and Pd^0 during lean and rich cycling has also been suggested as another advantage of Pd over Pt [4]. Salasc et

al. [113] demonstrated that a $Pd/BaO/Al_2O_3$ catalyst stored more NO_X than $Pt/BaO/Al_2O_3$ at 300°C, but the Pt containing catalyst stored slightly more at 400°C[123]. The $Pd/BaO/Al_2O_3$ sample was also able to completely reduce all stored NO_X at 300°C, while the Pt-based catalyst exhibited incomplete reduction. Salasc et al. [113] also demonstrated the beneficial role of BaO during reduction; where the Pt/Al_2O_3 and Pd/Al_2O_3 catalysts slowly deactivated during extended rich periods, but the $Pt/Ba/Al_2O_3$ and $Pd/Ba/Al_2O_3$ reduced most of the gas phase NO_X at 400°C. $Pt/BaO/Al_2O_3$ in comparison to $Pd/BaO/Al_2O_3$ showed more significant deactivation during extended rich periods, which led the authors to conclude that Pd was less susceptible to self poisoning mechanisms. Migration of NO_X species originating from decomposition of barium nitrate to noble metal sites or spillover of hydrocarbons to the BaO or interactions between the precious metal and storage component could explain why BaO has such a positive effect on the sustained NO_X reduction activity of NSR materials. Lastly, Pd^{2+} and Pd^0 were observed during lean and rich cycling for $Pd/BaO/Al_2O_3$, but only metallic Pt was observed for $Pt/Ba/Al_2O_3$. Recently, Weiss et al. [114,115] proposed that NO oxidation on Pd was also affected by the size of the particles, which was discussed in the previous section regarding Pt. In that case, NO oxidation turnover rates were insensitive to oxidative or reductive pretreatments because PdO was formed rapidly and is thermodynamically favored for NO oxidation conditions. Instead, the strength of the Pd-O bond determined NO oxidation turnover rates. Smaller particles have stronger bonds and fewer vacancies on the surface for NO oxidation to occur.

Abdulhamid et al. [25] demonstrated that a Pd-based NSR catalyst stored more NO_X than a Pt based catalyst when CO, C_3H_6 and C_3H_8 were used as model reductants, but the Pt-based catalyst stored more NO_X when H_2 was used. Additionally, Pd was the only precious metal tested that showed activity for reduction when C_3H_8 was used as a model reductant. While Pd

may seem more active, it is important to note that dispersion of Pt was 4%, while the dispersion of Pd was 15% and this may have affected the results by changing Pd/BaO and Pt/BaO interfacial contact areas, respectively. In another study by Abdulhamid et al. [27], Pd and Pt were compared using in-situ DRIFTS and reactor studies. Again, Pd seemed to be more active when CO or C_3H_6 was used as the reductant. Again however, differences in precious metal dispersion made elucidation of the results more complicated (5% for Pt and 12% for Pd). In both cases, the reduction of stored NO_X occurred through the formation of isocyanates, where higher concentrations of isocyanates were formed on Pd samples. In this case, the authors concluded that the lower NO_X storage and reduction properties were related to lower metal dispersion and/or lower metal/Ba interfacial area and not to inherent differences in the precious metals themselves. In a later study, Su et al. [112] reported that a $Pd/BaO/Al_2O_3$ catalyst had higher overall NO_X reduction efficiency than $Pt/BaO/Al_2O_3$ catalyst between 250 and 375 °C, but the performance was almost identical above 375 °C. The improvement in efficiency was related to higher activity for the oxidation/activity of propylene and higher activity for the formation of surface nitrite species. In this case, the metal dispersions were approximately the same (around 40%), but the molar concentration of Pd was approximately 2 times higher than Pt. Desikusumastuti et al. [52] also observed strong nitrite features for Pd containing catalysts and concluded that the highest concentration of surface nitrites will be present in samples with a strong Pd/BaO interaction. The sulfur resistance of Pd containing NSR materials has not been investigated, but Pd/Al_2O_3 diesel oxidation catalysts have been reported to be susceptible to sulfur poisoning [116]. Kolli et al. [116] observed losses of precious metal dispersion and decreased activity for oxidation reactions. The supports containing Pd exhibited higher total

sulfur than alumina samples alone, which further demonstrated the catalytic role of Pd in sulfur oxidation and storage on to the support.

RHODIUM

Very few studies have been performed using monometallic Rh as the precious metal for NSR systems [16,25,27,117,118]. Abdulhamid et al. [25] found $Rh/BaO/Al_2O_3$ to have poor NO_X storage capacity, but high reduction ability in comparison to Pt and Pd. The authors suggested the poor activity of supported Rh catalysts was due to lack of NO_X spillover from Rh to BaO. Rh also had the lowest activity for NH_3 formation, which could be explained by an increased ability to dissociate NO on the metal surface. This is in agreement with a study done by Breen et al. where Rh containing samples produced the smallest amount of ammonia [119]. In a later study, Breen et al. suggested that spillover from Rh to BaO may not be limiting storage-reduction activity and suggested that Rh may simply be a poor oxidation catalyst [16,120]. Alternatively, Huang et al. [117] observed better storage-reduction properties for $Rh/CaO/Al_2O_3$ over Pt or Pd supported on CaO/Al_2O_3, which demonstrates that NSR properties could be both a function of precious metal and storage component. Vijay et al. [118] observed similar storage amounts for $Pt/BaO/Al_2O_3$ and $Rh/BaO/Al_2O_3$ if long cycle times were used. Therefore, discrepancies on the role of Rh exist and further study is warranted, especially since many commercial catalysts contain mixtures of Pt and Rh. While the role of Rh in NO_X storage and reduction chemistry may still be unclear, Mahzoul et al. observed Rh to inhibit sulfur formation, which is a desirable attribute for NSR catalysts [121].

Other monometallic metals investigated include: Cu, Co, Fe, and Ag. HC-SCR systems commonly employ a Ag/Al_2O_3 catalyst and can achieve NO_X conversions as high as 79% [122,123]. Along these lines, Mihalova et al. [124] compared a $Ag/BaCO_3/Al_2O_3$ and

$Pt/BaCO_3/Al_2O_3$ catalyst and observed a maximum NO_X conversion of approximately 50% at 500 °C for Ag based samples, but 90% conversion at 350 °C for Pt based samples. While the Pt based sample initially had much higher activity, they were much more susceptible to sulfur poisoning. After sulfur exposure, the Ag sample was more active when compared to the Pt samples. In a series of publications, Vijay et al. [118,125,126] studied Co-containing NSR materials. They found that a 5%Co/15% Ba on alumina and 1%Pt/15% Ba on alumina stored equivalent amounts of NO_X when the catalysts were exposed to lean environments at 375 °C. XRD confirmed that Co was present as a highly oxidized Co_3O_4 phase. In comparison to Co, Pt was still a better oxidizing metal, but Co is much cheaper and could therefore be used in much higher amounts. Co was also more uniformly distributed on the support, which was thought to lead to better interfacial contact between the oxidizing metal and storage component. Unfortunately, Co exhibits poor reduction activity and another noble metal, most likely Rh, would need to be included to reach high conversions. Park et al. [127] also observed NSR activity for Co containing NO_X storage catalysts. Monometallic Fe samples were studied by Hendershot et al. [128,129] using high throughput experimentation and the presence of Fe was found to affect the performance significantly less than the Pt and Ba weight loadings. Wang et al. [130,131] synthesized a $Cu/K_2Ti_2O_5$ NSR catalyst because Cu is capable of simultaneous removal of SO_2 and NO_X in flue gases and they hoped to extend some of these desirable properties to NSR catalysts. They observed storage and reduction activity at higher temperatures (500 – 600 °C), but observed poor reduction activity at lower temperatures (200 – 400 °C). Ir based catalysts have been suggested to be highly active for SCR and DFT calculation have implied Pt/Ir to be an interesting bi-metallic system, but no experimental investigations have been performed using Ir to date [132–134].

BIMETALLIC

Most of the model NSR catalysts considered only contain Pt and Ba supported on Al_2O_3, but commercial catalysts consist of complex mixtures involving differing combinations of the following elements: Pt, Pd, Rh, Ba, K, Ce, La, Zr, Mg, Ti, and Al_2O_3 [31,45,102,135–138]. Sedlmair et al. used a Pt-Rh/BaO-$BaCO_3$/Al_2O_3 commercial catalyst in their studies [31,102]. Others have used formulations including Mg, Al, Ce, Zr, Ba, Pt, Pd, Rh, La, Fe, and Ti [136,139,140] or Pt, Rh, Ba, Ce and Al [138]. While many investigations have used either model or commercial bi-metallic catalysts [31,46,62,75,102,104,105,121,135–139,141–156], only a small number of these investigations have been devoted to understanding the specific role each metal plays on the observed catalytic performance [16,46,75,121,141,153]. Commercial catalysts typically contain a large number of elements because the addition of multiple promoters can increase activity, selectivity or improve catalyst lifetime. For example, Choi et al. [135] investigated sulfur poisoning on an industrial sample containing Pt, Pd and Rh, in addition to many other component. The reasoning for addition of three different metals could be as follows: Pt for the oxidation of NO to NO_2 [55,115], Pd for activation of saturated hydrocarbons [25,27,112,113], and Rh for its high reduction activity and low selectivity to ammonia [27,119]. However, the addition of multiple metals does not necessarily infer additive properties as observed during monometallic studies. Therefore, bimetallic and tri-metallic interactions must be carefully considered in order to determine if the additional metals provide increased catalytic performance. Otherwise, the higher costs associated with incorporation of additional precious metals is unwarranted. This section focuses strictly on Pt-Rh supported on BaO containing substrates. No literature was available for Pd containing bimetallic samples. The addition of

other elements will be discussed in section 1.3.4.3 on supports (MgO, TiO_2, ZrO_2 and La_2O_3) or section 1.3.4.4 on promoters (mainly Co, Fe and CeO_2).

Initially, Mahzoul et al. [46,121] observed that washcoat samples containing Pt, Rh, Ba, La, and Al stored more NO_X at saturation conditions than other standard washcoat formulations containing only Pt, Ba and Al_2O_3. The authors also determined that Rh inhibited the formation of sulfates. Amberntsson et al. [141] performed a detailed study on NO oxidation and reduction as a function of Pt and Rh loading. The NO_X storage capacity was observed to decrease as follows: 4% Pt > 2% Pt ≈ 2% Pt-1% Rh > 1% Pt-0.5% Rh > 1% Rh for samples containing equimolar amounts of BaO on alumina. The samples containing monometallic Pt performed much better when oxidation of NO to NO_2 was examined. To help understand why Rh negatively affected NO oxidation, the authors conducted XPS studies and found the surface coverage of Pt decreased by 70% in oxidizing conditions compared to reducing conditions. Conversely, Rh surface concentration increased by 35%. This inferred that the bimetallic samples consisted primarily of Rh on the surface during lean conditions, which helped explain the poor performance, since Rh has been reported to be a poor NO oxidation catalyst [16,120]. While initial inspection of Pt-Rh bimetallic catalysts inferred a negative influence for Rh incorporation, Amberntsson et al. [141] demonstrated that Pt-Rh bimetallic samples sustained much higher conversions when SO_2 was present in the exhaust gas. The bimetallic samples were not susceptible to deactivation like their monometallic counterparts, as seen in Fig. 8. NO oxidation on monometallic Rh samples deactivated very quickly, but monometallic Pt and Pt-Rh samples were stable during the time frame of the experiment. Conversely, NO reduction on monometallic Pt samples deactivated very quickly, whereas bimetallic Pt-Rh and monometallic Rh samples were stable. The authors concluded that addition of Rh was essential for good

overall performance of NSR catalysts even though the amount of NO_X stored was lower. Similarly, Schmeißer et al. and Kim et al. have found the incorporation of Rh leads to improved performance due to its high NO_X reduction ability even though it suppresses NO_X storage capacity [75,152].

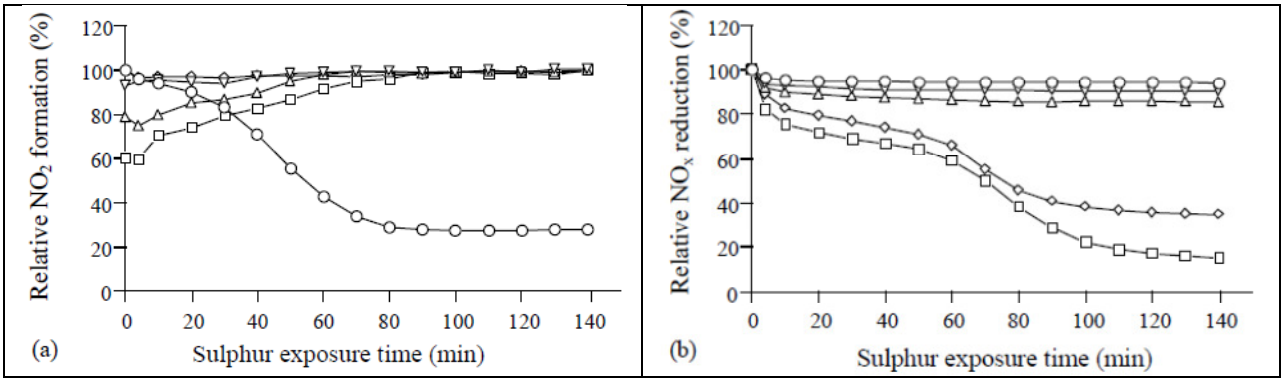

Figure 8. NO oxidation (a) and reduction (b) over (◊) 4 % Pt, (□) 2 % Pt, (Δ) 2 % Pt - 1% Rh, (**∇**) 1 % Pt – 0.5 % Rh, and (○) 1 % Rh catalysts containing equimolar amounts of BaO as a function of sulfur exposure, Amberntsson et al. [141].

Conversely, Breen et al. [16] performed a study using fast transient techniques and determined that the addition of Rh does not have a beneficial effect in NSR catalysts. Their investigation employed realistic 60 s lean periods followed by 1.2 s rich periods and they found that NSR activity to decreased as follows: 1.6 wt % Pt > 0.5 wt % Pt – 0.8 wt % Rh > 1.1 wt % Rh > 0.5 wt % Pt. However if the data was corrected for the percentage of metal atom exposed, the activity decreased as follows: 0.5 wt % Pt > 0.5 wt % Pt – 0.8 wt % Rh > 1.1 wt % Rh. The authors explained these results by introducing operational regimes, where NSR performance could either be storage limited catalysts or reduction limited. The 1.6 Pt and 0.5 Pt – 0.8 Rh samples were reduction-rate limited catalysts because they were incapable of completely

regenerating the storage component during rich periods and so conversion decreased with cycling time. The monometallic Rh catalyst was the only sample with a high enough reduction activity to completely regenerate the catalyst, but was limited by the storage-rate during lean phases. In this case, conversion of NO_X was low but remained constant with cycling time. While the study by Breen et al. [16] indicated low activity for Rh containing NSR catalysts, it should be noted that the authors excluded the role of sulfur and the bimetallic catalyst tested contained a molar ratio of 0.84 for Pt:Rh, respectively. The low ratio of Pt to Rh could exacerbate surface enrichment of Rh on the surface of Pt during lean periods, as observed by Amberntsson and coworkers [141]. Several surface science investigations reported diffusion of Rh into Pt particles even at room temperature [157–159], which further demonstrates that interconversion between Pt rich and Rh rich surfaces in different environments may be facile and should be considered when designing bimetallic catalysts. The ratio of Rh to Pt was also quite high in comparison to formulations typically employed for commercial catalysts [139].

1.3.3.2 Storage Materials

The storage component is usually selected from alkali metals and/or alkaline earth metals. Matsumoto [8,160] demonstrated that NO_X storage increased as the electronegativity decreased, but hydrocarbon conversion increased as the electronegativity increased. Fig. 9 demonstrates the inverse relationship between the NO_X storage ability and hydrocarbon (HC) conversion as a function of electronegativity.

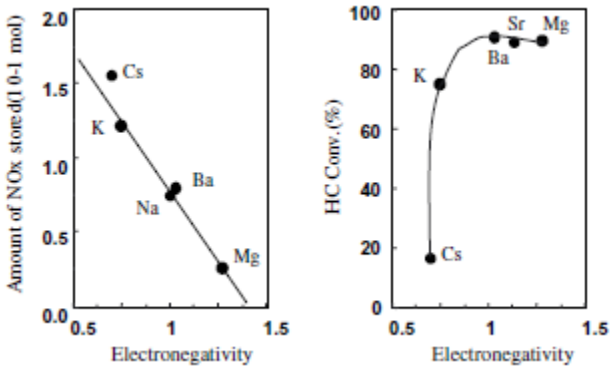

Figure 9. NO_X storage capacity and hydrocarbon conversion measurements for some alkali and alkaline earth elements including: Cs, K, Na, Ba, and Mg, Takeuchi and Matsumoto [160].

For these reasons, considerable efforts have been devoted to Ba as a storage component because it has desirable properties when examining both the lean and rich phases of NSR operation [21,22,32,39,61,73,94,100,161–163]. Recently, there has been interest in K because it may offer higher storage capacity [160], help stabilize stored nitrogen oxide species [164] and have better interaction with Pt [165]. Other storage materials include Li [166,167], Mg [163,167–170], Ca [167,169,170], Sr [169,171–173], and Na [167,174–177]. When considering these different storage materials, primary questions of concern include: (i.) Which storage material offers the best performance when sulfur resistance, thermal stability, NO_X storage capacity, HC conversion, and selectivity to N_2 are all considered? (ii.) What is the optimum loading of that storage material and what is the nature of the storage material therein? (iii.) How strongly does the storage material store NO_X and what types of species are present on the surface? (iv.) How does the metal-storage material interface affect the storage? The following two subsections will focus on the current understanding of these questions.

BA CONTAINING NSR MATERIALS

Ba represents the most commonly used element as a NO_X storage material. The optimum Ba loading has been reported as 6-12 wt % Ba [178], 16-23 wt % Ba [179] and 23 wt % Ba [73].

Generally higher amounts of Ba are capable of storing more NO_X, but loadings higher than 10 wt% can negatively affect noble metal dispersion [73,179]. Unfortunately, direct comparison between studies can be difficult because a wide range of loadings have been used: e.g., 8 wt% BaO/$BaCO_3$ [31], 8.3 wt% Ba [29], 9 wt% Ba [32], 13 wt% BaO [94], 16.3 wt% Ba [61], 17 wt% Ba [21], 18 wt% BaO [94], 20 wt% BaO [22], and concentrations up to 30 wt % Ba [73]. These samples will most likely exhibit different distributions and dispersions of Ba and/or differences in morphology of the Ba present on the surface. For example, Piacentini et al. [161] performed a study using XRD and TPD to examine the effect of varying the Ba loading from 4.5 to 28 wt % and concluded that the chemical nature of Ba was dependent on loading. They observed no evolution of CO_2 during TPD for Ba loadings of 4.5 wt %., but saw evolution of CO_2 in all samples with loadings of 9 wt % or higher. Fig. 10 depicts the observed changes in the chemical nature of Ba as a function of loading, where LT-$BaCO_3$ corresponds to desorption temperatures of 400-800°C and HT-$BaCO_3$ corresponds to bulk-like $BaCO_3$ with desorption temperatures approaching 1050°C. XRD patterns indicative of crystalline $BaCO_3$ were observed in samples with loadings of 16.7 wt % and higher.

Lietti et al. [39] also observed diffraction patterns indicating the presence of both monoclinic and orthorhombic $BaCO_3$ after calcination of a Pt/Ba/Al_2O_3 (1/20/100 w/w) at 500°C, but noticed with subsequent lean-rich cycling (lean: NO+O_2; rich: H_2) $BaCO_3$ was exchanged for BaO and/or $Ba(OH)_2$. In summary, researchers have reported that NSR catalysts contain only BaO [100,162], only $BaCO_3$ [27] and mixtures of BaO and $BaCO_3$ [163,180]. Differentiating between Ba phases is important because thermodynamic calculations infer $BaCO_3$ to be a relatively inactive storage component due to the higher stability of barium carbonates over barium nitrates, if bulk-like properties are assumed [44]. However, these

calculations do not account for support interactions with the dispersed compounds. As shown previously, these interactions can be significant, especially at lower loadings of Ba [161]. Cant and Patterson [32] concluded that CO_2 has no effect on NO_2 uptake, but others [29,44,45,181–183] reported a negative effect for CO_2 on the storage of NO_X. Since the active storage component is most likely BaO [44,47,184,185], but the catalyst may also contain significant amounts of $BaCO_3$ [27,39,161,163,180], it is important to establish a mechanism by which NO/NO_2 interacts with $BaCO_3$ to form BaO and/or $Ba(NO_3)_2$, especially in the presence of excess CO_2 because CO_2 is always going to be present in exhaust environments. Broqvist et al. [47] attempted to do so in a DFT study and they demonstrated decarbonation of the surface to be promoted by the presence of NO_2 and argued that forming a NO_3^{2-} species significantly reduces the energy cost for CO_2 desorption. Conversely, Sedlmair et al. [31] only noticed decarbonation of the surface if NO was present and NO_2 was not observed to facilitate decomposition of supported barium carbonates.

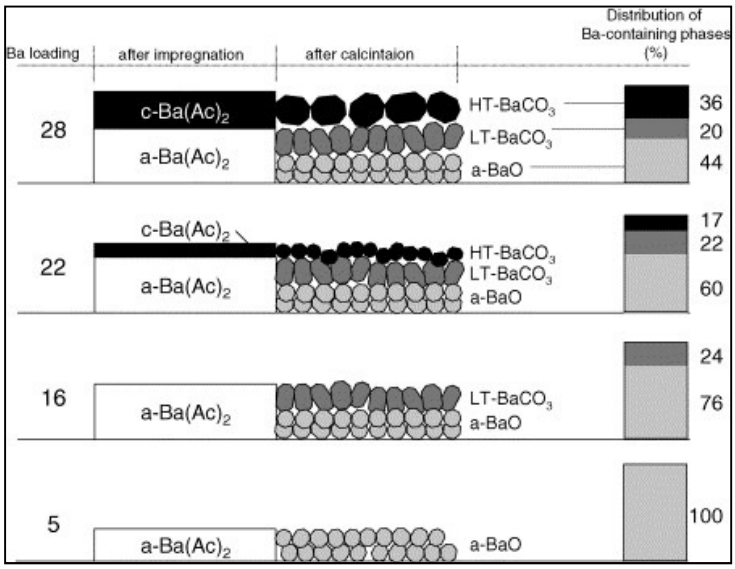

Figure 10. Pictorial representation of the chemical nature of Ba on Al_2O_3 at different loadings, Piacentini et al. [161].

In summary, characterization of calcined $Pt/BaO/Al_2O_3$ samples using XRD and FTIR have repeatedly shown the presence of a "bulk-like" $BaCO_3$ phase [34,37,161,179]. However, Frola et al. [179] and others have demonstrated that this phase undergoes a morphological transformation during NSR cycling treatments, in the absence of additional gas phase CO_2, leading to the formation of highly dispersed BaO [21,34,45,65]. Zhou et al. [186] demonstrated that calcining supported $Ba(NO_3)_2$ in air leads to the formation of $BaCO_3$, which indicates the reversibility of the exchange between barium nitrate and barium carbonate.

Storage of NO_X on $BaO/BaCO_3$ occurs through the formation of surface nitrites, surface nitrates and bulk-like nitrates depending on the NO_X source (i.e., NO, NO+ O_2, or NO_2), time of exposure, temperature and the presence of water [21,22,31,33,34,43,187]. For example, Seldmair et al. [31] exposed a $Pt/BaO/Al_2O_3$ (1/8/100 w/w) to NO at 50°C and observed formation of linear and bridging nitrites; increased exposure time led to formation of peaks corresponding to N-coordinated nitrites on alumina (1537 cm^{-1}), monodentate nitrites (1340 and 1440 cm^{-1}), linear nitrites on Ba (1422 cm^{-1}) and hyponitrites (1380 cm^{-1}). Exposure to NO_2 at 50°C resulted in the formation of linear barium nitrites (1419 cm^{-1}), bidentate nitrites (1203 and 1332cm^{-1}), chelating bidentate surface nitrates on Al_2O_3 (1564 cm^{-1}), and monodentate nitrates on BaO (1429 and 1332 cm^{-1}). Nova et al. [21,34,40] did not observe the formation of nitrites when a $Pt/Ba/Al_2O_3$ (1/20/100 w/w) was exposed to NO_2 at 350°C, but many others observed the formation of both nitrites and nitrates upon exposure of NO_2 [27,31,33,41]. Exposure of a $Pt/BaO/Al_2O_3$ (1/8/100 w/w) to NO + O_2 at 50°C led to the formation of surface nitrites on Ba (1200cm^{-1}), linear Ba nitrites (1419 cm^{-1}), bridging bidentate nitrates on Al oxide (1619 cm^{-1}), chelating bidentate surface nitrates (1561 and 1290 cm^{-1}), linear nitrites on Al (1479 cm^{-1}), and monodentate nitrates on BaO (1424 and 1332 cm^{-1}) [31]. The thermal stability of the adsorbed

NO_X species increased as follows: Al nitrites (linear, N-coordinated) < Ba nitrites (linear, monodentate) < Al nitrates (bridging bidentate, chelating bidentate) < Ba hyponitrites < Ba nitrates (monodentate). Therefore, under realistic exhaust conditions the stored species are most likely in the form of bidentate nitrates on alumina, monodentate nitrites on alumina, monodentate nitrates and nitrites on barium, and bridge bonded bidentate nitrites over barium [21,22,27,33,34,41,112], as summarized in Table 2.

Additionally, Szanyi et al. [188] demonstrated that both bidentate (surface: 1300 and 1574 cm^{-1}) and ionic (bulk: 1320 and 1420 cm^{-1}) nitrates are formed in BaO-containing samples and that the relative intensity of the ionic nitrates increase with BaO coverage. They also observed a transition from bidentate nitrates to ionic nitrates with increasing temperature in a 20 wt % BaO/Al_2O_3 sample. Conversely, a decrease in ionic nitrates was observed for the case of an 8 wt % BaO sample. Desikusumastuti et al. [50] also observed the formation of bulk $Ba(NO_3)_2$ from surface nitrites and nitrates at elevated temperatures. The study was performed using varying sizes of $BaAl_{2x}O_{1+3x}$ particles, which have previously been regarded as a source of deactivation for the BaO [162]. The authors demonstrated that Ba^{2+} ions could be extracted from the larger barium-aluminate particles to form $Ba(NO_3)_2$ and deactivation due to the formation of $BaAl_2O_4$ could be reversible. Hodjati et al. [189,190] also mentioned $BaAl_2O_4$ particles to be a viable NO_X storage material because they are unable to interact with CO_2 and may have some resistance to sulfur poisoning. Another factor known to affect the size of these particles is the presence of water. Szanyi et al. [187,191] demonstrated using TPD, XRD and FTIR that nitrated (NO_2 exposure) samples exposed to water form crystalline $Ba(NO_3)_2$ particles, which decomposed to highly dispersed BaO in the range of 640-940 K. Figs. 11 and 12 demonstrate the influence of water and temperature on stored NO_X.

Table 2. FTIR Band Assignments for Nitrite/Nitrate Species on Ba/Al_2O_3 NSR Catalysts

Structure	Assignment	Wavenumber (cm^{-1})	Ref.
Adsorbed on Al			
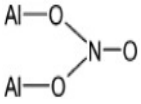	Bridging bidentate nitrate	1627-1619, 1180 - 1260	[31,33,34]
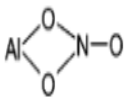	Chelating bidentate nitrate	1569-1561, 1180-1290	[31,33,34]
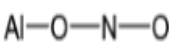	Linear nitrite	1537, 1480*, 1083	[31,33]
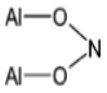	Bridged bidentate nitrite	1300, 1200-1230	[31,33,34]
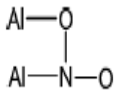	Bridged N-coordinated nitrite	1522, 1160	[31,33]
$Al^+NO_3^-$	Bulk Nitrate	1397	[33]
Al^+NO^-	Hyponitrite	1343	[33,34]
Adsorbed on Ba			
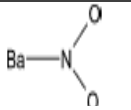	Monodentate nitrite	1440, 1340	[31,33,34]
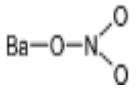	Monodentate nitrate	1429-1422, 1332	[31,33]
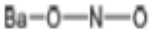	Linear nitrite	1422-1419	[31,33]
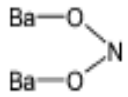	Bridged bidentate nitrite	1300, 1230	[31,34]
Ba^+NO^-	Hyponitrite	1316	[33,34]

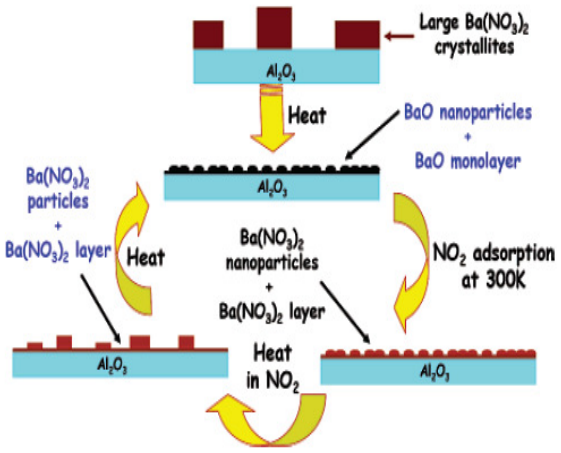

Figure 11. The effect of temperature on the morphology of BaO/Al_2O_3 NSR catalysts, Szanyi et al. [192,193].

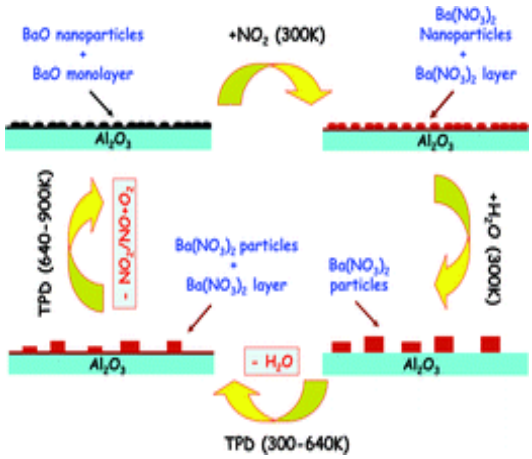

Figure 12. The effect of water on the morphology of BaO/Al_2O_3 NSR catalysts, Szanyi et al. [187,191].

Interaction of CO_X on Ba has also been studied because CO_X and NO_X could be competing for the same storage sites [37,179]. Epling et al. [37] studied $Pt/BaO/Al_2O_3$ (2/20/100 w/w) exposed to CO_2 at room and observed formation of surface Al- and/or Ba-bicarbonates (1232, 1448 and 1650 cm^{-1}), bidentate carbonates (1349 and 1598 cm^{-1}), CO bound to Pt (2030 cm^{-1}) and adsorbed CO_2 (2347 cm^{-1}). Heating led to a decrease in the peaks corresponding to bicarbonates, while the peak at 1448 cm^{-1} remained the same. This indicated that a stable, bulk-like barium carbonate phase had formed. A new peak at 1402 cm^{-1} also appeared and was assigned to unidentate carbonates. Exposure to CO + O_2 at RT led to a prominent band at approximately 2067 cm^{-1}, but the rest of the spectrum remained fairly clean. Heating resulted in formation of bidentate carbonates and bulk-like barium carbonate and closely resembled the spectra for the CO_2 adsorption experiments. At higher temperatures, the primary surface species formed were Ba-formates (1359, 1369 and 1585 cm^{-1}). Exposure to CO at higher temperatures resulted in substantially lower carbonate formation than in the case of CO_2 and CO + O_2, but formation of bulk like species was still observed, which demonstrated the tendency for BaO to form bulk like carbonates. H_2O was observed to facilitate interconversion between the

adsorbed species. In a room temperature study by Frola et al. [179], exposure of CO_2 led to bands assigned to surface carbonates, bridged carbonates on Ba and Al, bridged, chelating and a relatively small amount of monodentate carbonates on Ba sites, with relative intensities related to Ba loading. Interestingly, Frola et al did not notice the reformation of the bulk-like or orthorhombic $BaCO_3$ in the time scale of their experiments, which could point to an active phase comprised mainly of less stable surface carbonates. Table 3 depicts FTIR band assignments for carbon and sulfur containing species on Ba.

Table 3. FTIR Peak Assignments for C and S containing Species on Ba/Al_2O_3 NSR Catalysts

Assignment	Wavenumber (cm^{-1})	Ref
Carbon Containing Species		
Unidentate carbonate	1747, 1403	[37]
Bicarbonate	1656, 1448, 1238	[37]
Bridged carbonate	1620, 1280	[179]
Bidentate carbonate	1598-1530, 1350	[37,179]
Formate	1585, 1398-1357	[37]
Monodentate carbonate	1460, 1320	[179]
Isocyanates	2169, 2230	[37,179]
Adsorbed CO_2	2350	[37]
Sulfur Containing Species		
Hydrogen-bonded sulfites	3638, 3570, 972	[35]
Tri- coordinated sulfates on alumina	1318, 1040	[22,35,36]
Bulk barium sulfate	1249 1168	[22,35,36]
Surface bidentate barium sulfate	1107, 1060	[22,35,36]

One disadvantage of using Ba as a storage component is its high susceptibility to sulfur poisoning [6]. Mahzoul et al. [121] reported that BaO, alumina and ceria exposed to SO_2 formed various sulfate species, which in the case of $BaSO_4$ did not decompose until approximately

1000°C. Engstrom et al. [105] observed the degree of deactivation to be proportional to the amount of sulfur exposed. Fridell et al. and others have observed sulfur deactivation to be more severe during the rich phase [35,56,103,194–196]. Sedlmair et al. [36,102] demonstrated the appearance of bands at 1120 and 1060 cm^{-1} after 1 min of exposure, which were assigned to the S-O stretching vibrations of bidentate sulfates on BaO. After 5 min, bands at 1350 1248, 1155 and 1040 cm^{-1} appeared in addition to the bands in the range 1060-1000 cm^{-1}. The bands at 1248 and 1155 were assigned to bulk barium sulfate, while the bands at 1350 and 1040 cm^{-1} were assigned to the S-O vibration of tri-coordinated sulfate species on Al_2O_3. Flushing in He and reduction in propylene resulted in negligible changes, which demonstrated the high stability of the formed sulfate species. Others have also seen the formation of these surface and bulk sulfur species on Ba and Al_2O_3 [22,35,194,196]. Furthermore, BaO was observed to form $BaSO_4$ even in the absence of gas phase oxygen [22,108]. Courson et al. [30] demonstrated that regeneration of sulfur poisoned NO_X traps occurred more readily if the overall sulfur exposure during the poisoning process was lower. When the extent of poisoning was less than 30% of the BaO, the initial NO_X storage capacity could be completely recovered using an extended rich environment. However if the extent of poisoning was high, it was impossible to recover the initial NO_X storage capacity. Scheier et al. [197] determined that regeneration occurred more readily in rich environments (λ= 0.99-0.94), with λ= 0.94 showing the highest sulphate removal, and at higher temperatures (660-720°C). Increasingly rich environments at higher temperature also led to higher concentrations of effluent COS and H_2S. The authors suggested optimization of λ and the regeneration temperature to obtain selective desorption as SO_2. In summary, during lean conditions SO_2 can be oxidized over Pt to form surface and bulk barium sulfates[111], but SO_2 can also directly react with BaO to form $BaSO_4$ [22,71,108]. During rich periods, SO_2 was

reduced to form Pt-S and BaS [35,36,71,108], which can then be re-oxidized during subsequent lean conditions to form bulk like $BaSO_4$ [35,102,196]. Furthermore, cycling between lean and rich environments in the presence of sulfur seemed to preferentially poison sites near the Pt/BaO interface, which could explain the rapid deactivation of Ba containing NSR catalysts since the Pt/BaO interface is an important property of these materials, as discussed previously [36,71,102,111].

POTASSIUM CONTAINING NSR MATERIALS

Potassium is the 2nd most commonly used storage material in NSR catalysts. In comparison to Ba, K has been reported to exhibit higher storage capacity at higher temperatures, but lower storage capacity at lower temperatures [198]. Choi et al. studied the low temperature storage region using spaci-MS techniques to try and elucidate why K performance was inferior to Ba at low temperatures [19]. They observed the WGS reaction to have little impact on $Pt/K/Al_2O_3$ samples and suggested that CO may poison Pt sites below 200 °C. Later, Choi et al. found $Pt/K/Al_2O_3$ to be active for the WGS reaction, but only after all gas phase O_2 had been consumed by oxidation of CO to CO_2 [199]. Additionally, CO oxidation caused a considerable exotherm which raised the storage-phase temperature. Primary NO_X release/reduction was vigorous and proceeded shortly after the rich period began with small NO or N_2O slip. Secondary NO_X release/reduction occurred at later times and produced mainly NH_3. Production of NH_3 could be explained by *in situ* generation of H_2 though the WGS reaction, which then reacted with NO_X over Pt to form NH_3. One possible reason for the differences at low temperatures over $Pt/K/Al_2O$ NSR catalysts is the proposed increase in the thermal stability of nitrites/nitrates on K [198]. Park et al. compared BaO/Al_2O_3 and K_2O/Al_2O_3 using NO_2-TPD measurements and observed similar NO_2-TPD profiles, but co-impregnation of K and Ba did

induce a shift to higher temperatures for desorption of NO_X, which indicated that co-loading K and Ba could increase the stability of stored nitrates. Unfortunately, the Ba loading was only 6.8 wt % and the K loading was only 1.5wt%, which is much lower than typical NSR catalyst formulations. More recently Matarese et al. [200] reported that thermal release of NO_X from a $Pt/K/Al_2O_3$ catalyst began around 350 °C, which is very similar to values reported for the $Pt/Ba/Al_2O_3$ catalysts [34,201].

Numerous FTIR/DRIFTS studies have been conducted for $Pt/K/Al_2O_3$ samples [146,165,198,202–208]. Above 200 °C, storage occurred as an ionic nitrate (1380 cm^{-1}) on K and bidentate nitrates (1535 and 1320 cm^{-1}) on Al_2O_3. Below 200 °C, storage occurred as an ionic nitrite on K and a nitrite species on Al_2O_3. These nitrite species were later oxidized to nitrates by gas phase NO_2. Toops et al. [198], Prinetto et al. [165] and Liu et al. [206] all observed similar trends for NO_X adsorption as a function of temperature. At lower temperatures, storage occurred mainly as nitrites; but as the temperature was increased, storage occurred mainly as ionic nitrates on K. Thermal desorption of nitrates began at approximately 300 °C and all nitrites/nitrates were completely removed by 500 °C. These results are in agreement with the previously mentioned study by Park et al [164], as shown in Figs. 13 and 14. In this case, Liu et al. [206] used a TiO_2-ZrO_2 supported samples, whereas Toops et al. [198] and Prinetto et al. [165] used Al_2O_3 supported samples, but generally the trends were the same.

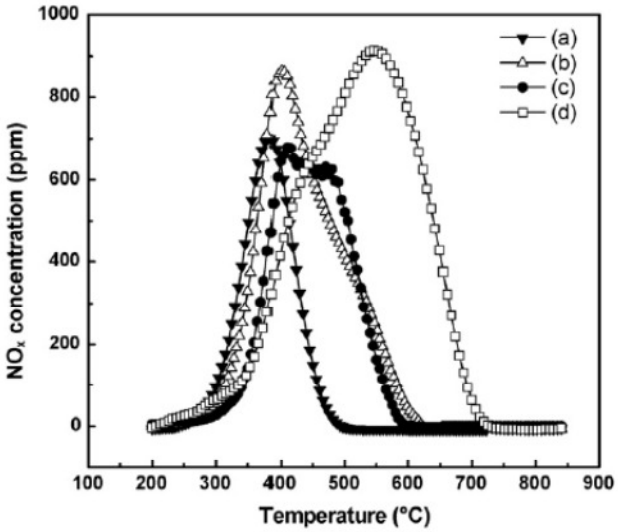

Figure 13. NO_2 evolution profiles for Ba and/or K supported on Al_2O_3 where (a) Pure Al_2O_3, (b) 6.7 wt % Ba/Al_2O_3, (c) 1.6 wt K/Al_2O_3, and (d) 6.7 wt % Ba and 2.7 wt % K/Al_2O_3, Park et al. [164].

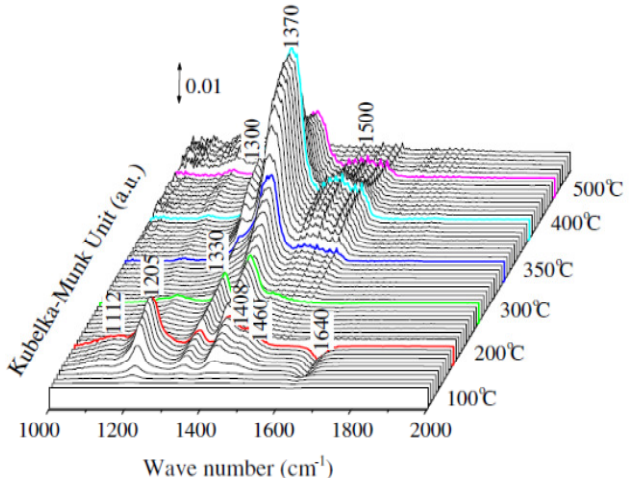

Figure 14. *In situ* DRIFTS spectra of $Pt/K/TiO_2$-ZrO_2 after exposure to 400 ppm NO + 5% O_2 for 10 min at temperatures of 100, 200, 300, 350, 400 and 500 °C, Liu et al. [206].

Lesage et al. [205] and Castoldi et al. [202] proposed that NO_X was stored according to a "nitrite" route, where NO_2 adsorbed as a nitrite and was then further oxidized to a nitrate by either gas phase NO_2 or O_2. Castoldi et al. [202] also proposed that NO_X may be stored by a disproportionation route as previously observed in the case of Ba. Toops et al. [198] go into more detail regarding NO_X storage mechanisms on K, but generally their mechanisms fit into the two listed above. Toops et al. [198] also proposed different types of K sites, as was the case for Ba [198,205,206]. Toops et al. [198] and Liu et al. [206] differentiated sites based on their proximity to Pt, whereas Lesage et al. [205] defined surface and bulk storage sites. Generally, sites in close proximity to Pt were thought to be responsible for rapid NO_X storage since Pt can oxidize NO to NO_2. Sites far from Pt, while capable of storage, were only significant during later times once all of the "fast" sites were filled. The sites farther from Pt probably rely on disproportionation and dismutation mechanisms and are really not relevant to NSR catalysts unless NO_2 is used as the NO_X source or very long storage times are employed. However,

disproportionation mechanisms are worth mentioning since they will always be operating simultaneously with the Pt-assisted NO_X storage mechanism and will therefore constitute some fraction of the total storage observed. On the contrary, Lesage et al. [205] argued that site differentiation based on location of Pt particles was unclear and proposed that storage initially occurred rapidly on surface potassium sites, where storage was controlled by the rate of NO oxidation. At later times, NO_2 must diffuse into the bulk for storage to occur, which was a slow process and led to dramatic NO_X slip.

The morphology of $Pt/K/Al_2O_3$ catalysts was investigated by Prinetto et al. [165] XRD patterns of a 1% Pt/ 5.4% K/Al_2O_3 (w/w) catalyst exhibited several low intensity peaks which inferred contributions from monoclinic K_2CO_3 and cubic K_2O. Subsequent FTIR experiments revealed strong peaks at 1570 and 1350 cm^{-1}, which were characteristic stretching frequencies for surface bidentate carbonates. A strong peak at 1420 cm^{-1} was not observed. Bulk K_2CO_3 only exhibited one stretching frequency at 1420 cm^{-1}. Furthermore, outgassing at 823 K or heating in NO_2 at 623 K followed by outgassing at 823 K was sufficient for removal of the peaks at 1570 and 1350 cm^{-1}. This inferred that carbonate species stored on K/Al_2O_3 at room temperature have low stability and were removed easily. The FTIR is in agreement with XRD patterns, where small amounts of K_2CO_3 were present on the samples before reaction. K also stabilized Pt, where sintering of Pt particles after reaction was lower on $Pt/K/Al_2O_3$ than Pt/Al_2O_3.

Direct comparisons between $Pt/Ba/Al_2O_3$ and $Pt/K/Al_2O_3$ catalysts have been reported by several groups [136,200,202,208,209]. Pieta et al. [208] and Matarrese et al. [200,209,210] reported $Pt/K/Al_2O_3$ to be a better catalyst for simultaneous soot removal and NO_X storage and reduction, but both catalysts were able to oxidize soot. Sakamoto et al. [211] compared K and

Ba supported catalysts on a millisecond time scale and revealed that NO_X release from $Pt/K/Al_2O_3$ samples was faster than $Pt/Ba/Al_2O_3$, which inferred $Pt/K/Al_2O_3$ to be more active during reduction while both samples demonstrated similar activity during storage. Alternatively, Castoldi et al. [202] observed that $Pt/K/Al_2O_3$ and $Pt/Ba/Al_2O_3$ catalysts had different activity if H_2 or NH_3 were used as reductants. $Pt/K/Al_2O_3$ was reported to be more active when NH_3 was used, while $Pt/Ba/Al_2O_3$ was more active when H_2 was used. The relative activity of the stored NO_X species and metal support interactions (i.e. Pt-K vs. Pt-Ba) were both suggested as a potential causes for this behavior. FTIR data supported the previous case, where the relative concentration of ionic nitrates to bidentate nitrates depended on the storage material, but higher activity at lower temperatures on $Pt/K/Al_2O_3$ during reduction may infer the latter case to be important as well. On the other hand, Prikhodko et al. [136] observed no significant differences between commercial $Pt/K/Al_2O_3$ and $Pt/Ba/Al_2O_3$ (formulations also included Pd, Rh, Ce, Mg and Zr) catalysts if longer regeneration times were used. Therefore, differences in $Pt/Ba/Al_2O_3$ and $Pt/K/Al_2O_3$ may be irrelevant during actual operation.

Potassium, like barium, was also susceptible to sulfur poisoning. Toops et al. [212] reported that deactivation due to sulfur exposure was dependent on the temperature and the time of exposure. Exposure of the LNT catalyst at 200 °C showed mild deactivation even after only 15 hours of exposure. However, NO_X storage capacity at this temperature was also low. At 400 °C, sulfur deactivation was rapid and the catalyst was completely deactivated after only 9 hours of exposure. Temperature programmed regeneration under rich conditions (5600 ppm CO, 3400 ppm H_2, 5% CO_2 and 5% H_2O) up to 800 °C mostly restored catalytic activity, which was not always true for Ba/Al_2O_3 samples [30]. Others have also shown deactivation of K containing catalysts in the presence of SO_2, where doping of Al_2O_3 into TiO_2-ZrO_2 to form a

nanocomposite-structure support seems to be especially promising for sulfur tolerance and removal. Nanocomposite-type supports are discussed in the follow section, where Fig. 16 represents the general idea [155,206,213–216]. Dissolution of K_2O in water could also be a problem since automotive catalysts can experience very high levels of water both from engine exhaust and ambient environmental conditions [164]. Lastly, $Pt/K_2Ti_2O_5$, $Cu/K_2Ti_2O_5$, $Pt-K/MgAl_2O_4$, $[Ca_{24}Al_{28}O_{64}]^{4+} \cdot 4O^-/K$, $K_XGa_XSn_{8-X}O_{16}$, K/La_2O_3 and $Pt/K-\beta Al_2O_3/Pt$ (electro-catalyst) have been investigated for NSR applications, but the results were omitted for brevity [130,131,217–223].

1.3.3.3 SUPPORTS

The support in an NSR catalyst primarily provides a surface to disperse precious metal and storage components, but it can also help with storage capacity, reduction activity, sulfur durability, thermal stability and may alter the catalytic activity of the metals or storage component. Alumina is by far the most commonly used support, but CeO_2, ZrO_2, TiO_2, MgO, varying mixtures of those elements, hydrotalcites and perovskites have all been tested for improved catalytic activity in NSR performance.

SINGLE OXIDE SUPPORTS

The first NSR catalysts were composed of Pt and Ba deposited on γ-Al_2O_3 [8]. Alumina was chosen because it offered a high surface area and methods for increasing the thermal stability and sulfur tolerance through incorporation of BaO, La_2O_3 and SiO_2 with and without heat treatments were previously established [7]. Shimizu et al. [224] demonstrated that NO_X storage and reduction rates could be altered simply by changing the support. NO_X storage capacity for Pt and Ba on various supports decreased as follows: $MgO > Al_2O_3 > ZrO_2 > SiO_2$. However, reduction activity for Pt and Ba on various supports decreased as follows: $Al_2O_3 >$

ZrO_2 > SiO_2 > MgO. The authors suggested that the inherent acid – base properties of the support either increased or decreased NO_X storage and reduction activity. Therefore, alumina exhibited a good compromise between NO_X storage and reduction. Corbos et al. [225] observed similar trends for mixed oxides. In addition to providing a surface to disperse Ba, alumina is also capable of storing some NO_X, as Lindholm et al. observed significant amounts of NO_X storage on Pt/Al_2O_3 samples with maximum storage occurring at 200 °C [182]. Westerberg et al. [33] assigned these species to monodentate, bidentate and bridged nitrites and nitrates on alumina and similarly found alumina to be an important storage component below 300 °C. Cant et al. [31,32] also observed storage on Al_2O_3, but the thermal stability of these species was much lower than those formed on Ba. Piacentini et al. [161,226–228] studied the thermal stability of carbonate and nitrate species on Pt – Ba samples supported on Al_2O_3, ZrO_2 and SiO_2 and found that the support significantly affected carbonate and nitrate stability on Ba. Decomposition of $BaCO_3$ supported on Al_2O_3 and SiO_2 began at around 250 – 300 °C, which was surprisingly low in comparison to the bulk decomposition temperature of approximately 800 °C. However, $BaCO_3$ supported on ZrO_2 decomposed primarily between 820 – 1000 °C, which was more similar to unsupported $BaCO_3$. In later works, Piacentini et al. [161,227,228] studied CeO_2 in comparison to SiO_2, ZrO_2, and Al_2O_3 and performed a detailed study on $Pt\text{-}Ba/Al_2O_3$ catalysts. They concluded that $Ba(NO_3)_2$ and $BaCO_3$ exhibit different thermal stabilities based on the support and loading of Ba. Formation of a low temperature $BaCO_3$ phase (LT-$BaCO_3$ – decomposition of $BaCO_3$ from 400 – 800 °C) was related to the storage activity for different samples. This phase was deemed the most relevant to NO_X storage and reduction because Ba is able to form stable NO_X species at temperatures of interest, but does not form bulk like $BaCO_3$. In summary, Pt and Ba supported on CeO_2 and ZrO_2 formed higher amounts of LT-$BaCO_3$ at

lower loadings, whereas Pt and Ba supported on Al_2O_3 and SiO_2 required higher loadings to form LT-$BaCO_3$. SiO_2 only formed $BaCO_3$ species at the highest loadings. The results from these studies are summarized in Fig. 15. Additionally, Cheng et al. [229] performed DFT calculations for NO_2 adsorption on unsupported BaO clusters and BaO clusters supported on γ-Al_2O_3. Their results indicated a synergistic effect between BaO and Al_2O_3 for NO_2 adsorption. They concluded that NO_2 preferentially binds to interfacial regions between BaO and Al_2O_3 for sub-monolayer coverages of BaO. While Pt-Ba/Al_2O_3 systems make good NSR catalysts, they are also susceptible to deactivation through formation of $BaAl_2O_4$ [162,192] or poisoning by sulfur [35,71,103,105,108,194,195]. Therefore, other single oxide and mixed-oxide supports have been investigated for increased thermal stability and sulfur tolerance.

Recently, CeO_2 has been suggested as a viable alternative to Al_2O_3. Maeda et al. [230] demonstrated that NO_X storage capacity decreased as follows for 1Pt/20 Ba (wt%) supported on CeO_2 > $Ce_{0.5}Zr_{0.5}O_2$ > Al_2O_3 > ZrO_2 > TiO_2 > SiO_2. However, reduction activity proceeded in the reverse order, which is in general agreement with others in the literature [224,225]. In previous works, Piacentini et al. [161,226–228] studied the effect of Ba loading on different supports and concluded that optimum Ba loading changed based on the support used. Therefore, CeO_2 could be excellent support for maximum NO_X storage efficiency. Unfortunately, Maeda et al. [230] found CeO_2 to be a poor support when reduction activity was studied. Poor reduction activity on CeO_2 was attributed to 1.) the basic nature of the support, which stabilized surface and bulk nitrates leading to longer regeneration times and 2.) high oxygen storage capacity, which provided facile oxygen during reduction and led excessive to consumption of reductants that could otherwise be used for the reduction of NO_X.

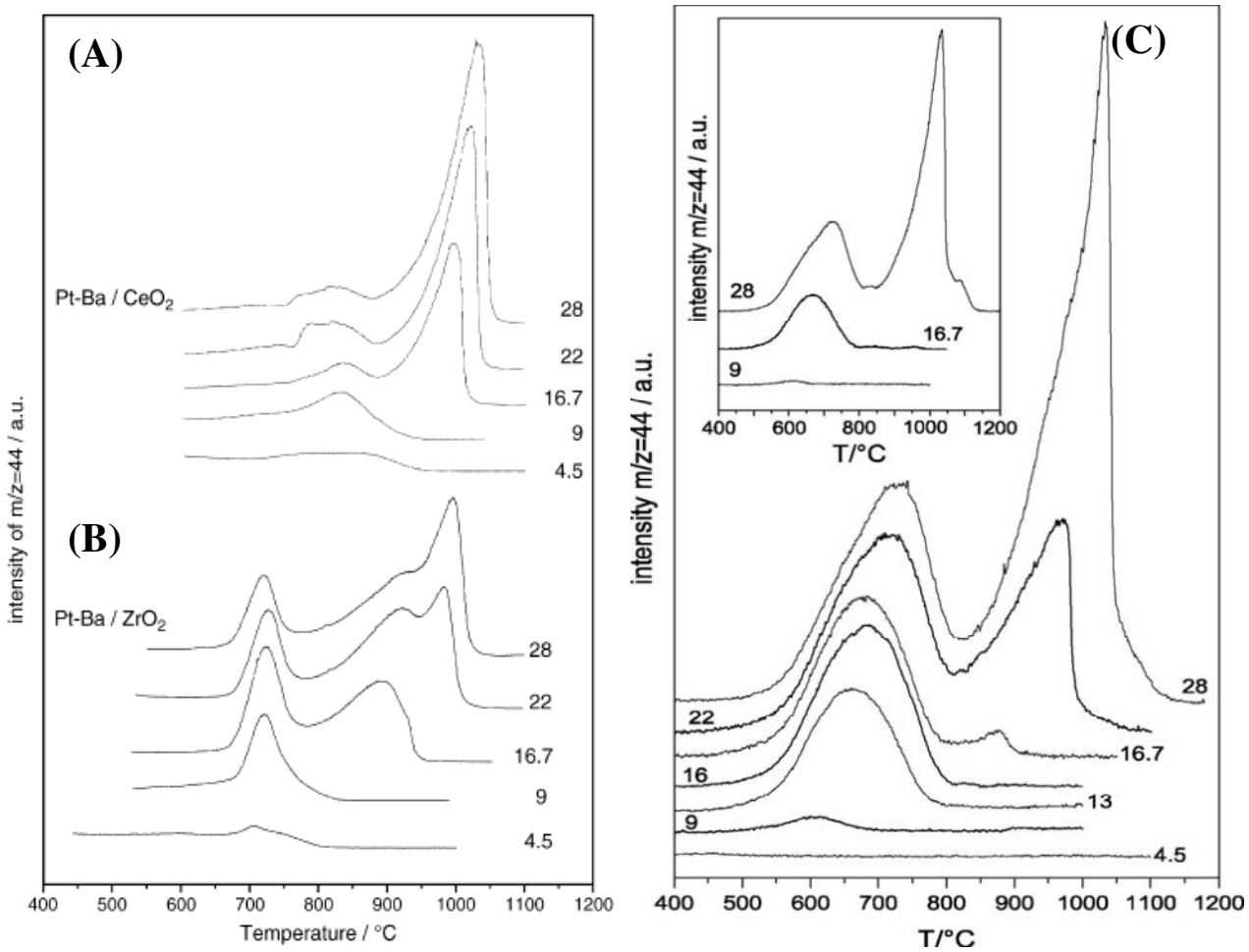

Figure 15. CO_2 evolution profiles of $BaCO_3$ decomposition formed during calcination at 500 °C of the $Ba(Ac)_2$ precursor for varying loadings of Ba on different supports where (A) Pt-Ba/CeO_2, (B) Pt-Ba/ZrO_2 and (C) Pt-Ba/Al_2O_3. Pt-Ba/SiO_2 not shown, Piacentini et al. [161,228].

Previously, Martin and Duprez [231] investigated the acidity and basicity of many support materials. CeO_2 was characterized as a very basic support with little acidity, whereas alumina has both acidic and basic properties. This helps explain why alumina exhibits good characteristics for NSR operation. Interestingly, 12 wt % CeO_2 doped alumina still retained most of its acidic properties, but also increased in basicity. Therefore, CeO_2 may be more beneficial as a promoter than as a support (this aspect will be discussed in section 1.3.3.4 on Promoters). While CeO_2 suffers from reduction activity, it has gained support in the literature because it has

been suggested to increase sulfur tolerance, promote the WGS reaction and stabilize Pt particles against sintering during high temperature excursions [101,109,151,232–234]. Kim et al. [109] observed BaS formation in Pt-BaO/CeO_2 to be much lower than Pt-BaO/Al_2O_3 samples, which implied that CeO_2 suppressed the formation of these crystallite species. However, the formation of sulfur species with lower oxidation states was enhanced. H_2-TPRX evolution profiles showed negligible formation of H_2S, which inferred the H_2S produced from reduction of $BaSO_4$ was readily re-adsorbed by CeO_2 to form ceria-sulfur complexes. The proposed mechanism was in agreement with S XANES spectra, where the initial and final intensities of sulfur compounds remained fairly constant. Kwak et al. [101] also observed better sulfur tolerance for Pt-BaO/CeO_2 samples and excellent resistance to Pt sintering. Casapu et al. [232,233] observed that sintering of Pt was prevented due to formation of a temporary perovskite that anchors Pt to the support. At lower temperatures in oxidizing environments (600 – 700 °C), Pt reacted with Ba and CeO_2 to form $BaPtO_3$. At higher temperatures (> 800 °C), formation of the double perovskite Ba_2PtCeO_6 was observed. Reduction of these species occurred from 130 – 210 °C, which demonstrated the reversibility of the thermal aging. An additional advantage of CeO_2 is that $BaCeO_3$ formed at high temperature were easily decomposed by CO_2 unlike $BaAl_2O_4$ [180,234]. Unfortunately, Ba supported on CeO_2 samples in the presence of CO_2 may form very stable bulk-like $BaCO_3$ species. Lastly, CeO_2 has been suggested as a potential storage component. Svedberg et al. [235] found both Al_2O_3 and Pt/CeO_2/Al_2O_3 stored considerable amounts of NO_X in the region of 100 – 200 °C, but still only half as much as Pt/BaO/Al_2O_3 systems. Philipp et al. [236] observed bands at 1162, 1277, 1067 and 823 cm^{-1} (chelating nitrites), 1021 and 974 cm^{-1} (cis-hyponitrites), 1097 cm^{-1} (trans-hyponitrites), and 792, 1322 and

1607 cm^{-1} (nitrates). Philipp et al. [236] and others [235,237]proposed CeO_2 to be a viable storage material at lower temperatures for lower Ba loadings.

SiO_2 is generally regarded as a woefully inadequate support for NSR components. Piacentini et al. and others observed virtually no storage when Pt-Ba/SiO_2 samples of varying Ba loading were exposed to NO_X [224–228]. Alternatively, ZrO_2, TiO_2 and MgO have potential for good NO_X storage-reduction properties. Yamato et al. [238] studied TiO_2 as a support because TiO_2 is well known to be resistant to sulfur poisoning. Li, Na, K, Cs, Sr, Ba and La were all tested as potential storage components for the Pt/TiO_2 based system. Pt-Na/TiO_2 and Pt-K/TiO_2 performed best for both storage and reduction when SO_2 was absent. In the presence of SO_2, only the Pt-Li_2O/TiO_2 samples activity remained unchanged. All other samples suffered from deterioration of NO storage activity. Although Pt-Li_2O/TiO_2 was outperformed by Na or K based catalysts in the absence of sulfur, it offered excellent sulfur tolerance not observed for other NSR catalysts. ZrO_2 is another promising support for NSR catalysts. As previously mentioned, Shimizu et al. [224] determined ZrO_2 to be less active than Al_2O_3 for NO_X storage, but more active for reduction of NO_X using H_2. However, Piacentini et al. [228] found ZrO_2 to be less active for reduction of NO_X, which was attributed to much lower surface areas of ZrO_2 supports. Lastly, the storage mechanism for NO_X on BaO/MgO systems was studied [239]. Storage proceeded through formation of barium-nitro species that later transformed to nitrite and/or nitrate species. This mechanism differs from the generally accepted mechanisms discussed in section 1.3.2.1 for Pt-BaO/Al_2O_3 systems. The deviation may be explained by the high basicity of MgO supports. Storage above 400 °C was observed, but was suppressed in comparison to lower temperatures. Reduction with CO led to formation of thermally stable $BaCO_3$, but transformation back to $Ba(NO_3)_2$ upon NO_2 exposure was possible. Albeit the

transformation required 90 min to complete, which was drastically longer than usual NSR lean operation times. Therefore, accumulation of CO_2 and subsequent deactivation may occur with increasing cycle time.

MIXED OXIDES

Many publications are devoted to investigation of various mixed oxides as supports. Generally, mixed oxides are of interest for several reasons including: 1.) they may promote higher NO_X storage capacity or storage rate, 2.) increase reduction activity, 3.) stabilize catalytic components against thermal degradation processes and 4.) increase sulfur tolerance of the NSR catalyst.

The most common supports, other than Al_2O_3, are mixed oxides containing mixtures of two or more of the following materials: SiO_2, CeO_2, ZrO_2, TiO_2 and/or Al_2O_3. Takahashi et al. [240] studied the influence TiO_2, ZrO_2 and mixtures of TiO_2-ZrO_2 and found that TiO_2 suppressed sulfur formation on supported Pt-K samples, whereas ZrO_2 prevented solid phase reaction of potassium with the support. At higher temperatures, ZrO_2 rich supports performed better than TiO_2 rich supports, but the opposite was true at lower temperatures. Initially, Corbos et al. [241] determined storage capacity increased as follows: Pt/20Ba/Si < Pt/20Ba/Al5.5Si < Pt/10Ba/Al < Pt/5Ba/CeZr < Pt/30Ba/Al5.5Si < Pt/20Ba/Al < Pt/10BaCeZr. Again, trends in basicity were used to explain storage capacity. CO_2 inhibited NO_X storage for all catalysts, but the effect was more pronounced on more basic supports and with increasing temperature. Water also had a detrimental effect, but the effect was observed more strongly for Al_2O_3 containing supports. While Ce-Zr systems offered the highest storage capacity, realistic experimental conditions favored the Pt/20Ba/Al5.5Si sample. In other works, Corbos et al. [225,241,242] studied the effect of sulfur and aging on similar sets of samples. They found all samples were

negatively affected by sulfur, but could be regenerated after treatment in H_2 at 550 °C. Interestingly, only the $Pt/Ce_{0.7}Zr_{0.3}O_2$ sample was regenerated completely. Additionally, $Ce_{0.7}Zr_{0.3}O_2$ samples exhibited $BaSO_4$ reduction temperatures around 100 °C lower in comparison to Al_2O_3 containing samples. This led the authors to conclude that mixtures of CeO_2 and ZrO_2 could provide better results when compared to conventional Al_2O_3 based systems when sulfur tolerance was considered. Continued work on $Ce_XZr_{1-x}O_2$ mixed oxides predicted Ce rich samples to be particularly interesting because they are especially resistant to sulfur poisoning and produced very little NH_3 during reduction, but the OSC of the materials did lead to higher consumption of reductants during reduction [243]. Other studies on CeO_2-ZrO_2/Al_2O_3[244], $Ce_XZr_{1-x}O_2$ [99], Al_2O_3 doped TiO_2-ZrO_2 [214] and TiO_2-Al_2O_3 [166,245] have been performed in an attempt to further elucidate the role of the support and/or how mixtures of support materials can provide improved results over Al_2O_3 supported samples. Preliminary results indicated positive effects for mixed oxide supports over single oxide options. One particularly interesting example of a novel support combined ZrO_2, TiO_2 and Al_2O_3 to form a thermally stable, sulfur resistant nanocomposite [155,213,215]. Imagawa et al. [155] prepared these nanocomposite samples using conventional co-precipitation techniques. $Al(NO_3)_3 \cdot 9\ H_2O$, $Zr(NO_3)_2 \cdot 2\ H_2O$ and $TiCl_4$ were dissolved in ion exchanged water and then an ammonia containing solution was added for co-precipitation. The synthesized nanocomposite of Al_2O_3 and ZrO_2-TiO_2 (AZT) was then compared to physical mixtures of Al_2O_3 and ZrO_2-TiO_2 prepared in the same way. The nanocomposite samples were much more thermally resistant than samples prepared by physically mixing. Al_2O_3 was suggested to act as a diffusion barrier against aggregation of ZrO_2-TiO_2 particles at high temperatures. Fig. 16 depicts this concept and provides supporting TEM micrographs of the nanocomposite. Further work by Imagawa et al. focused on sulfur durability

of AZT and Ti-doped AZT [155,213]. They found catalysts consisting of Pt, Rh, Ba, and K supported on AZT were much more resistant to both sulfur poisoning and thermal aging than physical mixtures of Al_2O_3 and ZrO_2-TiO_2. Additionally, Ti-doped AZT samples offered increased sulfur tolerance in comparison to the AZT supported samples.

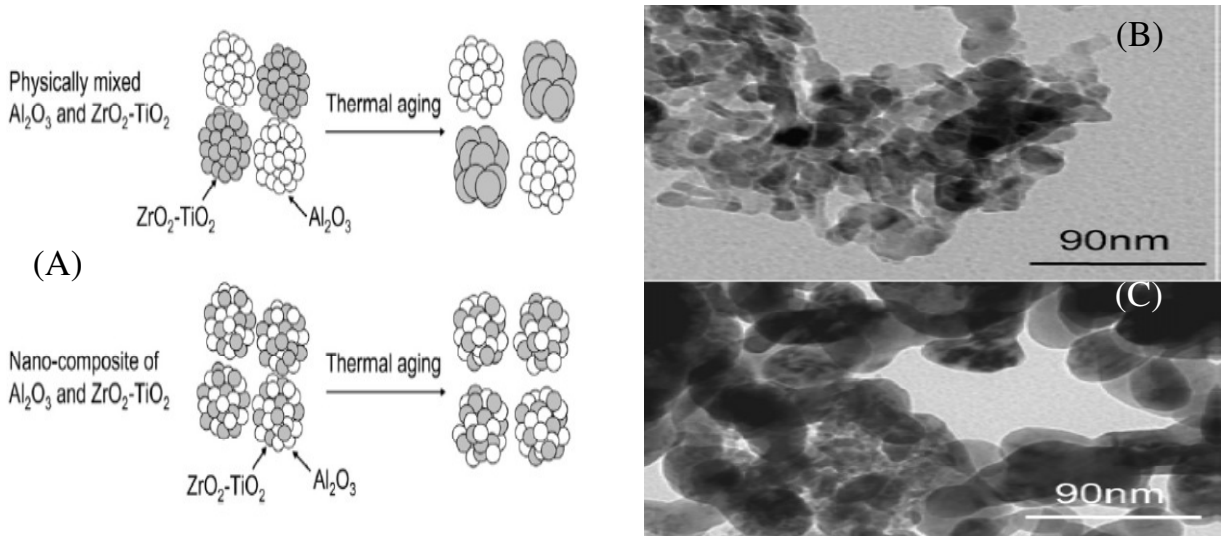

Figure 16. (A) Theoretical concept describing differences in aggregation phenomena for a physical mixture of Al_2O_3 and ZrO_2-TiO_2 vs. a nanocomposite of Al_2O_3 and ZrO_2-TiO_2, (B) FE-TEM micrograph for nanocomposite of Al_2O_3 and ZrO_2-TiO_2 after calcination at 1173 K and (C) FE-TEM micrograph for physical mixture of Al_2O_3 and ZrO_2-TiO_2 after calcination at 1173 K, Imagawa et al. [215].

Hydrotalcites and perovskites are another type of support material applied to NSR catalysts. Centi et al. [246] studied hydrotalcite (HT)-type compounds impregnated with Pt and/or Cu and found they generally outperformed Pt-Ba/Al_2O_3 catalysts prepared by incipient wetness impregnation. The HT catalysts were prepared using a commercially available precursor with an atomic ratio of 66:34 for Mg^{2+} and Al^{3+}, respectively. The most active HT sample contained both 1 wt % Pt and 4% Cu. At low temperatures, the Pt-Cu/HT samples outperformed Pt-Ba/Al_2O_3; however, at intermediate and high temperatures the Pt-Ba/Al_2O_3 sample demonstrated higher NO_X conversion. When sulfur tolerance was studied, Pt-Cu/HT

deactivated less than the Pt-Ba/Al_2O_3 sample, but deactivation was still observed. Hydrothermal treatments were also less detrimental to the performance of Pt-Cu/HT samples in comparison to both Pt-Ba/Al_2O_3 and Pt/HT. Formation of Pt-Cu alloys was suggested as one reason for higher thermal stability and sulfur resistance [246,247]. Fornasari et al. [247,248] demonstrated that the Mg/Al ratio in HT derived samples plays a crucial role in their performance. Samples with lower Mg/Al ratios performed better at lower temperatures, but samples with higher Mg/Al ratios performed better at higher temperatures. This was explained by different susceptibilities for the Mg(Al)O mixed oxide to form the more inactive spinel $MgAl_2O_4$ phase. Later, Morandi et al. [249] proposed that storage on Pt-Mg(Al)O and Pt/Cu-Mg(Al)O occurred through two competing storage mechanisms. NO_2 proceeded through a "dismutation route", while NO + O_2 proceeded through either the "dismutation route" or the "nitrite route". Storage of NO in the absence of O_2 was not observed. Equations 11 – 13 display the "dismutation route", where Equation 13 is the net result of Equations 11 and 12. Notice how similar these proposed storage mechanisms are to those presented for storage on BaO in Section 1.3.2.1.

$$2NO_2 + O^{2-}_{(s)} \rightarrow NO^-_{(s)} + NO^-_{3\,(s)} \quad (11)$$

$$NO^-_{2\,(s)} + NO_2 \rightarrow NO^-_{3\,(s)} + NO \quad (12)$$

$$3NO_2 + O^{2-}_{(s)} \rightarrow 2NO^-_{3\,(s)} + NO \quad (13)$$

Yu et al. [250] and Li et al. [251] proposed slightly different storage mechanisms for hydrotalcite based NSR catalysts. Li et al. [251] proposed that storage of NO_2 occurred without evolution of gaseous NO. Yu et al. [250] also mentioned Equation 13 listed above as a storage mechanism, but additionally mentioned storage through formation of adsorbed N_2O_4 and hyponitrites $(N_2O_2)^{2-}$. Generally, the use of hydrotalcite-like compounds in NSR catalysis can be

summarized by Fig. 17, where Pt-Mg(Al)O, Cu-Mg(Al)O, Pt/Cu-Mg(Al)O, CoMg/Al, Ca_2CoAl-oxide, Ca_2CoLaAl-oxide, Co-Mg, Pt/Co/Mg/Al, Pd/Co/Mg/Al, Ru/Co/Mg/Al and V/Co/Mg/Al have all been considered [246–253].

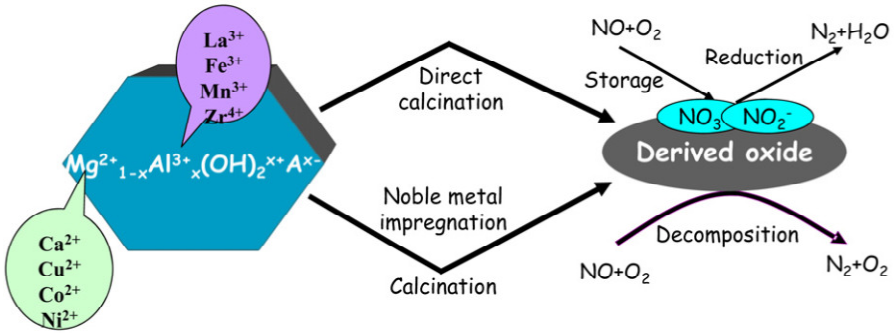

Figure 17 . Preparation of hydrotalcite-like catalysts for NO_X storage/reduction/decomposition applications, Yu et al. [252].

Li et al. [254] studied Ba-Fe-O perovskite type NSR materials prepared by the sol-gel method. After calcination at 750 °C, the main diffraction peaks detected by XRD were perovskite $BaFeO_3$, defect perovskite $BaFeO_{3-X}$, and $BaCO_3$. Calcination at 900 °C led to significant decreases in all three of these phases and an increase in spinel $BaFe_2O_4$, which translated into a NO_X storage capacity (NSC) decrease from 114.7 µmol/g to 15.4 µmol/g. Interestingly, the $BaFeO_3$ sample calcined at 750 °C retained 82% of its NSC during exposure to 100 ppm SO_2, while a reference Pt-Ba/Al_2O_3 samples only retained 15% of its storage capacity. So, perovskites may have lower NSC initially, but their long term sulfur durability may make them a viable alternative to conventional Pt-Ba/Al_2O_3 samples. Zhu et al. [255] observed high activity for direct decomposition of NO even in the presence of O_2 using $La_{2-X}Ba_XNiO_4$ ($x \leq 1.2$) perovskite-type materials. The authors suggested that doping Ba into La_2NiO_4 increased the

oxygen vacancy content, which increased the mobility of lattice oxygen in the perovskite and improved the redox capability of Ni. Ba was used as a promoter because perovskite-type materials traditionally suffer from strongly adsorbed oxygen species on the active site that are hard to remove during regeneration, which subsequently leads to deactivation for these types of materials. Ueda et al. [256] used a (La, Ba)(Fe, Nb, Pd)O_3 perovskite catalyst and obtained 47% NO_X conversion at 523 K, but only stored 3.1 – 11 μmol/g of NO_X, which was substantially lower than storage capacities for Pt-Ba/Al_2O_3 systems. In comparison, Xian et al. [257] measured NSC for a $BaFeO_{3-X}$ perovskite and found storage ranged from 578 – 222.9 μmol/g for samples calcined at 850 and 950 °C, respectively; whereas, a Pt/BaO/Al_2O_3 reference sample only stored 290 μmol/g. Sulfur tolerance was also much greater for the perovskite materials. They retained 61% and 86% of their NSC after calcination at 850 and 950 °C, respectively. The reference Pt/BaO/Al_2O_3 sample only retained 30 % of its initial NSC. Unfortunately, the authors did not measure the cycle averaged conversion for these samples. Recently, Kim et al. [172] demonstrated that a $La_{0.9}Sr_{0.1}MnO_3$ perovskite based LNT catalysts with precious metal loadings of 1.8 Pd/0.2 Rh (g liter^{-1}) outperformed a commercial Pt- based LNT with 1.6 Pt/0.3 Pd/ 0.2 Rh (g liter^{-1}) at 350 °C. Therefore, perovskite based samples could be viable alternative to Pt-Ba/Al_2O_3 because they may be more sulfur resistant and could reduce costs by up to 70% (incurred from incorporation of precious metals) in comparison to Pt based samples. Additionally, $K_2Ti_2O_5$ [130,131,223], Y_2O_3 doped MnO_X metal oxides [258], MnO_X-SnO_2 [259], $MgAl_2O_4$ [217], NbMCM-41 [260], NaY + NbMCM-41[260], $Ti_XZr_{1-X}O_4$ [261], MnO_X-CeO_2 [262], MnO_2/NaY composites [263], $La_{2-X}Sr_{1+X}Cu_2O_{6-\delta}$ ($0 < x < 2$) [173], MnO_y-ZrO_2 [264] and NaY [265] have all been investigated as NSR support materials and show some promise for future study.

1.3.3.4 PROMOTERS

The most common promoters for NSR systems are Rh, Ce, Fe and Co. K, Ni, Cu, Mn, Nd, Si, Ca, Mg, Ti, La or La_2O_3, WO_3, MoO_3, V_2O_5, and Ga_2O_3 have also been investigated. Rabinowitz et al. [143] demonstrated that addition of ceria drastically improved NO_X conversion on Pd/Rh TWCs, especially in combination with Rh, but could also increase the negative impact of sulfur due to its ability to store and release sulfur. Lin et al. [266] studied NO_X storage and reduction on CeO_2 and La_2O promoted $Pt/BaO/Al_2O_3$ and $Pt/SrO/Al_2O_3$ catalysts. $Pt_{2.5}Ce_{30.5}Ba_{33.4}Al_{100}$ and $Pt_{2.5}Ce_{22.5}Ba_{41.7}Al_{100}$ offered the highest storage capacity (1020 and 911 μmol g^{-1}, respectively) and conversion. The $Pt_{2.5}Ce_{30.5}Ba_{33.4}Al_{100}$ sample achieved 100% NO_X conversion at 400 °C. The La_2O promoted $Pt/BaO/Al_2O_3$ and La_2O or CeO_2 promoted $Pt/SrO/Al_2O_3$ exhibited much lower storage capacity and conversion. Similarly, Ji et al. [267] found mixing $Pt/BaO/Al_2O_3$ with Pt/CeO_2 in a 76:26 ratio improved NO_X storage capacity in the range of 200 – 400 °C. H_2-TPR and CO-TPR experiments suggested decreased stability of stored nitrite/nitrate species. Additionally, NO_X conversion and N_2 selectivity were higher for the mixed catalysts. Schmeisser et al. [75] performed dynamic rich/lean reactor studies in the absence of sulfur on Pt, Rh, Ce, Ba and Al_2O_3 containing NO_X storage and reduction materials and observed that ceria was a strong promoter for NO oxidation. Unfortunately, addition of Rh to a Pt/Ba/Ce/Al catalyst completely negated the beneficial role of ceria, which is counterintuitive since synergy of Rh/Ce systems has been demonstrated in TWCs [143]. However, the Pt-Rh/Ba/Ce/Al catalyst drastically outperformed Pt/Al, Pt/Ce/Al, Pt/Ba/Al, Pt/Ce/Ba/Al during steady-state reduction of NO_X in rich environments. This could be explained by high reduction activity of Rh. Unfortunately the authors did not isolate the effect of Rh incorporation on reduction activity (e.g., through analysis of Rh/Al, Rh/Ce/Al and Rh/Ba/Ce/Al

catalysts). Later, Ji et al. [151] studied the effect of adding physical mixtures of La_2O_3-stabilzed ceria to Pt-Rh/BaO/Al_2O_3 NSR catalysts. The ceria mixtures exhibited increased storage efficiency, NO_X conversion and decreased selectivity to NH_3 with increasing ceria content. Increased selectivity to N_2 was attributed to reaction of NH_3 with downstream oxygen stored by ceria. However, mixtures too high in ceria content caused decreased conversion of NO_X. Most likely because a significant portion of the reductant was consumed by oxygen stored in ceria, as evidenced by high reactor temperatures during reduction. Alternatively, the high catalyst temperature could increase the rate of NO_X release that slips from the catalyst before reduction can occur. In later works, Ji et al. and Easterling et al. [139,267,268] studied the effects of sulfur and road aging on Pt/Ba/Al systems promoted by physical mixtures of Pt/CeO_2. In all cases, the addition of ceria or CeO_2-ZrO_2 positively influenced the NO_X storage/reduction properties of the catalysts. Briefly, ceria or CeO_2-ZrO_2 addition can be summarized as follows: 1.) as a supplement to the main storage component – where deactivation of the Ba phase could be compensated by ceria, which could still participate in storage, 2.) ceria has shown to resist phase segregation – when Pt/BaO/Al_2O_3 samples were aged at high temperatures, sintering of Pt led to lower interfacial contact between Pt and BaO, which decreased spillover mechanisms and therefore lowered catalytic activity. Alternatively, sintering of Pt on CeO_2 is hindered due to a strong metal-support interaction, 3.) ceria containing samples exhibited superior sulfation/desulfation characteristics – The ability of ceria to trap and release sulfur could help protect Ba from high levels of sulfur accumulation. Similarly, Kaneeda et al. [174] found Mn and Ce played a beneficial role when incorporated into a RhPt–Naα/Al_2O_3 (α= Ti, Si, Mg, Ca, Mn, Co, Ni, La, and Nd) NSR catalyst. The resulting RhPt–NaMn-Ce/Al_2O_3 sample was then tested in a lean-burn engine and achieved high NO_X conversions even after being calcined at 700

°C, but higher calcination temperatures led to severe deactivation of the catalyst. Conversely, Zou et al. [216] observed a negative influence for both Ce and Co addition on a $Pt/K/TiO_2$-ZrO_2 catalyst. Initially, addition of Co or Ce (as a physical mixture or impregnated on the support) seemed positive because NSC increased from 194 μmol g^{-1} to 280 and 380 μmol g^{-1} for Co and Ce addition, respectively. However after sulfur exposure and subsequent regeneration, the promoted materials lost between 58% - 84% of the initial NSC; whereas the base $Pt/K/TiO_2$-ZrO_2 only lost 4% of the initial NSC.

Yamazaki et al. [269] studied transition metals as promoters for NSR catalysts. $Pt/Ba/Fe/Al_2O_3$, $Pt/Ba/Co/Al_2O_3$, $Pt/Ba/Ni/Al_2O_3$ and $Pt/Ba/Cu/Al_2O_3$ were compared with $Pt/Ba/Al_2O_3$, $Pt/Fe/Al_2O_3$, $Pt/Co/Al_2O_3$, $Pt/Ni/Al_2O_3$ and $Pt/Cu/Al_2O_3$. Prior to aging in 0.08% SO_2 for 5 hrs, addition of Fe, Co and Ni to $Pt/Ba/Al_2O_3$ or Pt/Al_2O_3 samples had no effect. After aging in SO_2, only addition of Fe had a positive effect on catalyst performance. Therefore, the authors concluded that addition of Fe could be beneficial, but addition of Ni and Co had no effect on NSR properties. Cu on the other hand, had a negative effect in all cases. However, Arena et al. [270] reported that Cu could be a promising promoter for addition to NSR catalysts because it was observed to increase NO_X reduction. Hammache et al. [271] also reported that Cu addition increased sulfur tolerance, but diminished NSC in comparison to a reference $Pt/Ba/Al_2O_3$ sample. Formation of a Pt-Cu alloy was suggested to alter the SO_2 oxidation activity of the catalysts, which led to lower deactivation due to sulfur poising. However, SO_2 exposure during reducing environments led to stable sulfur species that were not oxidized in subsequent lean phases. Therefore, activity that was lost during rich sulfur exposures could not be recovered.

Generally, the addition of Co and Fe seem to be more promising than addition of Ni or Cu. However, promotion using Fe yielded contradictory results in the literature. Fanson et al.

[43] studied Fe promoted Pt/BaO/Al_2O_3 samples and suggested that formation of a stable bulk-like nitrate phase inhibited sulfur poisoning, where formation of a bulk-like nitrate phase was not observed in samples without Fe. In a later study, Hendershot et al. [129] determined using high-throughput experimentation, where Pt, Ba and Fe loading were all varied systematically, that the most important catalytic components were Pt and Ba and suggested an optimum wt. loading of 1.25-1.5% Pt and 15-25% Ba. However, earlier publications by Hendershot et al. indicated a positive influence when Fe was incorporated into Pt/Ba/Al_2O_3 NSR catalysts [128,272]. Similarly, Le et al. [273] observed modest promotion of NSC by Fe and increased sulfur tolerance, but a decrease in NO_X conversion. Kayhan et al. [274] demonstrated that the morphology of the surface was dependent on the respective loading of Ba and Fe, which could help explain why contradictory results in the literature have been reported. Luo et al. [275] demonstrate that Fe encapsulates Pt, which decreases the Pt-Ba interaction and leads to decreased NO_X storage capacity. Additionally, Fe selectively catalyzes the reduction of $BaSO_4$ to BaS, which makes sulfur removal more difficult. Therefore, the addition of Co as a promoter may be more promising Fe. For example, Vijay et al. [125] demonstrated that addition of Mn or Fe to a Pt/Ba/Al_2O_3 slightly improved NSC, but addition of Co nearly doubled the NSC. Additionally, a 5% Co/15% Ba/Al_2O_3 (w/w) sample stored equivalent amounts of NO_X as the conventional 1% Pt/15% Ba/Al_2O_3 reference catalyst. While Co was capable of promoting high NSC, Vijay et al. [125] mentioned that incorporation of noble metals would still be necessary to catalyze reduction of stored NO_X since Co exhibited poor reduction activity. Later, Vijay et al. [118] demonstrated that a 0.25% Pt/5% Co/15% Ba/Al_2O_3 catalyst showed superior performance over a 1% Pt/15% Ba/Al_2O_3 catalyst, with ¼ the Pt loading. More recently, Vijay et al. [126] studied the NO_X storage and reduction mechanism for Co containing NSR catalysts. Co was

observed to exist in a highly oxidized state as Co_3O_4, but surface oxygen could be removed from the catalyst by 300 °C. In summary, the promotional role of Co was attributed to increased NO to NO_2 oxidation and increased interfacial contact between Co and Ba leading to increased NO_2 spillover onto Ba. Lastly, Kim et al. [153]examined the effect of Co and Rh promoters. Co was observed to catalyze NO oxidation; Rh catalyzed NO_X reduction. Conversely, Co inhibited NO_X reduction and Rh inhibited NO oxidation. Therefore, the loading of Co and Rh must be carefully balanced to negate the undesired properties of each promoter.

Dawody et al. [276] investigated WO_3, MoO_3, V_2O_5 and Ga_2O_3 as promoters in NSR catalysts for both NO oxidation and sulfur tolerance. In the absence of SO_2, WO_3 and MoO_3 exhibited the highest NO oxidation activity. NO oxidation on $Pt/MoO_3/Al_2O_3$ was least affected by SO_2. Therefore, the authors synthesized a Pt/MoO_3-BaO/Al_2O_3 sample to test for sulfur durability and found it deactivated more quickly than then reference $Pt/Ba/Al_2O_3$ sample. The deactivation method was not clear, but MoO_3 clearly did not increase sulfur tolerance. Lastly, physical mixtures of $Mn/Ba/Al_2O_3$ and $Pt/Ba/Al_2O_3$ have been reported to increase conversion of NO_X and increase sulfur tolerance [277,278]. Ultimately, Ce, Co, Fe, Mn and Rh promoted systems, with particular emphasis on Mn, Ce, Co and Rh, may be interesting for further study because they could lower precious metal requirements and increase sulfur tolerance while maintaining the high activity of conventional $Pt/Ba/Al_2O_3$ systems.

1.3.4 CONCLUSIONS

Since their inception in the mid 1990s, many investigations have been performed and considerable progress has been made in understanding the NO_X storage and reduction process. As evidence, the NO_X storage mechanism has mostly been resolved. However, many aspects of this system remain unsolved and elucidation of results from existing literature is difficult because

very few investigations employ the same conditions. This is in part due to the large number of adjustable parameters including: choice of support, choice of the storage component, loading of the storage component, impregnation method of the storage component, choice of noble metal, loading of noble metal, impregnation method of the noble metal, impregnation order for the noble metal and storage component, precursors employed for impregnation, choice of promoters (Rh, CeO_2 etc.), loading of promoters, lean gas environment (NO, NO+O_2, NO_2), rich gas environment (H_2, CO, C_3H_6), inclusion of CO_2, H_2O or both, lean period duration, rich period duration, S.V. employed, pretreatment used, and lastly the inclusion of sulfur. All of these aspects were covered is this review and it emerges that a fundamental understanding of how each parameter affects the observed operation is still lacking. Furthermore, contradictory reports in the literature are really not too surprising given the large number of adjustable parameters, which ultimately leads to significantly different conditions and/or catalysts in many cases that are ultimately used during evaluation of NSR catalysts and comparison between one study to another can be difficult.

In closing, determination of the reduction mechanism will define target parameters for future development of novel NO_X storage and reduction catalysts, where synergy between the support, storage component, precious metals and promoters in combination with high thermal and hydrothermal stability and increased sulfur tolerance are desirable attributes for the next generation of NO_X storage and reduction catalysts.

1.4 REAL SYSTEMS

1.4.1 EARLY CATALYTIC CONVERTER SYSTEMS

Fig. 18 shows three different simplified schematics of early catalytic converter systems [14]. In this case, the mixture-formation system is a black box description of the fuel-injection system and the downstream reciprocating piston arrangement represents a simplified example of a single cylinder in an internal combustion engine, where additional details related to fuel-injection, mixing and combustion strategies is out of the scope of this work. Fig. 18A shows an engine exhaust system equipped with a two-way catalytic converter. The catalytic converter in this case is referred to as a two-way catalyst because it only oxidizes CO and HCs. The secondary oxygen added would result in a net lean environment, which favors oxidization of CO and HCs, but any NO_X emitted from the engine would not be reduced under these conditions, as discussed at-length previously. The schematic shown in Fig. 18B, is a two-catalyst system, but would still not be considered a three-way catalyst since the upstream catalyst is only responsible for the reduction of NO_X and the downstream catalyst is only responsible for the oxidation of CO and HCs. However, this system would be able to effectively remove all three pollutants simultaneously. In this case, the engine would likely be tuned slightly rich to effect NO_X reduction over the upstream catalyst, which explains why it is necessary to introduce secondary air over the downstream catalyst to oxidize CO and HCs. The schematic shown in Fig. 18C represents a true three-way (TWC) system and has been the design of choice for automobiles from the late 70s to the present. Notice that a lambda/O_2 sensor has now been included and that it is connected to a feedback controller, which tunes the mixture-formation system to ensure that the exhaust gas is as close to the stoichiometric regime as possible. Kaspar et al. [279] and Shelef and McCabe [280] previously discussed the advantages of both on-board diagnostics

(OBD) and oxygen storage capacity (OSC) on TWC systems, as summarized in Fig. 19. Without OSC, the TWC spends a significant amount of time outside the optimum AFR, which results in lower conversion efficiencies for CO, HCs and NO_X. With OBD and OSC, the TWC spends the majority of the time very near the optimum AFR; as a result, conversion efficiencies higher than 95% are achieved [279].

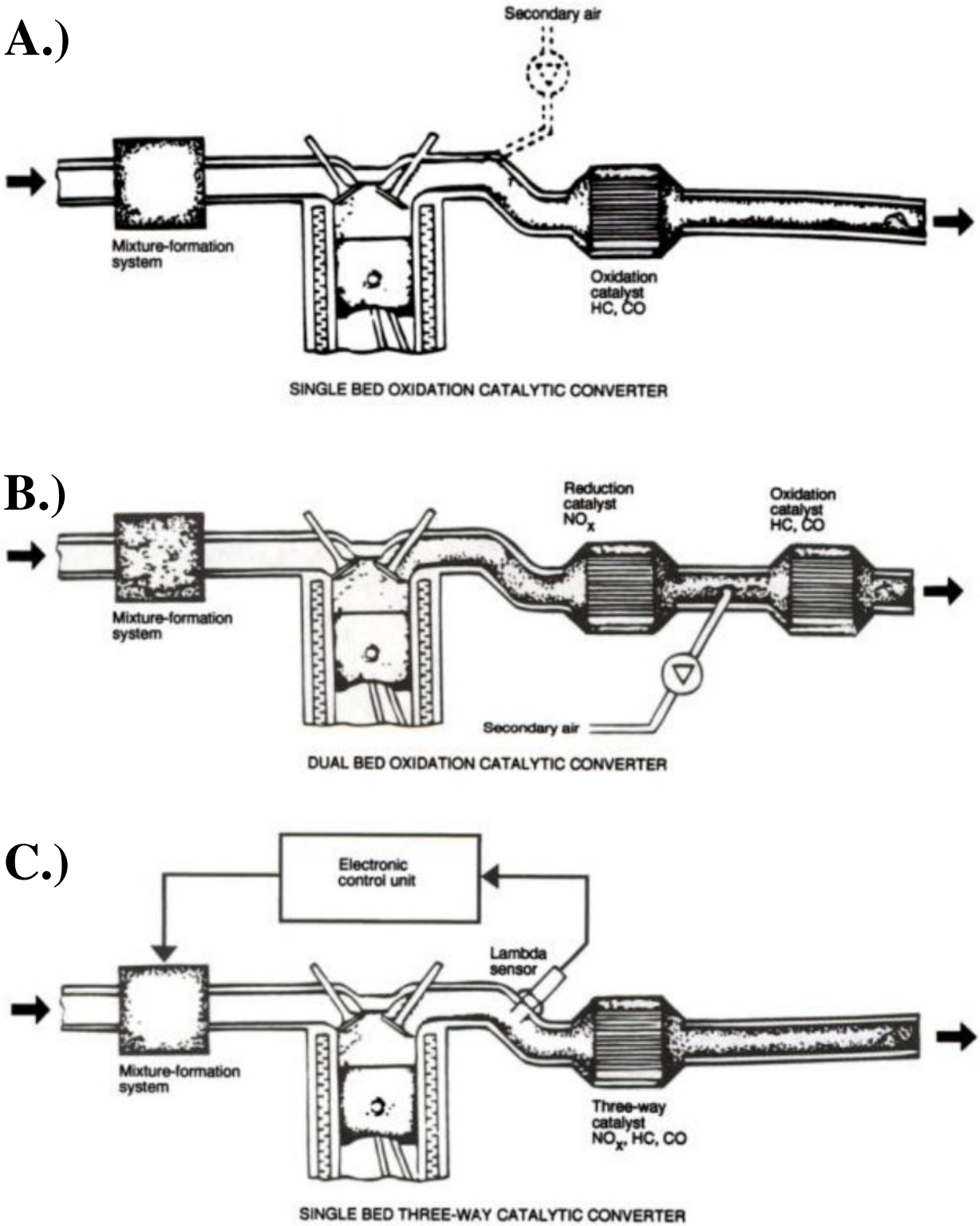

Figure 18. Schematics showing early catalytic converter systems, Faiz et al. [14].

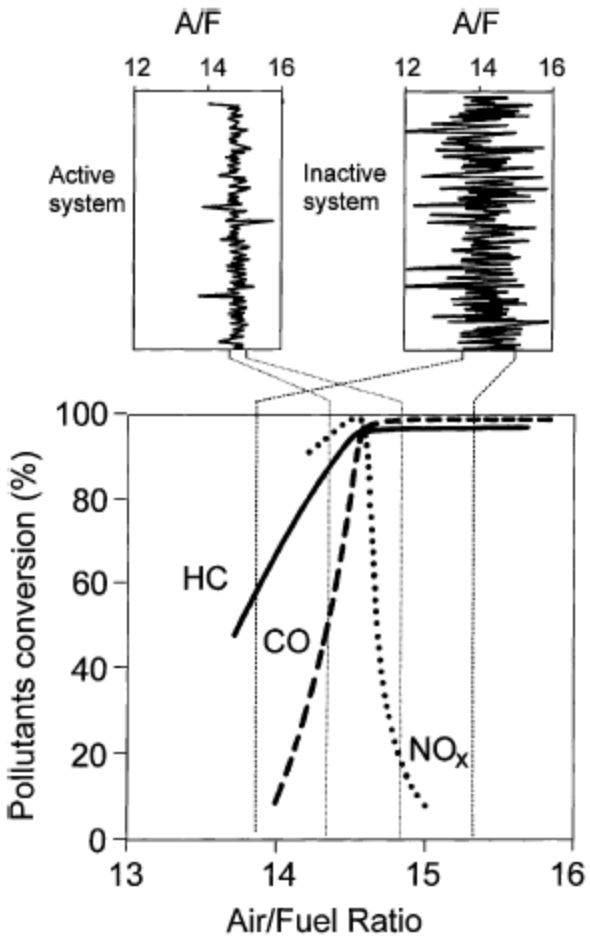

Figure 19. Effect of the AFR, advanced on-board diagnostics (OBD) and oxygen storage capacity (OSC) on the operation of TWC systems, Kaspar et al. [279].

1.4.2 MODERN CATALYTIC CONVERTER SYSTEMS

In the 1990s, in California especially, a series of low-emission standards were implemented that started the progression towards a 10-fold reduction in HC emission and a 20-fold reduction in NO_X emissions [281]. In the case of HCs, 50-80% of the total HCs emissions are emitted during the cold-start period during FTP testing (i.e., the first 90-180 s of operation) before the TWC reaches the HC-light off temperature (≈300 °C) [15]. Practically, this means that a vehicle could fail an emissions test based on cold-start HCs alone after only 2 min. into a

23 min. test. As a result, close-coupled TWCs were implemented. These catalysts could achieve light-off within 10 s of operation and are composed of proprietary blends of metal oxides used to stabilize the Al_2O_3 and prevent Pd sintering [15]. Fig. 20 shows two possible examples of close-coupled catalysts. In one case, a small, close-coupled catalyst is used primarily to convert HCs, while the larger downstream, under-floor TWC is responsible for the majority of the CO oxidation and NO_X reduction that takes place. The latter example shows a much larger close-coupled TWC that simultaneously converts all three pollutants, but at higher temperatures in comparison to the under-floor catalyst shown in the first example.

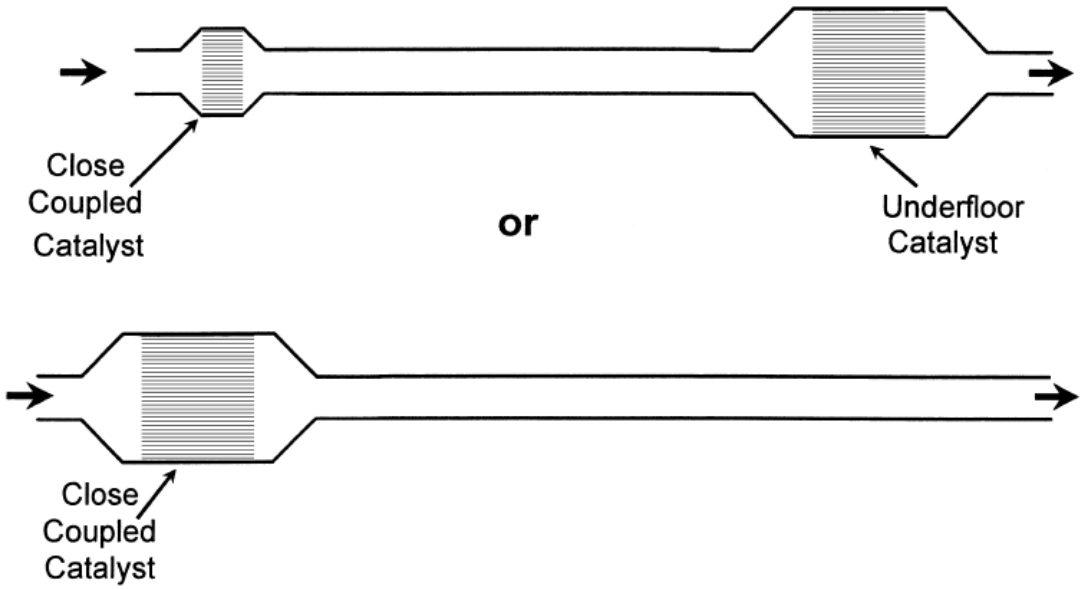

Figure 20. Two examples comparing the location and size of close-coupled TWCs [15].

The combination of TWCs and close-coupled TWCs has allowed auto manufactures to effectively meet emissions standards, but only for gasoline engines operating in the stoichiometric regime. Table 4 shows typical exhaust compositions for a diesel engine, four-stroke spark-ignited gasoline engine and a four-stroke spark-ignited lean burn gasoline engine

[279]. The conditions were included for the two-stroke engine for comparison, but will not be discussed. Notice that in the case of diesel engines and lean-burn gasoline engines, the O_2 concentration is very high (e.g., 4-15%). Comparison of these AFRs (26 and 17, respectively) with the results shown in Fig. 19 clearly demonstrates that poor performance in terms of NO_X conversion is expected if a TWC-only system was used. So for diesel engines or lean-burn gasoline engines, different/new catalytic technologies are required. Figs. 21 - 25 summarize the most recent architectures suggested that are capable of removing lean-NO_X, but still meeting the CO, HC and PM regulations.

The following chapters focus on the systems shown in Figs. 21 and 22 (Chapters 2 and 3) and in Fig. 23 (Chapter 4). Additional information regarding those systems is presented in the introductions of each corresponding chapter. The systems shown in Figs. 24 and 25 were included for comparison, since they provide corollary examples, but are not the specific focus of this dissertation since they were designed for diesel engines.

Table 4. Typical Exhaust composition for several common commuter vehicles, Kaspar et al. [279].

Exhaust Components and conditions[a]	Diesel Engine		Four-stroke spark-ignited engine		Four-stroke lean-burn spark-ignited engine		Two-stroke spark-ignited engine	
NO_X	350–1000	ppm	100–4000	ppm	≈1200	ppm	100–200	ppm
HC	50–330	ppm C	500–5000	ppm C	≈1300	ppm C	20,000–30,000	ppm C
CO	300–1200	ppm	0.1-6	%	≈1300	ppm	1-3	%
O_2	10–15	%	0.2-2	%	4-12	%	0.2-2	%
H_2O	1.4-7	%	10-12	%	12	%	10-12	%
CO_2	7	%	10-13.5	%	11	%	10-13	%
SO_X	10–100[b]	ppm	15–60	ppm	20	ppm	≈20	ppm
PM	65	mg/m^3						
Temperatures (test cycle)	r.t. - 650	°C	r.t. – 1100[c]	°C	r.t. - 850	°C	r.t. - 1000	°C
GHSV (hr-1)	30,000-100,000		30,000-100,000		30,000-100,000		30,000-100,000	
λ (A/F)[d]	≈1.8 (26)		≈1 (14.7)		≈1.16 (17)		≈1 (14.7)[e]	

[a] N_2 is remainder
[b] For comparison: diesel fuels with 500 ppm of sulfur produce of about 20 ppm of SO_2
[c] Close-coupled TWC
[d] λ defined as ratio of actual A/F to stoichiometric A/F, λ=1 at stoichiometry (AFR_{STOICH} = 14.7)
[e] Part of the fuel is employed for scavenging of the exhaust, which does not allow for a precise definition of the A/F ratio.

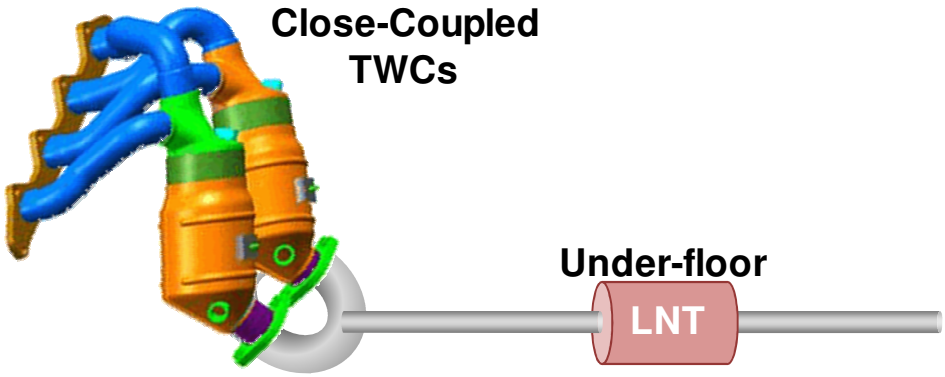

Figure 21. Close-coupled TWC, under-floor LNT configuration, as present on the BMW 120i (Model Year, 2009).

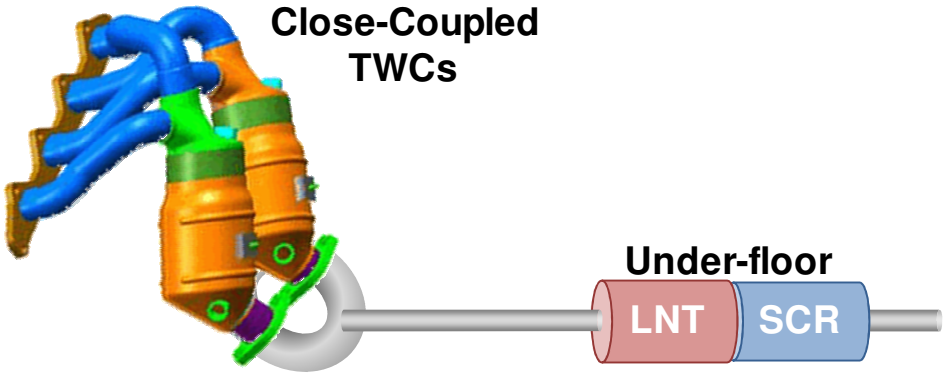

Figure 22. Close-coupled TWC, under-floor LNT + SCR configuration. *(Further discussed in Chapter 3.)*

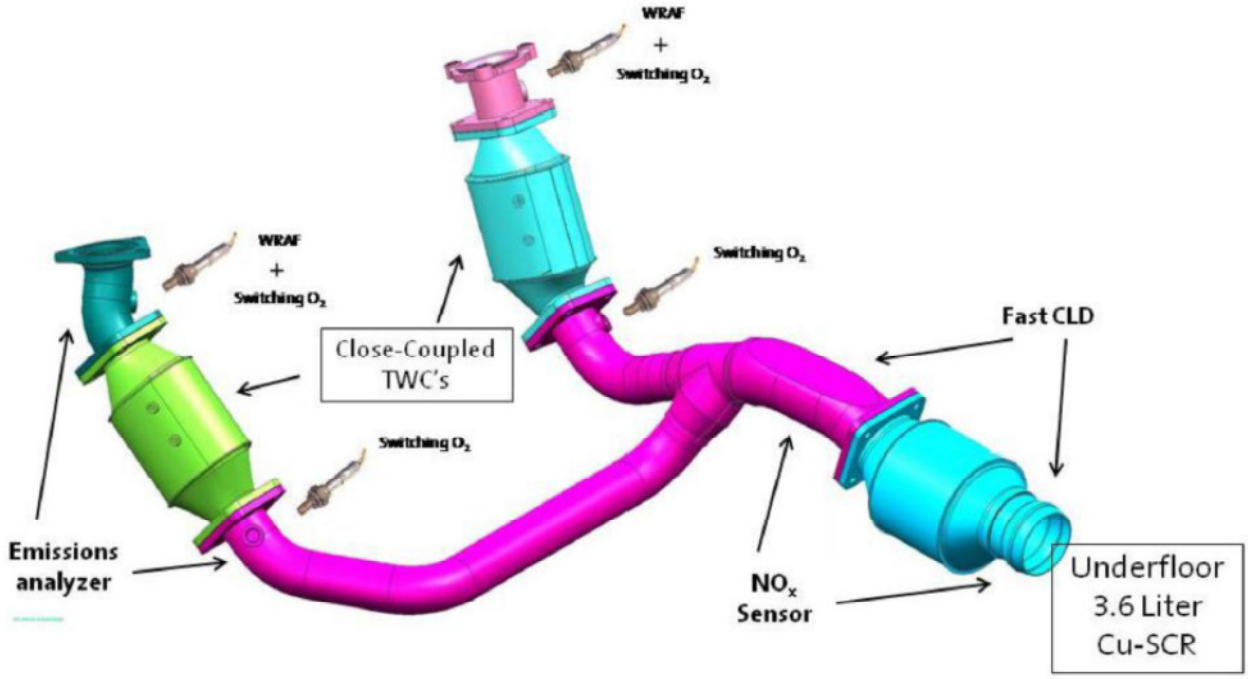

Figure 23. Layout of the passive-NH_3, urea-less TWC + SCR approach, Li et al [282]. *(Further discussed in Chapter 4.)*

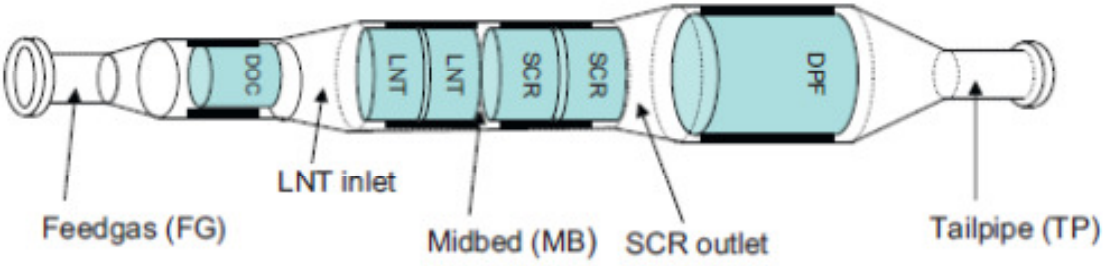

Figure 24. Layout of the emissions system for a light-duty diesel vehicle containing a diesel oxidation catalyst (DOC) and LNT + SCR configuration and a diesel particulate filter (DPF), McCabe et al. [283].

.

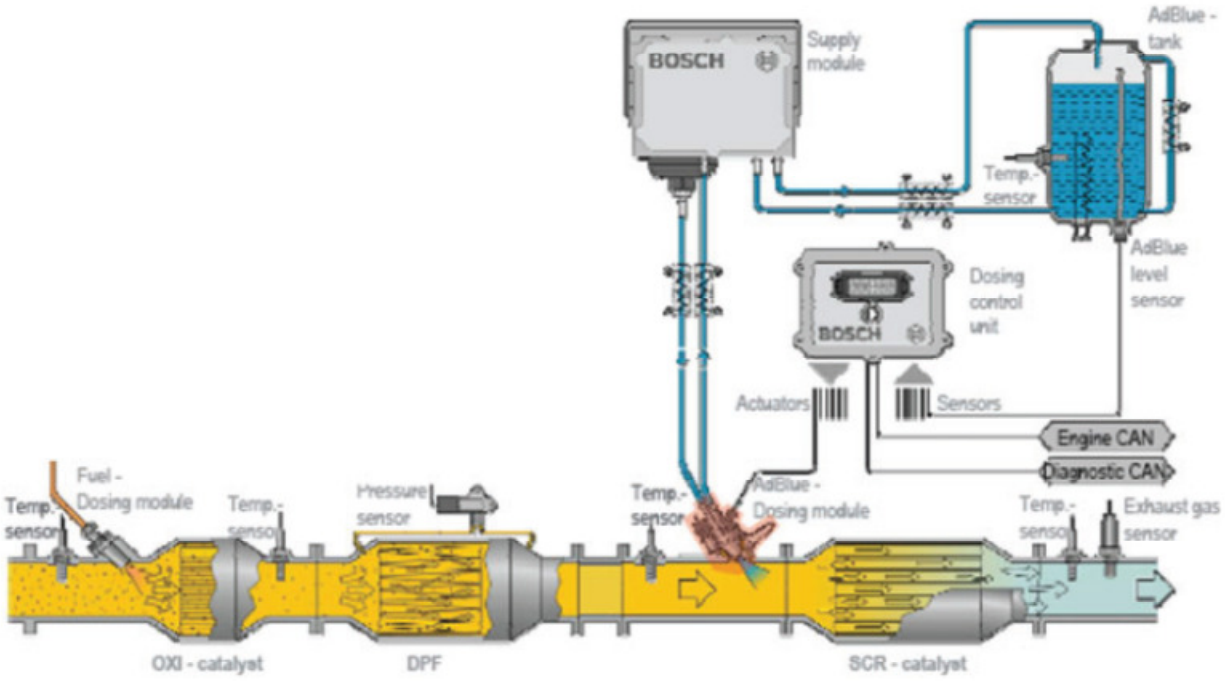

Figure 25. Layout of the modern medium- or heavy-duty DPF-SCR system (based on urea), Johnson et al. [284].

.

CHAPTER 2. *IN SITU* FTIR INVESTIGATION OF THE ROLE OF SURFACE ISOCYANATES IN THE REDUCTION OF NO_X BY CO AND C_3H_6 OVER MODEL $Pt/Ba/Al_2O_3$ AND $Rh/Ba/Al_2O_3$ NO_X STORAGE AND REDUCTION (NSR) CATALYSTS

2.1 PREFACE

Monometallic Pt- and Rh-containing model NO_X storage and reduction (NSR) catalysts were investigated by *in situ* FTIR spectroscopy in order to determine the type of species present on the surface under simulated lean exhaust conditions and to identify potential reaction intermediates during reduction by CO and propylene. The effect of precious metal selection, temperature, and water presence on NO_X storage and reduction chemistry was considered. The formation of surface isocyanate (NCO) species was observed during all cycling experiments, even in the presence of H_2O, which prompted additional investigation on the role of these species in the NO_X reduction mechanism. Stability and reactivity experiments with Ba/Al_2O_3, $Pt/Ba/Al_2O_3$ and $Rh/Ba/Al_2O_3$ confirmed that the reactions of NCO with NO and O_2 - producing N_2 - are metal catalyzed pathways, while reaction of NCO with H_2O - producing NH_3 - is not. The contribution of NCO-related pathways to the overall N_2 production mechanism could be significant, since quantification of the FTIR results suggests that up 30% of the total N_2 produced could be directly related to the reaction of NCO with O_2.

2.2 INTRODUCTION

Lean-burn engines have attracted the attention of automobile manufactures due to the higher engine efficiencies achieved under these conditions, translating into better fuel economy and lower CO_2 emissions. For example, Heck and Farrauto [1] reported that lean-burn engines can achieve efficiencies 20 - 30% higher than conventional engines. However, three-way catalysts (TWCs) employed for the oxidation of carbon monoxide (CO) and hydrocarbons (HCs) and the reduction of nitrogen oxides (NO_X) in conventional engine exhausts are not effective in reducing NO_X in the presence of excess O_2. Since their introduction in the mid 1990s [8,285], NO_X storage and reduction (NSR) catalysts have been shown to represent a viable solution for the removal of NO_X from lean exhausts. To date, numerous investigations have been performed on NSR catalysts and the results are summarized in several recent reviews [3,4,6]. Briefly, common NSR formulations consist of noble metals (mainly Pt, Pd or Rh) and an alkaline/alkaline earth component (mainly Ba or K) supported on γ-Al_2O_3. During the lean phase (60 - 120 s in length), NO is oxidized to NO_2 on the precious metal, with the NO_2 spilling over onto the storage component where it is initially stored in the form of a nitrite and can be further oxidized to a nitrate with increasing time [22,34,40,74,86,117]. During the rich phase (1 - 2 s in length), the storage component is regenerated and the accumulated nitrites and/or nitrates are reduced to N_2, NH_3 or N_2O, with N_2 being the desirable product [16,62].

While the NO_X storage mechanism is fairly well understood by now and widely accepted, the NO_X reduction mechanism strongly depends on the reductant used with many critical details still to be resolved [42]. For example, Nova et al. [23,60,63,64] have proposed that the reduction of stored NO_X by H_2 is a Pt-catalyzed pathway that proceeds through an NH_3 intermediate, where subsequent reaction of NH_3 with adsorbed nitrates is responsible for the production of N_2. In fact

several groups agree that NH_3 is a critical reaction intermediate when H_2 is used as the reducing agent [66,67,286].

Similar agreement regarding the nature of the reaction intermediates has not been reached for the cases when CO and hydrocarbons (HC) are used as reductants, in part because significantly fewer investigations have been performed using such reductants [24–28,43,59,107,287–290]. The mechanism of the reduction of NO_X by CO is currently thought to proceed through an isocyanate (NCO) intermediate, which can react with NO, O_2, stored nitrites/nitrates and H_2O to form N_2 or NH_3 [24,27,43,287–290]. The NH_3 formed by the hydrolysis of NCO can further react with stored NO_X, thus contributing to overall N_2 formation [64]. However, Lesage et al. suggested that formation of NCO species was undesirable and attempted to avoid it through rational catalyst design [145,146]. The presence of high concentrations of CO_2 and H_2O vapor in automotive exhausts, further affects the formation and reaction of surface NCO indirectly through the water gas shift (WGS) and steam reforming reactions. These reactions competitively consume the CO and HCs needed for the formation of NCO species, while at the same time they generate H_2 that can readily react with such species [20,64].

Historically, the role of NCO species in other types of NO_X reduction schemes has been examined and debated at length. Lorimer and Bell [291] for example, reported that an NCO related NO reduction pathway on three way catalysts (TWCs) accounts for less than 5% of the total NO reduction and is therefore of limited significance. Others also observed NCO formation under the stoichiometric TWC conditions, but similarly concluded that the NCO species were spectators in this environment [292–295]. Under lean exhaust conditions however, and over hydrocarbon-SCR type of catalysts many groups have postulated that NCO species contribute

significantly as intermediates to the overall reduction of NO [5,296–305]. However, as Burch et al. [5] have pointed out, the lack of kinetic data comparing the rate of removal of surface NCO species to the rate of formation of N_2 still represents a major problem in validation of NCO-related mechanisms.

The goal of this work is to investigate the formation and reaction of surface NCO on model NSR catalysts under conditions approaching those of realistic exhausts. *In situ* Fourier transform infrared (FTIR) spectroscopy was used in these efforts. The effects of the type of precious metal used (i.e., Pt vs. Rh), the presence of water, the reductant selection (i.e., CO vs. C_3H_6) and the temperature (250 and 350 °C) were considered. Since NCO formation was observed under all conditions studied, the stability and reactivity of these species in different gas environments was investigated in detail in an effort to determine the extent to which an NCO related reaction pathway contributes to the overall NO_X reduction mechanism.

2.3 EXPERIMENTAL

2.3.1 CATALYST PREPARATION

A set of 17 wt % Ba/Al_2O_3, 1 wt % Pt/17 wt % Ba/Al_2O_3 and 0.5 wt % Rh/17 wt % Ba/Al_2O_3 catalysts were prepared by a step-wise incipient wetness impregnation process. For simplicity, the catalyst samples will subsequently be referred to as Ba/Al_2O_3, $Pt/Ba/Al_2O_3$ and $Rh/Ba/Al_2O_3$, respectively. Prior to impregnation, the Catalox SBa-200 γ-Al_2O_3 (Sasol; 192 m^2/g) support was calcined in air for 24 h at 600 °C. Ba was deposited first on the support by adding an aqueous solution of barium acetate (Alfa Aesar) to the calcined Al_2O_3. Samples thus prepared were first dried, and then calcined in air for 12 h at 600 °C. Aqueous solutions of rhodium (III) nitrate hydrate (Sigma-Aldrich) or tetraammineplatinum (II) nitrate (Sigma-

Aldrich) were then impregnated onto the Ba/Al_2O_3 material to prepare the $Pt/Ba/Al_2O_3$ and $Rh/Ba/Al_2O_3$ catalysts, where the nominal weight loadings of the noble metals were chosen to yield equal molar loadings. The catalysts were then dried and subsequently calcined in air for 5 h at 500 °C. The loadings of Pt and Rh were then verified by Atomic Absorption Spectroscopy (AAS) measurements performed using a Perkin Elmer AAnalyst 400 spectrometer. The Ba loading was verified by further elemental analysis (Galbraith Laboratories). Table 5 provides a list of the catalysts used in this investigation and includes some of basic characterization results for these materials.

Table 5. Characterization of the catalysts used in this investigation.

Catalyst Name	Pt Loading		Rh Loading		Ba Loading	Metal Dispersion	SSA
	(wt %)	(μmol g^{-1})	(wt %)	(μmol g^{-1})	(wt %)	(%)	(m^2 g^{-1})
Ba/Al_2O_3	-	-	-	-	13.4	-	153
$Pt/Ba/Al_2O_3$	1.01	52	-	-	13.4	25	178
$Rh/Ba/Al_2O_3$	-		0.49	48	13.4	30	169

2.3.2 BET Surface Area and H_2-Chemisorption

BET surface area measurements and H_2-chemisorption of O_2-precovered metals was performed using a ChemBET-3000 analyzer (Quantachrome Instruments). Prior to the BET measurements, the catalysts were outgassed in He for 12 h at 200 °C. The surface area was then

determined using the multipoint BET method for adsorption of N_2 at -196 °C. The SSA values determined for the catalysts used in this investigation are shown in Table 5.

Prior to chemisorption measurements, the catalysts were outgassed in He for 12 h at 200 °C, heated in He to 300 °C, reduced in H_2 for 2 h at 300 °C, flushed with He for 2 h at 300 °C to remove all H_2 and finally, cooled back to room temperature in He. Following this pretreatment, O_2 titration of the exposed metal atoms was performed using 100 μL pulses of pure O_2. Consecutive O_2 pulses were introduced until no further uptake of O_2 was observed. Subsequent flushing with He for 15 min ensured removal of any excess oxygen before 100 μL pulses of pure H_2 were introduced over the O_2-precovered metals. Similarly, H_2 was pulsed until no further uptake of H_2 was observed. The stoichiometry for the adsorption of H_2 on an O_2-precovered metal was assumed to be 3:1 (i.e. $3[H] + O\text{-}M \rightarrow H\text{-}M + H_2O$) [306,307]. Both O_2- and H_2-chemisoroption measurements with the O_2-pretreated Ba/Al_2O_3 catalyst indicated negligible uptake of O_2 and H_2, respectively, suggesting that the Ba phase is inert under these conditions. The % dispersions of the precious metals calculated from the chemisorption measurements are shown in Table 5.

2.3.3 SCANNING TRANSMISSION ELECTRON MICROSCOPY

Scanning transmission electron microscopy (STEM) images were collected using a JEOL 2100F 200 kV FEG-STEM/TEM microscope equipped with a CEOS Cs corrector on the illumination system. The geometrical aberrations were measured and controlled to provide less than a $\pi/4$ phase shift of the incoming electron wave over the probe-defining aperture of 15.5 mrad. High-angle annular darkfield (HAADF) STEM images were obtained with a Fischione Model 3000 HAADF detector with a camera length such that the inner cut-off angle of the

detector was 50 mrad. The scanning acquisition was synchronized to the 60 Hz AC electrical power to minimize 60 Hz noise in the images and a pixel dwell time of 16μs was chosen.

2.3.4 FOURIER TRANSFORM INFRARED SPECTROSCOPY (FTIR)

FTIR spectra were collected with a Nexus 470 FTIR spectrometer (Thermo-Fischer Scientific) operated in transmission mode with a resolution of 2 cm^{-1}. Catalyst samples were used as self supported wafers (≈ 15-22 mg cm^{-2}). Immediately following analysis, the wafers were weighed and all spectral intensities were adjusted to an average sample size of 18.8 mg cm^{-2}. A homemade cell was used for the *in situ* collection of spectra, consisting of a stainless steel tube (≈35mm x 12 cm) with cooling water flanges welded to each end. The flanges were machined to accommodate polished NaCl windows (32mm x 3mm – Alfa Aesar) held in place by Viton O-rings. Cooling water was passed through the flanges to keep the O-ring temperature below 100 °C. The cell was wrapped in a 400 W, 4 ft heating cord (Glas-Col), which allowed heating up to 400 °C. A thermocouple was placed in close proximity to the sample for temperature measurement. A gas manifold with five mass flow controllers and two needle valves was used to prepare and deliver gas mixtures to the cell. Certified gas mixtures (National Welders) of 1.00% NO/He, 1.00% H_2/He, 0.965% NO_2/He, 0.975% C_3H_6/He, 2.985% CO/He, 9.990% O_2/He, and UHP He were used as sources for the different gas components. The total gas flow through the cell was maintained at 100 cm^3 min^{-1} throughout all experiments.

Background spectra were collected following treatment of the samples in a NO/O_2 environment for 10 h at 400 °C in order to exchange residual carbonates with nitrites/nitrates, followed by reduction in H_2 for 1 h at 400 °C in order to completely remove any stored nitrites/nitrates. The background spectra collected after such pretreatment did not exhibit any significant bands in the 1000 - 1650 cm^{-1} region, confirming the complete removal of any

residual carbonate and nitrate components on the surface. Similar behavior has also been observed and reported in the literature by other groups [34,290]. Samples were then oxidized in 10% O_2/He for 5 h at 400 °C, flushed with He for 1 h at 400 °C and then cooled in He to either 250 °C or 350 °C to initiate *in situ* spectra collection.

Storage experiments were conducted at 350 °C in either 1000 ppm NO/He, 1000 ppm NO/5% O_2/He, 1000 ppm NO_2/He or 1000 ppm CO/He. Cycling experiments employed three discrete phases each lasting 2 min: a lean phase during which samples were exposed to a 1000 ppm NO/5% O_2/He mixture; a He flushing phase used to remove any residual NO and O_2 and to minimize thermal effects due to the introduction of the reductant into an O_2 rich environment [61]; and a rich phase during which samples were exposed to either 9000 ppm CO/He or 1000 ppm C_3H_6/He mixture. The effect of H_2O during cycling was also investigated. During these experiments water was introduced by bubbling an additional He stream through a VLE saturator held at 20.9 °C in order to achieve a 1% (mol.) H_2O concentration in the final gas flow.

In a separate set of experiments, NCO species were formed on the catalyst surface at 350 °C by first a 1000 ppm NO/5% O_2/He mixture to the samples for 2 min in order to increase the concentration of nitrite and nitrate species on the surface. Next, He was flowed over the samples for 2 min to flush all O_2 from the cell, followed by 9000 ppm CO/He for 2 min to reduce the stored NO_X species and generate surface NCO species. Finally, He, 9000 ppm CO/He, 1000 ppm NO/He, 1000 ppm O_2/He or 1000 ppm H_2O/He were used to investigate the stability and reactivity of the surface NCO species in these gas mixtures.

2.3.5 Product Analysis

A flow reactor system equipped with a quadruple mass spectrometer (Leybold Inficon, Model type – TSPTT300) was employed for the analysis of the gaseous products formed during

the reaction of NCO and other surface species with He, 1000 ppm NO/He or 1000 ppm O_2/He at the end of the rich phase. These measurements were conducted in parallel and under the same conditions with the stability and reactivity measurements performed and monitored by *in situ* FTIR, as described in the previous section. In order to differentiate between CO and N_2 formed, isotopically labeled ^{13}CO (Sigma Aldrich – 99 atom % ^{13}C, <5 atom % ^{18}O) was used as the reductant and the following m/z signals were followed for identification of the products: N_2 (28), ^{13}CO (29), NO (30), N_2O (44), $^{13}CO_2$ (45) and NO_2 (46). Prior to catalyst evaluation, cycling was performed in an empty quartz reactor and the resulting m/z signals were used as a baseline. Additionally, the m/z signals were normalized to a constant leak rate, which was necessary in order to correct for changes in the baseline caused by large differences in the average molecular weight of the gas mixtures (lean vs. rich) entering the mass spectrometer.

2.4 RESULTS AND DISCUSSION

2.4.1 CATALYST CHARACTERIZATION

The results of Table 5 indicate that the Pt and Rh catalysts compared in this study are very similar in terms of their compositions and structural characteristics (i.e. molar metal loading, metal dispersion and surface area). As a result, a direct comparison of the concentration of surface species formed – including NCO – and rates of consumption can directly demonstrate differences in the behavior of the two metals as compared to differences in surface area and/or particle size and dispersion.

STEM images collected from different regions of the Pt/Ba/Al_2O_3 catalyst indicates that Ba was present both as an amorphously distributed phase and in large crystalline regions on the Al_2O_3 support. Fig. 26A depicts one such Ba crystallite region, where corollary elemental

analysis (Fig. 26C) confirmed only the presence of Ba. Additional bright regions in Fig 26A lacking crystalline structure were assigned to amorphously distributed BaO and/or $BaCO_3$. The significant difference in the morphology of the two regions of the same material shown in Figs. 26A and 26B demonstrates the heterogeneous nature of the $Pt/Ba/Al_2O_3$ material. Interestingly, the formation of large, crystalline Ba regions was suppressed for the Ba/Al_2O_3 catalyst. While crystalline regions were also observed, in that case, they were generally much smaller, less frequent and exhibited duller edges than those observed for the noble metal containing catalysts, where Pt and Rh may be assisting in the formation of these large, crystalline Ba phases during calcination. Similar SEM results for a $Pt/Ba/Al_2O_3$ sample were previously reported by Vijay et al. [126].

The small (≈2-3 nm) bright spots observed in Fig. 26B most likely represent Pt particles. EDX measurements (Fig. 26D) confirmed the presence of both Pt and Ba in the region of Fig. 26B, although definitive assignment of individual particles is difficult because the molecular weights of Pt and Ba are similar and the loading of Ba is high. It should be pointed out that no 2-3 nm particles were observed in the STEM images of the non-metal containing Ba/Al_2O_3 sample, further supporting assignment of such particles to the noble metal component. Confirmation of the Pt particles located on top or immediately next to a Ba phase, as commonly portrayed in the literature [3,6,66,308] is exceedingly difficult. However, our STEM images suggest that Pt and Ba appear to be in close contact. HRTEM micrographs collected by Frola et al. [179] exhibited similar findings, where crystalline $BaCO_3$ regions observed on "as prepared" catalysts partially masked the presence of Pt. Subsequent conditioning resulted in clear identification of Pt particles on the support, but the location of the Ba containing phase became less clear.

Interestingly, Ji et al. [139] did not observe any large, $BaCO_3$ crystallite regions and Pt was clearly visible in their STEM images of an "as prepared" Pt-Rh/Ba/La-Al_2O_3 washcoat catalyst.

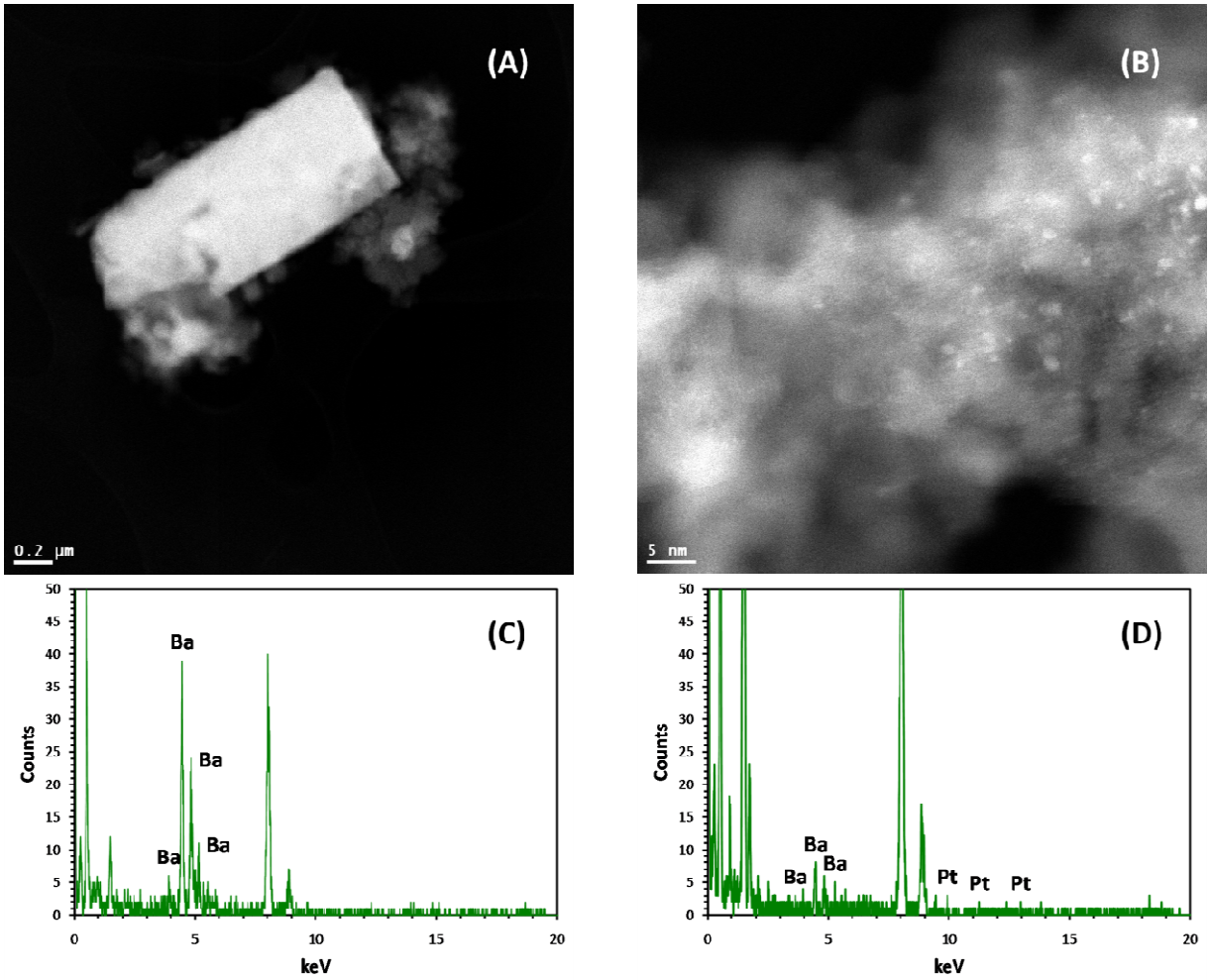

Figure 26. STEM images and corresponding EDX analyses of two different regions of the Pt/Ba/Al_2O_3 catalyst used in this investigation.

2.4.2 Storage of NO_X and CO at 350 °C

In order to identify and assign the different FTIR bands observed during cycling, separate nitrate and carbonate storage experiments were performed with the Pt- and Rh-containing

samples. Band assignments were made according to previously published results, as summarized in Table 6.

Table 6. FTIR band assignments.

Species	Wavenumbers (cm^{-1})	Reference
NO_X Species on Ba		
Bidentate nitrate	970-1050, 1200-1320, 1540-1650	[34,40]
Monodentate nitrate	1290-1330, 1425-1540	[31,33]
Ionic nitrate	1038, 1300-1360, 1400-1460	[34,37,40,188]
Monodentate nitrite	970-1340, 1410-1500	[31,33,34]
Bidentate nitrite	1230, 1300	[31,34]
CO_X Species on Ba		
Bridged bidentate carbonate	1020-1060, 1320-1340, 1610-1650	[37,179]
Chelating bidentate carbonate	1060, 1350-1380, 1550-1600	[37,179]
Monodentate carbonate	1440, 1740	[37,179]
Ionic carbonate	1430-1450	[37,179]
NCO Species on Al_2O_3 and Ba		
Octahedral Al^{3+} isocyanate	2260	[24,27,145]
Tetrahedral Al^{3+} isocyanate	2222	[24,27,145]
Ba^{2+} isocyanate	2162	[24,27,145]

Introduction of a NO/O_2 mixture to $Pt/Ba/Al_2O_3$ at 350 °C initially resulted in the appearance of three bands centered at 1467, 1300 and 1210 cm^{-1} in the corresponding spectrum (Fig. 27A). These bands were rapidly converted (<1 min) to bands centered at 1547, 1465, 1418, 1306 and 1024 cm^{-1}. Since many of the vibrations of nitrate species overlap (see Table 6), it is difficult, if not impossible, to definitively differentiate between these species on the surface [287]. However, nitrites can be distinguished from nitrates and the bands at 1300 and 1210 cm^{-1} have been previously assigned to bidentate nitrite species on Ba [40]. Bands at 1547, 1465, 1418, 1306 and 1024^{-1} are most likely associated with monodentate, bidentate or ionic nitrates on

Ba, where the bands at 1418, 1306 and 1024 cm^{-1} have been widely assigned in the literature to ionic ("bulk-like") nitrates [74,179,188]. The results shown in Fig. 27A indicate that the storage of NO_X in the presence of O_2 on $Pt/Ba/Al_2O_3$ proceeds via a nitrite to nitrate route, where this mechanistic pathway has already been established by our group and others in the literature [22,34,40,117]. Finally, in agreement with previous literature reports, our results show that at 350 °C surface nitrates are the dominant storage species at times relevant to NO_X storage (60 - 120 s). Identical results were also obtained with the $Rh/Ba/Al_2O_3$ sample (not shown for brevity).

The NO_X storage capacity of the $Pt/Ba/Al_2O_3$ and $Rh/Ba/Al_2O_3$ samples was estimated by integration of the bands in the 1050 -1650 cm^{-1} region. A similar approach has been also followed by Saito et al. [309]. The resulting area can then be plotted as a function of storage time. The $Pt/Ba/Al_2O_3$ and $Rh/Ba/Al_2O_3$ samples exhibited similar storage capacity, as shown in Fig. 28. Corollary experiments performed in a fixed bed reactor yielded similar results. These results may at first appear surprising since Rh is, in general, assumed to be less active than Pt in NO oxidation [16] and Abdulhamid et al. [25] previously reported a lower NO_X storage capacity for $Rh/Ba/Al_2O_3$ than $Pt/Ba/Al_2O_3$. In another publication however, Abdulhamid et al. [27] reported that $Rh/Ba/Al_2O_3$ outperformed $Pt/Ba/Al_2O_3$ in NO_X storage. Large differences in precious metal dispersion were listed as the most likely reason for this behavior, since Pt and Rh dispersions were 5% and 31%, respectively. In contrast, Vijay et al. [118] observed similar storage capacities for $Pt/Ba/Al_2O_3$ and $Rh/Ba/Al_2O_3$ if long cycle times were used, which is similar to our experimental protocol. Overall it appears in our case that with the same metal loading and particle size (i.e., dispersion) both metals exhibit similar behavior.

Introduction of CO to $Pt/Ba/Al_2O_3$ at 350 °C resulted in the appearance and subsequent growth of bands centered at 1569, 1336 and 1057 cm^{-1} in the spectrum of this material (Fig. 27B). These bands can be assigned to carbonate species on Ba [37,179]. An additional weak band was observed at 2020 cm^{-1} and can be assigned to a Pt carbonyl species [24]. Identical results were also obtained with the $Rh/Ba/Al_2O_3$ sample with the carbonyl band in this case appearing at 2006 cm^{-1}.

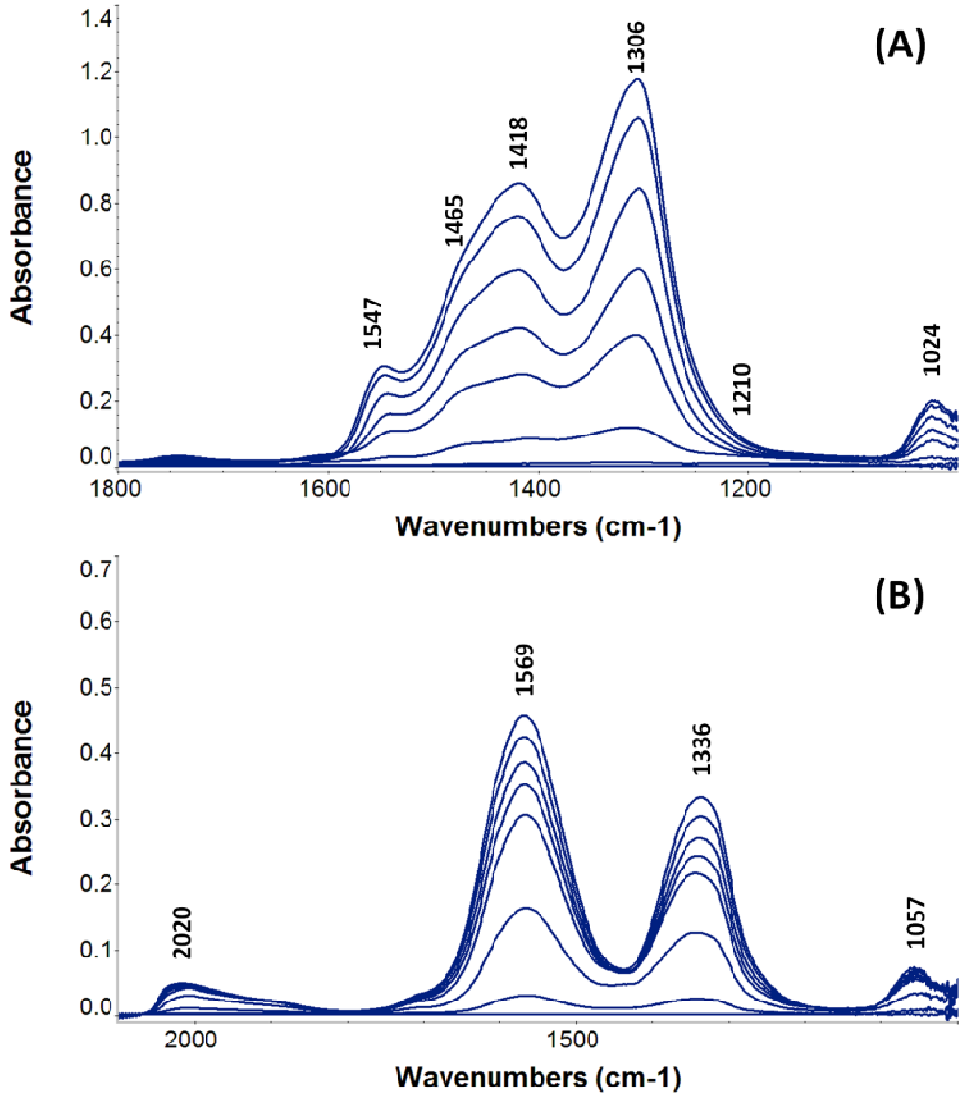

Figure 27. *In situ* FTIR spectra of a $Pt/Ba/Al_2O_3$ catalyst during exposure to (A) 1000 ppm NO/5% O_2 in He and (B) 1000 ppm CO in He mixtures at 350 °C (Spectra shown at 0, 0.5, 1, 2, 3, 5, 10 and 20 min of exposure).

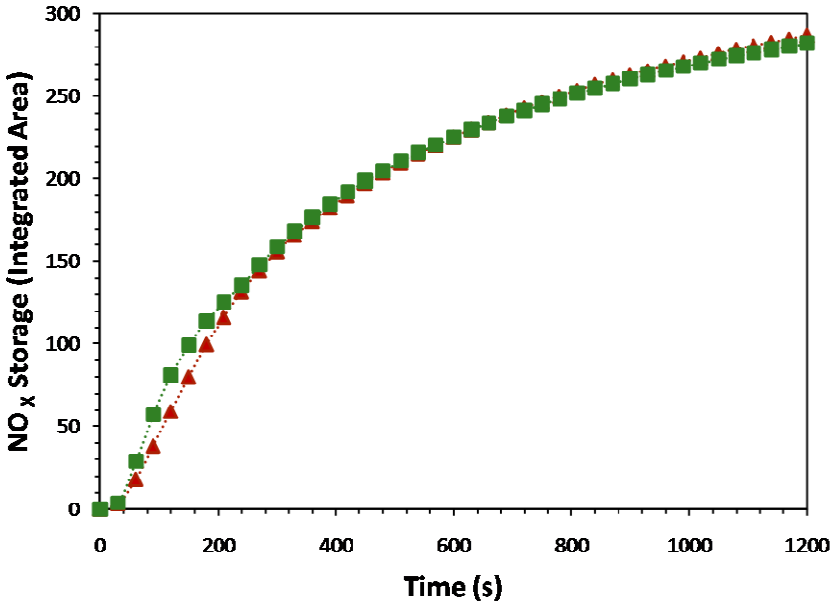

Figure 28. NO_X storage capacity of (▲) $Pt/Ba/Al_2O_3$ and (■) $Rh/Ba/Al_2O_3$ in a 1000 ppm NO/5% O_2 in He mixture at 350 °C (obtained by integration of FTIR bands in the 1050 - 1650 cm^{-1} region).

2.4.3 NO_X Storage-Reduction Cycling Studies

In situ cycling studies between NO_X storage and reduction conditions were conducted at two different temperatures in order to investigate potential differences in the NO_X storage and reduction mechanisms. Fig. 29 shows one such example of NSR cycling monitored with FTIR spectroscopy using CO as the reducing agent at 350 °C over $Pt/Ba/Al_2O_3$. In this case, the spectra collected were plotted in a 3D representation in order to more clearly show the NSR cycling behavior. The bands in the 1200 - 1650 cm^{-1} region of the spectrum are characteristic of nitrite/nitrate and carbonate species adsorbed on the surface and the bands at 2030, 2162 and 2221 cm^{-1} appear when CO is introduced as the reductant molecule. The first several lean and rich phases are denoted in Fig. 29 and help show the distinct changes observed in the spectra

under different NSR cycling conditions. Fig. 29 also clearly shows the reproducibility of both the cycling protocol used in our experiments and the behavior observed on the surface from cycle to cycle. In the following sections, closer examination of the lean and rich phases will be conducted using 2D figures because the band assignments are more clearly resolved in this representation of the data.

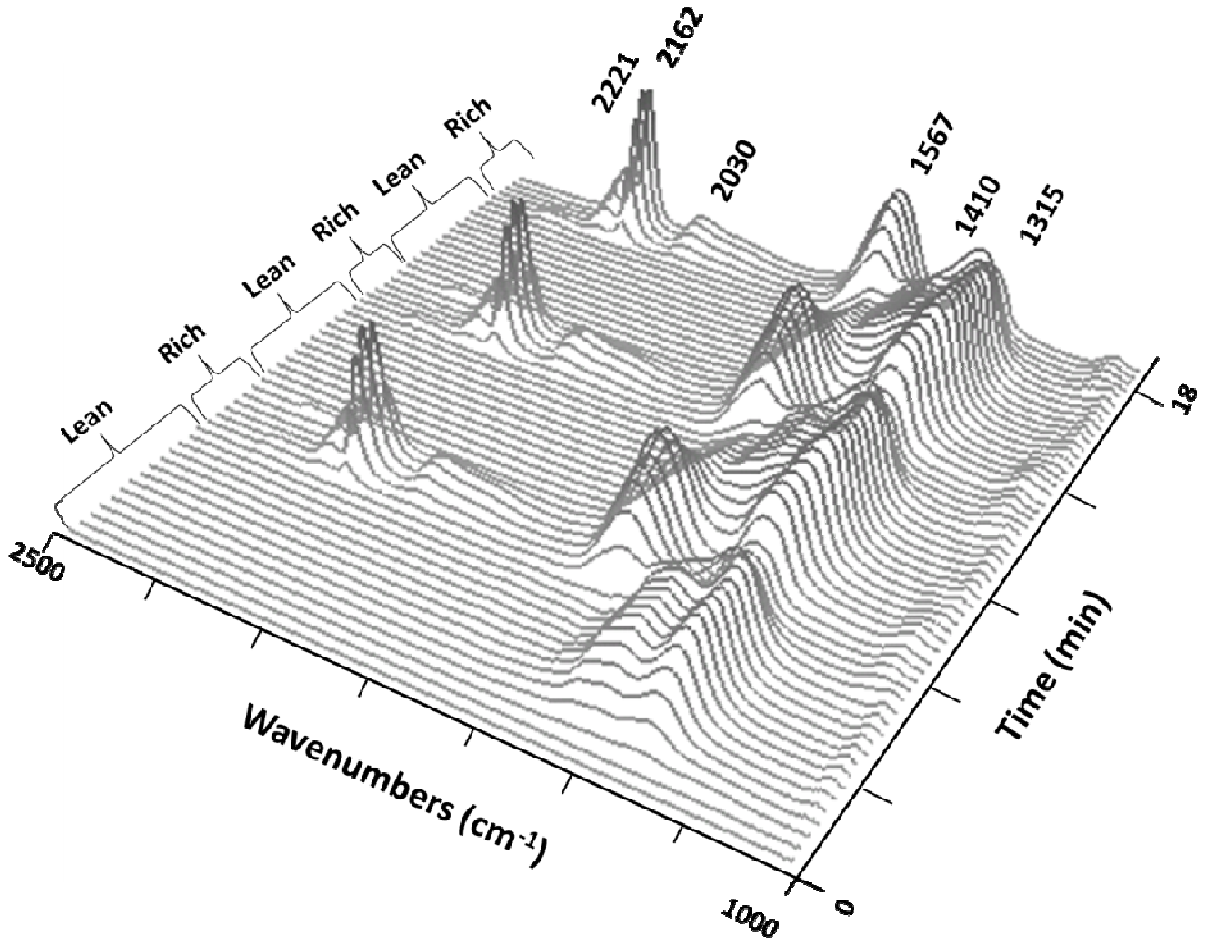

Figure 29. A 3D plot showing the *in situ* spectra collected during three lean-rich phases of NO_X storage-reduction cycling on $Pt/Ba/Al_2O_3$ using CO as the reducing agent at 350 °C.

CO CYCLING AT 250 °C

In situ FTIR spectra collected during such cycling over $Pt/Ba/Al_2O_3$ at 250 °C are shown in Fig. 30. CO was used as the reducing agent in this case. For clarity, the first lean cycle is shown in this figure because spectra collected during subsequent lean cycles contain both carbonate and nitrite/nitrate features, which makes elucidation of the different bands more complex. The spectra of Fig. 30 indicate that during NO_X storage at 250 °C, both in the absence (Fig. 30A) and presence (Fig. 30C) of 1% H_2O, bands centered at approximately 1360 and 1200 cm^{-1} are formed in the corresponding spectra. The band at 1200 cm^{-1} was previously assigned to bidentate nitrite species on Ba [40]. Assignment of the band at 1360 cm^{-1} is more ambiguous since monodentate nitrite, monodentate nitrate and ionic nitrate species on Ba have features in this area [31,33,34,40,179,188]. It has been reported that Al_2O_3 could also contribute to NO_X storage at this temperature [33], although in our case such a contribution in unlikely because no bands attributed to nitrates on Al_2O_3 were observed in the vicinity of 1600 cm^{-1}. Overall, it is apparent from Figs. 30A and 30C that the Ba nitrite species represents the dominant NO_X storage form at 250 °C, for storage times corresponding to realistic NSR operations (i.e., 60-120 s). The presence of water does not have a significant effect during storage, since Figs. 30A and 30C are qualitatively very similar. Epling et al. [29] previously reported that the presence of water was detrimental to NO_X storage, especially at lower temperatures. This effect may not have been observed in our case due the lower concentration of H_2O used (1% vs. 8%).

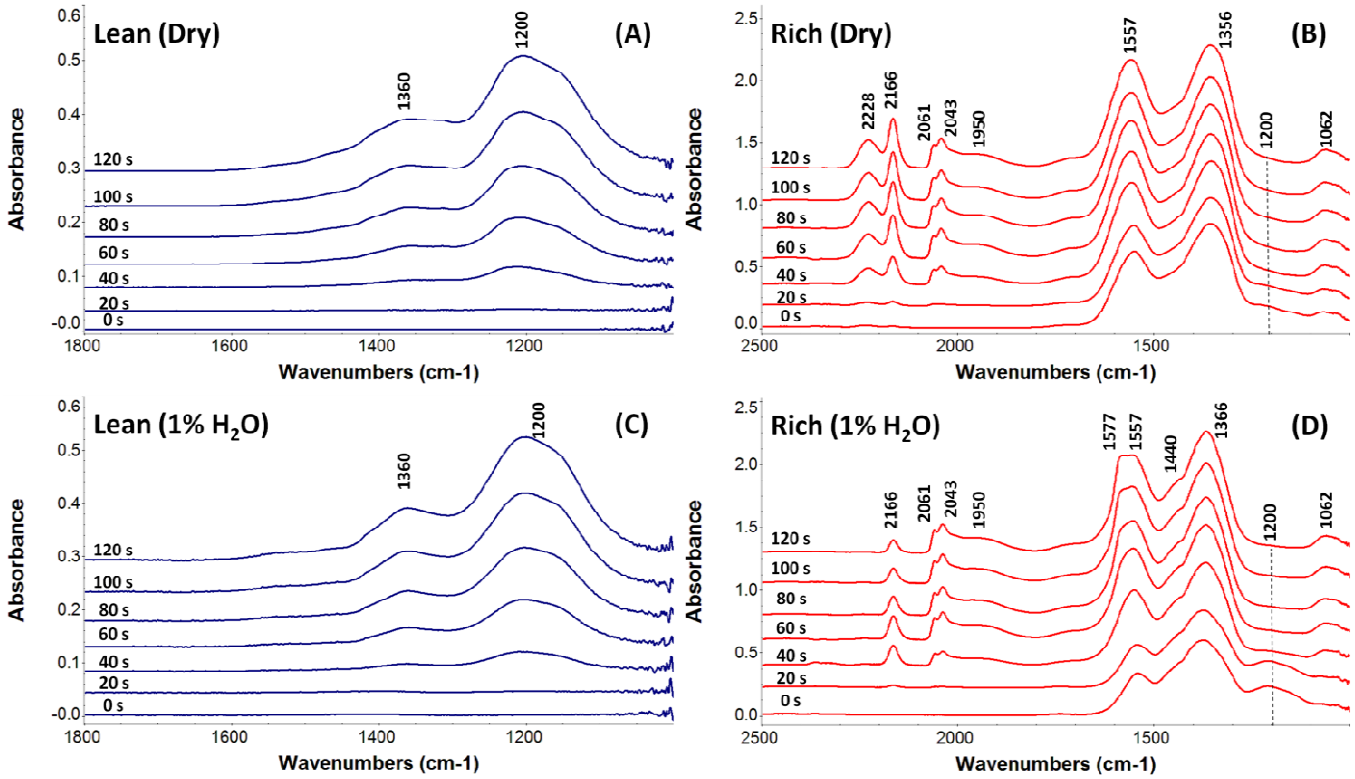

Figure 30. *In situ* spectra collected during NO_X storage-reduction cycling on $Pt/Ba/Al_2O_3$ at 250 °C. Panes (A) and (C) display spectra collected during the first lean periods (conditions: 1000 ppm NO/5%O_2/He); panes (B) and (D) display spectra collected during the rich periods (conditions: 9000 ppm CO/He). Spectra in panes (A) and (B) were collected during dry cycling; spectra in panes (C) and (D) were collected in the presence of 1% H_2O.

Figs.30B and 30D show spectra collected during the rich phase of cycling in the absence and presence of 1% H_2O, respectively. In the absence of H_2O, bands at 2228, 2166, 2061, 2043, 1950, 1557, 1356 and 1062 cm^{-1} are present in the spectra collected during rich phases (Fig. 30B). The bands at 1557, 1356 and 1062 cm^{-1} can be assigned to Ba carbonate features, in agreement with the results of the storage measurements described in Section 2.4.2. It is worth noting that significant contributions from carbonate features carry over from cycle to cycle since these species are stable under both lean and rich conditions at this temperature. Furthermore, spectra collected during the subsequent lean phase indicated slow growth of the band centered at approximately 1200 cm^{-1}, characteristic of stored nitrites on BaO, which indicates that a

significant portion of the Ba storage sites are saturated with relatively stable carbonate species that are not removed during lean phases at 250 °C.

The bands at 2061 and 2043 cm^{-1}, as well as the broad band centered at approximately 1950 cm^{-1}, can be assigned to linear and bridged CO carbonyls on Pt sites [27,310,311]. Finally, the bands at 2228 and 2166 can be assigned to NCO species adsorbed on Al^{3+} and Ba^{2+} sites, respectively [24]. The NCO bands are fairly intense in comparison to the other surface species observed, leading some groups to postulate that these species may be intermediates in the reduction process [24,27,43].

Spectra collected at 250 °C during the rich phase in the presence of 1% H_2O (Fig. 30D) showed significant differences in the NCO region when compared to the corresponding spectra collected under dry conditions. More specifically no Al NCO band (2228 cm^{-1}) was observed in this case, while the band associated with the Ba NCO species (2166 cm^{-1}) had significantly lower intensity. Additionally, the Ba NCO band also increases, reaches a maximum and then decreases as the rich phase progresses. Similar behavior has previously been reported by Lesage et al. [145]. Several factors may be contributing to this effect. First, it is possible that H_2O could inhibit the formation of NCO species through the formation of hydroxyl groups that block active Pt sites and thus decrease the surface concentration of the NCO precursors [312,313]. However in this case, one would expect the surface concentration of Pt carbonyls to decrease as well. Given that the intensities of the carbonyl peaks in the 1900- 2100 cm^{-1} region are essentially the same in the spectra of Figs. 30B and 30D, this explanation appears to be less plausible.

Alternatively, it is also possible that the presence of H_2O initiates the WGS reaction, which in turn decreases the concentration of CO available for adsorption and reaction with N adatoms on the surface [64]. Once again however, a decreased CO concentration should have

resulted in a decrease in the intensity of the carbonyl bands that was not observed. Thus, the most likely explanation is that the surface NCO species are formed at the same rate and to the same extent as under dry case, but weaker band intensities are observed because in the presence of H_2O, they are rapidly hydrolyzed to NH_3 [24,64].

Cycling in the presence of H_2O also affects, to a lesser extent, the carbonate and nitrite/nitrate bands. For example, the carbonate band at 1356 cm^{-1} appears to shift to 1366 cm^{-1}, while a shoulder at 1440 cm^{-1} is also formed, along with a new band at 1577 cm^{-1}, which overlaps with the band at 1557 cm^{-1} and significantly contributes to the overall spectral intensity in that region of the spectrum. The appearance of the new bands at 1577 and 1366 cm^{-1} can attributed to the formation of surface formate species in addition to the surface carbonates [298]. Furthermore, the presence of the band at 1440 cm^{-1}, which was previously assigned to bulk Ba carbonate [34,179], indicates that bulk-type carbonates are formed in the presence of water . This result is not surprising since Szanyi et al. [187,191] noticed similar behavior for transition of surface Ba nitrates to bulk Ba nitrates in the presence of water. Further comparison between Figs. 30B and 30D indicates that lower concentrations of carbonates and higher concentrations of nitrites are present on the surface during cycling in the presence of H_2O. This in turn, may suggest that water facilitates storage and release of NO_X at 250 °C. These results are in agreement with the results of a recent study on the effect of H_2O conducted by Nova et al. [64].

CO AND C_3H_6 CYCLING AT 350 °C

In situ cycling experiments were also performed at 350 °C, where the effects of precious metals and reductant selection were also considered. Fig. 31 shows spectra collected during cycling at 350 °C over the $Pt/Ba/Al_2O_3$ catalyst, in the presence and absence of H_2O and with 9000 ppm CO used for the reduction phase.

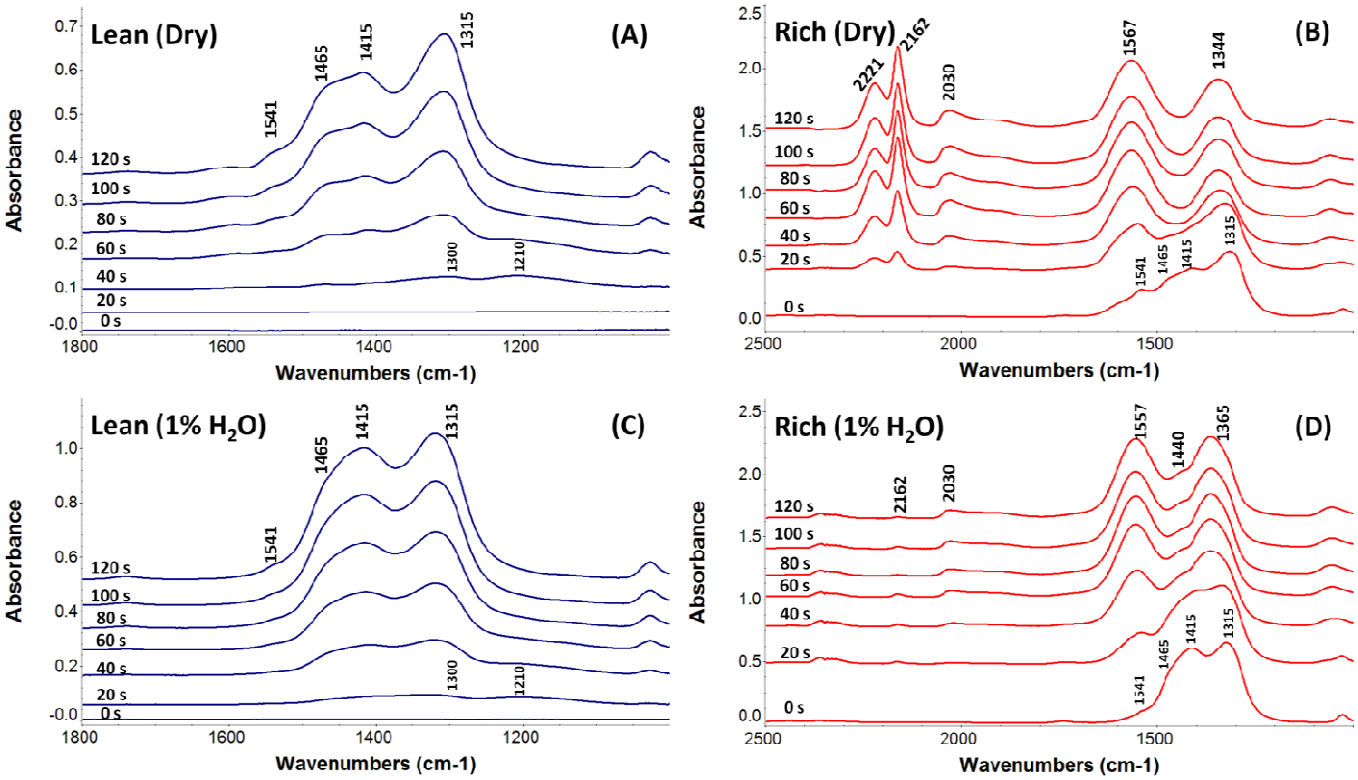

Figure 31. *In situ* spectra collected during NO_X storage-reduction cycling on $Pt/Ba/Al_2O_3$ at 350 °C. Panes (A) and (C) display spectra collected during the first lean periods (conditions: 1000 ppm NO/5%O_2/He); panes (B) and (D) display spectra collected during the rich periods (conditions: 9000 ppm CO/He). Spectra in panes (A) and (B) were collected during dry cycling; the spectra in panes (C) and (D) were collected in the presence of 1% H_2O.

During the 1st lean phase, bands appeared immediately in the spectra at 1300 and 1210 cm^{-1}, while additional bands also appeared at 1541, 1465, 1410 and 1315 cm^{-1} with increased exposure time (Figs. 31A and 31C). As discussed in the previous sections and with the aid of Table 6, the initial bands at 1300 and 1210 cm^{-1} can be assigned to Ba nitrites, while the bands at 1541, 1465, 1410 and 1315 cm^{-1} can be assigned to Ba nitrates. The most significant difference observed between the cycling experiments at 250 and 350 °C was that storage of NO_X at 250 °C occurred mainly in the form of surface nitrites, where as storage at 350 °C occurred mainly in the form of surface nitrates. It is also clear that the dominant NO_X storage form on the surface is a function of storage temperature and contact time, in agreement with previous literature reports

[40,112]. Differentiation between the types of NO_X species stored on the surface is important because nitrites have lower thermal stability and are therefore expected to be more reactive than nitrates [31,112]. Therefore, storage of NO_X as Ba nitrites instead of nitrates may be favorable for NSR cycling, but NO_X slip due to thermal release of nitrites during exotherms created by introduction of reductants to lean environments also represents a problem [61]. The presence of H_2O does not appear to affect storage significantly, consistent with the storage results obtained at 250 °C.

Spectra collected under dry conditions during the rich phase of cycling over the same $Pt/Ba/Al_2O_3$ catalyst are shown in Fig. 31B. In contrast to the results obtained at 250 °C, prior to the introduction of CO (Fig. 31B, 0 s), the surface is mostly free of carbonate species and the nitrate bands at 1541, 1410 and 1315 cm^{-1} are the dominant features in the spectrum. Hence, it appears that most of the carbonate species formed during the previous rich phase were removed during the subsequent lean phase, indicating a faster exchange between barium carbonates and nitrates at 350 °C. Following the introduction of CO, the intensity of the nitrate bands decreases, while new carbonate bands appear at 1567 and 1344 cm^{-1}. Furthermore, significant amounts of NCO species are formed both on Al and Ba as indicated by the appearance of strong corresponding bands at 2221 and 2162 cm^{-1}, respectively.

The presence of H_2O significantly affects the concentration of surface NCO at 350 °C. Spectra collected under these conditions (Fig. 31D) indicate that the Al NCO species are no longer present, while the intensity of the band at 2162 cm^{-1} corresponding to the Ba NCO species is dramatically reduced in intensity. In agreement with the results from 250 °C, the Ba NCO band also grows intensity, reaches a maximum and then decreases as the rich phase progresses, where the dramatic decrease in intensity due to the presence of water makes this behavior much

harder to distinguish in Fig. 31D. The effect of temperature and the presence of H_2O on the concentration of NCO species formed during cycling using CO as the reducing agent is more clearly demonstrated in Fig. 31, where the integrated intensities of the bands in the NCO region (i.e. 2100-2350 cm^{-1}) is plotted as a function of time. The results of Fig. 31 clearly show that higher concentrations of surface NCO species were formed under dry conditions at 350 °C than at 250 °C. Szailer et al. [24] previously reported that the highest concentrations of NCO were formed at 250 °C, but in their experimental protocol, NO_2 was first adsorbed on BaO at room temperature and the temperature was then ramped in the presence of CO up to 300 °C. The thermal stability of NCO was also investigated in the same study and it was concluded that their decomposition does not start until approximately 350 °C. In contrast, Abdulhamid et al. [27] have also reported that higher concentrations of surface NCO are formed during *in situ* DRIFTS measurements at 350 °C rather than at 250 °C, in agreement with our observations. Additionally, Fanson et al. [43] concluded that the concentration of surface NCO species formed is strongly related to the amount of NO_X stored on Ba. Therefore, the higher concentration of NCO species observed at 350 °C can be attributed to the increased NO_X storage at this temperature. Furthermore, the subtlety between amount of NO_X stored at different temperatures and the reaction leading to the formation of surface NCO species demonstrates that attempts to decouple the reduction process from the NO_X storage process may result in misleading conclusions, since storage under different conditions most likely results in differences in both the amounts and type of NO_X species stored on Ba.

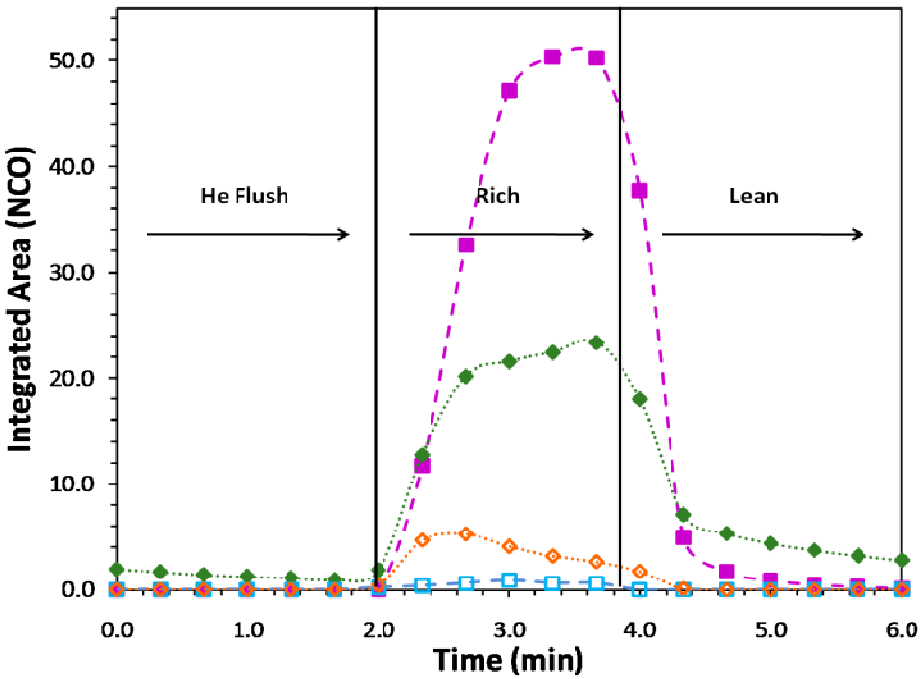

Figure 32. Concentrations of surface NCO species formed on $Pt/Ba/Al_2O_3$ under different conditions: (■) 350 °C in the absence of H_2O, (□) 350 °C in 1% H_2O (◆) 250 °C in the absence of H_2O and (◇)250 °C in 1% H_2O (Lean: mixture of 1000 ppm NO/5% O_2/He; Rich: mixture of 9000 ppm CO/He).

The results of Fig. 32 also demonstrate the effect of water on the concentrations of surface NCO at 250 and 350 °C. While the effect is strong at both temperatures, the observed decrease is less at 250 °C presumably because of a lower rate of hydrolysis in this case. At 350 °C changes were also observed in the carbonate and nitrate bands (Fig. 32D). More specifically, new bands appear to form at 1365 and 1557 cm^{-1} and a shoulder at 1440 cm^{-1} was also observed. Again, the formation of bands at 1365 and 1557 cm^{-1} can be assigned to surface formate species in addition to surface carbonates [298]. The shoulder at 1440 cm^{-1} can be assigned to a bulk $BaCO_3$ species [34,179]. The formation of this band in the presence of water was in agreement with our results from 250 °C. A promotional effect of the presence of H_2O addition during CO cycling at 350 °C has been described by other groups [28,64], however such an effect could not be discerned through examination of the FTIR spectra alone since the rate and extent of

reduction of stored NO_X species cannot be determined due to the overlapping of carbonate and nitrate bands.

Similar experiments were also performed using C_3H_6 as the reducing agent and the spectra collected are shown in Fig. 33. For brevity, only spectra collected during the rich phase are shown since the storage phase is unaffected by the choice of reducing agent. The concentration of C_3H_6 (i.e., 1000 ppm) was selected in order to keep the reductant potential of CO and C_3H_6 the same and therefore obtain results that are directly comparable. Spectra collected under rich conditions indicate the presence of several types of carbon-containing surface species, with characteristic bands in the 1250-1600 cm^{-1} region. In addition to carbonates, the formation of formates and carboxylates is also expected when a hydrocarbon reductant is used [298]. Due to the overlapping of the respective bands, band assignments in this region should be regarded as tentative. Nevertheless, comparison of the spectra collected in the presence of CO and C_3H_6 (Fig. 31 and Fig. 33) indicates that in both cases the nitrate bands are no longer present in the spectra, thus providing evidence that both reducing agents can effectively reduce the stored nitrates. Abdulhamid et al. [26] previously investigated the effect of the reductant used during NSR and concluded that the reducing activity follows the order: H_2>CO>C_3H_6>>C_3H_8 . While H_2 and CO were reported to be significantly more active than C_3H_6, C_3H_6 was also shown to reduce stored NO_X to an appreciable extent. These previous results appear to be consistent with our FTIR data, although detailed information regarding the rate and extent of reduction cannot be discerned through examination of the FTIR spectra alone.

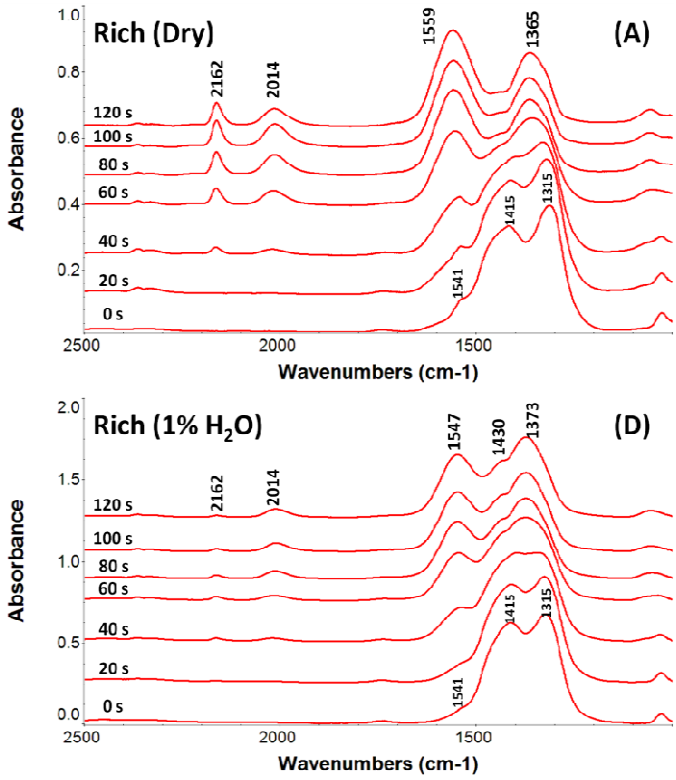

Figure 33. *In situ* spectra collected during NO_X storage-reduction cycling on $1Pt/17Ba/Al_2O_3$ at 350 °C. Panes (A) and (B) display spectra collected during rich periods (conditions: 1000 ppm C_3H_6/He). Spectra in pane (A) were collected during dry cycling; the spectra in pane (B) were collected in the presence of 1% H_2O.

Once again, the formation of a barium NCO band (2162 cm^{-1}) was observed under rich conditions even in the presence of 1% H_2O, although their surface concentration was dramatically reduced in this case. However, no aluminum NCO species are formed even in the absence of H_2O since the corresponding band at 2221 cm^{-1} is not present in the spectra. Furthermore, the concentration of Ba NCO species is significantly lower than the corresponding case during the use of CO. This observation can be attributed to either the *in situ* generation of H_2O (from oxidation of C_3H_6) and/or to the lower reducing activity of C_3H_6. Water formed *in situ* can decrease the concentration of NCO species through one of the possible mechanisms already described, with the hydrolysis of the NCO species being the most likely explanation. An

additional factor to consider is that by having the reductant potential of CO and C_3H_6 the same, we have effectively lowered the amount of carbon present during reduction to ⅓ of the corresponding carbon in the presence of CO. The formation of surface NCO species during the reduction of stored nitrates by C_3H_6 was previously interpreted to suggest that the reduction by CO and C_3H_6 proceed through the same pathway [26]. It is possible however, that *in situ* generation of CO from C_3H_6 may be the pathway leading to NCO formation in the presence of C_3H_6.

The presence of surface NCO during reduction in the presence of H_2O even in small concentrations is particularly interesting, because it is generally believed that such species are rapidly hydrolyzed to NH_3 in the presence of H_2O [24,145]. The results from Figs. 30D, 31D and 33B suggest that the rate of their formation is faster than the rate of their hydrolysis, which is supported by the maximum in NCO concentration on the surface as the rich phase progresses in the presence of H_2O. However, at this point, and prior to the analysis of the rates of reactivity that follows, it is not possible to assess their involvement in the overall NO_X reduction mechanism.

Comparisons of the amounts of NCO formed over Pt- and Rh- containing catalysts is attempted in Fig. 34. The data shown were generated by integrating the NCO bands formed under rich conditions and plotting the integrated area as a function of time. As mentioned previously, the amount of stored NO_X was approximately the same on the $Pt/Ba/Al_2O_3$ and $Rh/Ba/Al_2O_3$ catalysts, which is important since the concentration of NCO species formed is known to be dependent on the amount of stored NO_X [43]. Therefore, the effect of the nature of the noble metal can only be observed when the amount of stored NO_X during the lean phase is constant, as was the case here. Indeed, the type of noble metal used appears to affect the

concentration of NCO species formed. When CO is used as the reducing agent higher concentrations of NCO species are formed on the $Pt/Ba/Al_2O_3$ catalysts (Fig. 34A), where the opposite is true when C_3H_6 is used as the reducing agent (Fig. 34B).

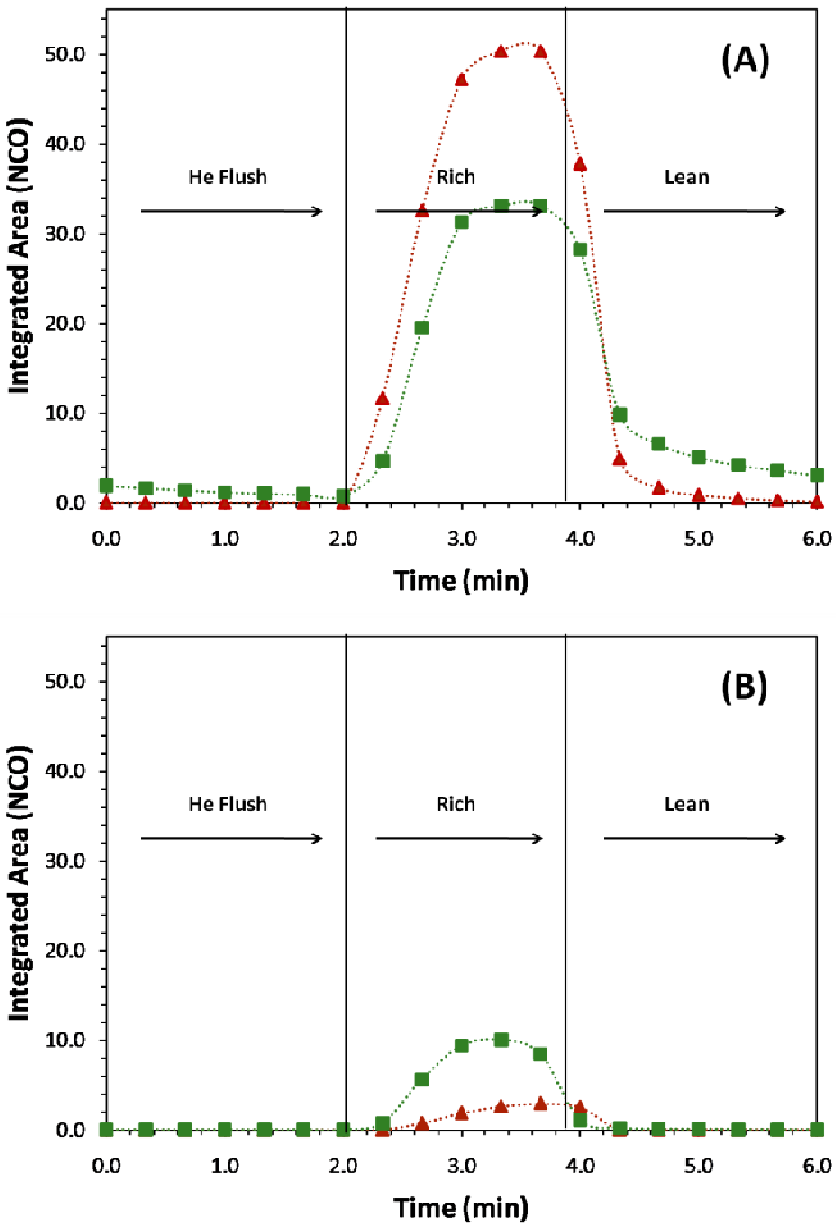

Figure 34. Comparison between the amounts of NCO species formed on (▲) $Pt/Ba/Al_2O_3$ and (■) $Rh/Ba/Al_2O_3$ at 350 °C in the absence of H_2O (Lean: 1000 ppm NO/5% O_2/He; Rich: pane (A) 9000 ppm CO/He; pane (B) 1000 ppm C_3H_6/He).

2.4.4 THE STABILITY/REACTIVITY OF NCO SPECIES AT 350 °C

In order to understand better the role of surface NCO in the NSR mechanism, their stability and reactivity was investigated in different gas mixtures.

Spectra collected during exposure of a $Pt/Ba/Al_2O_3$ catalyst at the end of the rich phase to He or a 1000 ppm O_2/He mixture at 350 °C are shown in Fig. 35. The NCO bands at 2221 and 2162 are present in the initial spectra since the NCO species were generated during and are present at the end of the rich phase. The results indicate that the NCO species are relatively stable under He, since both bands were still clearly visible after 5 min. The intensity of the band at 2221 cm^{-1} (Al-NCO species) decreased faster than that of the band at 2162 cm^{-1} (Ba-NCO species), indicating the higher stability of the Ba-NCO at this temperature. The intensity of the carbonyl band at 2030 cm^{-1} also decreased with time, indicating that adsorbed CO is removed from Pt at this temperature, and thus CO poisoning due to strong adsorption on Pt appears unlikely at 350 °C, as previously suggested by Abdulhamid et al [26,27]. When a 1000 ppm O_2/He mixture was used instead (Fig. 35B), the NCO species were rapidly removed from the surface, and no indication of any of the corresponding bands could be found in the spectra after 2 min on stream. This significant difference between the stability of NCO species in He and O_2/He strongly indicates that a reaction is taking place between the surface NCO species and O_2.

Additional reactions were also considered with NO and H_2O and the results of the corresponding experiments are summarized in Fig. 36, which shows the normalized integrated intensities of the NCO bands observed on $Pt/Ba/Al_2O_3$ and $Rh/Ba/Al_2O_3$ during exposure at the end of the rich phase to He, O_2/He, NO/He and H_2O/He mixtures at 350 °C. Results obtained with the Ba/Al_2O_3 are also included in Fig. 36. The concentration of NCO on this material is approximately 20% of that on $Pt/Ba/Al_2O_3$ or $Rh/Ba/Al_2O_3$. Since the presence of noble metals

is known to catalyze the formation of these species [314,315], it is not surprising that their concentration is dramatically lower. Actually, as previously outlined by Alexeev et al. [176], it is more surprising that these species are formed at all, especially in high enough concentrations to be observable, since the reaction was previously believed to occur only on the surfaces of metals. Clearly, this is not the case and Forzatti et al. [290] recently described this phenomenon for Ba/Al_2O_3 in more detail.

Some differences were observed between the NCO stability/reactivity in He, shown in Fig. 36A. The reaction of NCO species with residual surface nitrites/nitrates cannot be excluded in this case, since Nova et al. [64] reported that CO treatment at 350 °C only removes approximately 80% of the NO_X stored on $Pt/Ba/Al_2O_3$. Similarly, Forzatti et al. [290] reported removal of only 22% of the NO_X stored on Ba/Al_2O_3 and 43% of the NO_X stored on $Pt/Ba/Al_2O_3$ following CO TPSR treatment up to 400 °C. While some of the stored NO_X was converted and remained as NCO on the surface, residual nitrites/nitrates could be present as well. The notion that a reaction with another surface species is responsible for the decreased intensities observed in Fig. 36A is also supported by previous reports by Forzatti et al. [290] who observed that NCO species were stable at 350 °C, even under vacuum, and Szailer et al. [24] who reported that thermal decomposition of surface NCO begins at temperatures slightly above 350 °C and is not completed even at 450 °C. The results of Fig. 36A further show that the reaction of NCO with residual nitrites/nitrates is significantly slower than the corresponding reactions shown in the other gas mixtures investigated. Surface distribution and diffusion of the NCO and the residual nitrites/nitrates could account for this effect, as well as for differences observed between the different metals.

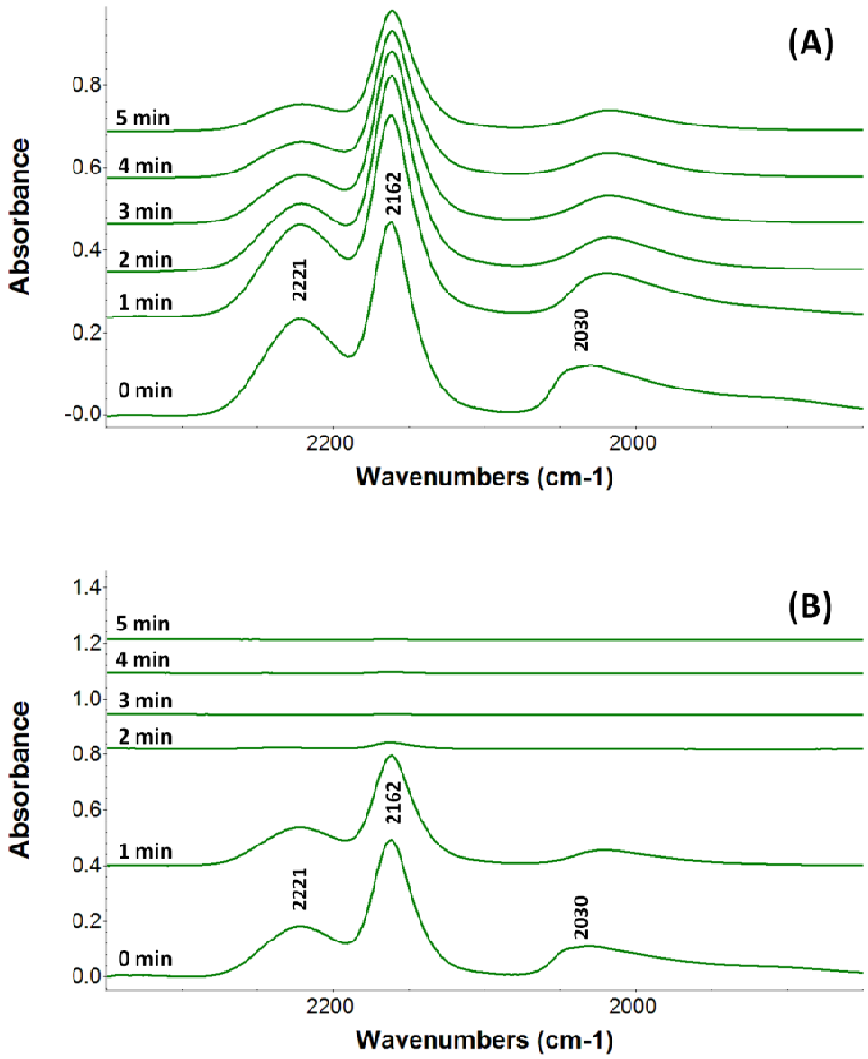

Figure 35. Spectra collected during exposure of a $Pt/Ba/Al_2O_3$ catalysts at the end of the rich phase to (A) He or (B) 1000 ppm O_2/He at 350 °C.

The results obtained during the reaction of surface NCO species with O_2, NO and H_2O are shown in Figs. 36B, 36C and 36D, respectively. The reactivity of NCO with these molecules has been well documented in the literature [24,28,145,176,288,290,299,302,316,317]. In contrast, exposure of surface NCO species to CO did not result in a decrease in their concentration, even after prolonged, in agreement with previously published results on the stability of NCO in CO [318]. An initial increase was observed in the NCO concentration during

the reaction with NO (Fig. 36C). These additional NCO species formed can be attributed to the reaction of NO with CO adsorbed on the surface or residual gas phase CO in the FTIR cell.

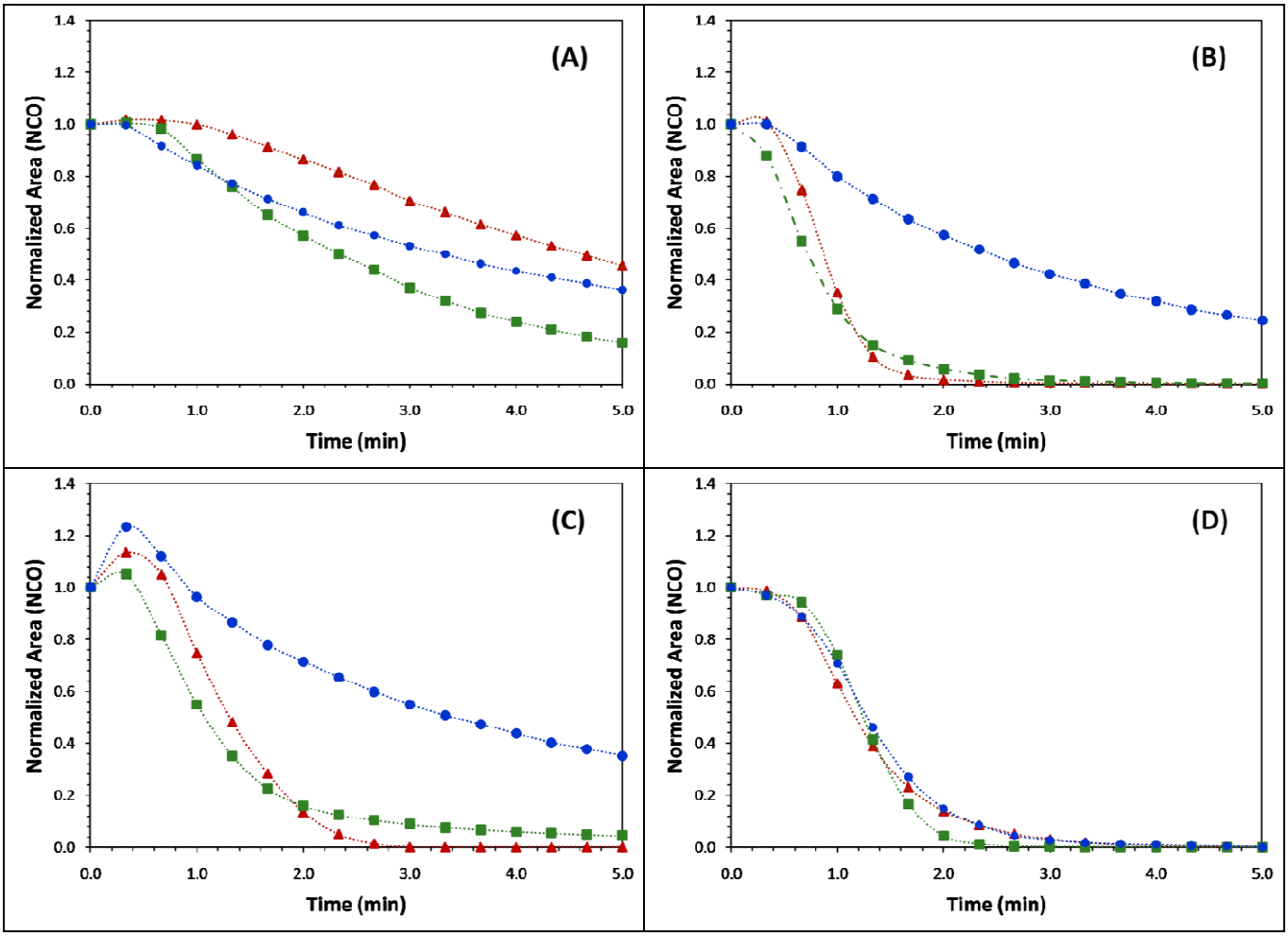

Figure 36. Normalized integrated intensity of NCO bands observed on (●) Ba/Al_2O_3, (▲) $Pt/Ba/Al_2O_3$ and (■) $Rh/Ba/Al_2O_3$ during exposure at the end of the rich phase to (A) He, (B) 1000 ppm O_2/He, (C) 1000 ppm NO/He and (D) 1000 ppm H_2O in He at 350 °C.

The results of Fig. 36 further indicate that the reaction of surface NCO species with NO and O_2 is a metal catalyzed reaction, since a significant difference in the rate of removal of NCO is observed between the Ba/Al_2O_3 and the $Pt/Ba/Al_2O_3$ and $Rh/Ba/Al_2O_3$ materials. Very little difference however, is observed in both cases over the noble metal containing catalysts. In contrasts, the rapid removal of NCO in the presence of H_2O over the Ba/Al_2O_3 material, and the

similar rates observed in this case with all three materials demonstrate that a precious metal is not necessary for this reaction to occur. Finally, the reactions of surface NCO with NO, O_2 and H_2O on $Pt/Ba/Al_2O_3$ and $Rh/Ba/Al_2O_3$ all exhibited similar activity, with the majority of the NCO species being removed from the surface after approximately 2 min.

Fig. 37 shows the evolution of N_2 from the $Rh/Ba/Al_2O_3$ catalyst during the rich phase and subsequent exposure to He, O_2 and NO. As shown in Fig. 37A, N_2 is generated during the rich phase, but not during subsequent exposure to He after the rich phase ends, although the results of Fig. 36A indicate a gradual decrease in surface NCO concentrations in this case. This indicates that the NCO species present on the $Rh/Ba/Al_2O_3$ surface at the end of rich period did not significantly decompose to gas phase N_2 or react quickly enough with residual nitrites/nitrates to produce N_2. It is possible that the decomposition products of the surface NCO were re-adsorbed as nitrites/nitrates, but an increase in surface nitrite/nitrate concentrations could not be observed in our results due to strong overlapping of the nitrite/nitrate and carbonate bands. Forzatti et al. [290] however, were able to observe formation of nitrites during similar experiments. In our case, the concentration of NCO species on the surface may simply not have been high enough to allow us to observe such formation.

Exposure of the surface NCO species to 1000 ppm O_2/He resulted in the formation of significant amounts of N_2, as shown in Fig. 37B. Evolution of N_2 during two discrete periods – i.e. during the rich phase and during the subsequent lean phase – has previously been observed by Breen et al. [16] and Scholtz et al. [28,319,320] during NSR operation. At the end of rich phases, nitrites/nitrates, carbonates and NCO species were the only species observed on the surface. Exposure of nitrites/nitrates or carbonates to O_2 increases the stability of these species and does not result in evolution of N_2. Some authors [16] have also suggested the NH_3 may be

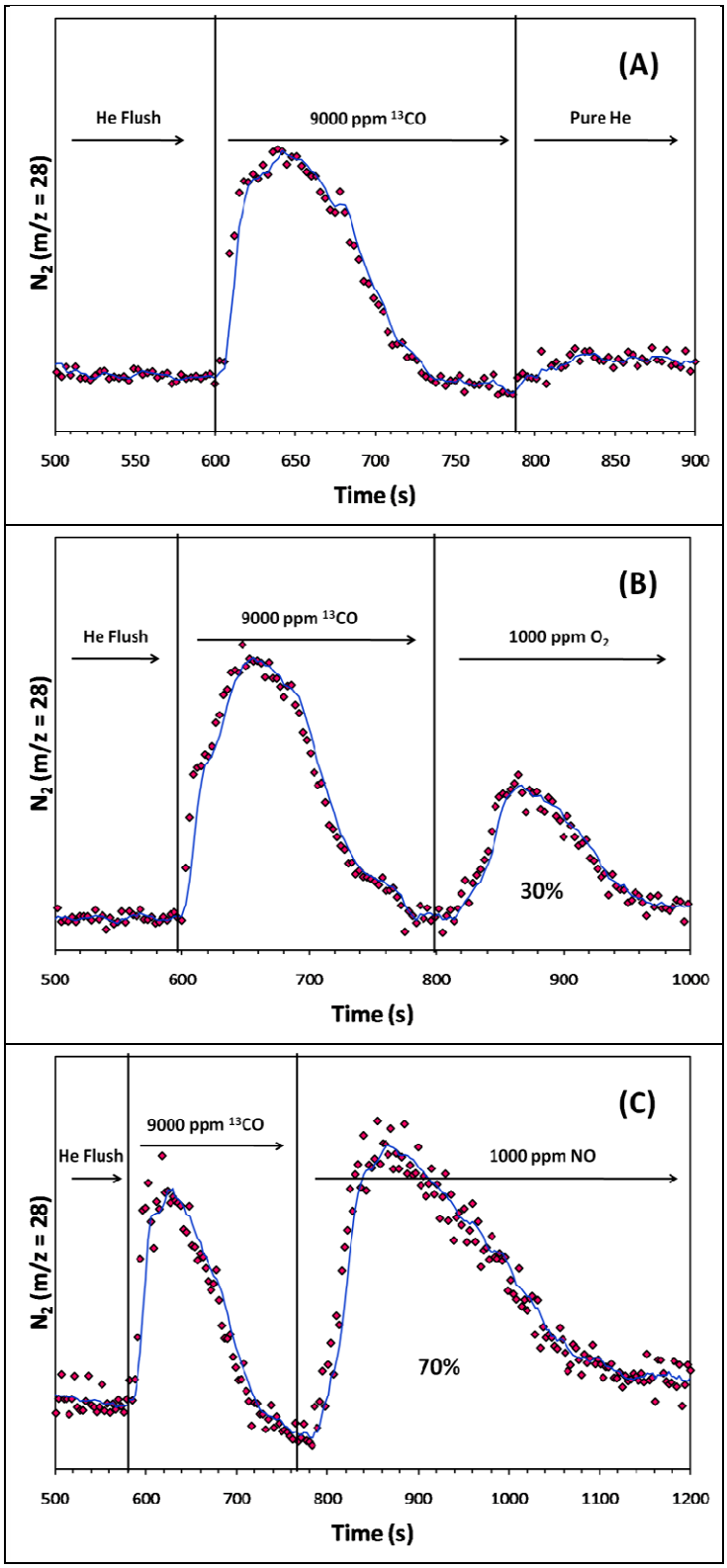

Figure 37. N_2 profiles (m/z = 28) obtained during the reaction of stored NO_X with ^{13}CO and the subsequent reaction of residual NCO species with (A) He, (B) 1000 ppm O_2/He or (C) 1000 ppm NO/He on $Rh/Ba/Al_2O_3$ at 350 °C.

stored on the catalyst during the rich phase, but the formation of significant amounts NH_3 in the absence of H_2O and H_2, as well as subsequent storage and oxidation to N_2 is unlikely under our conditions [175]. It is therefore reasonable to assume that the N_2 produced during the exposure to O_2 is the product of the reaction between surface NCO and O_2. Integration of the two N_2 peaks observed in our case (Fig. 37B) indicated that approximately 30% of the total N_2 production resulted from the reaction of NCO species with O_2.

Exposure of the surface NCO species to 1000 ppm NO/He also resulted in the formation of a second N_2 peak, which in this case was even larger than the first N_2 peak (Fig. 37C), constituting approximately 70% of the total N_2 produced. Comparison between the N_2 peaks shown in Figs. 37B and 37C confirmed while the first peaks were approximately the same in both cases, the N_2 peak observed during NO exposure was approximately 5 times larger than the one observed during O_2 exposure. Stoichiometric calculations indicate that reaction of NCO species with NO theoretically results in twice as much N_2 produced. Since in both cases similar amounts of NCO species were completely removed from the catalyst surface (see Figs. 36B and 27C) the remaining N_2 formed is in all likelihood the result of reactions between the gaseous NO and other surface reducing agents. Evidence to this direction is provided in Fig. 36C, which shows additional surface NCO formation upon introduction of NO, indicating that an NCO species may act as an intermediate even for this addition N_2 formation. The small increase observed in Fig. 36C is misleading since it represents the net difference during the first 30-60 s between NCO formation and consumption. NCO consumption during this initial period is at its highest point, as indicated by the very steep slope of the N_2 production curve in Fig. 37C.

Overall, the results of Fig. 36 and 37 indicate that surface NCO contribute to a significant percentage of the overall amount of N_2 formed, when CO is used as the reducing agent. While it

is difficult to quantify the exact amount, it could exceed in some cases 30% of the total. Furthermore, such species could be responsible for N_2 retention on the NSR catalyst surface during the rich phase and contribute to a second N_2 release observed during NSR operation at the onset of the lean phase.

2.5 CONCLUSIONS

The results of *in situ* FTIR measurements conducted with $Pt/Ba/Al_2O_3$ and $Rh/Ba/Al_2O_3$ catalysts of very similar molar loading and dispersion of precious metals indicate that surface nitrites are the predominant NO_X storage form at 250 °C, while surface nitrates become the predominant storage form at 350 °C. The presence of water did not have a significant effect during storage. Surface isocyanates (NCO) were formed under a variety of conditions investigated and their concentration was dependent on the temperature, the reductant selected, the presence of H_2O and the type of precious metal used. The highest concentrations of surface NCO species were observed during dry conditions with CO used as the reductant at 350 °C. The NCO stability measurements demonstrate that these species are stable in CO and moderately stable in He. In contrast, the reaction of surface NCO species with NO and O_2 is fast and catalyzed by precious metals, with no difference observed between Pt and Rh. A similarly fast reaction is also observed with H_2O, even in the absence of the noble metal component. Comparison of N_2 evolution amounts during the rich phase and subsequent reaction of residual NCO species with O_2 and NO confirmed that reaction of NCO species could contribute significantly to the total amount of N_2 formed, when CO is used as the reducing agent. These

species represent a reduced form of stored N_2 that could be responsible for N_2 release observed at the onset of the lean phase.

2.6 ACKNOWLEDGEMENTS

The authors gratefully acknowledge financial support from the National Science Foundation (Division of Chemical, Bioengineering, Environmental and Transport Systems (CBET); Award ID 0730937). The authors further acknowledge Dr. Douglas Blom and the University of South Carolina Electron Microscopy Center for instrument use, scientific and technical assistance.

CHAPTER 3. NH_3 FORMATION OVER A LEAN NO_X TRAP (LNT) SYSTEM: EFFECTS OF LEAN/RICH CYCLE TIMING AND TEMPERATURE

3.1 PREFACE

A commercial lean NO_X trap (LNT) catalyst containing Pt, Pd, Rh, BaO, and CeO_2 was evaluated in this investigation. The effects of lean/rich cycle timing on the NO_X, CO and C_3H_6 conversions and on the NH_3 and N_2O selectivities were considered. Two distinct lean/rich cycling regimes were identified. At low temperatures, NO_X release and reduction were kinetically limited. As a result, a longer, lower-concentration rich dose favored increased cycle averaged NO_X conversions. For example, extending the rich period from 5 to 15 s at 250 °C, while holding the overall reductant dose constant, resulted in an increase in cycle averaged NO_X conversion from 59 to 87%. At high temperatures, the opposite was found to be true. Above 450 °C, NO_X release and reduction occurred very rapidly and shorter, higher concentration rich doses yielded significantly higher NO_X conversions. For example, extending the rich period from 5 to 15 s at 500 °C, while holding the overall rich dose constant, resulted in a decrease in the cycle averaged NO_X conversion from 76 to 54%. The selectivities to NH_3 and N_2O were found to be primarily a function of temperature, with both being higher at lower temperatures. The effect of cycle timing and reductant concentration were of secondary importance. In contrast, NH_3 and N_2O yields were significantly affected by the cycle timing since they depend on the NO_X conversion. Therefore, any combination of changes in the lean/rich timing protocol or reductant concentrations that resulted in increased NO_X conversion also resulted in increased NH_3 and N_2O yields for a given temperature. As a result, concerted control of NH_3 generation

by varying the lean/rich cycle timing was demonstrated, although the effect was relatively small near the optimum temperature (i.e., 350 – 400 °C) of the LNT catalyst. In contrast, both at lower and higher temperatures, variations in the rich cycle duration resulted in NH_3/NO_X ratios that could extend the region of operation for a close-coupled LNT-SCR system. However, N_2O yield also increased with NH_3 yield under the same conditions.

3.2 INTRODUCTION

Lean-burn engines are more fuel efficient and produce less overall CO_2 per mile when compared to traditional stoichiometric-burn ones. However, meeting NO_X emission regulations for lean-burn engines through the use of advanced catalytic converter technologies still represents a significant technical challenge. Over the past 15 years, lean NO_X trap (LNT) [4] and selective catalytic reduction (SCR) [321] catalysts have been identified as two promising systems for the removal of NO_X from the exhausts on lean-burn engines. In several recent publications and patents, there has been considerable discussion regarding the advantages of combining these two technologies into a coupled LNT-SCR system [154,156,283,322–338]. As a brief review, LNTs are designed to function under periodic lean/rich environments, where NO_X is stored in the form of nitrites or nitrates on a storage component (e.g., Ba) during lean periods typically lasting 60 - 120 s [4,339]. As time elapses, the storage component becomes saturated with NO_X and a subsequent rich step, typically lasting 1 - 5 s, must be employed to reduce the stored NO_X and in the process regenerate the storage component. Catalytic formulations used commercially generally include platinum group metals (PGM; e.g., Pt, Pd and Rh) supported on a BaO and CeO_2-modified γ-Al_2O_3 [4]. While N_2 is obviously the most desirable product during NO_X reduction, NH_3 and N_2O can also be formed and under certain conditions, the selectivity to these

undesirable by-products can be significant. For example, Ren and Harold [340] reported selectivities to NH_3 of 40%, or greater, for a series of model LNT catalysts operating below 200 °C. At similar temperatures, Bonzi et al. [330] attributed the high selectivity to NH_3 to a combination of significant NH_3 formation and slow subsequent reaction of the NH_3 formed with the remaining stored nitrites/nitrates. This reaction becomes significantly faster at higher temperatures, thus contributing to reduced NH_3 selectivities. While NH_3 formation over the LNT catalyst is undesirable in a single catalyst system, it also clearly demonstrates the potential for a coupled LNT-SCR configuration.

In contrast to LNT catalysts, NH_3-SCR catalysts are operated under steady-state conditions and were originally designed for use in stationary applications [2,341]. Current commercial SCR catalytic formulations include V_2O_5-WO_3/TiO_2 or Cu/Fe exchanged zeolites [2,341], with the zeolite-based materials favored for automotive applications due to their lower temperature activity, as well as their ability to store significant amounts of NH_3 under transient conditions [342,343]. Initially, commercialization of zeolite-based SCR catalysts was limited due to hydrothermal stability issues, but recent advances in this area have led to the development of hydrothermally stable Cu-zeolite catalysts that are active over a broad temperature range [342,344]. Zeolites are particularly attractive for a coupled LNT-SCR configuration because of their ability to store NH_3 generated over the LNT catalysts during short rich cycles, which is stable under lean conditions. NH_3 thus stored can be used in the subsequent lean cycle to reduce NO_X that is not trapped by the LNT catalyst. As outlined by Bonzi et al [330], the LNT-SCR configuration has the advantage of both increasing the selectivity to N_2 and the overall NO_X conversion when compared to a single LNT system. For example, Lindholm et al. [338] reported a cycled averaged NO_X conversion of 99.5% for an LNT-SCR system operating at 300 °C, but

also observed increases in the NO_X conversion and N_2 selectivity over the entire temperature range (200 – 400 °C) investigated when compared to a single LNT system. Similarly, Xu et al. [283] recently reported that LNT-SCR systems have the additional benefit of requiring a lower PGM content for the LNT, increasing the temperature window for high NO_X conversion and mitigating catalyst deactivation due to aging. In summary, a consensus has emerged that addition of an SCR catalyst, either in series, as a physical mixture or in a layered geometry, to an LNT exhaust system can result in significant improvements in overall catalytic performance. However, the majority of these investigations have either been performed under typical LNT cycling conditions (e.g., 60 s lean, 5 s rich) or under extended isothermal step conditions and the role of cycle timing has not been investigated in detail.

In this manuscript, the role of both lean and rich LNT cycle timing is addressed with specific emphasis placed on the amount of NH_3 generated in relation to the amounts NO_X and CO slip from the LNT catalyst. In addition, N_2O formation was closely monitored under these conditions. Finally, the concept of concerted control over the NH_3 generation by the control of cycle timing and conditions is introduced with the goal optimizing the LNT-SCR system as a function of the under-floor catalyst temperature.

3.3 EXPERIMENTAL

3.3.1 CATALYTIC MATERIAL

A fully-formulated LNT monolith (wash-coated honeycomb cordierite monolith removed from a Lean-GDI, BMW 120i, Model Year 2009) was utilized in the present investigation. On the vehicle, the LNT catalyst brick of 413 cell per square inch (cpsi) is used in an under-floor configuration. The catalyst has now been adopted as the new representative commercial LNT

catalyst in the Crosscut Lean Exhaust Emissions Reduction Simulations (CLEERS) research community [345].

3.3.2 CATALYST CHARACTERIZATION

Semi-quantitative metals screening of the LNT catalyst using Inductively Coupled Plasma - Mass Spectrometry (ICP-MS) was conducted by Galbraith Laboratories, Inc. (Knoxville, Tennessee). Inductively Coupled Plasma-Atomic Emission Spectroscopy (ICP-AES), which afforded quantitative results, was also conducted by Galbraith Laboratories, Inc.

A JEOL JXA-8200 SuperProbe Electron Probe MicroAnalyzer (EPMA) was used to map the elemental composition of the catalyst washcoat. Samples were prepared for imaging by mounting them in epoxy and polishing. The spot size was approximately one cubic micron, which is smaller than the typical grain size of the constituent phases. A Hitachi 4800 field emission gun scanning electron microscope (FEG-SEM) with an EDAX energy dispersive spectroscopy (EDS) x-ray detector was also used to measure the element composition of individual grains. Since the sample was heterogeneous and porous, no attempt was made to calibrate the x-ray intensities with standard samples. Therefore the compositional data is likely accurate to no less than one percent and should be viewed more as a relative comparison between different grains in the wash coat.

3.3.3 CATALYTIC EVALUATION

Lean/rich cycling was performed using a laboratory bench-flow reactor, as described in more detail elsewhere [135,346]. Briefly, the LNT monolithic core (2.1 cm wide X 5.5 cm long; SV=30,000 hr^{-1}; ≈9150 standard cm^3/min) was tightly wrapped in Zetex insulation tape and inserted into a horizontal quartz tube reactor. The reactor was heated using a horizontal bench-

top furnace (Lindberg/Blue M). Lean/rich gas mixtures were prepared using pressurized gas cylinders (UHP, Air Liquide) and a system of mass flow controllers (Unit Instruments Series 7300, Kinetics Electronics). A rapid switching 4-way valve system was used to alternate between the lean and rich gas mixtures. Water was introduced using a peristaltic pump (Cole-Parmer) that fed into a heated, flash-vaporization zone held at 350 °C. All gas lines downstream of the water introduction zone were heated and quartz chips were placed upstream of the monolithic core to ensure that the feed gas temperature reached the set point temperature prior to contacting the catalyst. Three thermocouples were used to measure the temperature. The first was placed 1 cm upstream of the core and was used to record the inlet/set-point temperature. The second thermocouple was placed in the middle of the monolithic core and was used to record the actual monolith temperature. The third was placed 1 cm downstream of the core and was used to record the temperature exiting the core. After exiting the reactor, the gas was fed to an MKS MultiGas^{TM} 2030 HS FT-IR analyzer, which allowed for continuous tracking (5 Hz) of NO, NO_2, N_2O, NH_3, CO, C_3H_6, CO_2 and H_2O concentrations. Prior to the reactor measurements, the as-received catalyst was "de-greened" at 700 °C in a 10% H_2O/air mixture for 16 h to establish reproducible performance. Unless otherwise denoted, all calculations were performed using the last 4 cycles obtained during lean/rich cycling, where Eqns. 14-16 were used to calculate the cycle averaged NO_X, CO and C_3H_6 conversion, respectively.

$$X_{NO_X} = \frac{\int NO_{X_{Fed}} - \int NO_{X_{Slipped}}}{\int NO_{X_{Fed}}} \times 100 \tag{14}$$

$$X_{CO} = \frac{\int CO_{Fed} - \int CO_{Slipped}}{\int CO_{Fed}} \times 100 \tag{15}$$

$$X_{C_3H_6} = \frac{\int C_3H_{6_{Fed}} - \int C_3H_{6_{Slipped}}}{\int C_3H_{6_{Fed}}} \times 100 \tag{16}$$

Eqns. 17-20 were used to calculate the NH_3 and N_2O yields and selectivities, respectively. The total amount of products formed was calculated based on the total amount of NO_X consumed. Since N_2 formation could not be quantified by the FTIR analyzer, the N_2 yield and selectivity was calculated using a nitrogen mass balance by assuming that NH_3, N_2O, and NO_X were the only nitrogen containing by-products formed.

$$Y_{NH_3} = \frac{\int NH_{3_{Produced}}}{\int NO_{X_{Fed}}} \times 100 \quad (17)$$

$$S_{NH_3} = \frac{\int NH_{3_{Produced}}}{\int NO_{X_{Fed}} \times X_{NO_X}} \times 100 \quad (18)$$

$$Y_{N_2O} = \frac{\int N_2O_{Produced}}{\int NO_{X_{Fed}}} \times 100 \quad (19)$$

$$S_{N_2O} = \frac{2 \times \int N_2O_{Produced}}{\int NO_{X_{Fed}} \times X_{NO_X}} \times 100 \quad (20)$$

A total of 81 sets of conditions were considered in this investigation, consisting of combinations of nine temperatures (150 – 550 °C, in 50 °C increments) and nine different cycle timing protocols. The lean period gas concentration was held constant at 500 ppm NO, 8% O_2, 5% H_2O and 5% CO_2 in N_2. The rich period included a variable amount of reductants with a balance of 5% H_2O and 5% CO_2 in N_2. The required amount of reductants (i.e., H_2, CO and C_3H_6) in the rich dose was calculated by adding the stoichiometric amount of reductant required to completely reduce all of the NO_X fed plus the required amount of reductants required to consume all of the O_2 storage capacity of the LNT catalyst. The calculated rich dose (i.e., the total number of moles of reductant required) was then held constant and the rich cycle duration was varied. Therefore, shorter rich cycle times (e.g., 5 s) contained higher concentrations of reductants, while longer rich cycle times (e.g., 10 and 15 s) contained lower concentrations of

reductants. Once the total amount of reductants needed was determined, their relative concentrations were calculated based on a 18:6:1 ratio for CO:H_2:C_3H_6, respectively. This ratio is considered to be representative of rich engine exhaust [347].

The oxygen storage capacity (OSC) on the LNT catalyst was measured by cycling (60 s lean / 5 s rich) in a lean gas mixture comprised of 10% O_2, 5% H_2O and 5% CO_2 in N_2 and a rich gas mixture comprised of X% CO, 5% H_2O and 5% CO_2 in N_2. The CO concentration was adjusted during this cycling (0.1% increments) until consistent breakthrough of CO was observed by both the FT-IR analyzer and lambda sensor (ECM AFRecorder 1200A air-fuel ratio meter). Fig. 38 demonstrates the OSC protocol for cycling at 550 °C. The results demonstrate that a CO concentration of 1.6% resulted in minimal CO breakthrough during rich periods. The lambda sensor reading, which was used as a secondary metric for CO breakthrough (λ<1.00=rich), never dipped below 1.00, which implied incomplete consumption of the OSC. Alternatively, when the CO concentration was increased to 1.7%, breakthrough of CO was consistently measured by the FT-IR analyzer. In this case, the CO breakthrough also coincided with a lambda sensor reading of approximately 0.96 at the end of the rich period. Therefore, an OSC of 1.7% CO was used in the calculations to determine the reductant concentration necessary during the rich periods at 550 °C. Table 7 displays the OSC values measured for the LNT catalyst as a function of temperature. For temperatures below 300 °C, a value of 1.6% was assumed because the kinetics of O_2 consumption required longer times than provided in the 5 s rich period and accurate measurements could no longer be obtained.

Table 8 shows the calculated reductant concentrations for different cycling times for an OSC corresponding to 1.6% CO. As shown in the Table, these concentrations varied both with the lean cycle timing (since the total amount of NO_X fed varies in this case) and rich cycling

timing (since the total amount of reductants fed has to remain constant regardless of the length of the rich period). Slightly higher concentrations were used at temperatures above 450 °C due to the increase in the OSC to 1.7% CO (not shown for brevity).

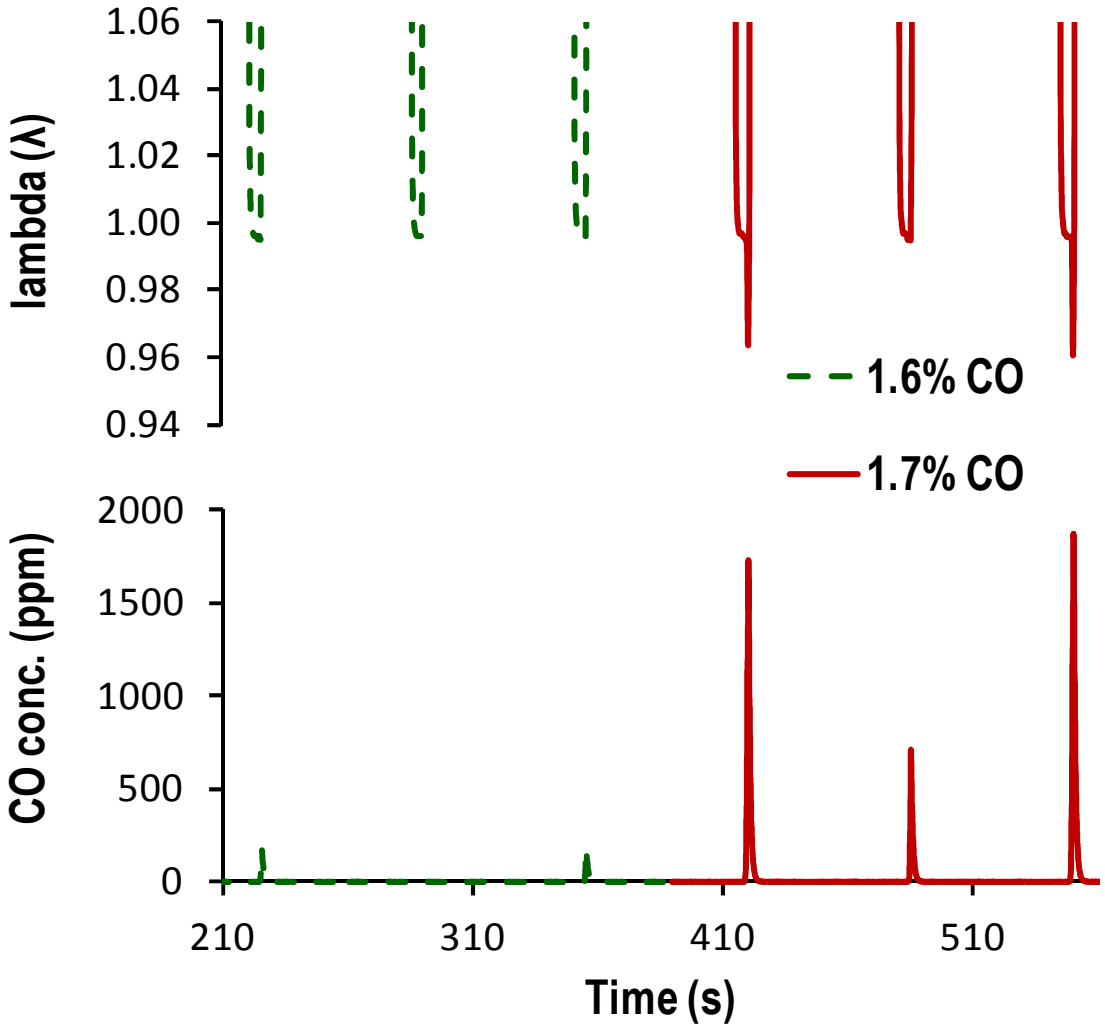

Figure 38. OSC measurement performed at 550 °C over the LNT catalyst (See experimental section for conditions).

Table 7. OSC values measured for the LNT catalyst at different temperatures.

Temperature (°C)	**OSC** (CO %)
350	1.6
400	1.6
450	1.7
500	1.7
550	1.7

Table 8. Calculated reductant concentrations for the cycle timing protocols used in this investigation in the 150 – 400 °C range (OSC = 1.6% CO).

	Reductant Concentrations		
Lean/Rich Timing (s)	**CO** (%)	**H_2** (%)	**C_3H_6** (%)
60/5	2.01	0.67	0.112
60/10	1.01	0.34	0.056
60/15	0.67	0.22	0.037
120/5	2.83	0.94	0.157
120/10	1.42	0.47	0.079
120/15	0.94	0.31	0.052
180/5	3.65	1.22	0.203
180/10	1.82	0.61	0.101
180/15	1.22	0.41	0.068

3.4 RESULTS AND DISCUSSION

3.4.1 CATALYST CHARACTERIZATION

Semi-quantitative inductively Coupled Plasma-Mass Spectrometry (ICP-MS) analysis of the LNT catalyst indicated the presence of Mg, Al, Ce, and Ba as major components. Other elements of significance included Zr, La, Pt, Pd, and Rh. The results of inductively Coupled Plasma-Atomic Emission Spectroscopy (ICP-AES) also indicated the presence of Pt, Pd, Rh, Ba,

Ce, Zr, and La on the LNT catalyst used. The loadings of these elements are summarized in Table 9.

Table 9. Elemental composition of the LNT catalyst used in this investigation.

	Lean GDI, BMW 120i (2009) loading (g/L)
Pt	2.2
Pd	0.8
Rh	0.3
Total PGM (g/L)	*3.3*
PGM Ratio (Pt/Pd/Rh)	*7/3/1*
Ba	19.9
Ce	55.5
Zr	4.3
La	2.5

The wash coat was composed of three separate layers of roughly equal thickness, which suggests that three separate dip coats were conducted during processing. Of the elements measured, the Ba elemental map obtained by EPMA revealed these three layers the best, as shown in Fig. 38. Mud-cracks normal to the substrate surface, which stop at the layer interfaces, also indicate that three separate drying steps were performed during processing of the wash coat. The elemental composition of these three layers appears to be identical.

Three compositionally distinct domains (or grains) were observed in the washcoat using EPMA: a CeO_2 phase with low amounts of La, Zr, Pt and Pd (Ce/Zr mixed oxide domain); a Mg/Al oxide spinel phase with some Ce and Pd also present (Mg/Al mixed oxide domain); and in a few spots, an Al_2O_3 phase with Rh, as well as some Pd present (Al oxide domain). In addition to these three domains, there was another type of grain rich in Ba (results not shown), as in the case of the old CLEERS reference LNT [135,346]. As discussed in the experimental section however, no attempt was made to calibrate the x-ray intensities with standard samples and the results shown in Fig. 41 were included as a qualitative comparison between different

grains in the wash coat. Generally, the number of Ba-rich grains appeared to be rather limited, which may indicate a more uniform Ba dispersion in this LNT catalyst in comparison to a different LNT catalyst formulation considered in previous investigations [135,346]. The Mg/Al mixed oxide domain exhibits a bimodal grain size distribution with large 5 – 10 µm grains interspersed with submicron-sized grains. Fig. 40 shows a cross-section of the washcoat with the bright particles corresponding to the Ce/Zr mixed oxide domain and the darker matrix representing the Mg/Al mixed oxide domain. The compositions of the Ce/Zr and coarse-grained Mg/Al mixed oxide domains measured with EDS are shown in Fig. 41.

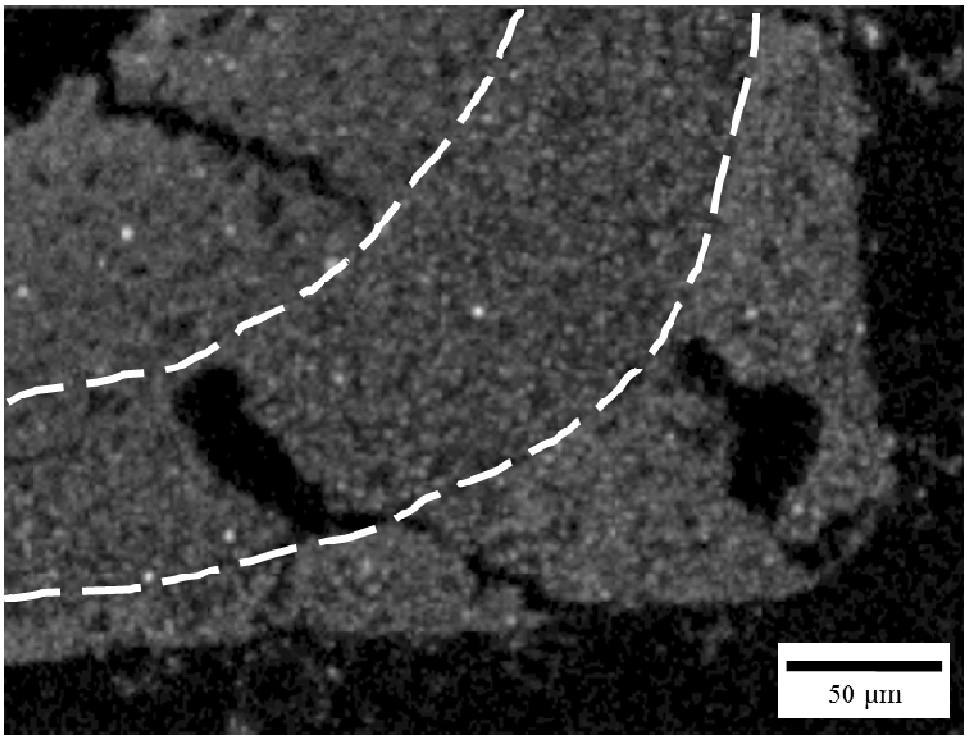

Figure 39. EPMA map for Ba in a washcoat corner of the front section of the LNT catalyst brick. White dashed lines separate the three apparent layers of the washcoat.

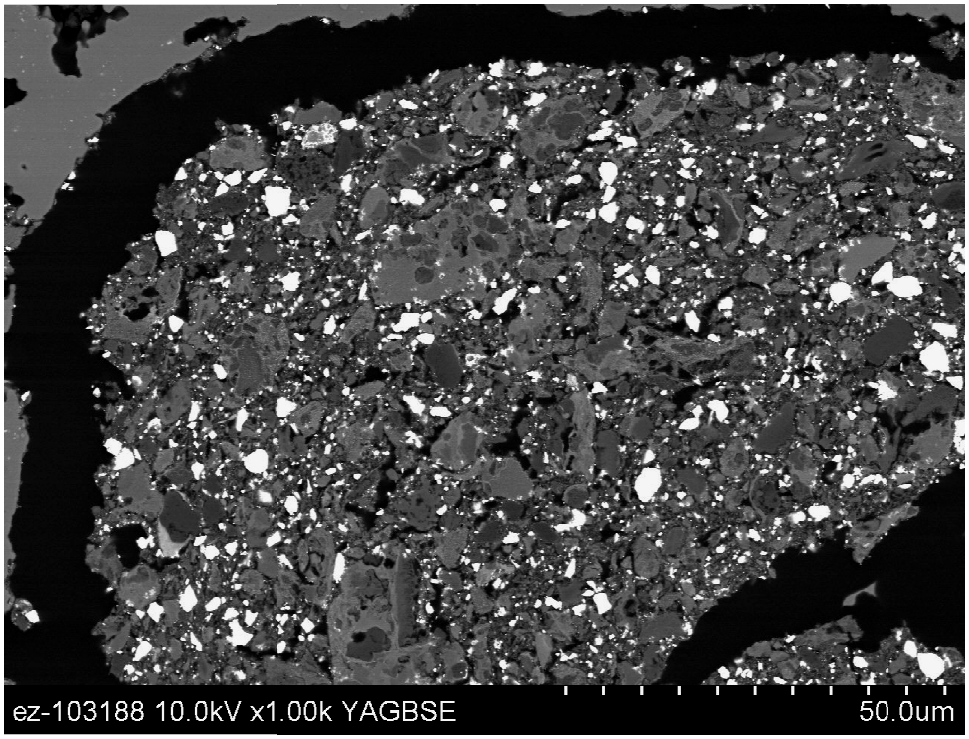

Figure 40. SEM image of the washcoat cross-section.

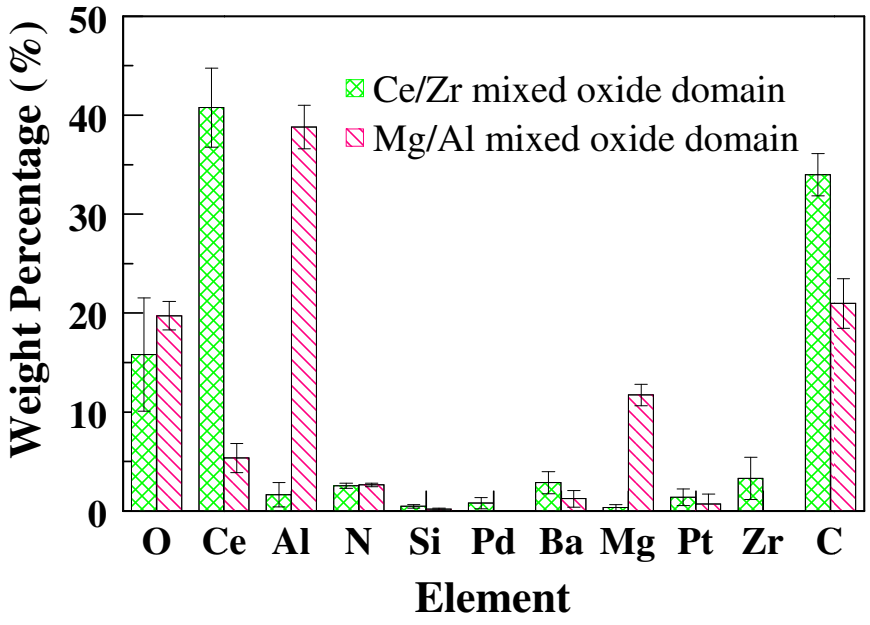

Figure 41. Approximate elemental compositions in weight percentage of the two primary phases in the washcoat as measured by EDS (carbon signal originating from the mounting epoxy).

3.4.2 REPRESENTATIVE LEAN/RICH CYCLING OVER THE LNT CATALYST

Reactor effluent concentrations observed at 300 °C during 60 s lean/5 s rich cycling over the LNT catalyst used in this investigation are shown in Fig. 42 as a representative example for the performance of this catalyst. As expected, low concentrations of NO_X were observed during the lean period indicating that the majority of NO_X was stored on the LNT catalyst. As the reactor feed was switched to the rich mixture (after 60 s) and the regeneration of the LNT catalyst was initiated, a significant un-reacted NO_X release was observed simultaneously with the formation of N_2O. Previous literature reports have addressed both of these observations [140,151,346,348–351], with the NO_X release attributed to the slower NO_X reduction kinetics at this temperature in comparison to the surface nitrite/nitrate decomposition [140,151] and the N_2O formation linked to the relative concentrations of surface NO and N intermediates present [140,151,346,348–351]. Subsequent formation and breakthrough of NH_3 and CO were also observed during the rich cycle, with an approximately 2.5 s delay between the onset of the rich cycle and the appearance of these products in the reactor outlet. The delay for NH_3 has previously been attributed to the reaction of NH_3 formed upstream on the LNT catalyst with downstream surface nitrites/nitrates and oxygen stored on the catalyst [23,60,286,351,352]. Likewise, the delay in CO breakthrough is most likely a combination of several contributing factors including the amount of CO reacting with stored NO_X and oxygen, as well as its participation in the water gas shift reaction (WGS). The near-simultaneous appearance of CO and NH_3 in the reactor outlet during reduction is an important feature of the LNT catalyst behavior in light of its potential use in an LNT-SCR configuration. While NH_3 could be stored in the SCR material, CO storage and/or oxidation over the downstream SCR catalyst under rich conditions is highly unlikely. Therefore, for practical implementation of the LNT-SCR

technology, the amount of CO slip from the LNT catalyst needs to be closely monitored as a function of operating conditions and or catalytic formulation and eventually converted to CO_2.

Table 10 summarizes the performance of the LNT catalyst at 300 °C (60 s lean/5 s rich) and provides corollary results calculated from the results shown in Fig. 42. The majority of NO_X fed to the reactor during the lean cycle is stored and reduced during the subsequent rich step, resulting in a cycle averaged NO_X conversion of 99.2%. Interestingly, the selectivity to N_2 for this cycle timing protocol and temperature is fairly low (59.2%), in agreement with other investigations conducted under similar conditions [151,340]. A significant percentage of the stored NO_X (29.0%) reacted to form NH_3, where the NH_3 production is approximately 62 μmol/cycle, while the total amount of NO_X slip is only 1.6 μmol/cycle. The difference between the amount of NH_3 produced and NO_X slip as well as the difference in time evolution of the two species demonstrate the need for NH_3 storage on the SCR, since equimolar NH_3 and NO_X amounts are needed for optimum LNT-SCR operation. The selectivity to N_2O was also high (11.8%) under these conditions, while CO and C_3H_6 conversions were relatively low (87.1 and 77.5%, respectively). Once again, we should point out that the data from this cycling condition were included only as a representative example because they demonstrate both the potential advantages and drawbacks of LNT operation under conditions favorable for NH_3 production. In subsequent sections, the NH_3 and N_2O trends will be discussed in more detail.

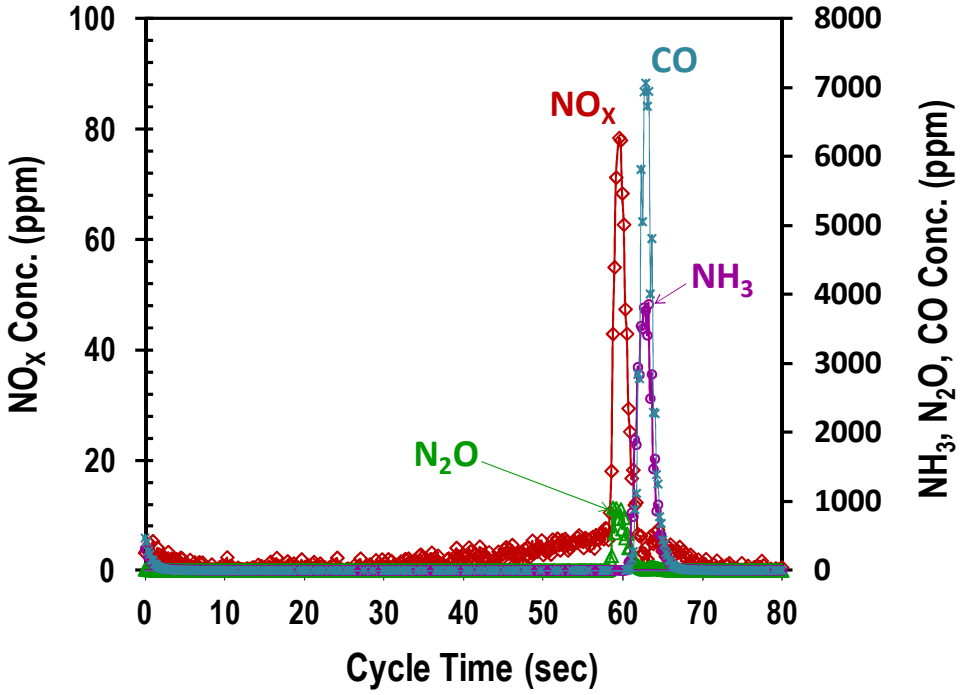

Figure 42. A 60 s lean/5 s rich cycling experiment performed at 300 °C, where the NO_X, (■) NO_2, (▲) N_2O, (●) NH_3 and (x) CO concentrations are plotted as a function of cycle time.

Table 10. Summary of the cycling performance of the LNT catalyst at 300 °C (60 s lean/5 s rich).

	60/5	
X_{NOx}	99.2	%
X_{CO}	87.1	%
X_{C3H6}	77.5	%
NO_X Fed (lean)	214.8	µmol/cycle
NO_X Stored	214.2	µmol/cycle
NO_X Slip (total)	1.6	µmol/cycle
NO_X Slip (rich)	1.1	µmol/cycle
NH_3 Produced	61.9	µmol/cycle
N_2O Produced	12.5	µmol/cycle
Y_{NH3}	28.8	%
Y_{N2O}	5.8	%
S_{NH3}	29.0	%
S_{N2O}	11.8	%
S_{N2}	59.2	%

3.4.3 CYCLE AVERAGED NO_X, CO AND C_3H_6 CONVERSIONS

The results shown in Fig. 43 summarize the cycle averaged NO_X conversions measured in this investigation at different temperatures and under different lean/rich cycle timing protocols. These results indicate that with respect to NO_X conversion the optimum operating temperature for this LNT catalyst is between 350 and 400 °C. Cycling conducted using a 60 s lean period resulted in cycle averaged NO_X conversions over 80% from 300 – 450 °C temperature range. However as the extent of the lean period duration was increased, the temperature window for high NO_X conversion was decreased. As a result, longer lean periods (e.g., 120 and 180 s, respectively) can only be used if the LNT catalyst is operated at, or very near, an optimum temperature of 350 – 400 °C. For all timing protocols investigated, dramatic decreases in the cycle averaged NO_X conversion were observed at temperatures below 300 °C and above 450 °C. Under such conditions, higher cycle averaged NO_X conversions were observed for longer rich periods in the low temperature regime (i.e., below 300 °C). By contrast at temperatures above 450 °C, the highest cycle averaged NO_X conversions were observed for shorter (5 s) rich periods. The results for the two extreme cases (i.e., 250 and 500 °C) are further displayed in the two limiting cases displayed in Fig. 44.

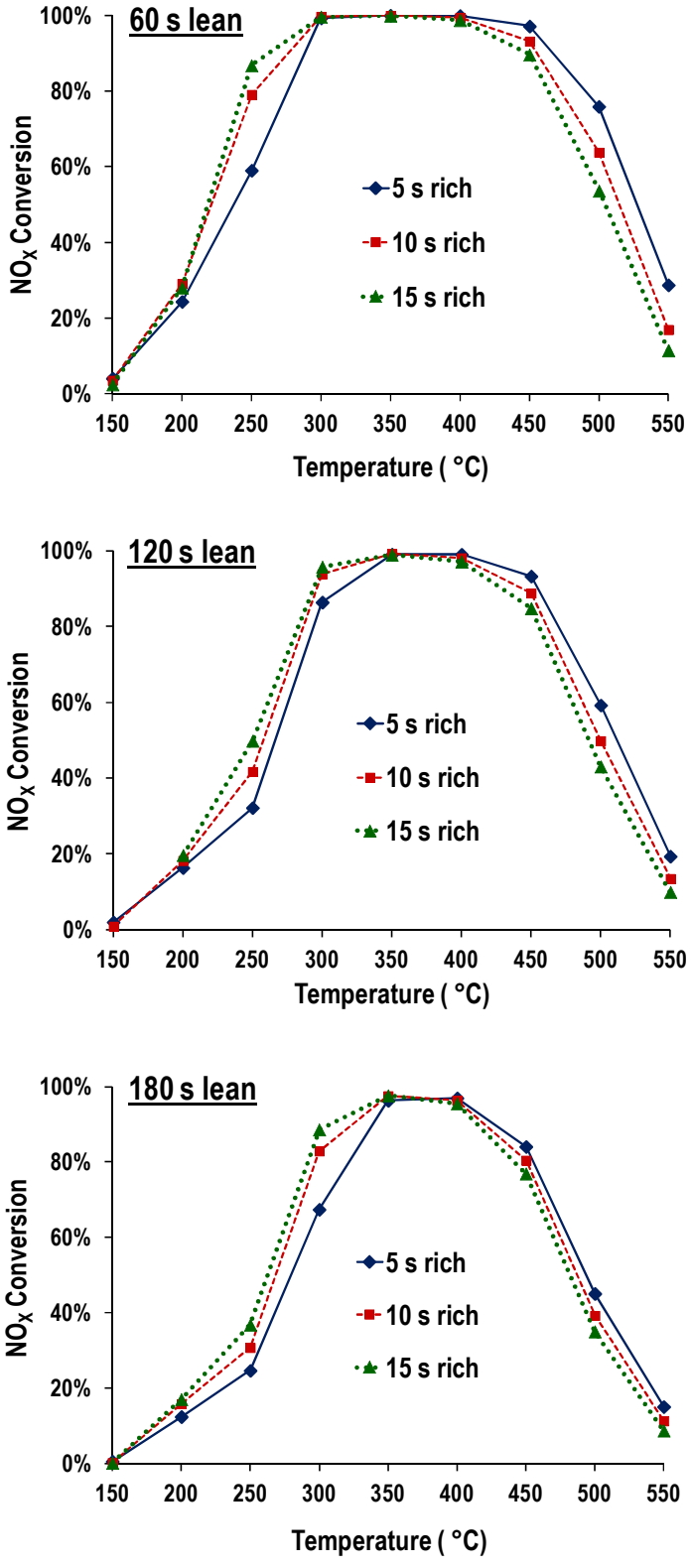

Figure 43. Cycle averaged NO_X conversions obtained for the LNT catalyst as functions of temperature for different lean/rich cycle timing protocols.

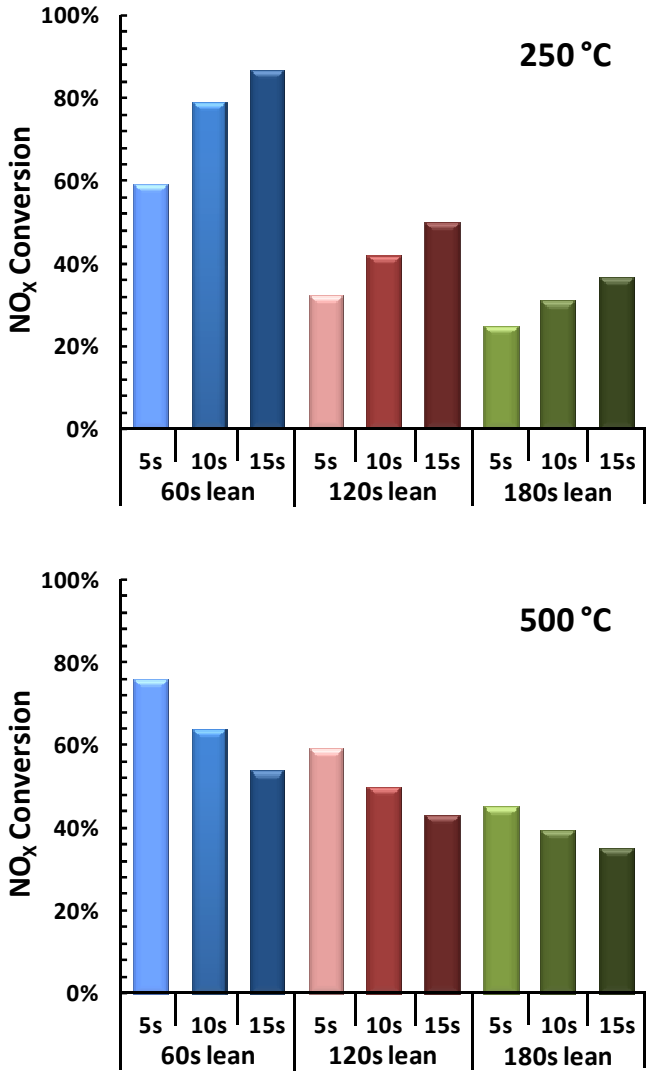

Figure 44. Cycle averaged NO_X conversions obtained for the LNT catalyst for different lean/rich cycle timing protocols at 250 and 500 °C.

The results shown in Fig. 44 can be rationalized considering differences in the relative rates of NO_X release and reduction as a function of temperature. For example, at 250 °C both the NO_X release and its subsequent reduction take place at lower rates, which explains why longer, lower concentration rich doses are more effective. In this case, extending the rich period led to a significant increase in the cycle averaged NO_X conversion from 59 to 87% for a 60 s lean period with 5 and 15 s rich periods, respectively. While the rich period duration was increased, the total

number of moles of reductant was held constant, as discussed in the experimental section. Thus it becomes apparent that because of the slow NO_X release and reduction kinetics a more extended temporal distribution of the reductants can optimize the NO_X conversion characteristics of the LNT catalyst. At 500 °C, NO_X release and reduction are no longer kinetically limited and as a result, shorter, high concentration rich doses are needed to effectively reduce the NO_X that is rapidly released from the LNT catalyst. This behavior is not surprising since thermal release of NO_X is favored even in the absence of a reducing agent at temperatures exceeding 470 °C for ceria containing LNTs [150]. In summary, longer, lower concentration rich doses result in higher NO_X conversions at below 300 °C, while shorter, higher concentration rich doses achieve the same result at temperatures above 450 °C. Breen et al. [353] similarly observed increased NO_X conversions for longer, lower concentration rich doses, but concluded that such timing protocols were always more effective regardless of the operating temperature. Al-Harbi et al. [354] also observed increased NO_X conversions at 500 °C for shorter rich periods, but the effects in their case was more modest than what was observed over the LNT catalyst used in our study. Ultimately, Al-Harbi et al. [354] concluded that the simultaneous increase in NH_3 generation for the shorter, higher concentration, rich doses at high temperatures negated the benefits of increased NO_X conversion. However in an LNT-SCR configuration, NH_3 generation can be mitigated by the downstream SCR catalysts and might even be desirable.

The cycle averaged CO and C_3H_6 conversions are shown in Fig. 45. Since both the CO and C_3H_6 conversions were largely insensitive to the cycle timing, only data for the 60 s lean period are shown. In all cases, the LNT catalyst exhibited low CO and C_3H_6 conversions below 200 °C, indicating a low reactivity between these two reductants and NO_X at these temperatures. This is consistent with previous results reported by Abdulhamid et al. [26], which indicate that

CO is not as effective as H_2 in reducing NO_X at temperatures below 200 °C. Furthermore, more recent investigations by different groups [28,64,288,289,339] indicate that hydrolysis of isocyanates and hydrogen production via the WGS reaction exhibit significant activity above 250 °C, which may explain the higher consumption of CO observed in Fig. 45 at these temperatures. However, the most important factor for the higher CO conversions observed in the 300 – 500 °C temperature range may be the relative amounts of NO_X stored and CO fed, as shown in Fig. 46, since it becomes apparent that at these temperatures, the CO conversion tracks very closely the amount of NO_X stored on the LNT catalyst. Above 500 °C, where the thermal desorption of NO_X becomes thermodynamically favored, the CO conversion is no longer strongly related to the amount of NO_X stored, but it also appears to be affected by the WGS reaction equilibrium conversion, as implied by a comparison of the slopes of the two lines. The results in Fig. 46 suggest that CO may be involved in two parallel reactions; the direct reduction of stored NO_X and the WGS reaction, which yields H_2 that can subsequently reduce stored NO_X. The relative contribution appears to be dependent reduction temperature.

The C_3H_6 cycle-averaged conversion curves shown in Fig. 45B resemble typical, steady-state light-off curves although the data were collected under cycling conditions. Once again, the differences due to the length of the rich cycle are minimal. In the absence of H_2O, Abdulhamid et al. [26] reported that propylene shows limited activity towards the reduction of NO_X when compared to CO and H_2 at 250 °C, but similar activity with the other two reductants at 350 °C. Furthermore, Resini et al. [355] reported that the steam reforming of propene over a Pd-Cu/Al_2O_3 catalyst yielding CO and H_2, which could reduce stored NO_X as discussed previously, becomes significant at temperatures above 275 °C. Both reports appear to be consistent with the data of Fig. 45, which suggests increased activity above 200 °C, reaching complete conversion of

C_3H_6 at 350 °C. However, it is not possible to differentiate from this data between the amounts of C_3H_6 consumed during the direct reduction of NO_X and the amount converted to CO and H_2 via steam reforming. Finally, the results of Fig. 45B indicate that hydrocarbon slip may represent a problem for LNT catalyst operation lower temperatures, where NH_3 formation is favored, as will be discussed below.

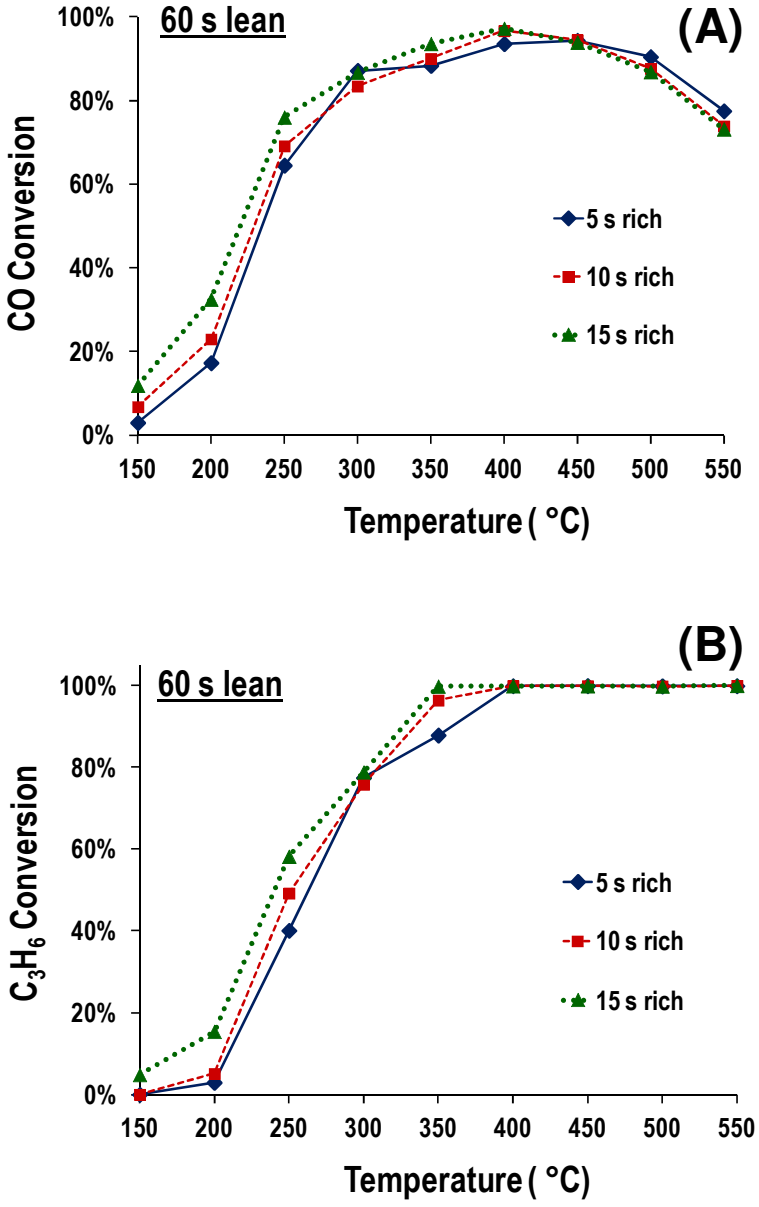

Figure 45. Cycle averaged CO (A) and C_3H_6 (B) conversions obtained for the LNT catalyst as functions of temperature for different lean/rich cycle timing protocols.

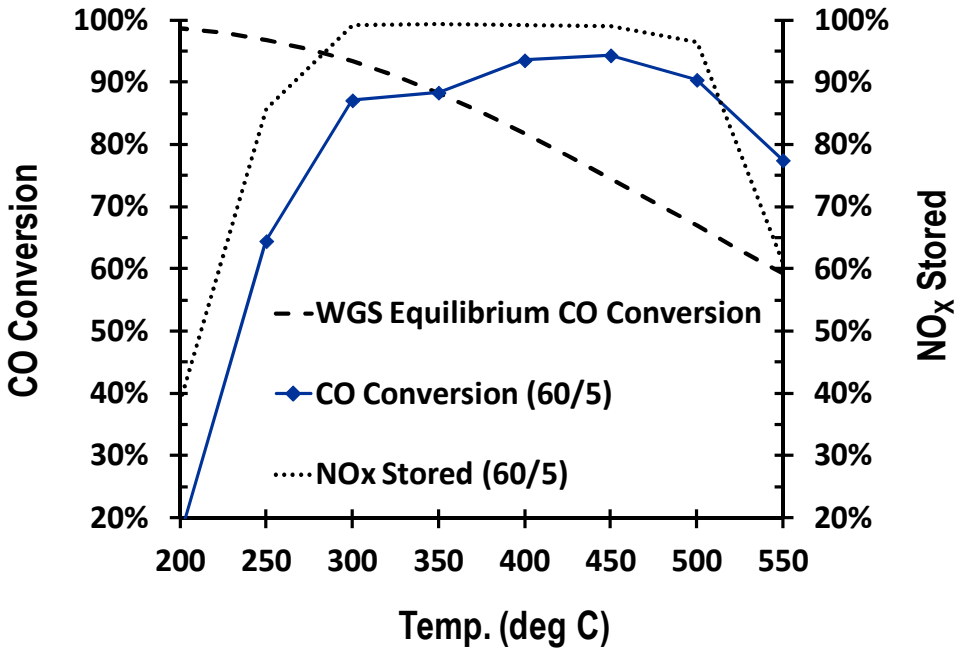

Figure 46. Cycle averaged CO conversion obtained for the LNT catalyst in comparison to the amount of NO_X stored and the WGS equilibrium conversion as a function of temperature (60 s lean / 5 s rich).

3.4.4 NH_3 AND N_2O YIELD AND SELECTIVITY

The results shown in Fig. 47 summarize the cycle-averaged NH_3 yield and NO_X slipped for the set of conditions considered in this investigation. This side by side comparison of NH_3 yield and NO_X slipped can be used as an indicator of the feasibility of an LNT-SCR configuration, since in this setup NH_3 stored downstream is used to reduce NO_X that "slips" from the LNT catalyst. Along these lines, the results shown in Fig. 47 demonstrate that it may be possible to select the appropriate temperature and cycling conditions to achieve the desired NO_X and NH_3 amount reaching the SCR catalyst. For example, if the length of the lean period is set at 60 s and the catalyst temperature is 250 °C, the length of the rich period pulse can be used to control the amount of NH_3 formed. When 10 or 15 s rich pulses are used, an NH_3 yield of 46%

is observed, while the corresponding NO_X slip is 21% and 13% of the total NO_X fed, respectively. Since the SCR reaction requires a 1:1 NH_3:NO_X ratio, as shown Eqn. 18,

$$4NH_3 + 4NO + O_2 \rightarrow 4N_2 + 6H_2O \quad (18)$$

under these conditions the amount of NH_3 generated is approximately twice the amount needed to operated a downstream SCR catalyst.

Consequently, the SCR catalyst would quickly become saturated with adsorbed NH_3 and significant concentrations of NH_3 instead of NO_X could appear in the final exhaust stream. This indicates that in this case the overall LNT-SCR configuration operates with excess reducing agent due to the longer than needed rich cycles. Not surprisingly then, when a 5 s rich cycle is used, the NO_X slip is approximately 41%, while the NH_3 yield is only 29%. In this case, more NO_X would be slipped from the catalyst system than NH_3. The downstream SCR catalyst would improve the cycled averaged NO_X conversion, as previously observed by Lindholm et al. [338], but not all of the NO_X slipped from the LNT could be converted to N_2. In summary, the results shown in Fig. 47 can be used to determine the theoretical "best-case" scenario for an LNT-SCR configuration for a specific set of conditions, assuming that all of the NH_3 produced over the LNT catalyst can be stored on the SCR and subsequently used to reduce NO_X. However in practice, complete storage and reaction of the NH_3 formed may not be possible. Further analysis of the results in Fig. 47 indicates the presence of two temperature ranges for potential application of concerted control of the cycling timing protocol in an LNT-SCR configuration: one between 250 and 300 °C, and the second between 400 and 450 °C. Significant NO_X slip was observed below 250 °C and above 450 °C without sufficient NH_3 formation observed to allow for

operation of a downstream SCR catalyst. On the other end of the spectrum, almost complete NO_X conversion is observed between 300 and 400 °C; in this case, the NH_3 formed over the LNT catalyst represents a problem because very little NO_X remains to react with NH_3 over the SCR catalyst.

Regardless of the length of the lean/rich cycle used, the NH_3 yield peaked at either 250 or 300 °C (Fig. 47), but NH_3 selectivity always reached a maximum at 250 °C, as shown in Fig. 48. The NH_3 selectivities measured at 250 °C are in excellent agreement with previously reported results by Ren and Harold [340] over a similar series of catalysts even though in their case H_2 was used as the reducing agent and CO_2 and H_2O were not simultaneously present in the feed. In contrast, below 250 °C, Ren and Harold [340] reported significantly higher NH_3 selectivities than in our case most likely due to the use of H_2 and its higher reduction potential over CO for temperatures below 250 °C [26,356]. Furthermore, the narrow NH_3 selectivity maximum at 250 °C, for a variety of cycle timing and reductant concentration conditions, clearly illustrates that the selectivity to NH_3 is primarily controlled by the reaction temperature over the LNT catalyst used. At temperatures below 250 °C, the slow formation of surface isocyanates and the low rate of the WGS reaction, which represent the two most likely pathways to NH_3 formation [24,60,64,286,339], can account for the low NH_3 yields.

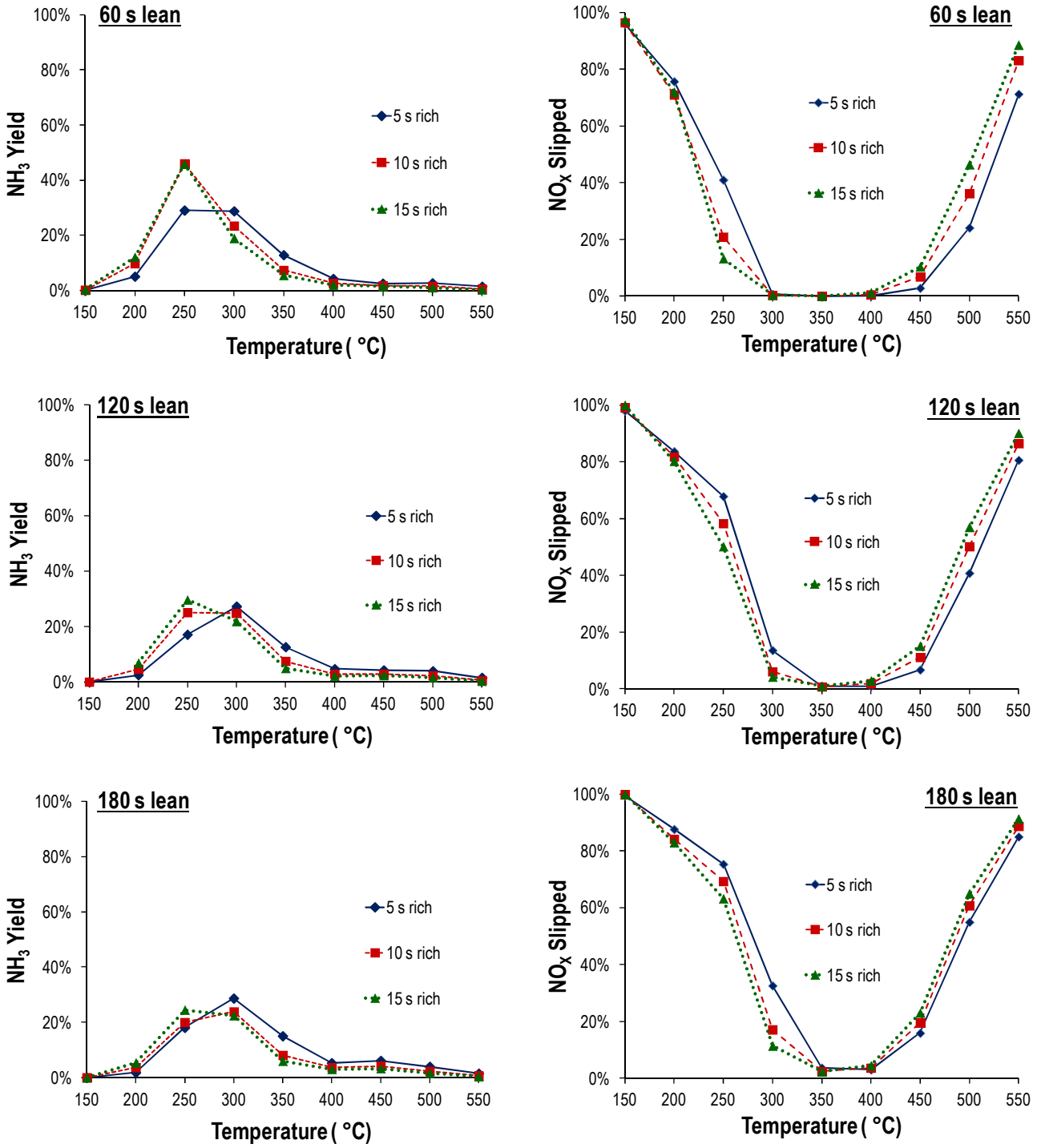

Figure 47. Cycle averaged NH_3 yield and NO_X slip from the LNT catalyst as functions of temperature and lean/rich cycle timing.

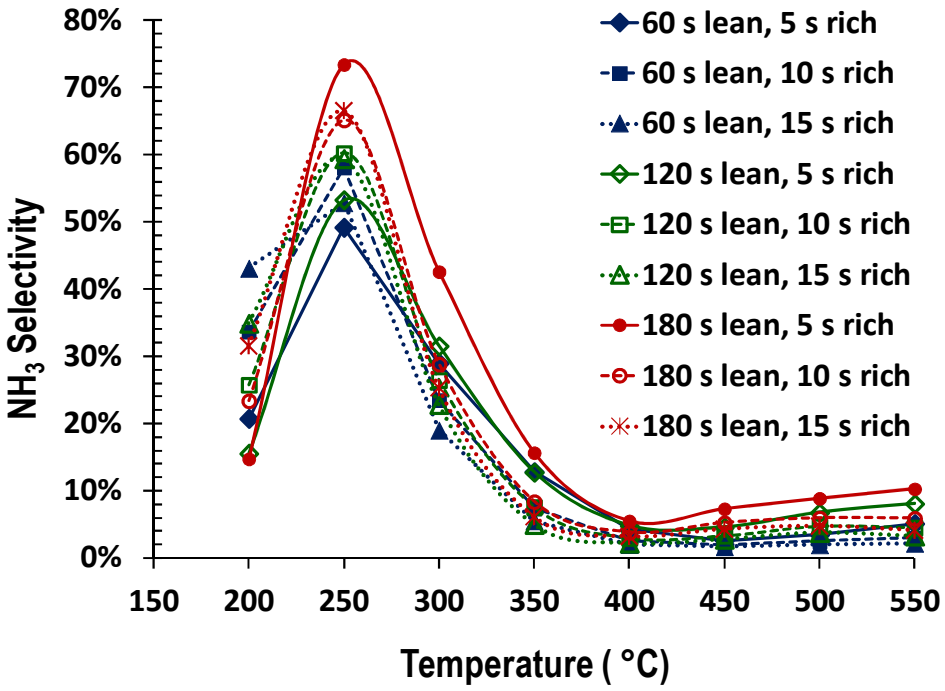

Figure 48. Cycle averaged NH_3 selectivity obtained for the LNT catalyst as a function of temperature and lean/rich cycle timing.

Cycle-averaged N_2O yield and selectivity are shown as functions of temperature and cycle timing in Fig. 49. The results indicate that the N_2O yield shows a maximum at approximately the same temperature range as the NH_3 yield (i.e., 250 – 300 °C). As a result, N_2O production will be an issue if the LNT catalyst operates under the most favorable conditions for NH_3 production. In a recent publication however, Wang and Crocker [335] demonstrated that N_2O reduction over a downstream Cu-chabazite SCR catalyst can significantly reduce the amount of N_2O ultimately present in the exhaust of the overall after-treatment system; in their case, complete reduction of N_2O was reported at 315, 350 and 450 °C when H_2, NH_3 and CO, respectively, were used as the reducing agents. Furthermore, Wang and Crocker [335] reported significant decreases N_2O formation by 225 °C in an LNT-SCR configuration and complete removal by 275 °C. Consequently, one can conclude that the presence of a downstream SCR

catalyst will significantly reduce the amount of N_2O slipped from the LNT catalyst at temperatures above 250 °C, but N_2O slip will still be a problem at temperatures below 250 °C.

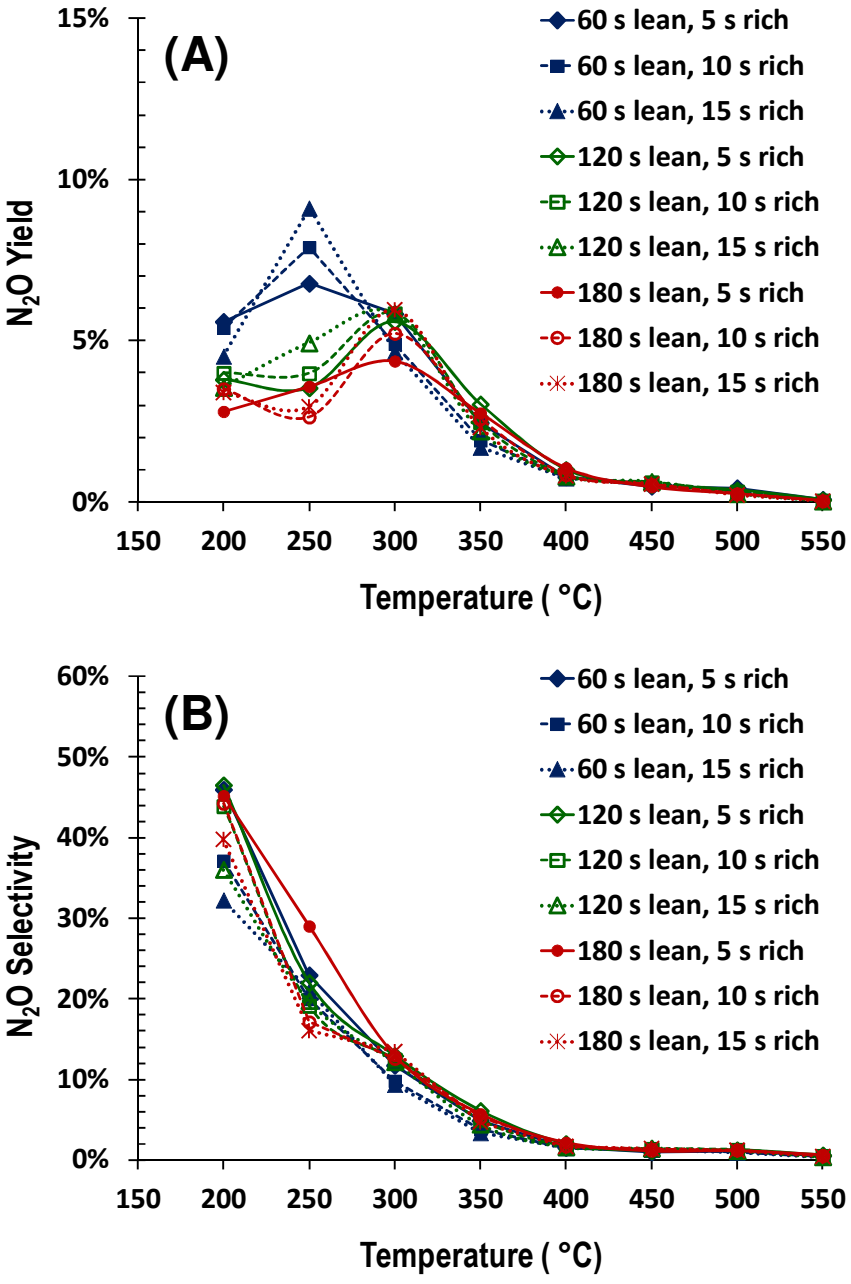

Figure 49. Cycle averaged N_2O yield (A) and selectivity (B) obtained for the LNT catalyst as functions of temperature and lean/rich cycle timing.

In comparison to NH_3 selectivity, the selectivity to N_2O did not exhibit a maximum but instead it decreased monotonically as the temperature was increased (Fig. 49B). Once again, changes in the lean/rich cycle timing had a relatively small impact on the N_2O selectivity, in agreement with the results discussed above for the NH_3 selectivity, further supporting the conclusion that the predominant factor controlling NH_3 and N_2O selectivity over the LNT catalyst is the operating temperature.

Finally, the NH_3 and N_2O yields can be affected by the NO_X storage–reduction regime under which cycling is conducted. For example, the results shown in Fig. 50 depict two limiting cases for the NH_3 and N_2O yields. The cycle averaged NO_X conversions observed under these conditions are shown in Fig. 44. As previously discussed, the NO_X release and reduction kinetics were slower at 250 °C; therefore, longer, lower reductant concentration rich doses resulted in increased overall NO_X conversions. The amount of NO_X stored by the LNT catalyst at 250 °C also increased with the length of the rich cycle, with the 60 s lean/5 s rich and 60 s lean/15 s rich combinations resulting in 185 and 202 μmol of stored NO_X, respectively. As seen in Fig. 50, extending the length of the rich cycle also resulted in higher NH_3 and N_2O yields even though the reductant concentrations were lower in this case. Initially this result appears to contradict previous observations by Pihl et al. [351], where higher reductant concentrations resulted in increased NH_3 and N_2O yields. However, one has to consider that at lower temperatures the product distribution is significantly affected by the NO_X release and reduction kinetics in addition to the reductant concentration. At 250 °C for example, the increased NH_3 and N_2O yields can be attributed to a combination of increased NO_X conversion, which is affected by the length of the rich cycle, and constant selectivities to NH_3 and N_2O, which are almost independent of the length of the rich cycling duration (Figs. 48 and 49B). As a result, if

the NO_X conversion and the amount of NO_X stored increase without a significant change in the product selectivities, the yield to those products increases as well. Alternatively at 500 °C, the higher reductant concentrations used during shorter rich cycles results in both higher NO_X conversions and higher NH_3 and N_2O yields, consistent with the results reported by Pihl et al. [351]. In this case, the NO_X stored on the LNT catalyst is released very quickly and high concentrations of reductant are needed to reduce all of the NO_X released. The amount of NO_X stored is also not affected by the length of the rich cycle, since the catalyst regeneration is very fast.

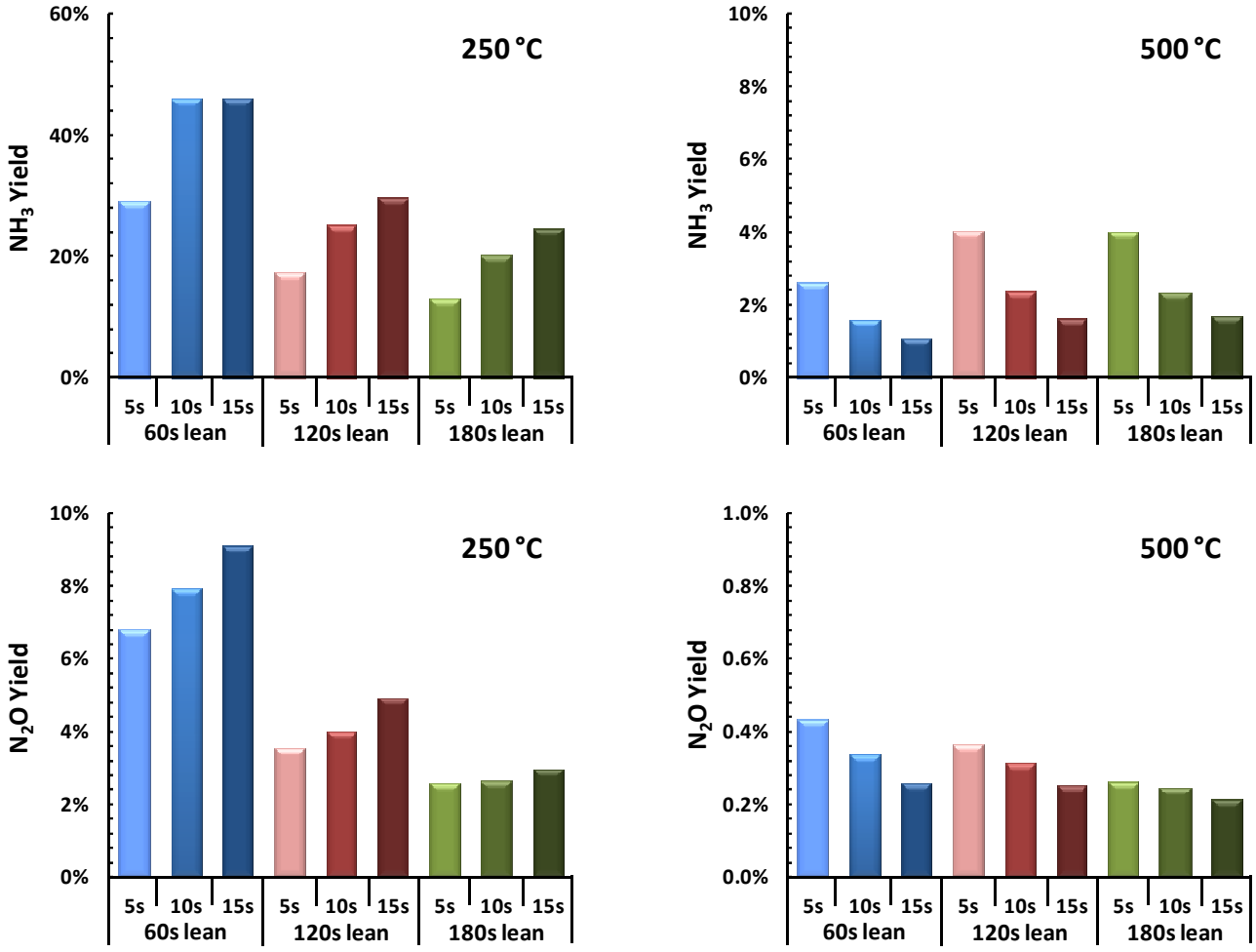

Figure 50. Cycle averaged NH_3 and N_2O yields obtained for the LNT catalyst for different lean/rich cycle timing protocols at 250 and 500 °C.

At this point, it is important to differentiate between regeneration limited conditions (e.g., ≤ 250 – 300 °C) and storage limited conditions (e.g., ≥450 °C), as previously discussed by Breen and Burch [16,353], because the kinetics of storage and regeneration have major implications on the observed catalytic performance for the production of NH_3, as indicated by our results. At low temperatures when NO_X release and regeneration are kinetically limiting, a longer, lower concentration rich cycle results in higher NO_X conversion than a shorter, higher concentration rich cycle because extending the length of rich cycle is critical for achieving complete regeneration. In this case, despite the lower selectivity to NH_3, more NH_3 is actually produced because of higher NO_X conversions. At higher temperatures, this is no longer the case and higher concentration, albeit short rich cycles, results in both higher NH_3 yield and selectivity, as previously reported by others [351,356].

3.4.5 REACTOR EFFLUENT PROFILES

Concentration profiles for NO, NO_2, NH_3, CO, N_2O and C_3H_6 observed downstream of the LNT catalyst during a 5 s rich cycle following a 60 s lean cycle are shown for different temperatures in Fig. 51. As it becomes apparent from the results, these profiles vary significantly with temperature. For both NO and NO_2, for example, at temperatures above 450 °C maxima in the effluent concentrations are observed within the first 1-2 s following the switch to rich conditions. As previously reported [140,151], the reason for this behavior is that NO_X is released much faster than it is reduced. At 550 °C, the maximum in the total NO_X concentration approached 4500 ppm, which is actually 9 times higher than the total NO_X concentration present in the feed. The NO and NO_2 profiles just prior to the switch to rich conditions at 60 s also demonstrate the poor storage capacity of the LNT at this temperature, since the NO_X concentration has already reached the feed concentration. At all other temperatures, with the

exception of 200 °C, where storage is significantly limited, very low breakthrough of NO_X is observed prior to the onset of the rich period. Significant concentrations of NO_X are also observed during the rich cycle downstream of the LNT catalyst in the lower temperature range (i.e., 200 – 300 °C). In this case however, the maxima are lower and are more evenly distributed during the entire rich cycle and even extend in to the first 1 – 2 s of the subsequent lean cycle. This behavior can be attributed to the lower reduction activity of the LNT catalyst at these temperatures.

The appearance of NH_3 downstream of the LNT catalyst did not coincide with the onset of the rich cycle. Instead, a delay was observed at all temperatures examined; in fact, for temperatures above 350 °C, no NH_3 was observed until approximately 4 sec into the 5 s rich cycle. This delay in NH_3 breakthrough has previously been attributed to NH_3 decomposition and oxidation and/or reaction with stored nitrites/nitrates as the NH_3 propagates through the catalyst bed [23,286,351,352,356]. Since higher temperatures favor these NH_3 reactions, especially for catalysts containing significant amount of OSC as in this case, the delay increases with reaction temperature. The CO concentration profiles closely matched the behavior observed for NH_3, with the exception of the lower temperature studied (200 °C), where apparently no significant CO-NO_X reaction takes place. The overall amount of CO in the LNT effluent stream reaches a minimum between 350 and 400 °C and then begins to increase as the temperature is further raised. The 350 – 400 °C temperature range represents the optimum operating temperature for this catalyst, where the amount of reductants fed most closely matches the amount of NO_X stored. At higher temperatures (>450 °C), the NO_X storage capacity of the LNT catalyst is reduced and as a result the reduction process becomes unbalanced during the rich cycle.

The C_3H_6 concentration profiles closely match those of CO at temperatures below 350 °C, which is consistent with results previously reported by Abdulhamid et al. [26] for H_2, CO and C_3H_6 at these temperatures. Above 350 °C, no C_3H_6 was observed in the effluent from the LNT catalyst. In contrast, CH_4 formation was observed starting at 350 °C, although the amount of CH_4 produced was relatively low. For example, the maximum CH_4 concentration did not exceed 150 ppm for any condition, yielding a cycled averaged concentration below 6 ppm. Hydrocarbon yields and selectivities can be rationalized via a complex network of parallel reactions incorporating oxidation, reforming and hydrogenolysis steps. The final concentration observed depends on the relative rates of these reactions, which change significantly with temperature and a detailed analysis of this network is beyond the scope of the current manuscript.

Finally, the N_2O profiles (Fig. 51) indicate the presence of N_2O in the effluent immediately after the transition from lean to rich conditions. At lower temperatures (i.e., ≤ 300 °C) an additional period of increased N_2O production was also observed during the transition from rich back to lean conditions. Results previously reported by Breen et al. [16] also showed two periods of N_2O production at 250 °C, but not 350 °C, in agreement with our results. In general, N_2O formation is believed to occur over LNT catalysts when low H_2/NO_X ratios are present on the catalyst surface, frequently associated with transition from lean to rich environments [16,26,140,335,348,349]. At lower temperatures, where the N_2O generation is especially pronounced, NO dissociation occurs slowly and N_2O formation is favored through coupling of an adsorbed N and NO adatom, especially in the absence of high H_2 concentrations [16]. Conversely, NH_3 formation is favored at high H/NO_X ratios, which are more likely to be present as regeneration proceeds in later stages of the rich cycle [140]. The NH_3 and N_2O

profiles shown in Fig. 51 are consistent with these previous postulations, with the production of N_2O and NH_3 generally being mutually exclusive. An alternative pathway for the production of N_2O during the rich to lean transition could be the reaction of residual surface isocyanates (NCO) with NO or O_2. We have previously reported the presence of surface NCO species during cycling studies over a model LNT catalyst even in the presence of H_2O at 250 °C [339] and have shown along with others [288] that these species can react with NO or O_2, yielding N_2O. The surface concentration of isocyanates is significantly reduced at temperatures above 300 °C, which coincides with the disappearance of N_2O during the rich to lean transition in the profiles of Fig. 51, providing further support to the hypothesis that an isocyanate-based reaction mechanism may be responsible for this second period of N_2O production.

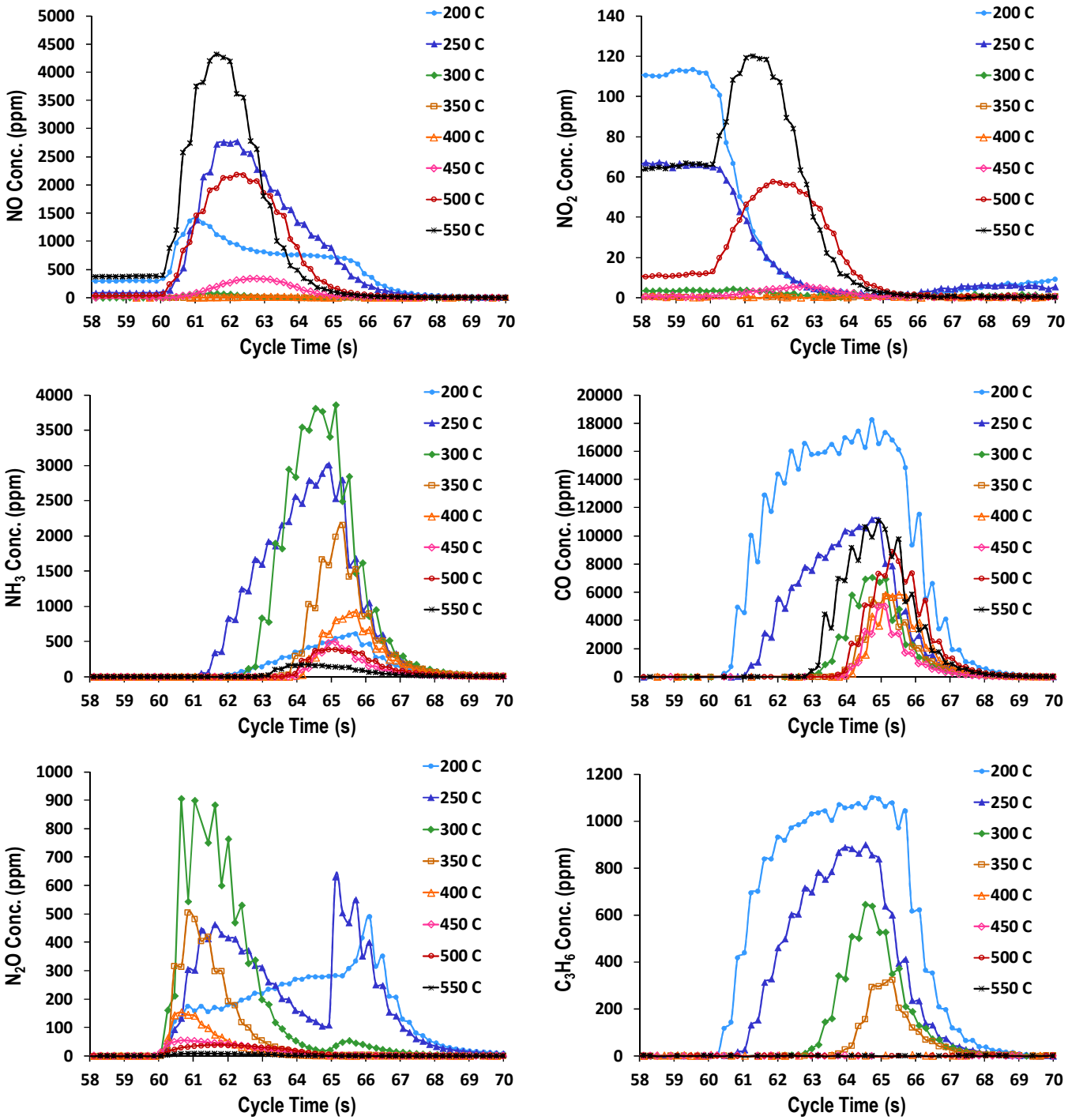

Figure 51. LNT reactor effluent profiles for NO, NO_2, NH_3, CO, N_2O and C_3H_6 observed during a 5 s rich cycle following a 60 s lean cycle at different temperatures.

3.5 CONCLUSIONS

The results of the activity measurements performed in this study over a commercial catalyst and realistic lean/rich cycling conditions indicate the presence of two distinctly different kinetic regimes. At temperatures below 300 °C, NO_X release and subsequent reduction were kinetically limiting. Therefore, longer, lower concentration rich pulses result in increased cycle averaged NO_X conversions. For example, extending the rich cycle from 5 to 15 s at 250 °C, while holding the overall reductant amount constant, resulted in an increase in cycle averaged NO_X conversion from approximately 59 to 87%, respectively. At temperatures above 450 °C, the opposite is true. Under these conditions, NO_X release and reduction occurs rapidly and shorter, higher concentration rich pulses are needed to achieve high NO_X conversions. For example, rich cycles of 5 to 15 s at 500 °C – once again, with a constant overall reductant amount – resulted in cycle averaged NO_X conversions of approximately 76 and 54%, respectively. The selectivities to NH_3 and N_2O are primarily functions of temperature and are higher at lower temperatures. The effect of cycle timing and reductant concentrations were of secondary importance on these selectivities. NH_3 and N_2O yields however, are significantly affected by the cycling timing parameters, since these strongly affect NO_X conversion as indicated above. The effects of cycling parameters are much less pronounced around the optimum operating temperature (i.e., 350 – 400 °C) of the LNT catalyst indicating that the maximum in NO_X conversion observed under these conditions is fairly robust. Finally, concerted control of NH_3 generation by varying the lean/rich cycle timing was demonstrated. The most significant effects, in terms of both NO_X conversion and NH_3 yield, were observed either by extending the rich cycle at lower temperatures (i.e., kinetically limiting regime) or by shortening the rich cycle at higher temperatures (i.e., storage limiting regime). In both cases, NH_3/NO_X ratios close to

stoichiometry could be obtained at the effluent of the LNT, demonstrating the potential for extending the region of operation with the utilization of a coupled LNT-SCR system. N_2O yields however, also increased with NH_3 yields, especially at low temperatures, indicating that an efficient LNT-SCR configuration will also need to covert N_2O downstream of the LNT catalyst.

3.6 ACKNOWLEDGEMENTS

A portion of this research was sponsored by the U.S. Department of Energy, Office of Energy Efficiency and Renewable Energy, Vehicle Technologies Program. The authors thank program managers Ken Howden and Gurpreet Singh for their support. This manuscript has been co-authored by UT-Battelle, LLC, under Contract No. DE-AC05-00OR22725 with the U.S. Department of Energy. The United States Government retains and the publisher, by accepting the article for publication, acknowledges that the United States Government retains a non-exclusive, paid-up, irrevocable, world-wide license to publish or reproduce the published form of this manuscript, or allow others to do so, for United States Government purposes. Additionally, the authors would like to acknowledge the contributions of Wei Li, Chang Kim and Kushal Narayanaswamy of General Motors in addition to Davion Clark and Christopher Owens of Umicore for discussions and guidance in this portion of our research.

CHAPTER 4. PASSIVE-AMMONIA SELECTIVE CATALYTIC REDUCTION (SCR): UNDERSTANDING NH_3 FORMATION OVER CLOSE-COUPLED THREE WAY CATALYSTS (TWC)

4.1 PREFACE

In the passive-NH_3, TWC-SCR system, NH_3 is formed over a close-coupled three-way (TWC) during rich periods and then stored on a downstream selective catalytic reduction (SCR) catalyst for use in a subsequent lean period. NH_3 formation over TWCs during steady-state operation is well known, but NH_3 formation during cycling is poorly understood. In this investigation, NH_3 formation under steady-state and lean/rich cycling conditions was investigated using four commercial catalysts including: 1.) a Pd-only, high precious metal loading (HPGM) catalyst, 2.) a Pd/Rh + CeO_2, low (LPGM) catalyst, 3.) a combination of the HPGM and LPGM (Dual-Zone) catalysts and 4.) a lean NO_X trap (LNT) operated as a TWC. NH_3 formation during steady-state operation was shown to be dependent on the AFR (air-to-fuel ratio), temperature and catalytic formulation. Generally, the NH_3 yield decreased as follows: HPGM $\geq$ Dual-Zone $>>$ LPGM $\approx$ LNT. Catalysts containing Rh and/or CeO_2 generally produced less NH_3, but all of the formulations could produce significant amounts of NH_3 if operated under sufficiently rich conditions. The AFR was determined to be a sensitive parameter that could be used to tune NH_3 generation. At higher temperatures, progressively richer AFRs were necessary to achieve high NH_3 yields. During cycling, richer AFRs were required to generate NH_3 in comparison to the steady-state results. The HPGM catalyst demonstrated the most robust NH_3 formation in comparison to the amount of NO_X slipped for all of the

temperatures considered, with an optimum operating region from approximately 400 to 450 °C. At moderate temperatures (275 – 500 °C), inclusion of NO_X storage capacity (i.e., results collected for the LNT) dramatically increased the amount of NH_3 produced in relation to the amount of NO_X slipped, even though the LNT catalyst generally exhibited the lowest NH_3 yield for steady-state operation. This implied that inclusion of an "optimum" amount of NO_X storage capacity could significantly improve the performance of the TWC-SCR system. CO slip was observed under all conditions favorable for NH_3 generation, and with therefore need to be addressed. N_2O formation, on the other hand, was generally insignificant for temperatures above 400 °C, which is a unique advantage of TWC-SCR system.

4.2 INTRODUCTION

Lean-burn engines are more fuel efficient and produce less CO_2 than traditional, stoichiometric-burn ones [1,282,357,358]. Unfortunately, a fleet-wide implementation of lean-burn engines has not occurred because the development of cost effective catalysts capable of meeting current emissions regulations under lean-burn exhaust conditions still represents a major technical challenge. Since the late 1970s, three-way catalysts (TWC) have been employed for the simultaneous reduction of nitrogen oxides (NO_X) and oxidation of unburned hydrocarbons and carbon monoxide (CO) present in engine exhaust. However, TWCs only sufficiently remediate pollutants if operated in a very narrow region near the stoichiometric combustion regime and exhibit very low NO_X conversion if operated under the high O_2 conditions encountered in lean-burn engine exhausts [279]. Two existing solutions for the reduction of lean exhaust NO_X include lean NO_X trap (LNT) and NH_3-selective catalytic reduction (NH_3-SCR) catalysts. Operation of these systems has been summarized in several recent reviews [2,4,6,279,359,360].

Briefly, LNTs are designed for operation in periodic lean (≈60 s) and rich (≈5 s) environments. During lean periods, NO is oxidized to NO_2 over precious metal sites (e.g., Pt, Pd, Rh) and then subsequently stored on an alkali or alkali-earth storage component (e.g., Ba) in the form of nitrites or nitrates [22,339]. As storage elapses, the storage component becomes saturated with NO_X and a brief rich period must be employed to regenerate the catalyst and convert stored NO_X to N_2. Commercial formulations include relatively high weight loadings of Pt (≈2 – 3 wt%), with smaller amounts of Pd and/or Rh, supported on a Ba containing high surface area γ-Al_2O_3 [4,135]. Conversely, NH_3-SCR catalysts do not rely on cycling strategies and instead operate through the selective reaction of NH_3 with NO_X in the presence of large amounts of excess oxygen, where NH_3 is typically provided via on-board storage of urea – which is rapidly hydrolyzed to NH_3 under automotive exhaust conditions [2]. Commercial SCR catalytic formulations typically include V_2O_5-WO_3/TiO_2 or Cu/Fe exchanged zeolites [2,279,359,360]. In Europe, V_2O_5-WO_3/TiO_2 based formulations were introduced in 2005 for heavy-duty diesel applications, but high activity for SO_2 oxidation, toxicity of volatile vandia species (>650 °C) and poor activity and selectivity above 550 °C generally make the zeolite based formulations more attractive for lean-gasoline applications [360]. Zeolite-based catalysts also store significantly more NH_3 than their V_2O_5 based counterparts [341,343]. Initially, commercialization of zeolite based SCR catalysts was limited because of substantial problems related to hydrothermal stability, but recent advances in zeolite technology have led to the discovery of hydrothermally stable, small pore, metal-exchanged zeolites that are active over a broad temperature range [342,344]. Stabilization of the zeolite structure using a metal oxide coating has also been demonstrated [361].

Both LNT and SCR technologies suffer from different, but significant drawbacks. For example, LNT catalysts require high platinum group metal (PGM) loadings, which results in a significant cost per catalyst, and they are also particularly susceptible to sulfur poising; therefore, periodic, high-temperature regenerations schemes are required that can partially degrade LNT performance [4,359]. NH_3-SCR catalysts are comparatively inexpensive, but the dosing system required to deliver urea to the exhaust stream is expensive and does not seem practical for smaller gasoline engines. The urea dosing system also requires on-board storage of urea to function (e.g., a 30-litre tank) and customer resistance to the additional "fuel" tank, the lack of existing infrastructure, a relatively high freezing point (approx. -12 °C) and long-term stability issues (>32 °C) are all topics of considerable concern. With these considerations, NH_3-SCR is emerging as the key technology for large vehicle applications, while LNT catalysts are favored for smaller engines [359].

Recently however, researchers at GM have demonstrated a new technology referred to as the "passive-ammonia" or "urealess" SCR approach [282,357,358,362–364]. As in the case of LNT systems, the passive-NH_3 approach is based on periodic lean-rich cycling mode of operation, but does not include an LNT catalyst. Instead, a close-coupled TWC is used to generate NH_3 during periods of rich operation. The NH_3 is then stored on a downstream, under-floor SCR catalyst. After a sufficient amount of NH_3 has been stored, the engine switches back to lean operation and the stored NH_3 is used to reduce NO_X that slips un-reacted from the upstream TWC. This is particularly attractive in gasoline applications because it allows the vehicle resort back to stoichiometric operation if necessary. Ultimately, the successful operation of the passive approach relies on the following factors: 1.) robust and selective NH_3 generation over the TWC, 2.) significant storage of NH_3 on the downstream SCR catalyst, 3.) efficient

utilization of stored NH_3 for NO_X reduction and 4.) optimization of the required lean/rich engine timing, where a higher ratio of lean to rich time increases efficiency gains.

Of these, the selective generation of NH_3 over the TWC is arguably the most important aspect of the passive-NH_3 approach. While the potential for NH_3 formation over TWCs is well known [120], early research efforts were focused on avoiding NH_3 formation. Even so, subsequent reactor screening experiments [365–367], engine chassis dynamometer studies [368–372] and tunnel investigations [373–375] confirmed NH_3 slip from vehicles equipped with TWCs, where NH_3 generation was not necessarily expected under typical operating conditions. Heeb et al. [371,372] clearly demonstrated that NH_3 was produced as a secondary pollutant over the TWC and was not generated by the engine. They further argued that NH_3 standards should be included in future regulations. While NH_3 slip from TWCs may be unfavorable in the traditional sense, in this case the main goal is to produce NH_3 over the TWC for use in a downstream SCR catalyst.

In this manuscript, we focus on NH_3 generation over a series of TWCs including: a high PGM, low PGM, dual-zone TWC and a TWC with NO_X storage capacity. The catalysts were evaluated under both steady-state and lean-rich cycling conditions using commercial monolithic cores loaded into a bench-core reactor. The effects of catalytic formulation, temperature and steady-state vs. cycling conditions on NH_3 generation will be discussed.

4.2 EXPERIMENTAL

4.2.1 CATALYSTS

Four fully formulated cores (wash-coated honeycomb cordierite monoliths) were used in the present investigation and have been summarized in Table 11. Three of the cores were

obtained from a commercial 1.3 L TWC that is employed in a 6-speed, Chevy Malibu (Model Year: 2009). The catalyst deign was constructed using a dual-zone approach, where the front and rear sections were intentionally synthesized using different formulations. The first 62 mm (0.6 L) section of the monolith is a Pd-only, high platinum group metal (HPGM), Pd-only TWC (0/4/0 g of Pt/Pd/Rh, respectively) and the rear 73 mm (0.7 L) section is a low platinum group metal (LPGM), Pd/Rh TWC (0/0.8/0.21 g Pt/Pd/Rh, respectively – which also contained CeO_2). In this case, the HPGM catalyst, the LPGM catalyst and the combination of the two were independently evaluated, where the HPGM catalyst was placed upstream of the LPGM catalyst in the Dual-Zone designation – as is the case on the vehicle.

Table 11. Elemental compositions of the four catalysts used in this investigation.

Catalysts	Cat. Volume (on vehicle) (L)	PGM loading (g/L of Pt/Pd/Rh)	Oxygen Storage Capacity (OSC)	NO_X Storage Capacity (NSC)
1.) High PGM TWC	0.6	0/6.7/0	No	No
2.) Low PGM TWC	0.7	0/1.14/0.3	Yes (CeO_2-based)	No
3.) Dual-Zone (1+2)	1.3	0/3.7/0.16	Yes (CeO_2-based)	No
4.) LNT as TWC	2.6	2.2/0.8/0.3	Yes (CeO_2-based)	Yes (Ba-based)

In addition to the TWCs, a lean NO_X trap catalyst (LNT) was evaluated under identical conditions as the TWCs. Obviously, the LNT also included a significant amount of NO_X storage capacity (NSC) – leading to the designation: TWC with NSC. The LNT catalyst is employed in a lean-GDI, BMW 120i (Model year: 2009). More detailed information regarding the characterization of this catalyst can be found in a recent manuscript [376]. Briefly, semi-quantitative metals screening conducted using ICP-MS (inductively coupled plasma mass spectroscopy) conducted at Galbraith Laboratories confirmed Mg, Al, Ce and Ba as major

components, with other elements of interest including: Zr, La, Pt, Pd, and Rh. Subsequent electron microscopy with complementary elemental analysis exposed three compositionally distinct grains including: a Ce/Zr mixed oxide domain, a Mg/Al mixed oxide domain and an Al oxide domain. In this case, Pt, Pd and Ba all seemed to be preferentially deposited on the Ce/Zr domain.

4.2.2 EVALUATION

Catalytic evaluation was performed using a laboratory bench-flow reactor, as described in more detail elsewhere [135,376]. Briefly, the monolithic cores were tightly wrapped in Zetex insulation tape and inserted into a horizontal quartz tube reactor. The quartz tube was heated using a horizontal bench-top furnace (Lindberg/Blue M). Gas mixtures were prepared using pressurized gas cylinders (UHP, Air Liquide) and a bank of mass flow controllers (Unit Instruments Series 7300, Kinetics Electronics). A rapid switching 4-way valve system was used to alternate between the lean and rich gas mixtures, when necessary. Water was introduced using a peristaltic pump (Cole-Parmer) that fed into a heated, flash-vaporization zone held at 350 °C. All gas lines downstream of the water introduction zone were heated and quartz chips were placed upstream of the monolithic core to ensure that the feed gas temperature reached the set point temperature prior to contacting the catalyst. Three thermocouples were used to measure the temperature. The first was placed 1 cm upstream of the core and was used to record the inlet/set-point temperature. The second thermocouple was placed in the middle of the monolithic core and was used to record the actual monolith temperature. The third was placed 1 cm downstream of the core and was used to record the temperature exiting the core. After exiting the reactor, the gas was fed to an MKS MultiGas^{TM} 2030 HS FT-IR analyzer, which allowed for continuous tracking (5 Hz) of NO, NO_2, N_2O, NH_3, CO, C_3H_6, CO_2 and H_2O. Prior to the

reactor measurements, the as-received catalyst was "de-greened" at 700 °C in a humidified air (2.7% H_2O) mixture for 16 h to establish reproducible performance.

STEADY-STATE EXPERIMENTS

Steady-state experiments were conducted in order to measure NH_3 formation over TWCs as a function of catalytic formulations and temperature and compare the results to those obtained during cycling. A realistic gas mixture containing: 0.15% NO, 1.8% CO, 0.60% H_2, 0.10% C_3H_6, 5% CO_2, 5% H_2O and variable amount of oxygen was used, where the oxygen content was systematically changed in order to vary the air to fuel ratio (AFR). The inlet gas temperature was varied from 150 to 550 °C, in 50 °C increments, at a space velocity (S.V.) of 75,000 hr^{-1}, where the monolithic core volume (≈0.8" x 0.45", W x L) was used to calculate the required flow rate necessary to achieve the desired S.V. The reductant ratio was set to 18:6:1 for $CO:H_2:C_3H_6$, respectively, which is representative of rich-tune engine exhaust. In this case, an AFR of 14.59 was calculated to represent stoichiometric operation for the previously described gas mixture containing 1.59% O_2. Table 12 summarizes the conditions for steady-state operation, where the corresponding AFR varies with the O_2 content as previously described. The NO_X conversion, CO conversion and C_3H_6 conversion were calculated using equations 19 – 21.

$$X_{NO_X} = \frac{\int NO_{X_{Fed}} - \int NO_{X_{Slipped}}}{\int NO_{X_{Fed}}} \times 100 \tag{19}$$

$$X_{CO} = \frac{\int CO_{Fed} - \int CO_{Slipped}}{\int CO_{Fed}} \times 100 \tag{20}$$

$$X_{C_3H_6} = \frac{\int C_3H_{6_{Fed}} - \int C_3H_{6_{Slipped}}}{\int C_3H_{6_{Fed}}} \times 100 \tag{21}$$

In the case of steady state operation, the integral can be simplified as shown in Eqn. 22, where the average NO_X concentration at steady state is divided by the feed concentration.

$$X_{NO_X} = \left(1 - \frac{NO_{X,SS}}{NO_{X,Fed}}\right) \times 100 \tag{22}$$

Similarly, Eqns. 23-26 were used to calculate the NH_3 and N_2O yield and selectivity, respectively.

$$Y_{NH_3} = \frac{\int NH_{3_{Produced}}}{\int NO_{X_{Fed}}} \times 100 \tag{23}$$

$$S_{NH_3} = \frac{\int NH_{3_{Produced}}}{\int NO_{X_{Fed}} \times X_{NO_X}} \times 100 \tag{24}$$

$$Y_{N_2O} = \frac{\int N_2O_{Produced}}{\int NO_{X_{Fed}}} \times 100 \tag{25}$$

$$S_{N_2O} = \frac{2 \times \int N_2O_{Produced}}{\int NO_{X_{Fed}} \times X_{NO_X}} \times 100 \tag{26}$$

In the case of selectivity, NO_X was excluded as a product and the total number of moles of N_2, NH_3 and N_2O formed was determined by multiplying the total NO_X fed by the cycle averaged NO_X conversion, which was calculated using Eqn. 19. The calculations were performed in this manner because N_2, and other diatomic molecules (e.g., O_2 and H_2), cannot be measured using the FT-IR gas analyzer.

Table 12. Reaction conditions for the steady-state catalytic evaluation of TWCs, with calculated AFRs and λ values.

AFR ($AFR = \frac{mass_{air}}{mass_{fuel}}$)	λ ($\lambda = \frac{AFR_{act}}{AFR_{stoich}}$)	O_2 (%)	NO (%)	CO (%)	H_2 (%)	C_3H_6 (%)	CO_2 (%)	H_2O (%)
14.59	1.000	1.590	0.15	1.8	0.60	0.10	5	5
14.54	0.996	1.525	0.15	1.8	0.60	0.10	5	5
14.52	0.995	1.510	0.15	1.8	0.60	0.10	5	5
14.40	0.987	1.340	0.15	1.8	0.60	0.10	5	5
14.20	0.973	1.060	0.15	1.8	0.60	0.10	5	5
14.00	0.960	0.790	0.15	1.8	0.60	0.10	5	5

CYCLING EXPERIMENTS

The TWCs were also analyzed under lean/rich cycling conditions, where cycle timing was fixed according to the NO_X concentration. The rich and lean-NO_X concentrations exiting a lean-burn engine under these conditions were estimated to be 1500 ppm and 750 ppm, respectively using a recent publication by Parks et al. [377]. As a point of reference, this rich:lean NO_X ratio of 2:1 is fairly conservative if compared to recent data published by Kašpar et al. [279]. The cycle timing was then fixed so that equivalent amounts of NO_X were delivered in the lean and rich periods. The rich period duration was set to 20 s, which corresponded to a 40 s lean period for equivalent NO_X delivery at a S.V. of 75,000 hr^{-1}, as in the case of the steady-state experiments. Similarly, the inlet gas temperature was varied from 150 – 550 °C, in 50 °C increments. Two rich phase concentrations were selected for investigation. The first corresponded to an AFR ratio of 14.4, which is slightly rich. The second corresponded to an AFR of 14.2, which was richer than the first case, but not so rich that a significant fuel penalty would result [357]. The gas concentrations for the lean and rich cycling experiments are shown in Table 13. The cycle averaged NO_X, CO, C_3H_6 conversions and NH_3 and N_2O yield and selectivity, respectively, were calculated using Eqns. 19 – 21 and 23 – 26 using the last 4 cycles after the periodic steady state had been achieved, as demonstrated previously [376].

Table 13. Reaction conditions for lean/rich cycling evaluation of TWCs, with calculated AFRs and λ values.

AFR	λ	Duration (s)	O_2 (%)	NO (%)	CO (%)	H_2 (%)	C_3H_6 (%)	CO_2 (%)	H_2O (%)
Lean									
24.00	1.65	40	8.0	0.075	-	-	-	5	5
Rich 1									
14.40	0.987	20	1.34	0.15	1.8	0.60	0.10	5	5
Rich 2									
14.20	0.973	20	1.06	0.15	1.8	0.60	0.10	5	5

4.4 RESULTS AND DISCUSSION

4.4.1 STEADY-STATE NH_3 FORMATION

EFFLUENT GAS PROFILES AT 250 °C

The results shown in Fig. 52 demonstrate the effluent gas concentrations for NO_X, NH_3, N_2O, CO and C_3H_6 during steady-state operation over the HPGM, Pd-only TWC (Fig. 52A) and LPGM, Pd/Rh TWC (Fig. 52B) as a function of the AFR. The inlet gas temperature, measured 1 cm in front of the TWC, was set to 250 °C. During operation, the lowest mid-core temperature under these conditions was approximately 430 °C, 180 °C higher than the inlet temperature, which demonstrates that co-feeding reductants in the presence of O_2 (where the O_2 conc. was adjusted in order to vary the AFR) resulted in a significant exotherm over TWCs. For stoichiometric operation (i.e., AFR = 14.59), the exotherm approached 250 °C.

Fig. 52 also shows that the product distribution obtained over TWCs was strongly dependent on the AFR. For stoichiometric operation, both the CO and NO_X conversion exceeded 99.8% and the exiting concentrations of NO_X, CO and C_3H_6 were effectively zero. However, a slight change in the AFR resulted in dramatic changes in the concentrations of NO_X and CO observed in the reactor effluent. C_3H_6, on the other hand, was not observed in the AFR

range considered in this investigation, nor were any other hydrocarbons; however, it is expected that a significant amount of the C_3H_6 being fed is being converted to CO over these catalysts, especially under rich conditions. Tagliaferri et al. [378] previously reported similar results for C_3H_8 conversion under similar conditions. Even though the AFR was expected to dramatically affect the product distribution, the acute sensitivity of the TWCs to the operating conditions, especially for lean operation, was quite impressive. For example, when the AFR was tuned very slightly lean (e.g., AFR=14.63 or λ=1.003) over the HPGM catalyst, the NO_X conversion plummeted to 44%. Similar behavior was observed over the LPGM catalyst, but the NO_X conversion only dropped to 73% in that case. As Taylor [379] previously explained, Rh demonstrates high activity for the selective reduction of NO_X to N_2, even under slightly lean environments. Therefore, the higher NO_X conversion over the LPGM case under lean conditions can most likely be attributed to the presence of Rh on the catalyst. The LPGM catalyst also produced less N_2O than the HPGM catalyst under slightly lean conditions, where significantly higher levels of N_2O formation over Pd/Al_2O_3 in comparison to Rh/Al_2O_3 have previously been reported [380]. The presence of CeO_2 on the LPGM catalyst may have also suppressed N_2O formation, as previously reported by Oh [381].

During rich operation (i.e., AFR<14.59), both of the TWCs produced NH_3 and slipped CO. Over the HPGM catalyst, the concentration of CO slipped as the AFR was tuned from 14.59 to 14.4 increased linearly, but subsequently richer operation resulted in an exponential increase in the concentration of CO slipped. NH_3 formation over the HPGM catalyst similarly increased as the AFR was decreased from 14.59 to 14.4. Progressively richer operation did result in minimal increases in the NH_3 yield, but >95.0% of the incoming NO_X had already reacted to form NH_3 by an AFR of approximately 14.35. The results obtained over the LPGM

catalyst were generally similar, but the NH_3 yield was noticeably lower. For example at an AFR of 14.4, the NH_3 yield was only 54.0% over the LPGM catalyst in comparison to 90.0% over the HPGM catalyst under the same conditions. Even when operated under significantly richer environments, the LPGM catalyst never reached the high NH_3 yields observed over the HPGM catalyst. Conversely, the amount of CO slipped under rich conditions over the LPGM catalyst was lower in comparison to the HPGM case if compared at an AFR of 14.2.

It should be noted, that under these conditions of low NH_3 yield that neither N_2O or NO_X were observed, which once again suggests that the N_2 yield was increasing for the Rh and CeO_2 containing LGPM. Schlatter et al. [120] previously explained that the main role of Rh in TWCs was to selectively reduce NO_X to N_2 instead of NH_3. They demonstrated that Rh-only TWCs generated significantly less NH_3 than Pd/Rh or Pt/Rh TWCs under rich conditions. Furthermore, when the Pt and Rh TWCs were physically separated and the Rh catalyst was placed upstream of the Pt catalyst, significantly less NH_3 was generated than when Pt catalyst was placed upstream of the Rh catalyst. These results clearly demonstrate that Rh-only and Rh promoted TWCs more selectively reduce NO_X to N_2 under rich conditions. This is in agreement with an earlier publication by Kobylinski et al. [382], where Pt and Pd catalysts mainly produced NH_3 under rich conditions, while Rh and Ru catalysts were significantly more selective towards N_2 formation.

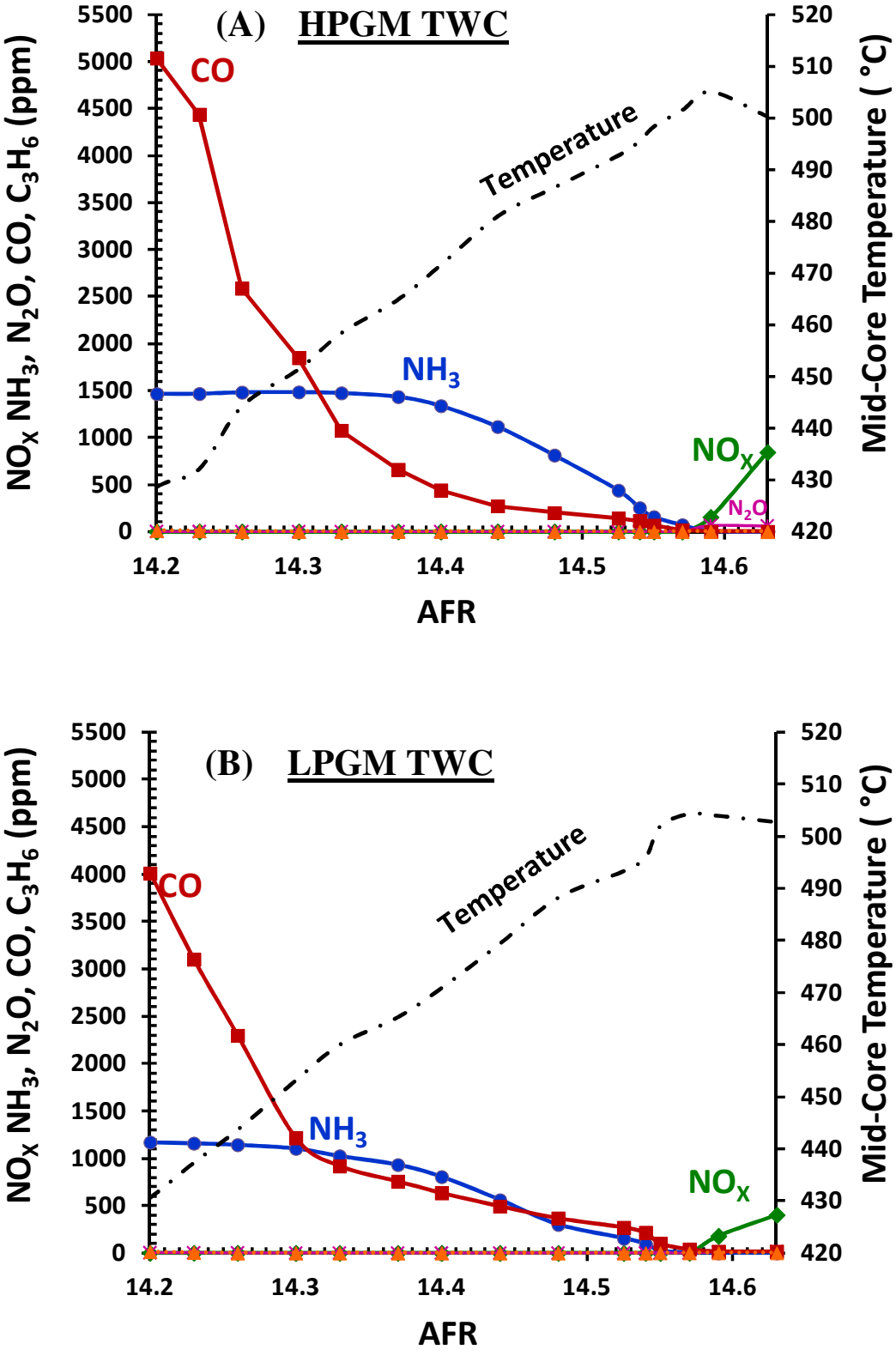

Figure 52. Effluent gas concentrations for (◆) NO_X, (●) NH_3 (X) N_2O, (■) CO and (▲)C_3H_6 over (A) HPGM, Pd-only TWC and (B) LPGM, Pd/Rh TWC, respectively. (S.V. 75,000 hr^{-1}, Inlet Temp. = 250 °C, Reaction conditions shown in Table. 12).

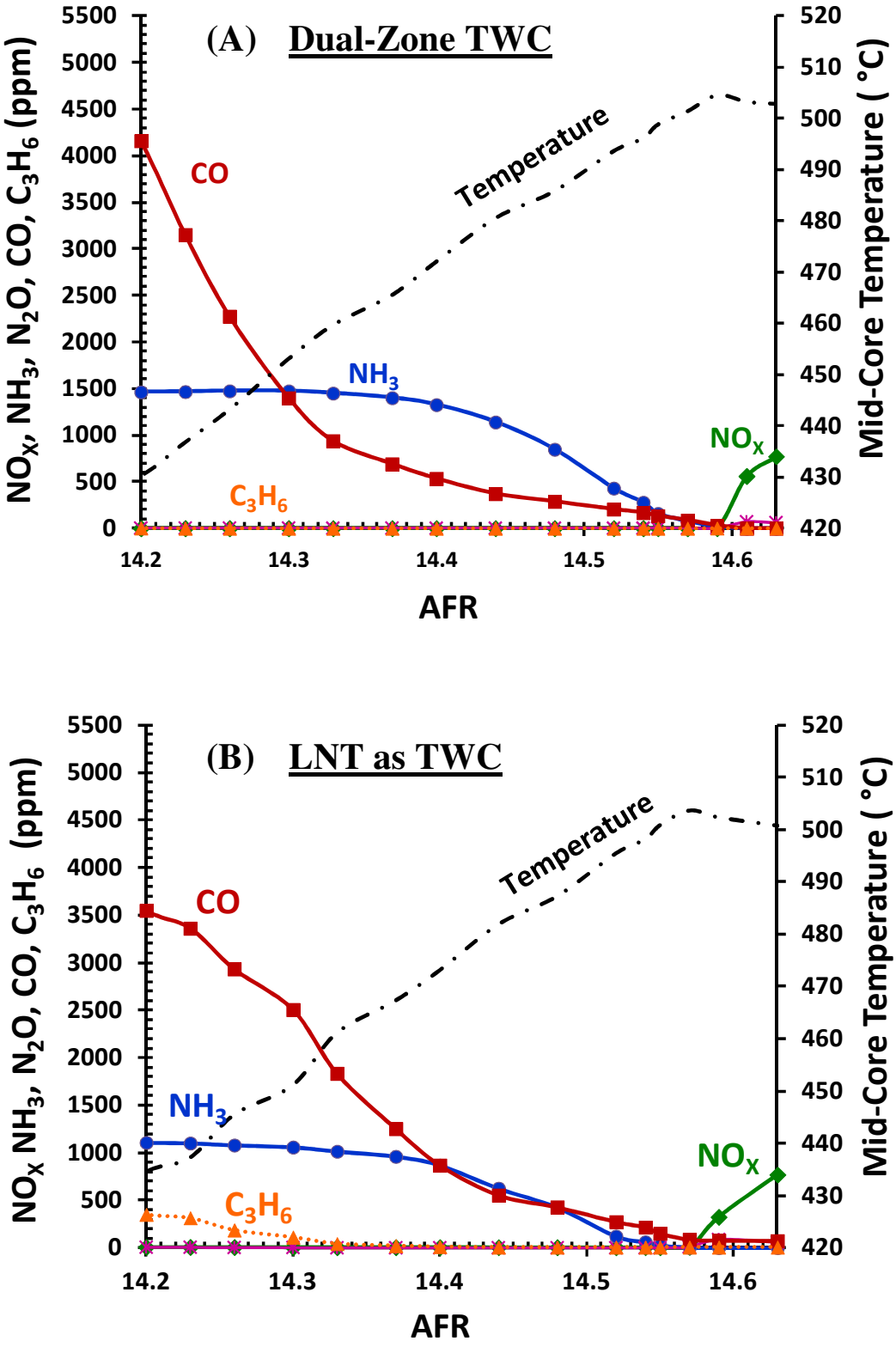

Figure 53. Effluent gas concentrations for (◆) NO_X, (●) NH_3 (X) N_2O, (■) CO and (▲)C_3H_6 over (A) Dual-Zone TWC and (B) LNT as TWC, respectively. (Same conditions as Fig. 52).

The presence of CeO_2 on the LPGM catalyst may also be significant as CeO_2 has previously been reported to: preserve noble metal dispersion, increase the thermal stability of the support, promote water gas shift (WGS) activity and steam reforming, store and release oxygen, and promote CO oxidation [383]. CeO_2 has also been reported to enhance NO decomposition, via spillover of oxygen onto the partially reduced CeO_2, and favorably alter the kinetics for CO oxidation and NO_X reduction [379]. In this case, the CeO_2 on the LPGM catalyst appeared to affect the WGS activity, where the CO concentration at an AFR of 14.2 was approximately 4000 ppm instead of 5000 ppm for the LPGM and HPGM catalysts, respectively. Unfortunately, as discussed by Kaspar et al. [383], the role of CeO_2 in the NO/H_2 or $NO/H_2/CO$ reaction on TWCs is still unclear and very few investigations have addressed the issue [384,385]. Therefore, further comments regarding the role of CeO_2 on NH_3 formation under rich conditions over the LPGM catalyst cannot be made. Given the extensive nature of research performed on TWCs, the reader is referred to the following reviews for a more exhaustive discussion on the effects of CeO_2 and Rh on TWC performance and/or specifics of TWC operation [2,279,379,383,385–387].

In summary, Fig. 52 clearly demonstrates that the AFR is a sensitive parameter that can be used to tune NH_3 generation over TWCs. This is important because in the passive NH_3, TWC-SCR approach, selective NH_3 generation over the close-coupled TWC will ultimately dictate operation conditions (i.e., cycle timing) for the downstream SCR catalyst. Additionally, the desired NH_3 yield can be balanced using a threshold limit for CO slip deemed to be tolerable. For example, steady-state operation of the HPGM catalyst at an AFR ratio of 14.2 would result in a slightly higher NH_3 yield, but the concentration of CO slipped from the TWC under these conditions would also be an order of magnitude higher than for operation at an AFR of 14.4.

Lastly, while CO slip can be minimized, it cannot be eliminated merely by tuning the AFR, as CO was observed under all conditions favorable for NH_3 generation over the TWCs.

Fig. 53 depicts the results collected over the Dual-Zone TWC (Fig. 53A) and over the LNT as TWC (Fig. 53B), respectively. As discussed in Section 4.2.1, the Dual-Zone TWC was a combination of the HPGM and LPGM catalysts placed in series, where the HPGM catalyst was always placed upstream of the LPGM catalyst. Interestingly, the NH_3 profile observed over the Dual-Zone catalyst was effectively identical, within experimental error, to the NH_3 profile observed over the HPGM catalyst (Fig. 52A). This is a strong indication that both NO_X reduction and NH_3 formation occurred in the front section of the Dual-Zone catalyst over the HPGM section. While NH_3 formation over the downstream LPGM catalyst cannot be excluded, it is unlikely because, as previously discussed, this catalyst was significantly less selective for NH_3 formation. Furthermore, if the majority of NH_3 was indeed produced over the HPGM section, this indirectly suggests that NH_3 decomposition over the Rh and CeO_2 containing LPGM section did not occur, at least at these temperatures. While Kobylinski et al. [382] previously reported NH_3 decomposition over Rh and Ru containing TWCs, significant activity was not observed until 500 °C if CO was present in the gas mixture. In this case, the AFRs most favorable for NH_3 generation yielded corresponding catalyst temperatures below 470 °C and CO was always observed during NH_3 generation, as previously discussed. Conversely, the amount of CO slipped over the Dual-Zone catalyst under rich conditions was reduced and more closely resembled the results obtained over the LPGM catalyst (Fig. 52B), where higher WGS activity was previously suggested to account for the lower CO concentrations. These results are consistent with an earlier report by Schlatter et al. [120], where the NH_3 concentration profile as a function of the oxygen concentration obtained over a Rh catalyst placed upstream of a Pt

catalyst was nearly identical to the monometallic Rh catalyst. Similarly, the NH_3 profile obtained over a Pt catalyst placed upstream of a Rh catalyst was nearly identical to the monometallic platinum catalyst. Taken together, this indicates that the Dual-Zone catalyst may be able to combine the high NH_3 yield of the HPGM catalyst and lower CO slip of the LPGM catalyst, which are both desirable attributes of a TWC in the passive-NH_3, TWC-SCR approach.

The results obtained over the LNT as TWC are shown in Fig. 53B, where the NH_3, NO_X and CO profiles generally mirror results obtained over the LPGM catalyst. Again, similarities in the LNT and LPGM catalyst formulations most likely explain why analogous behavior was observed. Unfortunately, C_3H_6 breakthrough was observed for AFRs below 14.3. This behavior was not expected, but could be explained because LNT catalysts are typically operated at significantly lower SVs than TWCs and the dip-coating procedure may have been altered accordingly. Additionally, the LNT catalyst contained Pt as a primary component instead of Pd, where Pd has long been reported to exhibit better activation of HCs than Pt [27,112,279].

QUANTIFIED NH_3 YIELD (150 – 550 °C)

The results shown in Fig. 54 compare the quantified NH_3 yield as a function of the mid-core temperature at a constant AFR over the entire family of TWCs considered in this investigation. In all cases, the inlet temperature, prior to contacting the catalyst, was varied between 150 °C to 550 °C. As Fig. 54 demonstrates however, the mid-core temperature was always considerably higher than the set point temperature, as previously observed in Figs. 52 and 53. This shifted the temperature range of consideration from 150 to 550 °C to approximately 350 to 700 °C. While this may appear to be on the high side, close-coupled TWCs can experience temperatures as high as 900 – 1100 °C and operation from 350 – 700 °C was therefore viewed to be a representative temperature range [15]. Recent engine dynamometer

results collected using a federal test procedure (FTP) drive cycle (data omitted for brevity) confirmed that the average operating temperature for a close coupled TWC ranged from 400 – 500 °C, with excursions up to 700 °C.

Fig. 54A displays the richest condition considered (AFR = 14.0) and demonstrates that all of the TWCs considered in this investigation generated significant amounts of NH_3 over a broad temperature window if they are operated under sufficiently rich conditions. In this case, the HPGM, Pd-only TWC clearly generated the most NH_3, over the widest temperature range, but the Dual-Zone catalyst also generated significant amounts of NH_3 and was generally indistinguishable from the HPGM catalyst until the temperature exceeded 500 °C. Interestingly, the difference in the NH_3 yield between the HPGM and Dual-Zone catalyst occurred at approximately the same temperature as Kobylinski et al. [382] previously reported significant activity for NH_3 decomposition over Rh containing TWCs. Since the rear section of the Dual-Zone formulation was based on a $Pd/Rh/CeO_2$ combination, NH_3 decomposition over the downstream LPGM section could explain why lower NH_3 yields were observed at higher temperatures. Decreased NH_3 yield over the LPGM catalyst in comparison to the HPGM catalyst was also clearly evident, where the HPGM catalyst always produced more NH_3 than the LPGM catalyst even for the lowest temperatures considered. Similarly, decreased NH_3 yield over the LPGM catalysts was most likely caused by the presence of Rh and/or CeO_2 [120]. Fig. 54A also clearly demonstrates the similarities in operation between: (1) the HPGM and Dual-Zone catalyst and (2) the LPGM and LNT, as previously discussed (Figs. 52 and 53).

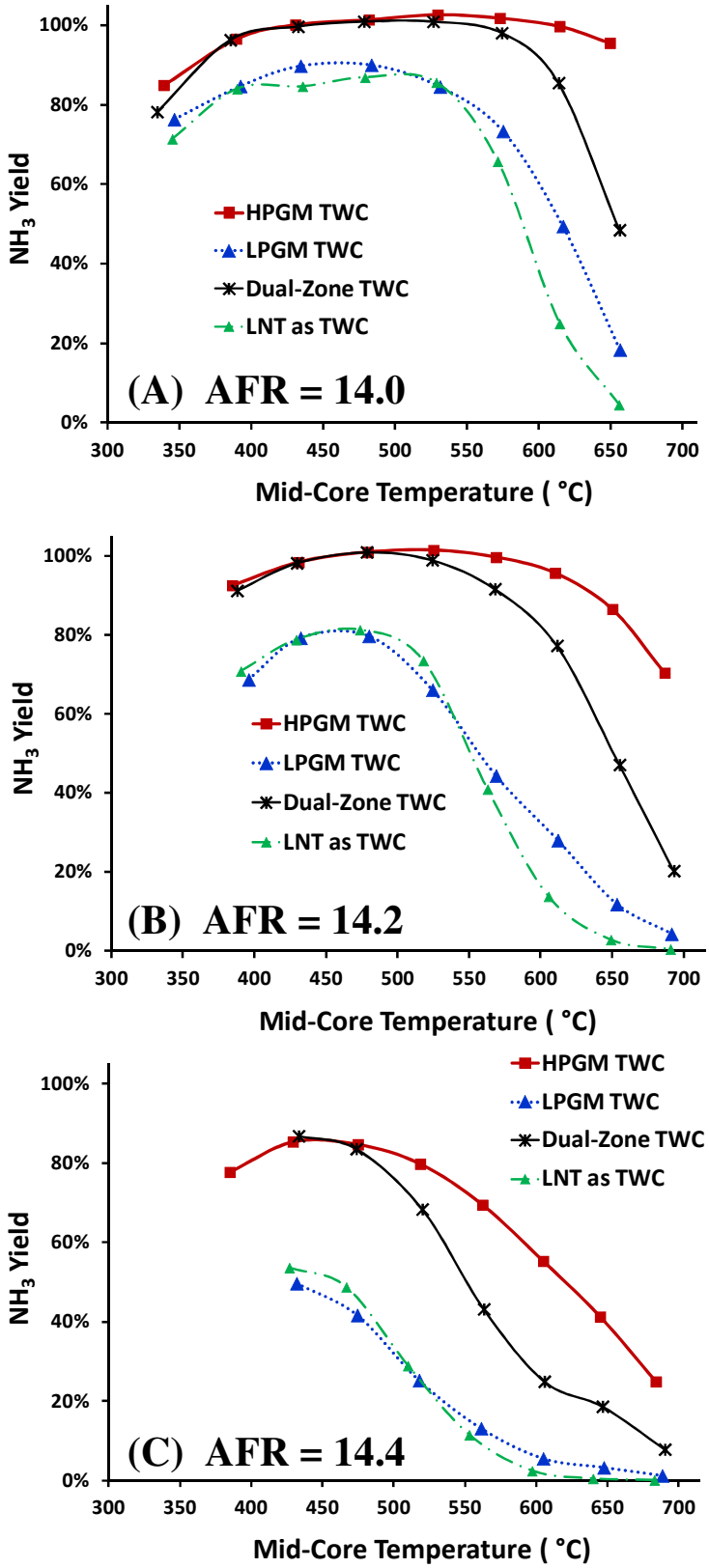

Figure 54. Quantified NH_3 yield as a function of catalyst temperature for AFRs of (A) 14.0, (B) 14.2 and (C) 14.4.

When the AFR ratio was increased from 14.0 to 14.2 (Fig. 54B), the differences in performance between the catalytic formulations became much more pronounced and only the HPGM catalyst maintained a high NH_3 yield over the entire temperature range. In all other cases, a significant decline in the NH_3 yield was observed. This is especially apparent for the LPGM and LNT catalysts for temperatures above 550 °C and reasonable NH_3 yields were only observed over a fairly narrow temperature range from 400 to 525 °C. Similarly, when the AFR was increased from 14.2 to 14.4 (Fig. 54C), even more significant impacts on the NH_3 yield were observed. Now, even the HPGM catalyst was unable to maintain a high NH_3 yield over the entire temperature range. In summary, Figs. 52-54 have shown that the AFR ratio, catalyst temperature and catalytic formulation are all sensitive parameters that dictate the amount of NH_3 that can be generated over TWCs. Generally, the NH_3 yield decreased as follows: HPGM $\geq$ Dual-Zone >> LPGM $\approx$ LNT, where tuning the AFR progressively closer to stoichiometric operation resulted in less NH_3 production in all cases. The differences between the catalytic formulations also became more pronounced as the operating conditions approached stoichiometric operation. This conclusion is more clearly seen in Fig. 55, where operation of the HPGM, Pd-only catalyst (i.e., the catalyst with the highest NH_3 yield used in this investigation) required subsequently richer and richer AFRs to achieve maximum NH_3 yield as the inlet gas temperature was increased.

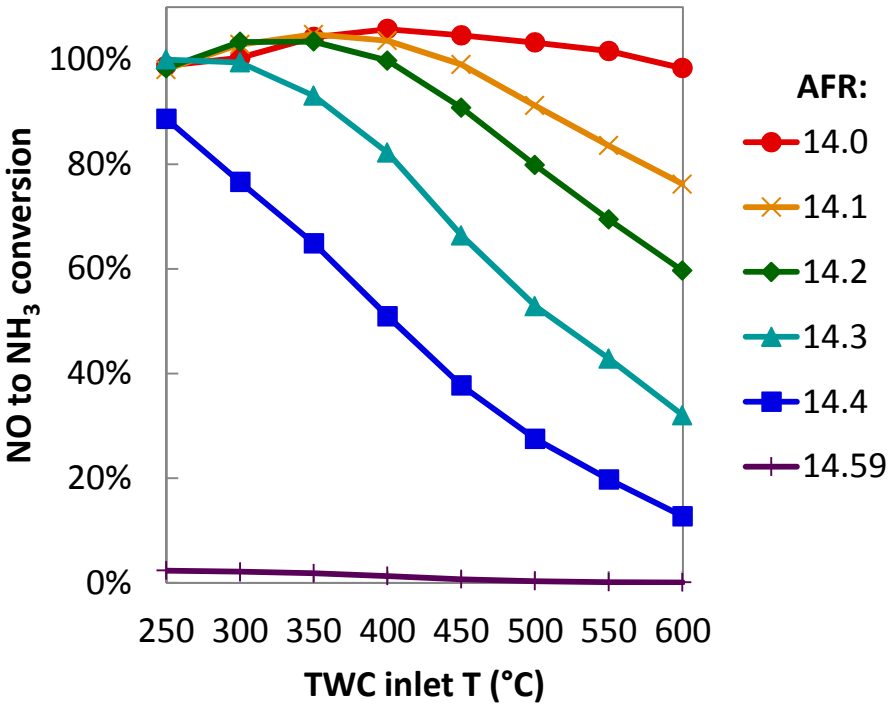

Figure 55. Quantified NH_3 yield over the HPGM, Pd-only TWC as a function of the AFR and temperature.

The mechanism for NH_3 formation over Pt, Pd and Rh catalysts has long been reported to proceed via hydrogenation of a N adatom by dissociatively adsorbed H_2 [382,386,388–391]. For example, Pirug and Bonzel [388] reported an increase in the N_2, N_2O, NH_3 and H_2O concentrations at approximately 170 °C during reaction of NO + H_2 over a Pt foil for a H_2/NO ratio of 0.5. This temperature corresponded almost identically to the dissociation temperature for NO over the same foil and led the authors to conclude that NO dissociation must precede the formation of N_2, N_2O and NH_3. They also noticed little NH_3 formation for a H_2/NO ratio of 0.5, but significant NH_3 formation when the H_2/NO ratio was increased to 5, which indicated that a high H_2/NO ratio on the metal surface in addition to NO dissociation was required for NH_3 formation. Similar results have also been reported over Pd [389] and Rh [390]; but in the case of

Rh, NH_3 decomposition was observed by 325 °C. This is in excellent agreement with the CO-free results reported by Kobylinski et al. [382] over supported Rh catalysts. Gahndi et al. [392] similarly observed minimal NH_3 decomposition over Pt and Pd catalysts at approximately 500 °C, but significant (>80%) NH_3 decomposition over a Ru catalyst by 370 °C.

These features of the NH_3 formation mechanism are clearly evident in Figs. 52-55, where high reductant to NO_X ratios favored NH_3 formation at intermediate temperatures. Under those conditions, NO dissociation occurs rapidly and NH_3 decomposition is slow. At elevated temperatures, higher NH_3 yields were observed for formulations where catalytic NH_3 decomposition was less likely. For temperatures below 400 °C, N_2O was also observed, but the yield was generally insignificant. This behavior was initially counterintuitive since rich operation implies a high H_2/NO ratio and N_2O formation should therefore be unlikely. However, as the temperature was decreased, NO dissociation most likely becomes rate-limiting – where the temperature for NO dissociation has been reported between 125 – 225 °C [388–390] – and the likelihood that a N adatom will react with a molecularly adsorbed NO instead of another N adatom increases.

4.4.2 NH_3 FORMATION DURING LEAN/RICH CYCLING

LEAN/RICH CYCLING PROFILES AND NH_3 YIELDS

The preceding sections demonstrated the potential for NH_3 formation over all four of the catalysts investigated, where changes in the catalyst formulation, temperature and AFR all affected the amount of NH_3 that could be formed. However, these results were obtained during steady-state operation under a constant rich environment. In the passive-NH_3, TWC-SCR approach, the TWC must also be able to generate significant amounts of NH_3 during lean/rich cycling. The results shown in Fig. 56 demonstrate lean/rich cycling over the HPGM, Pd-only

TWC for a rich period AFR ratio of 14.2. The top left pane shows the NO, NO_2 and NO_X concentration profiles collected over 4 representative lean/rich cycles at 250 °C, where the first 40 s represents lean operation, followed by 20 s of rich operation. As previously discussed, this cycle timing was chosen in order to keep the total number of moles of NO_X delivered during lean and rich periods the same. As shown, NO_X breakthrough during lean operation (e.g., 0 - 40 s) occurred rapidly over the HPGM TWC. The sigmoidal shape of the NO_X breakthrough curve indicated that some NO_X storage was taking place, even though the HPGM TWC does not contain Ba as a NO_X storage component. Furthermore, the effluent NO_X concentration at the end of the lean period was only 680 ppm instead of 750 ppm, which provided additional evidence of NO_X storage. At lower temperatures, NO_X storage on the TWC might be expected, since significant NO_X storage on Al_2O_3 has previously been reported for temperatures below 300 °C [33]. At 40 s, the conditions were switched back to rich operation. As in the case of LNT catalysts, a NO_X spike was observed at the lean to rich interface. Over LNT catalysts, the decomposition of stored nitrites/nitrates has been reported to occur more rapidly than NO_X reduction at these lean/rich interfaces [140,151]. Additionally, slower NO_X reduction over partially oxidized metal sites has also been reported to contribute to NO_X slip [6]. In this case, it would appear that similar NO_X release mechanisms were occurring over the TWC and co-feeding NO_X during the rich period may have made NO_X release even more likely.

During rich periods, the effluent NO_X concentration was always zero, excluding the brief period of NO_X slip, which indicated that NO_X reduction during rich periods even under lean/rich cycling was facile. The corollary N_2O, CO and NH_3 concentration profiles for lean/rich cycling

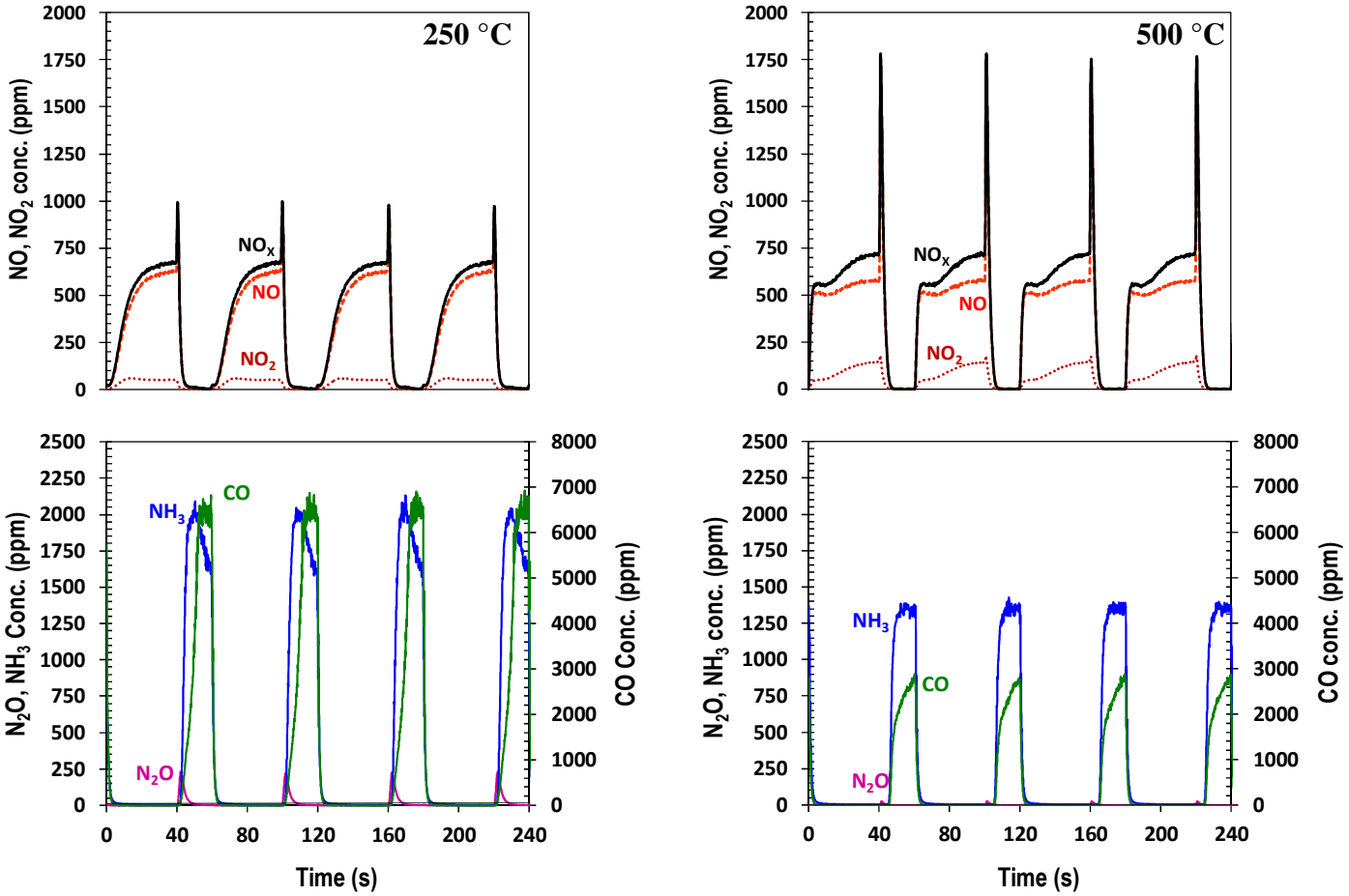

Figure 56. Lean/rich cycling over the HPGM, Pd-only TWC at 250 and 500 °C, respectively. (Reaction conditions shown in Table 13: Lean/Rich2 – AFR=14.2).

at 250 °C are shown in the bottom portion of the left-hand pane in Fig. 56. In this case, an N_2O spike was observed at the lean/rich transition, which rapidly decreased as the rich period continued. Again, N_2O formation over LNT catalysts has been shown to be a strong function of temperature and the ratio of adsorbed N and NO adatoms to reductants [140,151,346,349,351,356]. At the beginning of the rich period, the stored NO_X was rapidly released and N_2O was formed until a net reducing environment was attained, where comparison between the concurrently decreasing N_2O and increasing CO concentrations supports this assessment. Significant amounts of NH_3 were also produced during the rich periods. In this

case, the peak concentration exceeded 2000 ppm. Since only 1500 ppm of NO_X was fed during rich periods, peak values exceeding 1500 ppm implied that the NO_X stored on the TWC could be converted to NH_3. As the rich period progressed, the NH_3 concentration declined because all of the stored NO_X had been consumed. If the rich period duration had been extended, the NH_3 and CO concentration values would have eventually reached the steady-state concentrations.

At 500 °C, NO_X breakthrough occurred even more rapidly and a nearly-rectangular step-function for the NO_X profile was observed, which implied that very little NO_X was stored at this temperature. However, and surprisingly, minimal NO_X storage was still observed. The transition from lean to rich conditions at 500 °C also resulted in a significantly higher NO_X slip concentration, where any NO_X stored over Al_2O_3 under these conditions would most likely be released extremely rapidly. Similarly, N_2O formation was observed at the lean/rich interface, but the concentration was significantly reduced, where higher temperatures generally favor less N_2O formation during cycling [351]. The amount of CO slipped also decreased. This was most likely the result of higher activity for the water gas shift (WGS) reaction at this temperature. In both cases (250 and 500 °C), complete NO_X conversion was observed during rich periods and therefore cannot explain increased CO consumption. Alternatively, deeper oxidation of the support and/or precious metals during lean periods could potentially contribute to increased CO consumption at higher temperatures [393]. At 500 °C, NH_3 production was delayed until approximately 5 s into the rich period. Then, the NH_3 concentration rapidly increased and the average concentration observed during the last 5 s of the rich period was approximately 1350 ppm. Under steady-state conditions, the average NH_3 concentration for an AFR of 14.2 was approximately 1300 ppm, while the average CO concentration was approximately 3600 ppm. As Fig. 56 demonstrates however, the CO concentration was still in a state of rapid transience when

the rich period was ended. If the rich period had been extended, the CO and NH_3 would eventually reach the steady-state values as previously discussed. Another key feature is that the NH_3 reaches its maximum value considerably faster than CO, which suggests that the timing can be adjusted to maximize NH_3 formation while reducing the CO slip. In summary, one particularly desirable feature of the HPGM TWC is its ability to rapidly produce significant amounts of NH_3 that are virtually identical to the steady-state values, even during cycling.

The NO_X and NH_3 profiles observed in Fig. 56 were then integrated and averaged over four cycles to obtain the cycled averaged NO_X slip and NH_3 yield. The ratio of these was then used as an additional metric for catalyst performance, as shown in Eqn. 27.

$$\alpha = \frac{\int NH_{3_{Produced}}}{\int NO_{x_{Slipped}}} \tag{27}$$

For example if $\alpha = 1$, the amount of NH_3 produced during the rich period is equal to the amount of NO_X slipped during the lean period and a TWC-SCR system constructed using a "perfect" SCR catalyst (i.e., an SCR catalyst that could trap all of the NH_3 produced and then use 100% of that NH_3 for NO_X reduction) would achieve 100% NO_X conversion. In reality, a perfect SCR catalyst does not exist, but the cycle averaged α was used to determine the most promising operating conditions and catalysts.

The results shown in Fig. 57 display the cycle averaged α obtained for the HPGM catalyst as a function of temperature for rich AFRs of 14.4 and 14.2, respectively, where the solid dashed line demonstrates the critical $\alpha \geq 1$ threshold. Unfortunately for the AFR of 14.4 (with minimum associated fuel penalty), an $\alpha \geq 1$ was not observed for any of the temperatures considered, even though significant amounts of NH_3 could be formed under these same conditions during steady-state operation (Fig. 54C). In fact, NH_3 formation above 350 °C for the rich AFR of 14.4 was especially poor. This is an important result because it implies that richer

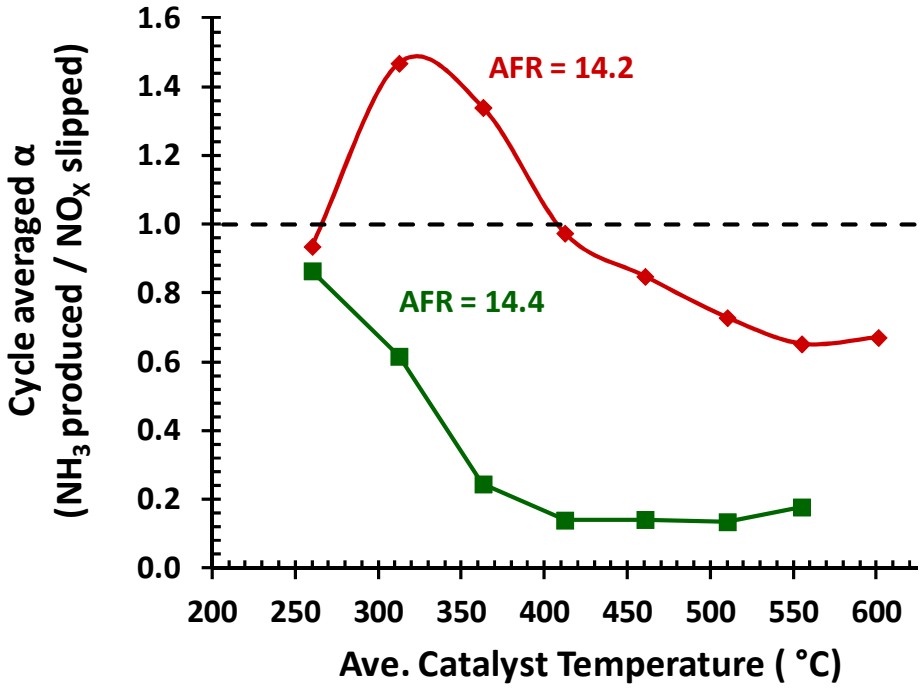

Figure 57. The cycle averaged α as a function of temperature for rich period AFRs of 14.4 and 14.2, respectively.

AFRs are required during cycling in comparison to steady-state operation. Generally, operation as close as possible to stoichiometric regime during rich periods is desired because it minimizes the rich period fuel penalty, but clearly an AFR of 14.4 will not suffice. The differences in NH_3 formation between cycling and steady-state can most likely be attributed to H_2/CO/C_3H_6 oxidation reactions that occur during the first few seconds of rich operation before a net reducing environment is achieved, where the reductants consumed during this time could otherwise be used for production of NH_3 under steady-state conditions. Reduction of OSC, reduction of oxidized precious metal sites and reaction of reductants in the concentration front that propagates through the catalyst bed during the lean/rich transition could all contribute to reductant consumption. As a side note, even the LNT (14.4 AFR data omitted for brevity) – where NO_X storage capacity, as shown in Fig. 61, can dramatically increase the NH_3 to NO_X ratio – never

achieved an $\alpha \geq 1$ for a rich AFR of 14.4. This provides even more substantial evidence that the slightly rich AFR of 14.4 will most likely never generate enough NH_3 during cycling to warrant operation under these conditions. For this reason, only results for rich AFRs of 14.2 were reported, with the exception of the results shown in Fig. 57.

For a rich AFR of 14.2, an $\alpha \geq 1$ was obtained from approximately 275 – 425 °C, which clearly demonstrates that the HPGM catalyst can generate enough NH_3 during cycling to theoretically operate a downstream SCR catalyst when operated under sufficiently rich conditions in an appropriate temperature range. At 350 °C, the cycle averaged α reached a maximum at 1.47, which further supports the previous conclusion of NO_X storage capacity over the HPGM TWC (Fig. 56). In this case, an $\alpha > 1$ confirmed NO_X storage because equivalent doses of NO_X were fed in lean and rich periods and the upper limit for α would therefore be 1.0 unless some of the NO_X fed during lean periods was stored and converted to NH_3 during a subsequent rich period. In a similar investigation, Li et al. [357] reported an AFR of 14.2 to be the optimum rich condition for lean/rich cycling, which agrees well with the results reported here.

The results shown in Figs. 58 and 59 depict corollary lean/rich cycling experiments conducted over the LPGM and LNT as TWC, respectively. The NO_X profiles obtained during lean periods over the LPGM catalyst (Fig. 58) were very similar to the profiles obtained over the HPGM catalyst, which implied that the loading and ratio of precious metals on the TWCs did not have a significant impact on performance during lean periods. However, the results obtained over the LPGM catalyst during rich periods were dramatically different. For example at 250 °C, the peak NH_3 concentration approached 1700 ppm, which was above the feed NO_X concentration (1500 ppm) and additionally confirmed NO_X storage over the LPGM catalyst, but was substantially

lower than the peak NH_3 concentration observed for the HPGM catalyst. The corresponding cycle averaged α for the LPGM catalyst at this temperature was 0.9, where the cycle averaged α for the HPGM catalyst under the same conditions was 1.47. This indicated that the LPGM formulation would either require a longer rich times or a richer, rich period to generate the same amount of NH_3 as the HPGM catalyst. Li et al. [358] previously reported similar results for a Pd-only and Pd/Rh TWC and concluded that the Pd-only catalyst may be preferred in the TWC-SCR even though Pd/Rh catalysts have long been used for TWC-only configurations. The CO concentration profile obtained over the LPGM catalyst also displayed interesting behavior, where CO breakthrough occurred rapidly and approached 7000 ppm before declining briefly to 2000 ppm and then increasing back to 7000 ppm. The dip in the CO concentration can most likely be explained by the OSC capacity provided by CeO_2 on the LPGM catalyst, where Feio et al. [394] previously reported that reduction of CeO_2 on a $Pd/CeO_2/Al_2O_3$ catalyst did not begin until approximately 300 °C. Since the furnace temperature in this case was set to 250 °C, it is likely that reduction of CeO_2 was delayed until the catalyst temperature reached a temperature high enough to reduce CeO_2. Fig. 60 displays the temperature profiles for the four TWCs considered in this investigation and demonstrates the increase in temperature as a function of the rich period duration. In all cases, a 150 °C exotherm was observed by the end of the rich period. At 250 °C, light-off for the HPGM and Dual-Zone catalyst occurred more rapidly than light-off for the LPGM and LNT catalyst, respectively. At 500 °C, a dip in the CO concentration was not observed. Above 300 °C, temperature inhibited CO consumption should not occur since the catalyst temperature is well above 300 °C. NH_3 formation at this temperature was also substantially suppressed, where the peak concentration was only 200 ppm and declined throughout the rich period. This corresponded to a cycle averaged α of only 0.08. Clearly,

lean/rich cycling conducted over the LPGM catalyst at elevated temperatures resulted in very poor NH_3 yields, which further indicates that the LPGM formulation may be a particularly poor candidate for the TWC-SCR approach. Substantially lower NH_3 yields for the Rh containing LPGM TWC were also observed for the steady-state experiments, as previously discussed (4.4.1), and were previously attributed to higher rates of NO dissociation and/or NH_3 decomposition over Rh [43,47].

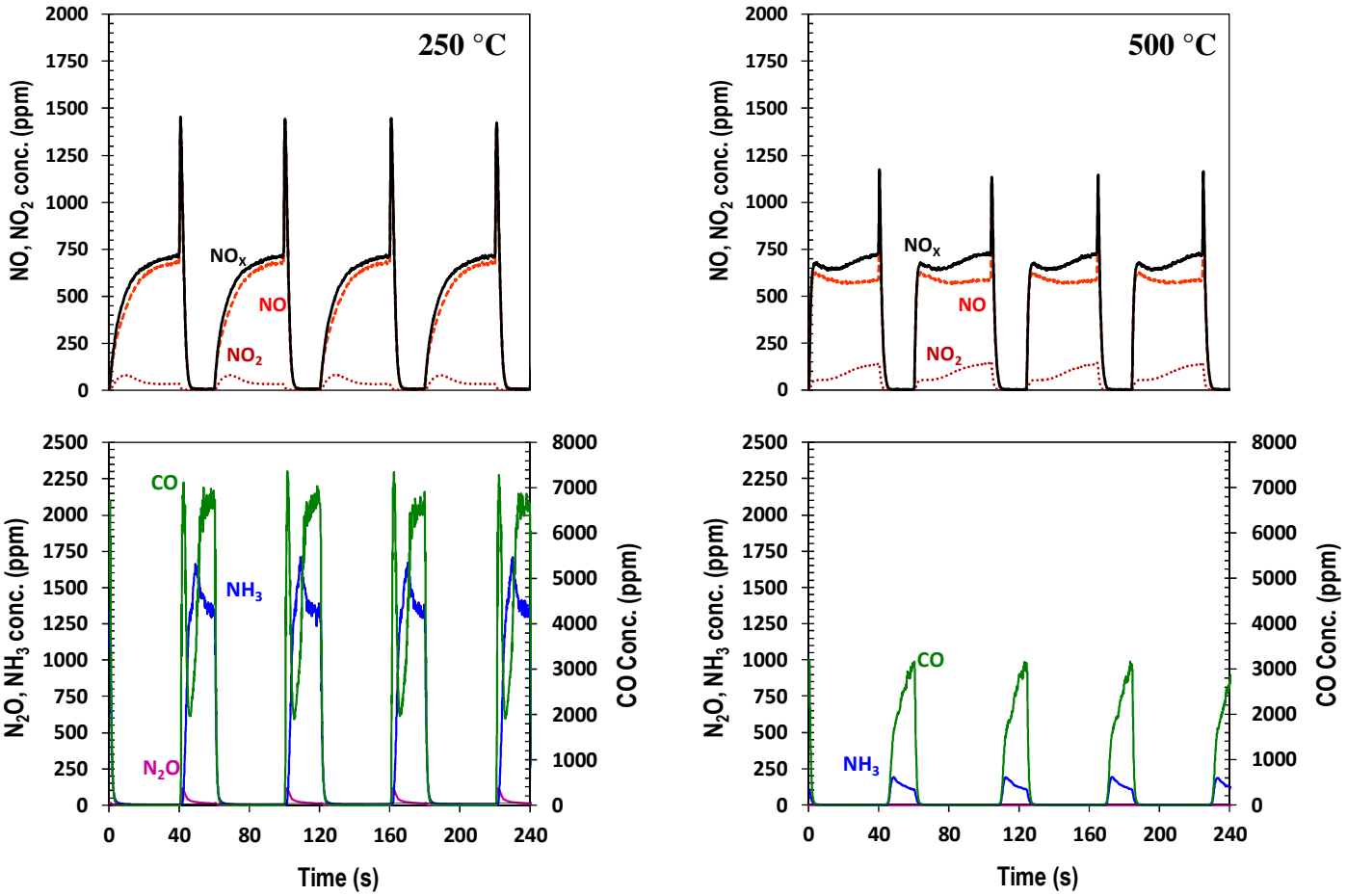

Figure 58. Lean/rich cycling over the LPGM, Pd/Rh TWC at 250 and 500 °C, respectively. (Same conditions as Fig. 56).

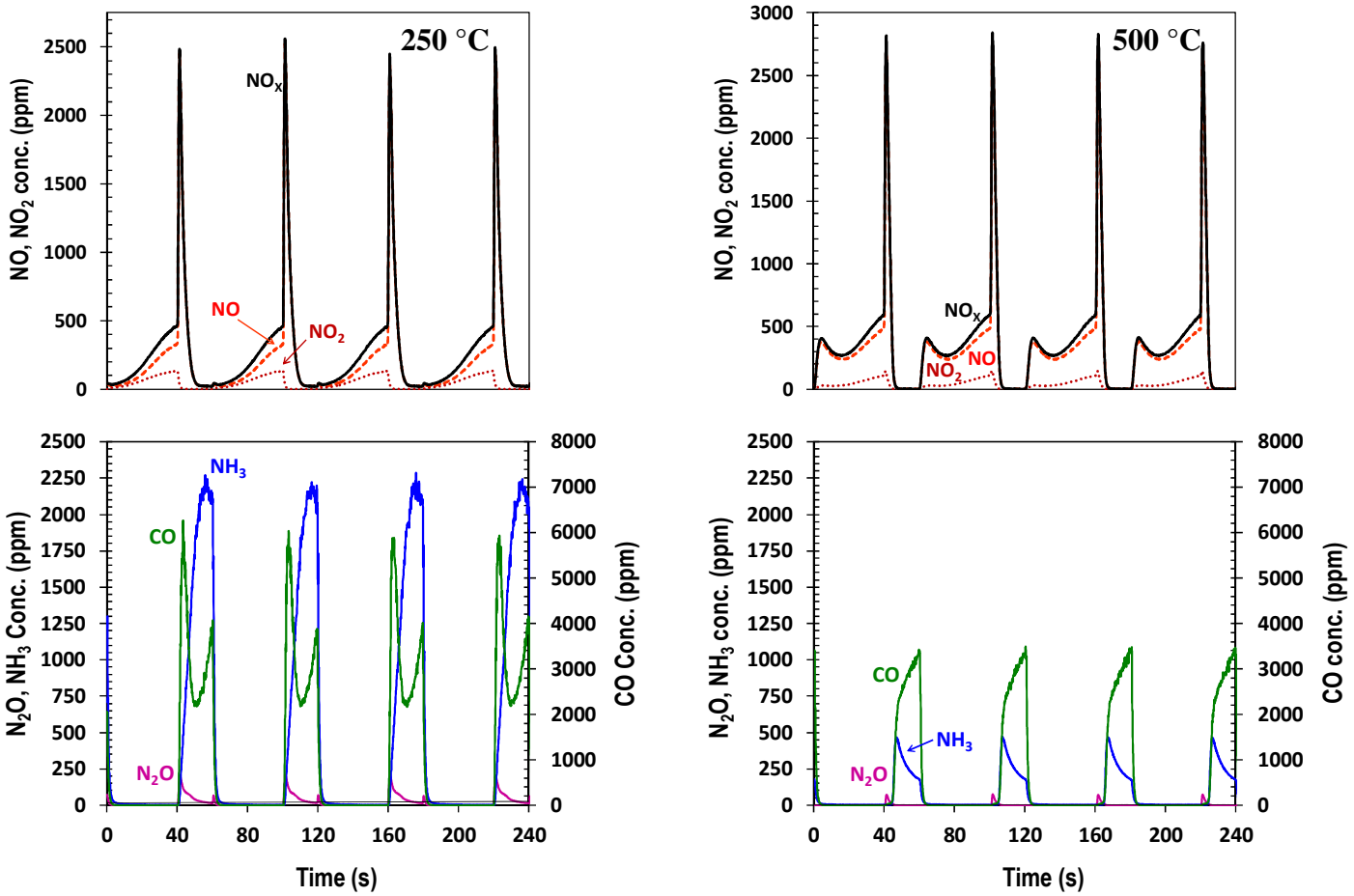

Figure 59. Lean/rich cycling over LNT as TWC at 250 and 500 °C, respectively. (Same conditions as Fig. 56)

The results for lean/rich cycling over the LNT are shown in Fig. 59, where a substantial number of publications [4,6] provide detailed examples of cycling results obtained over LNT catalysts. However in this case, the required cycle timing was substantially different from the usual LNT cycle timing protocol. We additionally wanted to clearly contrast cycling over TWCs in comparison cycling over LNT catalysts, since a relatively small number of publications [56,62,235,358,362] have provided examples of cycling over TWCs. For example at 250 °C, the NO_X profile over the LNT (Fig. 59) visibly depicts storage, where considerable storage was expected since the LNT catalyst contains Ba as a NO_X storage component. By the end of the

lean period, the outlet NO_X concentration was only 500 ppm and integration of the NO_X profile confirmed that approximately 75% of the NO_X fed during the lean period was stored. During the subsequent rich period, a significant amount of NH_3 was generated and the corresponding α was 1.82, where the α for the HPGM catalyst under the same conditions was 1.47. This is quite a significant result because a review of the steady-state results (Fig. 54B) would lead to the expectation of lower NH_3 yields over the LNT in comparison to the HPGM catalyst. This was not the case and demonstrates that NO_X storage capacity on the TWC is one way to alter the catalytic formulation to increase NH_3 formation during rich periods. A dip in the CO concentration was also observed, where reduction of stored NO_X in addition to reduction of OSC on the LNT could account for the additional CO consumption during rich periods. It is encouraging to note that this delay is not observed with all reductants, particularly NH_3. It may suggest that the reduction of the OSC occurs more preferentially with CO than with NH_3. At 500 °C, the LNT catalyst still stored NO_X, but significantly less (approximately 50% of the NO_X fed during the lean period was stored). This translated in to an improved NH_3 yield during the subsequent rich period in comparison to the LPGM catalyst (which mirrored the LNT catalysts under steady state operation), but the cycle averaged α was still only 0.20, while the α for the HPGM catalyst under the same conditions was 0.65. Again, a comparison of the results collected under steady-state condition would lead to the expectation of lower NH_3 yields over the LNT in comparison to the HPGM catalyst, as observed at 500 °C. In summary, incorporation of NO_X storage capacity could not overcome the inherently lower NH_3 production capabilities of the LNT catalyst at elevated temperatures.

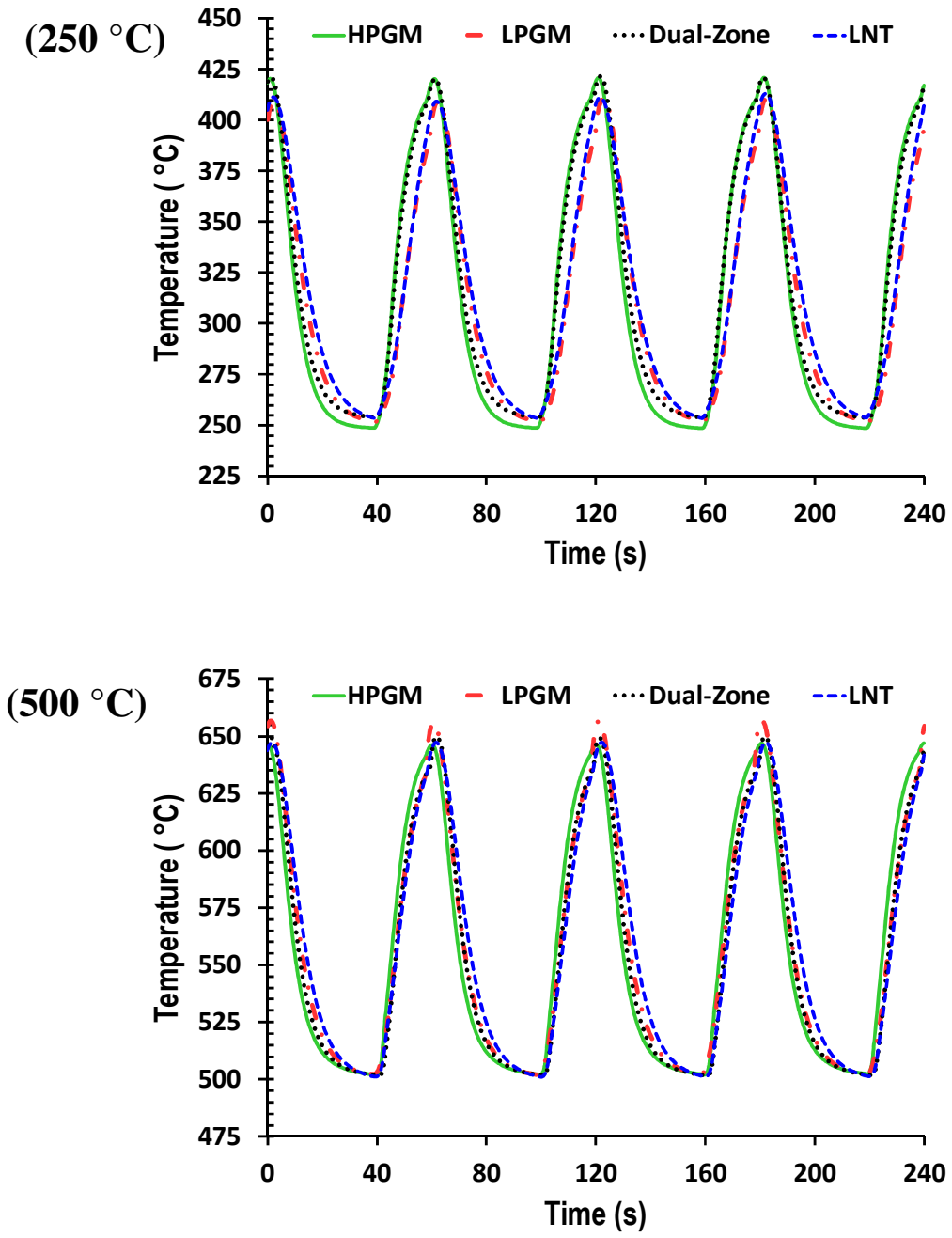

Figure 60. Typical temperature exotherms observed the HPGM, LPGM, Dual-Zone and LNT catalysts during cycling at 250 and 500 °C, respectively. (Rich period AFR = 14.2).

As previously mentioned, the results in Fig. 60 depict the mid-core catalyst temperature profiles for the four catalysts under consideration at 250 and 500 °C, respectively, as also shown in Figs. 56, 58 and 59. In both cases, the catalyst cooled during the first 40 s (e.g., lean

operation) to the furnace set point. At 40 s, the catalyst was switched back to rich operation and a rapid exotherm was observed. By the end of the 20 s rich period, the catalyst had approximately reached the temperature measured under steady-state conditions, which indicated that a rich period lasting longer than 20 s would be expected to yield both the product distribution and catalyst temperature exhibited under steady-state operation.

The results shown in Fig. 61 summarize the cycle averaged α values measured for all four catalysts as a function of temperature, where the dashed line again indicates the critical $\alpha \geq 1$ threshold. The LPGM catalyst generally exhibited the lowest NH_3/NO_X yields of all the catalysts considered in this investigation. The LPGM catalysts also exhibited a narrow temperature region for an $\alpha \geq 1$, where sufficient NH_3 could only be produced from approximately 325 °C to 400 °C. The Dual-Zone catalyst and HPGM catalyst exhibited nearly identical NH_3/NO_X yields, with the HPGM catalyst being slightly better at lower temperatures. The HPGM and Dual-Zone catalyst also exhibited a very similar temperature region with favorable NH_3/NO_X yields. However at higher temperatures, the Dual-Zone catalyst became noticeably inferior to the HPGM catalyst. Again, NH_3 decomposition over the downstream $Pd/Rh/CeO_2$ TWC likely consumed some of NH_3 formed on the upstream HPGM portion of the Dual-Zone catalyst [382]. While subtleties existed between the TWCs, a maximum α was generally observed between 300 – 400 °C with an optimum operation window between 275 – 425 °C. The maximum α for the TWCs also never exceeded 1.47 (HPGM), under these conditions. The LNT catalyst on the other hand, exhibited a maximum α at 400 °C and was able to maintain an $\alpha \geq 1$ for a larger temperature range from approximately 275 to 500 °C. The cycle averaged α near the optimum was especially pronounced and almost 5 times more NH_3, in comparison to the amount of NO_X slipped, was produced over the LNT catalyst. This is

additionally encouraging because this dramatic improvement was observed over a catalyst that demonstrated relatively poor NH_3 generation capabilities under steady-state operation, especially when compared to the HPGM catalyst. Therefore, the results in Fig. 61 clearly demonstrate that adding an "optimal" amount of NO_X storage capacity to a TWC could substantially increase the NH_3/NO_X yield and make the operation of passive TWC-SCR more efficient. Currently, the "optimal" amount of NO_X storage capacity has not been investigated. Sulfur poisoning of Ba sites at elevated temperatures [35,105] and long-term, high-temperature stability of the Ba storage component (e.g., formation of $BaAl_2O_4$) [162,192] will also need to be addressed, where the addition of CeO_2 may decrease losses in NO_X storage capacity in both cases [180,234,395].

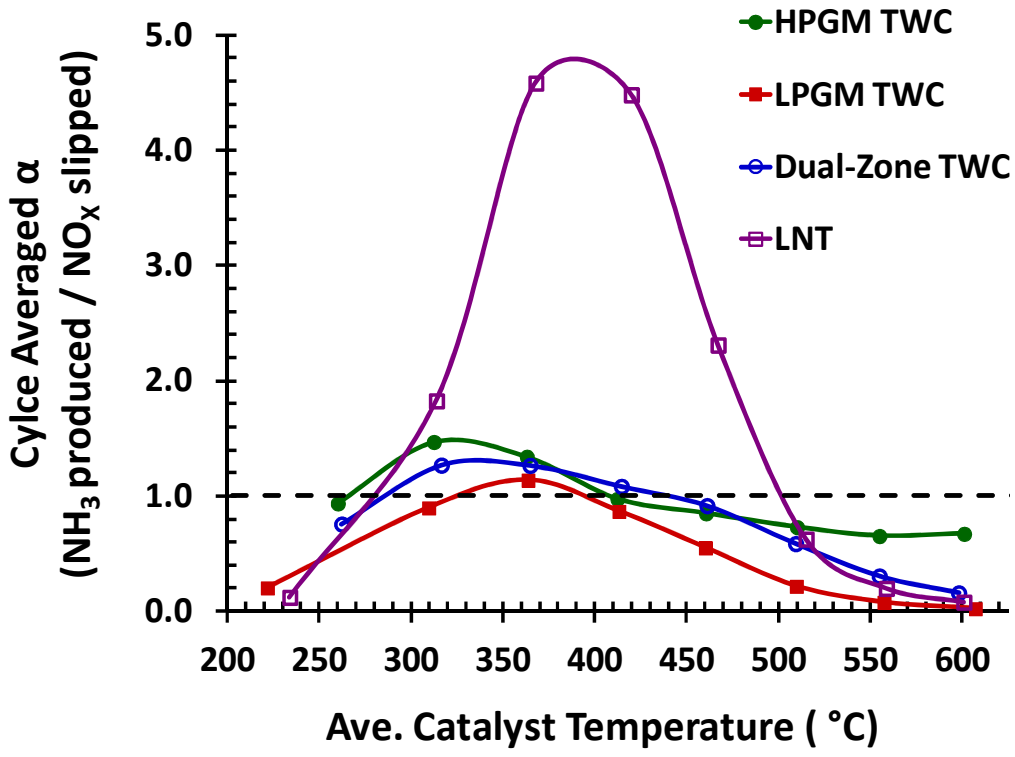

Figure 61. The cycle averaged α as a function of temperature for the HPGM, LPGM, Dual-Zone and LNT catalysts. (Rich period AFR = 14.2).

CYCLE AVERAGED NO_X, CO AND C_3H_6 CONVERSIONS AND N_2O YIELD

The results shown in Fig. 62 summarize the cycle averaged NO_X, CO and C_3H_6 conversion for all of the catalysts considered in this investigation. In the TWC-SCR system, the NO_X (and potentially C_3H_6 [334]) conversion would be improved by the inclusion of a downstream SCR catalyst. Conversely, the CO conversion would most likely not improve in the TWC-SCR system because additional CO oxidation/conversion over the downstream SCR catalyst under a net rich environment is highly unlikely unless the WGS reaction [396] and NH_3-SCR reaction occur simultaneously. For example, even in the presence of O_2, CO oxidation over a Cu-ZSM5 catalyst at 250 °C was minimal [397], while CO oxidation over a $Pd/CeO_2/Al_2O_3$ (0.155/20%, w/w) catalyst under similar conditions had approximately reached complete conversion [398]. Therefore, the cycled average NO_X conversion for the TWC-SCR system would be higher, but the CO and C_3H_6 conversions will most likely be very similar to the values reported here.

As previously discussed, cycle averaged NO_X conversions exceeding 50%, as designated by the dashed line, confirmed NO_X storage on the catalysts. The results obtained over the LNT were most pronounced and a cycled averaged NO_X conversion of approximately 90% was measured near the optimum operating temperature for that particular catalyst [376]. Generally, NO_X was stored on all of the catalysts considered, at least up to 500 - 550 °C; by 600 °C, the NO_X storage capacity had been eliminated even for the LNT catalyst. Direct NO decomposition over reduced precious metal sites could also occur after the catalyst was switched back to lean operation, but if occurring, this phenomenon would be expected to occur for a very brief period and account for minimal increases in the amount of NO reduced, since Amirnazmi, Benson and Boudart [399] reported a strong inhibiting effect for O_2 on NO decomposition.

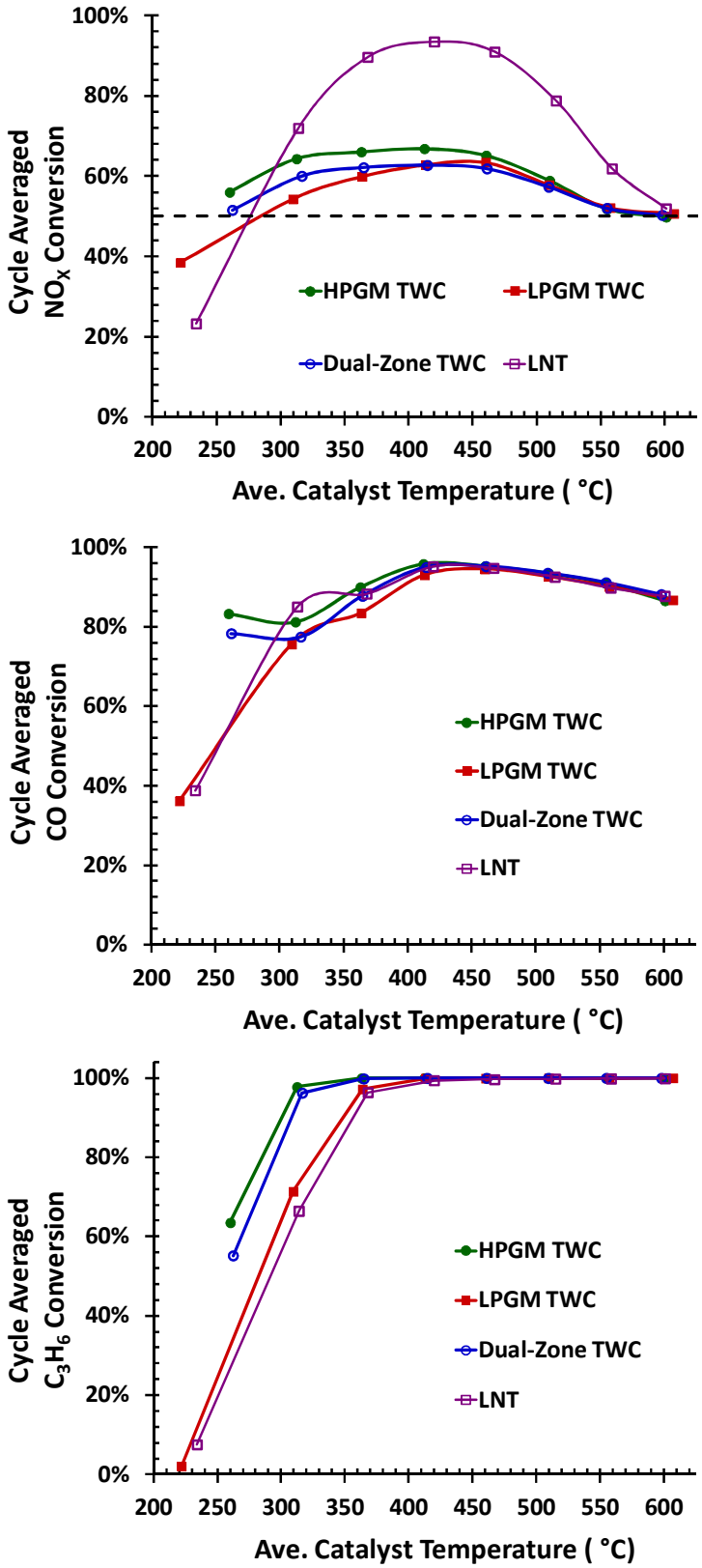

Figure 62. The cycled averaged NO_X, CO and C_3H_6 conversion as a function of temperature for the HPGM, LPGM, Dual-Zone and LNT catalyst. (Rich period AFR = 14.2).

Below 300 °C, the LPGM and LNT catalyst exhibited especially poor overall performance in comparison to the HPGM and Dual-Zone catalyst and correspondingly lower cycle averaged NO_X, CO and C_3H_6 conversions were measured. In this case, the lower PGM loadings on the LPGM and LNT catalyst most likely explain this behavior. For example, it is generally accepted that the easiest way to improve the low-temperature activity of a TWC is to increase the PGM loading [279]. As a result, the HPGM and Dual-Zone catalyst offered more robust performance as the temperature was decreased and complete NO_X conversion during rich periods was still observed for the lowest temperatures considered. Alternatively, the LPGM and LNT catalysts slipped significant amounts of NO_X during rich period, which explains why the NO_X conversion dropped below 50% for these catalysts. Additionally, complete light-off was not observed below 250 °C and in both cases the rich period temperature exotherm was below 100 °C, while the HPGM and Dual-Zone catalysts exhibited a temperature exotherm of approximately 150 °C. For complete light-off, an exotherm of approximately 150 °C was expected, as further demonstrated in Fig. 60. This further indicated that the LPGM and LNT catalyst underwent a longer and slower light-off process at the lowest temperatures considered, which ultimately resulted in poor overall performance.

The results obtained for the cycle averaged CO conversions were quite complex. As discussed, the poor CO conversion below 300 °C for the LPGM and LNT catalyst can most likely be explained by the lower activity of those catalysts at low temperatures. For the HPGM and Dual-Zone catalyst, this is not the case and the higher CO conversion was most likely a combination of rapid CO oxidation and NO_X reduction. As the temperature was increased above 300 °C, the WGS reaction most likely explains the additional increase in CO conversion that was observed. Light-off for the WGS reaction over a Pt/Al_2O_3 catalyst was previously reported to

occur around 275 °C [383]. Nova et al. [64] similarly reported significant WGS activity over a $Pt/Ba/Al_2O_3$ LNT catalyst by 300 °C. Reduction of stored NO_X, especially for the LNT catalyst at lower temperatures, could also contribute to CO consumption, and therefore makes deconvolution of the different effects even more difficult. As the temperature was increased above 450 °C, the CO conversions for all of the catalysts were effectively identical. This behavior was not surprising since all of the catalysts were highly active for CO oxidation, NO_X reduction and the WGS reaction under these conditions. The NO_X storage capacity also begins to decrease at these temperatures and the controlling factor for the measured CO conversion becomes the equilibrium conversion of the WGS reaction. The results for C_3H_6 conversion demonstrate a more typical light-off curve profile even though these results were collected under cycling conditions, which demonstrated that C_3H_6 conversion is primarily controlled by temperature. Abdulhamid et al. [27] previously reported significant activity for C_3H_6 above 350 °C, but poor utilization of the HC for lower temperatures, as also observed here. Again, differences in the C_3H_6 conversion measured at low temperature were most likely due to differences in PGM loadings.

In summary, comparison of the results in Fig. 61 with the results of Fig. 62 imply an optimum operating temperature for the TWC between 400 to 450 °C. In this fairly narrow regime, the cycled averaged NO_X conversion was high, all of the catalysts could stored some NO_X, the cycled averaged α was generally ≥1 (expect for the LPGM catalyst), a maximum in CO conversion was observed and lastly propylene conversion was 100%. Above 500 °C, the increased NO_X conversion provided via NSC was eliminated, the CO conversion began to decline (since both the WGS equilibrium conversion declines and less NO_X is stored) and only the HPGM catalyst generated enough NH_3 to yield a reasonable cycle averaged α. At lower

temperatures (275 – 400 °), the cycled averaged α was generally higher, but the CO conversion was significantly lower and C_3H_6 slip also became a problem under these conditions. Crocker et al. [334] previously reported that the conversion of NO_X by C_3H_6 and NH_3 was additive, but the amount of C_3H_6 stored in comparison to NH_3 was quite low so the majority of C_3H_6 might still be slipped from the SCR under these conditions. Therefore, operation at lower temperatures would only be feasible if the lean/rich cycle timing could be increased as a result of increased NH_3 production, which would limit the amount of CO and C_3H_6 released because less time would be spent operating rich.

The results shown in Fig. 63 depict the cycle averaged N_2O yield measured for all of the catalysts considered in this investigation. At low temperatures, a fairly significant amount of N_2O was formed, especially for the LPGM catalyst. Pihl et al. [351] previously observed that low temperatures favored N_2O formation over LNT catalysts. Burch and coworkers [3,16,400] similarly explained that at lower temperatures, NO dissociation occurs more slowly and therefore favors N_2O formation either through coupling of an adsorbed N and NO adatom or through an adsorbed $(NO)_2$ dimer. Bowker et al. [401] measured the sticking coefficient for NO on a Pd(110) surface and observed a decrease in the sticking coefficient with increasing temperatures and proposed that N_2O formation was favored at lower temperatures because the lifetime of molecular NO on the surface was longer. Obuchi et al. [389] similarly observed N_2O formation over a Pd foil at low temperatures, but N_2O formation over a Rh foil [390] was below the detection limit. The effect of catalyst formulation on N_2O formation has also been observed by Macleod et al. [380]. More recently, Ji et al. [140] discussed the role of the regeneration/oxidation front on N_2O formation, where transition from lean/rich or rich/lean

results in a reaction front that passes over the catalyst bed and alters the H/NO ratio on the metal surface.

In this case, the LNT catalyst generally produced the most N_2O, with the exception of results collected at the lowest temperature considered. Since the LNT is basically a TWC with Ba, it would appear that the addition of NSC increased the amount of N_2O formed. One potential reason for this behavior could be the "sea" of stored NO_X present on the catalyst when regeneration begins, which in turn increases the likelihood of high NO_X/H ratios during this transition. As the temperature was increased, the formation of N_2O decreased. By 400 °C, the formation of this undesirable global warming pollutant was substantially decreased. At the highest temperatures considered, N_2O formation was negligible. While N_2O was formed, the downstream SCR catalyst may actually further decrease the N_2O yields in the combined TWC-SCR system, as Wang and Crocker et al. [335] recently reported N_2O reduction over Cu-zeolite catalysts. Lastly, the simultaneous low N_2O yields for high NH_3 yields offered by the TWC-SCR system is potentially one of the most attractive aspects of this system because similar screening investigations conducted for LNT-SCR systems concluded that NH_3 and N_2O yields peaked under almost identical conditions for LNT catalysts [340,376].

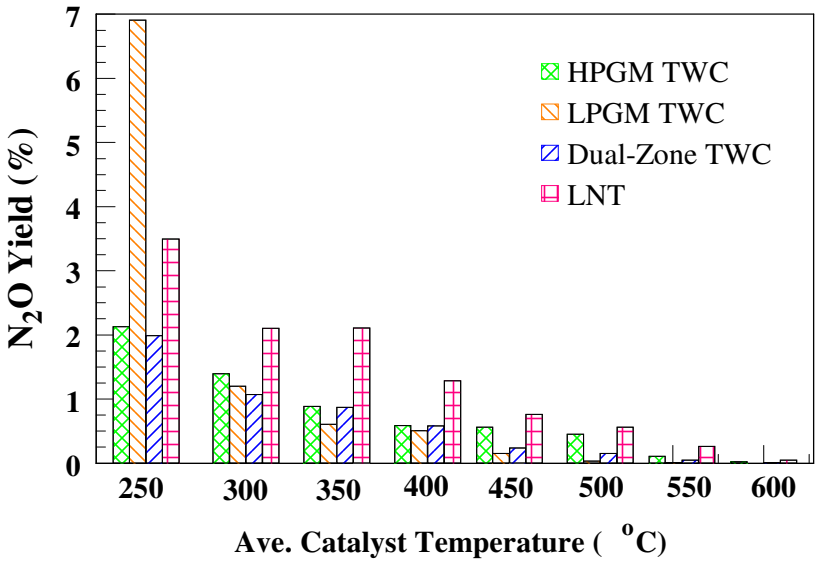

Figure 63. The cycled averaged N_2O yield as a function of temperature for the HPGM, LPGM, Dual-Zone and LNT catalyst. (Rich period AFR = 14.2).

4.5 CONCLUSIONS

NH_3 formation under steady-state and lean/rich cycling conditions was investigated using a HPGM, LPGM, Dual-Zone and LNT catalyst operated as a TWC. NH_3 formation during steady-state operation was dependent on the AFR, temperature and catalytic formulation. Generally, the NH_3 yield decreased as follows: HPGM $\geq$ Dual-Zone >> LPGM $\approx$ LNT. While all of the formulations could produce significant amounts of NH_3 if operated under sufficiently rich conditions, the selectivity to NH_3 for the LPGM and LNT and was always lower than the selectivity to NH_3 for the HPGM and Dual-Zone catalyst, respectively. The presence of Rh and/or CeO_2 in these formulations could explain why less NH_3 was observed. At higher temperatures, the Dual-Zone catalyst also produced less NH_3 than the HPGM catalysts and NH_3 decomposition over Rh and/or CeO_2 most likely explains why lower NH_3 yields were observed. The AFR was determined to be a sensitive parameter that could be used to control NH_3 generation and CO slip, where CO was always observed under conditions favorable for NH_3

formation. As the temperature was increased, a richer AFR was necessary to achieve the same NH_3 yield observed at lower temperatures.

For cycling, a significantly richer AFR was required to produce a similar amount of NH_3 observed during the steady-state experiments. Consumption of CO, and other reductants, in the lean/rich front that propagates through the catalyst bed, reduction of oxidized precious metal sites and oxygen storage capacity (OSC), especially for CeO_2 containing formulations, could explain why a richer AFR was necessary during cycling. The optimum catalysts and conditions were determined using a new parameter defined as the cycle averaged α (ratio of NH_3 produced to NO_X slipped). The HPGM catalyst demonstrated the most robust α over the entire temperature range considered, with an optimum between 275 to 400 °C. At moderate temperatures (275 – 500 °C), inclusion of NO_X storage capacity (i.e., results collected for the LNT) dramatically increased the amount of NH_3 produced in relation to the amount of NO_X slipped, even though the LNT catalyst generally exhibited the lowest NH_3 yields for steady-state operation. This implied that inclusion of an "optimum" amount of NO_X storage capacity could dramatically improve the performance of the TWC-SCR system. Above 500 °C, only the HPGM produced enough NH_3 to theoretically operate a TWC-SCR system. When the CO and C_3H_6 conversions were considered in addition to the NH_3 formation, the optimum temperature for this system was determined to be approximately 400 – 450 °C, but CO slip continue to be a concern. N_2O formation, on the other hand, was insignificant for temperatures above 400 °C, which is a unique advantage of TWC-SCR system.

4.6 ACKNOWLEDGEMENTS

A portion of this research was sponsored by the U.S. Department of Energy, Office of Energy Efficiency and Renewable Energy, Vehicle Technologies Program. The authors thank program managers Ken Howden and Gurpreet Singh for their support. This manuscript has been co-authored by UT-Battelle, LLC, under Contract No. DE-AC05-00OR22725 with the U.S. Department of Energy. The United States Government retains and the publisher, by accepting the article for publication, acknowledges that the United States Government retains a non-exclusive, paid-up, irrevocable, world-wide license to publish or reproduce the published form of this manuscript, or allow others to do so, for United States Government purposes. Additionally, the authors would like to acknowledge the contributions of Wei Li, Chang Kim and Kushal Narayanaswamy of General Motors in addition to Davion Clark and Christopher Owens of Umicore for discussions and guidance in this portion of our research.

CHAPTER 5. CONCLUSIONS

Lean-burn gasoline engines are more fuel efficient than conventional, stoichiometric-burn ones. Although the improvements are relatively modest, if implemented across the entire U.S. automotive fleet, lean-burn engines could have far-reaching implications on the amount of gasoline imported in the country on an annual basis. However, the development of cost-effective catalytic converter catalysts capable of meeting emission regulations for lean-burn vehicles still represents a major technical challenge. Currently, three-way (TWC), lean NO_X trap (LNT) and selective catalytic reduction (SCR) and combinations thereof represent the possible solutions. In this dissertation, the three most promising configurations were considered (i.e., TWC+LNT, TWC + LNT + SCR, and TWC + SCR).

In Chapter 2, a fundamental investigation of the NO_X reduction mechanism by CO and C_3H_6 in the presence of water was performed over $Pt/BaO/Al_2O_3$ and $Rh/BaO/Al_2O_3$ model LNT catalysts using *in situ* FTIR spectroscopy. Quantification of the FTIR results was then performed using corollary experiments monitored using mass spectroscopy. The FTIR results indicated that surface nitrites were the predominant NO_X storage form at 250 °C, while surface nitrates became the predominant storage form at 350 °C. The presence of water did not have a significant effect during storage. Surface isocyanates (NCO) were formed under a variety of conditions and their concentration was dependent on the temperature, the reductant selected, the presence of H_2O and the type of precious metal used. The reaction of surface NCO species with

NO and O_2 was fast and catalyzed by precious metals, with no difference observed between Pt and Rh. A similarly fast reaction was also observed with H_2O, even in the absence of the noble metal component. Comparison of N_2 evolution amounts during the rich phase and subsequent reaction of residual NCO species with O_2 and NO confirmed that reaction of NCO species could contribute significantly to the total amount of N_2 formed, when CO is used as the reducing agent.

In Chapter 3, a commercial LNT catalyst – obtained from a BMW 120i, lean-burn gasoline engine exhaust tailpipe – was evaluated during lean/rich cycling for potential application in an LNT-SCR system. The NH_3 yield in comparison to the NO_X was carefully tracked as a function of lean/rich cycle timing and temperature in order to determine if the cycle timing could be used as a parameter for concerted NH_3 generation. Two lean/rich cycling regimes were clearly identified. At low temperatures, NO_X release and reduction were kinetically limited. Therefore, a longer, lower concentration rich dose favored increased cycle averaged NO_X conversions. For example, extending the rich period from 5 to 15 s at 250 °C, while holding the reductant dose constant, resulted in an increase in cycle averaged NO_X conversion from 59 to 87%, respectively. At high temperatures, the opposite was true and shorter, higher concentration rich doses resulted in higher NO_X conversions. The selectivity to NH_3 and N_2O was shown to primarily be a function of temperature and the selectivity generally increased as the temperature decreased. NH_3 and N_2O yields, on the other hand, were significantly affected by the cycling timing any combination of changes in the lean/rich timing protocol or reductant concentrations that resulted in increased NO_X conversion also resulted in increased NH_3 and N_2O yield. Lastly, concerted control of NH_3 formation by varying the lean/rich cycle timing was demonstrated. While tuning the lean/rich timing could improve the

amount of NH_3 formed in comparison to the amount of NO_X slipped, the N_2O yield also increased under the same conditions.

In Chapter 4, NH_3 formation under steady-state and lean/rich cycling conditions was investigated using a three commercial TWCs and the LNT catalyst from Chapter 3 for application in a TWC-SCR system. NH_3 formation during steady-state operation was dependent on the AFR, temperature and catalytic formulation, but all of the formulations could produce significant amounts of NH_3 if operated under sufficiently rich conditions. The selectivity to NH_3 was always lower for the Rh and/or CeO_2 containing formulations. In all cases, the high precious metal loading, Pd-only TWC produced the most NH_3 during steady-state operation. For cycling, a significantly richer AFR was required to produce similar amount of NH_3 as observed during the steady-state experiments. Again, the Pd-only catalyst demonstrated the most robust NH_3 formation over the entire temperature range considered, with an optimum between 275 to 400 °C. However, inclusion of NO_X storage capacity (i.e., results collected over the LNT catalyst) demonstrated that NO_X storage capacity could significantly increase the amount of NH_3 produced in relation to the amount of NO_X slipped, even though the LNT catalyst generally exhibited the lowest NH_3 yields for steady-state operation. This implied that inclusion of an "optimum" amount of NO_X storage capacity could significantly improve the performance of the TWC-SCR system. When CO and C_3H_6 conversions were considered in addition to the NH_3 formation, the optimum temperature for this system was determined to be approximately 400 – 450 °C, but CO slip will still need to be addressed. N_2O formation, on the other hand, was insignificant for temperatures above 400 °C, which is a unique advantage of TWC-SCR system.

REFERENCES

[1] R.M. Heck, R.J. Farrauto, Catalytic Air Pollution Control: Commercial Technology, 3rd Ed., John Wiley & Sons, Inc., Hoboken, NJ, 2009.

[2] V.I. Parvulescu, P. Grange, B. Delmon, Catalysis Today 46 (1998) 233.

[3] R. Burch, Catalysis Reviews 46 (2004) 271.

[4] S. Roy, A. Baiker, Chemical Reviews 109 (2009) 4054.

[5] R. Burch, J.P. Breen, F.C. Meunier, Applied Catalysis B: Environmental 39 (2002) 283.

[6] W.S. Epling, L.E. Campbell, A. Yezerets, N.W. Currier, J.E. Parks, Catalysis Reviews 46 (2004) 163.

[7] C.H. Bartholomew, R.J. Farrauto, Fundamentals of Industrial Catalytic Processes, 2nd Ed., John Wiley & Sons, Inc., Hoboken, NJ, 2006.

[8] N. Takahashi, H. Shinjoh, T. Iijima, T. Suzuki, K. Yamazaki, K. Yokota, H. Suzuki, N. Miyoshi, S. Matsumoto, T. Tanizawa, T. Tanaka, S. Tateishi, K. Kasahara, Catalysis Today 27 (1996) 63.

[9] US EPA. The Plain English Guide to the Clean Air Act, (2007).

[10] US EPA. 2007 Progress Report: Vehicle and Engine Compliance Activities, (2008).

[11] US EPA. Air Pollution Control Orientation Course: Course 422, (n.d.).

[12] ICPP. Climate Change 2007: A Synthesis Report, (2007).

[13] US EPA. Regulations and Standards, (n.d.).

[14] A. Faiz, C.S. Weaver, M. Walsh, Air Pollution from Motor Vehicles: Standards and Technologies for Controlling Emissions, World Bank Publications, 1997.

[15] R.J. Farrauto, R.M. Heck, Catalysis Today 51 (1999) 351.

[16] J.P. Breen, R. Burch, C. Fontaine-Gautrelet, C. Hardacre, C. Rioche, Applied Catalysis B: Environmental 81 (2008) 150.

[17] Y. Li, S. Roth, J. Dettling, T. Beutel, Topics in Catalysis 16/17 (2001) 139.

[18] W.S. Epling, A. Yezerets, N.W. Currier, Catalysis Letters 110 (2006) 143.

[19] J.-S. Choi, W.P. Partridge, C.S. Daw, Applied Catalysis A: General 293 (2005) 24.

[20] P. Kočí, M. Schejbal, J. Trdlička, T. Gregor, M. Kubíček, M. Marek, Catalysis Today 119 (2007) 64.

[21] I. Nova, L. Castoldi, L. Lietti, E. Tronconi, P. Forzatti, F. Prinetto, G. Ghiotti, Journal of Catalysis 222 (2004) 377.

[22] Y. Su, M.D. Amiridis, Catalysis Today 96 (2004) 31.

[23] L. Lietti, I. Nova, P. Forzatti, Journal of Catalysis 257 (2008) 270.

[24] T. Szailer, J. Kwak, D. Kim, J. Hanson, C. Peden, J. Szanyi, Journal of Catalysis 239 (2006) 51.

[25] H. Abdulhamid, E. Fridell, M. Skoglundh, Applied Catalysis B: Environmental 62 (2006) 319.

[26] H. Abdulhamid, E. Fridell, M. Skoglundh, Topics in Catalysis 30/31 (2004) 161.

[27] H. Abdulhamid, J. Dawody, E. Fridell, M. Skoglundh, Journal of Catalysis 244 (2006) 169.

[28] C.M.L. Scholz, B.H.W. Maes, M.H.J.M. de Croon, J.C. Schouten, Applied Catalysis A: General 332 (2007) 1.

[29] W.S. Epling, J.E. Parks, G.C. Campbell, A. Yezerets, N.W. Currier, L.E. Campbell, Catalysis Today 96 (2004) 21.

[30] C. Courson, A. Khalfi, H. Mahzoul, S. Hodjati, N. Moral, A. Kiennemann, P. Gilot, Catalysis Communications 3 (2002) 471.

[31] C. Sedlmair, K. Seshan, A. Jentys, J.A. Lercher, Journal of Catalysis 214 (2003) 308.

[32] N.W. Cant, M.J. Patterson, Catalysis Today 73 (2002) 271.

[33] B. Westerberg, E. Fridell, Journal of Molecular Catalysis A: Chemical 165 (2001) 249.

[34] F. Prinetto, G. Ghiotti, I. Nova, L. Lietti, E. Tronconi, P. Forzatti, The Journal of … 105 (2001) 12732.

[35] H. Abdulhamid, E. Fridell, J. Dawody, M. Skoglundh, Journal of Catalysis 241 (2006) 200.

[36] C. Sedlmair, K. Seshan, A. Jentys, J.. Lercher, Catalysis Today 75 (2002) 413.

[37] W.S. Epling, C.H.F. Peden, J. Szanyi, The Journal of Physical Chemistry C 112 (2008) 10952.

[38] W. Bogner, M. Kramer, B. Krutzsch, S. Pischinger, D. Voigtlagnder, G. Wenninger, F. Wirbeleit, M.S. Brogan, R.J. Brisley, D.E. Webster, Applied Catalysis B: Environmental 7 (1995) 153.

[39] L. Lietti, P. Forzatti, I. Nova, E. Tronconi, Journal of Catalysis 204 (2001) 175.

[40] F. Prinetto, G. Ghiotti, I. Nova, L. Castoldi, L. Lietti, E. Tronconi, P. Forzatti, Physical Chemistry Chemical Physics 5 (2003) 4428.

[41] E. Fridell, H. Persson, L. Olsson, M. Skoglundh, Catalysis Letters 66 (2000) 71.

[42] P. Forzatti, L. Castoldi, I. Nova, L. Lietti, E. Tronconi, Catalysis Today 117 (2006) 316.

[43] P.T. Fanson, M.R. Horton, W.N. Delgass, J. Lauterbach, Applied Catalysis B: Environmental 46 (2003) 393.

[44] F. Rodrigues, L. Juste, C. Potvin, J.F. Tempère, G. Blanchard, G. Djéga-mariadassou, Catalysis Letters 72 (2001) 59.

[45] S. Balcon, C. Potvin, L. Salin, J.F. Tempere, G. Djéga-Mariadassou, Catalysis Letters 60 (1999) 39.

[46] H. Mahzoul, J.F. Brilhac, P. Gilot, Applied Catalysis B: Environmental 20 (1999) 47.

[47] P. Broqvist, I. Panas, H. Gro, The Journal of Physical Chemistry B 109 (2005) 9613.

[48] C. Yi, J. Szanyi, The Journal of Physical Chemistry C 113 (2009) 2134.

[49] C.-W. Yi, J.H. Kwak, J. Szanyi, Journal of Physical Chemistry C 111 (2007) 15299.

[50] A. Desikusumastuti, Z. Qin, M. Happel, T. Staudt, Y. Lykhach, M. Laurin, F. Rohr, S. Shaikhutdinov, J. Libuda, Physical Chemistry Chemical Physics 11 (2009) 2514.

[51] A. Desikusumastuti, T. Staudt, M. Happel, M. Laurin, J. Libuda, Journal of Catalysis 260 (2008) 315.

[52] A. Desikusumastuti, T. Staudt, Z. Qin, M. Happel, M. Laurin, Y. Lykhach, S. Shaikhutdinov, F. Rohr, J. Libuda, Chemphyschem : a European Journal of Chemical Physics and Physical Chemistry 9 (2008) 2191.

[53] W.F. Schneider, K.C. Hass, M. Miletic, J.L. Gland, The Journal of Physical Chemistry B 106 (2002) 7405.

[54] M. Miletic, J.L. Gland, K.C. Hass, W.F. Schneider, The Journal of Physical Chemistry B 107 (2003) 157.

[55] L. Olsson, H. Persson, E. Fridell, M. Skoglundh, B. Andersson, The Journal of Physical Chemistry B 105 (2001) 6895.

[56] L. Olsson, E. Fridell, Journal of Catalysis 210 (2002) 340.

[57] H. Yoshida, Y. Yazawa, N. Takagi, A. Satsuma, T. Tanaka, S. Yoshida, T. Hattori, Journal of Synchrotron Radiation 6 (1999) 471.

[58] M. Crocoll, S. Kureti, W. Weisweiler, Journal of Catalysis 229 (2005) 480.

[59] Z. Liu, J.A. Anderson, Journal of Catalysis 224 (2004) 18.

[60] I. Nova, L. Lietti, L. Castoldi, E. Tronconi, P. Forzatti, Journal of Catalysis 239 (2006) 244.

[61] K.S. Kabin, R.L. Muncrief, M.P. Harold, Catalysis Today 96 (2004) 79.

[62] E. Fridell, M. Skoglundh, B. Westerberg, S. Johansson, G. Smedler, Journal of Catalysis 183 (1999) 196.

[63] I. Nova, L. Lietti, P. Forzatti, Catalysis Today 136 (2008) 128.

[64] I. Nova, L. Lietti, P. Forzatti, F. Prinetto, G. Ghiotti, Catalysis Today 151 (2010) 330.

[65] S.S. Mulla, S.S. Chaugule, a. Yezerets, N.W. Currier, W.N. Delgass, F.H. Ribeiro, Catalysis Today 136 (2008) 136.

[66] A. Kumar, M.P. Harold, V. Balakotaiah, Journal of Catalysis 270 (2010) 214.

[67] R.D. Clayton, M.P. Harold, V. Balakotaiah, Applied Catalysis B: Environmental 84 (2008) 616.

[68] N. Cant, I. Liu, M. Patterson, Journal of Catalysis 243 (2006) 309.

[69] A. Lindholm, N. Currier, J. Li, A. Yezerets, L. Olsson, Journal of Catalysis 258 (2008) 273.

[70] D. Bhatia, R.D. Clayton, M.P. Harold, V. Balakotaiah, Catalysis Today 147 (2009) S250.

[71] Y. Sakamoto, K. Okumura, Y. Kizaki, S. Matsunaga, N. Takahashi, H. Shinjoh, Journal of Catalysis 238 (2006) 361.

[72] I. Nova, L. Castoldi, L. Lietti, E. Tronconi, P. Forzatti, Catalysis T 75 (2002) 431.

[73] L. Castoldi, I. Nova, L. Lietti, P. Forzatti, Catalysis Today 96 (2004) 43.

[74] U. Elizundia, R. López-Fonseca, I. Landa, M. a. Gutiérrez-Ortiz, J.R. González-Velasco, Topics in Catalysis 42-43 (2007) 37.

[75] V. Schmeißer, J. Riva Pérez, U. Tuttlies, G. Eigenberger, Topics in Catalysis 42-43 (2007) 15.

[76] J. Dawody, L. Eurenius, H. Abdulhamid, M. Skoglundh, E. Olsson, E. Fridell, Applied Catalysis A: General 296 (2005) 157.

[77] R.D. Clayton, M.P. Harold, V. Balakotaiah, C.Z. Wan, Applied Catalysis B: Environmental 90 (2009) 662.

[78] B.M. Shakya, M.P. Harold, V. Balakotaiah, Catalysis Today 184 (2012) 27.

[79] D. Bhatia, M.P. Harold, V. Balakotaiah, Catalysis Today 151 (2010) 314.

[80] B. Pereda-Ayo, R. López-Fonseca, J.R. González-Velasco, Applied Catalysis A: General 363 (2009) 73.

[81] U. Elizundia, R. Lopez-Fonseca, M.A. Gutiérrez-Ortiz, J.R. González-Velasco, Topics in Catalysis 52 (2009) 1808.

[82] D.H. Kim, Y. Chin, G.G. Muntean, A. Yezeretz, N.W. Currier, W.S. Epling, H. Chen, H. Hess, C.H.F. Peden, Industrial & Engineering Chemistry Research 45 (2006) 8815.

[83] J. Lee, H.H. Kung, Catalysis Letters 51 (1998) 1.

[84] E. Xue, K. Seshan, J.R.H. Ross, Applied Catalysis B: Environmental 11 (1996) 65.

[85] V. Medhekar, V. Balakotaiah, M. Harold, Catalysis Today 121 (2007) 226.

[86] J.A. Anderson, B. Bachiller-Baeza, M. Fernandez-Garcia, Physical Chemistry Chemical Physics 5 (2003) 4418.

[87] P. Schmitz, R. Kudla, a Drews, a Chen, C. Lowema, R. Mccabe, W. Schneider, C. Goralskijr, Applied Catalysis B: Environmental 67 (2006) 246.

[88] K. Otto, H.C. Yao, Journal of Catalysis 66 (1980) 229.

[89] G.S. Zafiris, R.J. Gorte, Journal of Catalysis 140 (1993) 418.

[90] S.M. Vesecky, P. Chen, X. Xu, W.D. Goodman, Journal of Vacuum Science & Technology 13 (1995) 1539.

[91] C.H.F. Peden, D.W. Goodman, D.S. Blair, P.J. Berlowitz, G.B. Fisher, S.H. Oh, The Journal of Physical Chemistry 92 (1988) 1563.

[92] P.J. Berlowitz, C.H.F. Peden, D.W. Goodman, The Journal of Physical Chemistry 92 (1988) 5213.

[93] T. Maunula, J. Ahola, H. Hamada, Applied Catalysis A: General 26 (2000) 173.

[94] J. Dawody, M. Skoglundh, S. Wall, E. Fridell, Journal of Molecular Catalysis A: Chemical 225 (2005) 259.

[95] A. Lindholm, N.W. Currier, J. Dawody, A. Hidayat, J. Li, A. Yezerets, L. Olsson, Applied Catalysis B: Environmental 88 (2009) 240.

[96] B. Pereda-Ayo, D. Divakar, R. López-Fonseca, J.R. González-Velasco, Catalysis Today 147 (2009) S244.

[97] R. Buchel, R. Strobel, F. Krumeich, a Baiker, S. Pratsinis, Journal of Catalysis 261 (2009) 201.

[98] R. Strobel, L. Madler, M. Piacentini, M. Maciejewski, A. Baiker, S.E. Pratsinis, Chemistry of Materials 18 (2006) 2532.

[99] R. Strobel, F. Krumeich, S. Pratsinis, a Baiker, Journal of Catalysis 243 (2006) 229.

[100] D.H. Kim, Y.-H. Chin, J.H. Kwak, C.H.F. Peden, Catalysis Letters 124 (2008) 39.

[101] J.H. Kwak, D.H. Kim, J. Szanyi, C.H.F. Peden, Applied Catalysis B: Environmental 84 (2008) 545.

[102] C. Sedlmair, K. Seshan, A. Jentys, J.A. Lercher, Research on Chemical Intermediates 29 (2003) 257.

[103] E. Fridell, H. Persson, L. Olsson, B. Westerberg, A. Amberntsson, M. Skoglundh, Topics in Catalysis 16/17 (2001) 133.

[104] A. Amberntsson, M. Skoglundh, M. Jonsson, E. Fridell, Catalysis Today 73 (2002) 279.

[105] P. Engström, a Amberntsson, M. Skoglundh, E. Fridell, G. Smedler, Applied Catalysis B: Environmental 22 (1999) L241.

[106] E. Fridell, A. Amberntsson, L. Olsson, A.W. Grant, M. Skoglundh, Topics in Catalysis 30/31 (2004) 143.

[107] Z. Liu, J. Anderson, Journal of Catalysis 228 (2004) 243.

[108] D.H. Kim, J.H. Kwak, J. Szanyi, S.J. Cho, C.H.F. Peden, The Journal of Physical Chemistry C 112 (2008) 2981.

[109] D.H. Kim, J.H. Kwak, J. Szanyi, X. Wang, G. Li, J.C. Hanson, C.H.F. Peden, Journal of Physical Chemistry C 113 (2009) 21123.

[110] D.H. Kim, J. Szanyi, J.H. Kwak, X. Wang, J.C. Hanson, M. Engelhard, C.H.F. Peden, The Journal of Physical Chemistry C 113 (2009) 7336.

[111] J. Dawody, M. Skoglundh, L. Olsson, E. Fridell, Journal of Catalysis 234 (2005) 206.

[112] Y. Su, K. Kabin, M. Harold, M. Amiridis, Applied Catalysis B: Environmental 71 (2007) 207.

[113] S. Salasc, M. Skoglundh, E. Fridell, Applied Catalysis B: Environmental 36 (2002) 145.

[114] B.M. Weiss, E. Iglesia, Journal of Catalysis 272 (2010) 74.

[115] B.M. Weiss, E. Iglesia, The Journal of Physical Chemistry C 113 (2009) 13331.

[116] T. Kolli, M. Huuhtanen, a. Hallikainen, K. Kallinen, R.L. Keiski, Catalysis Letters 127 (2008) 49.

[117] H.Y. Huang, R.Q. Long, R.T. Yang, Energy & Fuels 15 (2001) 205.

[118] R. Vijay, C. Snively, J. Lauterbach, Journal of Catalysis 243 (2006) 368.

[119] J.P. Breen, R. Burch, N. Lingaiah, Catalysis Letters 79 (2002) 171.

[120] J.C. Schlatter, K.C. Taylor, Journal of Catalysis 49 (1977) 42.

[121] H. Mahzoul, L. Limousy, J.. Brilhac, P. Gilot, Journal of Analytical and Applied Pyrolysis 56 (2000) 179.

[122] J.P. Breen, R. Burch, C.J. Hill, Catalysis Today 145 (2009) 34.

[123] K. Shimizu, J. Shibata, A. Satsuma, Journal of Catalysis 239 (2006) 402.

[124] A. Mihaylova, A. Naydenov, D. Kovacheva, E. Ivanova, D. Stoyanova, P. Stefanov, Catalysis Communications 10 (2009) 1288.

[125] R. Vijay, R.J. Hendershot, S.M. Rivera-Jiménez, W.B. Rogers, B.J. Feist, C.M. Snively, J. Lauterbach, Catalysis Communications 6 (2005) 167.

[126] R. Vijay, H. Sakurai, C.M. Snively, J. Lauterbach, Topics in Catalysis 52 (2009) 1388.

[127] J.-H. Park, H.J. Cho, S.J. Park, I.-S. Nam, G.K. Yeo, J.K. Kil, Y.K. Youn, Topics in Catalysis 42-43 (2007) 61.

[128] R.J. Hendershot, W.B. Rogers, C.M. Snively, B. a. Ogunnaike, J. Lauterbach, Catalysis Today 98 (2004) 375.

[129] R.J. Hendershot, R. Vijay, C.M. Snively, J. Lauterbach, Applied Catalysis B: Environmental 70 (2007) 160.

[130] Q. Wang, J.S. Chung, Applied Catalysis A: General 358 (2009) 59.

[131] Q. Wang, J. Zhu, S. Wei, J.S. Chung, Z. Guo, Industrial & Engineering Chemistry Research 49 (2010) 7330.

[132] J. Jelic, R.J. Meyer, Catalysis Today 136 (2008) 76.

[133] M. Haneda, T. Yoshinari, K. Sato, Y. Kintaichi, H. Hamada, Chemical Communications 12 (2003) 2814.

[134] C. Wogerbauer, M. Maciejewski, A. Baiker, U. Göbel, Journal of Catalysis 201 (2001) 113.

[135] J.-S. Choi, W.P. Partridge, M.J. Lance, L.R. Walker, J.A. Pihl, T.J. Toops, C.E. a. Finney, C.S. Daw, Catalysis Today 151 (2010) 354.

[136] V.Y. Prikhodko, K. Nguyen, J.-S. Choi, C.S. Daw, Applied Catalysis B: Environmental 92 (2009) 9.

[137] M. AL-Harbi, W.S. Epling, Applied Catalysis B: Environmental 89 (2009) 315.

[138] F. Rohr, U. Göbel, P. Kattwinkel, T. Kreuzer, W. Müller, S. Philipp, P. Gélin, Applied Catalysis B: Environmental 70 (2007) 189.

[139] Y. Ji, C. Fisk, V. Easterling, U. Graham, A. Poole, M. Crocker, J.-S. Choi, W. Partridge, K. Wilson, Catalysis Today 151 (2010) 362.

[140] Y. Ji, V. Easterling, U. Graham, C. Fisk, M. Crocker, J.-S. Choi, Applied Catalysis B: Environmental 103 (2011) 413.

[141] A. Amberntsson, E. Fridell, M. Skoglundh, Applied Catalysis B: Environmental 46 (2003) 429.

[142] C.K. Narula, S.R. Nakouzi, R. Wu, C.T.J. Goralski, L.F.J. Allard, Environmental and Energy Engineering 47 (2001) 744.

[143] H.N. Rabinowitz, S.J. Tauster, R.M. Heck, Applied Catalysis A: General 212 (2001) 215.

[144] H.Y. Huang, R.Q. Long, R.T. Yang, Applied Catalysis B: Environmental 33 (2001) 127.

[145] T. Lesage, C. Verrier, P. Bazin, J. Saussey, M. Daturi, Physical Chemistry Chemical Physics 5 (2003) 4435.

[146] T. Lesage, C. Verrier, P. Bazin, J. Saussey, S. Malo, C. Hedouin, G. Blanchard, M. Daturi, Topics in Catalysis 30/31 (2004) 31.

[147] P. Koci, M. Kubicek, M. Marek, Chemical Engineering Research and Design 82 (2004) 284.

[148] L. Olsson, R.J. Blint, E. Fridell, Industrial & Engineering Chemistry Research 44 (2005) 3021.

[149] T.J. Toops, B.G. Bunting, K. Nguyen, A. Gopinath, Catalysis Today 123 (2007) 285.

[150] Y. Ji, T.J. Toops, M. Crocker, Catalysis Letters 119 (2007) 257.

[151] Y. Ji, J.-S. Choi, T.J. Toops, M. Crocker, M. Naseri, Catalysis Today 136 (2008) 146.

[152] V. Schmeißer, U. Tuttlies, G. Eigenberger, Topics in Catalysis 42-43 (2007) 77.

[153] J.-G. Kim, H.-M. Lee, M.-J. Lee, J.-H. Lee, J.-G. Kim, J.-Y. Jeon, S.-K. Jeong, S.-J. Yoo, S.-S. Kim, Journal of Industrial and Engineering Chemistry 14 (2008) 841.

[154] E.C. Corbos, M. Haneda, X. Courtois, P. Marecot, D. Duprez, H. Hamada, Applied Catalysis A: General 365 (2009) 187.

[155] H. Imagawa, T. Tanaka, N. Takahashi, S. Matsunaga, A. Suda, H. Shinjoh, Applied Catalysis B: Environmental 86 (2009) 63.

[156] D. Chatterjee, P. Kočí, V. Schmeißer, M. Marek, M. Weibel, B. Krutzsch, Catalysis Today 151 (2010) 395.

[157] J.B. Park, J.S. Ratliff, S. Ma, D. a. Chen, Surface Science 600 (2006) 2913.

[158] O. Ozturk, J.B. Park, S. Ma, J.S. Ratliff, J. Zhou, D.R. Mullins, D. a. Chen, Surface Science 601 (2007) 3099.

[159] J.B. Park, J.S. Ratliff, S. Ma, D.A. Chen, The Journal of Physical Chemistry C 111 (2007) 2165.

[160] M. Takeuchi, S. Matsumoto, Topics in Catalysis 28 (2004) 151.

[161] M. Piacentini, M. Maciejewski, A. Baiker, Applied Catalysis B: Environmental 59 (2005) 187.

[162] T. Szailer, J.H. Kwak, D.H. Kim, J. Szanyi, C. Wang, C.H.F. Peden, Catalysis Today 114 (2006) 86.

[163] F. Basile, G. Fornasari, a. Gambatesa, M. Livi, a. Vaccari, Catalysis Today 119 (2007) 59.

[164] S.M. Park, J.W. Park, H.-P. Ha, H.-S. Han, G. Seo, Journal of Molecular Catalysis A: Chemical 273 (2007) 64.

[165] F. Prinetto, M. Manzoli, S. Morandi, F. Frola, G. Ghiotti, L. Castoldi, L. Lietti, P. Forzatti, Journal of Physical Chemistry C 114 (2010) 1127.

[166] J.-J. He, M. Meng, Z.-Q. Zou, X.-X. He, Catalysis Letters 136 (2010) 234.

[167] H. Iizuka, M. Kaneeda, N. Shinotsuka, O. Kuroda, K. Higashiyama, A. Miyamoto, Applied Catalysis B: Environmental 95 (2010) 320.

[168] S. Roy, N. van Vegten, A. Baiker, Journal of Catalysis 271 (2010) 125.

[169] A.L. Kustov, M. Makkee, Applied Catalysis B: Environmental 88 (2009) 263.

[170] F. Basile, G. Fornasari, a. Grimandi, M. Livi, a. Vaccari, Applied Catalysis B: Environmental 69 (2006) 58.

[171] A.L. Kustov, F. Ricciardi, M. Makkee, Topics in Catalysis 52 (2009) 2058.

[172] C.H. Kim, G. Qi, K. Dahlberg, W. Li, Science 327 (2010) 1624.

[173] M. Machida, N. Masuda, T. Kijima, Journal of Materials Chemistry 9 (1999) 1369.

[174] M. Kaneeda, H. Iizuka, T. Hiratsuka, N. Shinotsuka, Y. Kitahara, M. Arai, Chemical Engineering Journal 160 (2010) 93.

[175] B. Bahrami, V.G. Komvokis, U.G. Singh, M.S. Ziebarth, O.S. Alexeev, M.D. Amiridis, Applied Catalysis A: General 391 (2011) 11.

[176] O.S. Alexeev, S. Krishnamoorthy, C. Jensen, M.S. Ziebarth, G. Yaluris, T.G. Roberie, M.D. Amiridis, Catalysis Today 127 (2007) 189.

[177] O.S. Alexeev, S. Krishnamoorthy, M.S. Ziebarth, G. Yaluris, T.G. Roberie, M.D. Amiridis, Catalysis Today 127 (2007) 176.

[178] D. Mei, J.H. Kwak, J. Szanyi, Q. Ge, C.H.F. Peden, Catalysis Today 151 (2010) 304.

[179] F. Frola, M. Manzoli, F. Prinetto, G. Ghiotti, L. Castoldi, L. Lietti, The Journal of Physical Chemistry C 112 (2008) 12869.

[180] M. Casapu, J.-D. Grunwaldt, M. Maciejewski, M. Wittrock, U. Göbel, A. Baiker, Applied Catalysis B: Environmental 63 (2006) 232.

[181] W.S. Epling, G.C. Campbell, J.E. Parks, Catalysis Letters 90 (2003) 45.

[182] A. Lindholm, N. Currier, E. Fridell, A. Yezerets, L. Olsson, Applied Catalysis B: Environmental 75 (2007) 78.

[183] A. Amberntsson, H. Persson, P. Engström, B. Kasemo, Applied Catalysis B: Environmental 31 (2001) 27.

[184] P. Broqvist, I. Panas, E. Fridell, H. Persson, The Journal of Physical Chemistry B 106 (2002) 137.

[185] H. Grönbeck, P. Broqvist, I. Panas, Surface Science 600 (2006) 403.

[186] G. Zhou, T. Luo, R.J. Gorte, Applied Catalysis B: Environmental 64 (2006) 88.

[187] J. Szanyi, J.H. Kwak, D.H. Kim, X. Wang, J. Hanson, R.J. Chimentao, C.H.F. Peden, Chemical Communications (Cambridge, England) (2007) 984.

[188] J. Szanyi, J.H. Kwak, D.H. Kim, S.D. Burton, C.H.F. Peden, The Journal of Physical Chemistry B: Letters 109 (2005) 27.

[189] S. Hodjati, P. Bernhardt, C. Petit, V. Pitchon, A. Kiennemann, Applied Catalysis B: Environmental 19 (1998) 209.

[190] S. Hodjati, P. Bernhardt, C. Petit, V. Pitchon, A. Kiennemann, Applied Catalysis B: Environmental 19 (1998) 221.

[191] J. Szanyi, J.H. Kwak, D.H. Kim, X. Wang, R. Chimentao, J. Hanson, W.S. Epling, C.H.F. Peden, The Journal of Physical Chemistry C 111 (2007) 4678.

[192] D.H. Kim, Y.-H. Chin, J.H. Kwak, J. Szanyi, C.H.F. Peden, Catalysis Letters 105 (2005) 259.

[193] J. Szanyi, J.H. Kwak, J. Hanson, C. Wang, T. Szailer, C.H.F. Peden, The Journal of Physical Chemistry. B 109 (2005) 7339.

[194] J.A. Anderson, Z. Liu, M.F. García, Catalysis Today 113 (2006) 25.

[195] J. Dawody, M. Skoglundh, L. Olsson, E. Fridell, Applied Catalysis B: Environmental 70 (2007) 179.

[196] M. Happel, A. Desikusumastuti, M. Sobota, M. Laurin, J. Libuda, The Journal of Physical Chemistry C 114 (2010) 4568.

[197] E. Schreier, R. Eckelt, M. Richter, R. Fricke, Catalysis Communications 6 (2005) 409.

[198] T.J. Toops, D.B. Smith, W.P. Partridge, Catalysis Today 114 (2006) 112.

[199] J.-S. Choi, W.P. Partridge, W.S. Epling, N.W. Currier, T.M. Yonushonis, Catalysis Today 114 (2006) 102.

[200] R. Matarrese, L. Castoldi, L. Lietti, Catalysis Today 197 (2012) 228.

[201] C. Paze, G. Gubitosa, S.O. Giacone, G. Spoto, F.X. Llabres i Xamena, A. Zecchina, Topics in Catalysis 30/31 (2004) 169.

[202] L. Castoldi, L. Lietti, I. Nova, R. Matarrese, P. Forzatti, F. Vindigni, S. Morandi, F. Prinetto, G. Ghiotti, Chemical Engineering Journal 161 (2010) 416.

[203] T.J. Toops, D.B. Smith, W.P. Partridge, Applied Catalysis B: Environmental 58 (2005) 245.

[204] T.J. Toops, D.B. Smith, W.S. Epling, J.E. Parks, W.P. Partridge, Applied Catalysis B: Environmental 58 (2005) 255.

[205] T. Lesage, J. Saussey, S. Malo, M. Hervieu, C. Hedouin, G. Blanchard, M. Daturi, Applied Catalysis B: Environmental 72 (2007) 166.

[206] Y. Liu, M. Meng, Z. Zou, X. Li, Y. Zha, Catalysis Communications 10 (2008) 173.

[207] Y. Liu, M. Meng, X.-G. Li, L.-H. Guo, Y.-Q. Zha, Chemical Engineering Research and Design 86 (2008) 932.

[208] I.S. Pieta, M. García-Diéguez, C. Herrera, M. a. Larrubia, L.J. Alemany, Journal of Catalysis 270 (2010) 256.

[209] R. Matarrese, L. Castoldi, L. Lietti, P. Forzatti, Topics in Catalysis 42-43 (2007) 293.

[210] R. Matarrese, L. Castoldi, L. Lietti, P. Forzatti, Topics in Catalysis 52 (2009) 2041.

[211] Y. Sakamoto, S. Matsunaga, K. Okumura, T. Kayama, K. Yamazaki, N. Takahashi, T. Tanaka, Y. Kizaki, T. Motohiro, H. Shinjoh, Chemical Engineering Science 63 (2008) 5028.

[212] T.J. Toops, J.A. Pihl, Catalysis Today 136 (2008) 164.

[213] H. Imagawa, N. Takahashi, T. Tanaka, S. Matsunaga, H. Shinjoh, Applied Catalysis B: Environmental 92 (2009) 23.

[214] Z.-Q. Zou, M. Meng, X.-Y. Zhou, X.-G. Li, Y.-Q. Zha, Catalysis Letters 128 (2008) 475.

[215] H. Imagawa, T. Tanaka, N. Takahashi, S. Matsunaga, a Suda, H. Shinjoh, Journal of Catalysis 251 (2007) 315.

[216] Z.-Q. Zou, M. Meng, N. Tsubaki, J.-J. He, G. Wang, X.-G. Li, X.-Y. Zhou, Journal of Hazardous Materials 170 (2009) 118.

[217] N. Takahashi, S. Matsunaga, T. Tanaka, H. Sobukawa, H. Shinjoh, Applied Catalysis B: Environmental 77 (2007) 73.

[218] V.G. Milt, M.L. Pissarello, E.E. Miró, C.A. Querini, Applied Catalysis B: Environmental 41 (2003) 397.

[219] M. Harada, T. Mori, S. Awatsu, Research on Chemical Intermediates 29 (2003) 749.

[220] N. MacLeod, F.J. Williams, M.S. Tikhov, R.M. Lambert, Angewandte Chemie (International Ed. in English) 44 (2005) 3730.

[221] A. Gao, X. Zhu, H. Wang, J. Tu, P. Lin, Y. Torimoto, M. Sadakata, Q. Li, The Journal of Physical Chemistry. B 110 (2006) 11854.

[222] A. de Lucas-Consuegra, A. Caravaca, M.J. Martín de Vidales, F. Dorado, S. Balomenou, D. Tsiplakides, P. Vernoux, J.L. Valverde, Catalysis Communications 11 (2009) 247.

[223] Q. Wang, J.H. Sohn, J.S. Chung, Applied Catalysis B: Environmental 89 (2009) 97.

[224] K. Shimizu, Y. Saito, T. Nobukawa, N. Miyoshi, A. Satsuma, Catalysis Today 139 (2008) 24.

[225] E.C. Corbos, X. Courtois, N. Bion, P. Marecot, D. Duprez, Applied Catalysis B: Environmental 76 (2007) 357.

[226] M. Piacentini, M. Maciejewski, T. Bu, A. Baiker, Topics in Catalysis 30/31 (2004) 71.

[227] M. Piacentini, M. Maciejewski, a. Baiker, Applied Catalysis B: Environmental 66 (2006) 126.

[228] M. Piacentini, M. Maciejewski, a. Baiker, Applied Catalysis B: Environmental 72 (2007) 105.

[229] L. Cheng, Q. Ge, Surface Science 601 (2007) L65.

[230] N. Maeda, A. Urakawa, A. Baiker, The Journal of Physical Chemistry C 113 (2009) 16724.

[231] D. Martin, D. Duprez, Journal of Molecular Catalysis A: Chemical 118 (1997) 113.

[232] M. Casapu, J. Grunwaldt, M. Maciejewski, a Baiker, S. Eckhoff, U. Gobel, M. Wittrock, Journal of Catalysis 251 (2007) 28.

[233] M. Casapu, J.-D. Grunwaldt, M. Maciejewski, A. Baiker, R. Hoyer, M. Wittrock, S. Eckhoff, Catalysis Letters 120 (2007) 1.

[234] M. Yang, Y. Li, J. Wang, M. Shen, Journal of Catalysis 271 (2010) 228.

[235] P. Svedberg, E. Jobson, S. Erkfeldt, B. Andersson, M. Larsson, M. Skoglundh, Topics in Catalysis 30/31 (2004) 199.

[236] S. Philipp, A. Drochner, J. Kunert, H. Vogel, J. Theis, E.S. Lox, Topics in Catalysis 30/31 (2004) 235.

[237] M.O. Symalla, a. Drochner, H. Vogel, S. Philipp, U. Göbel, W. Müller, Topics in Catalysis 42-43 (2007) 199.

[238] K. Yamamoto, R. Kikuchi, T. Takeguchi, K. Eguchi, Journal of Catalysis 238 (2006) 449.

[239] C. Hess, J.H. Lunsford, The Journal of Physical Chemistry B 107 (2003) 1982.

[240] N. Takahashi, A. Suda, I. Hachisuka, M. Sugiura, H. Sobukawa, H. Shinjoh, Applied Catalysis B: Environmental 72 (2007) 187.

[241] E.C. Corbos, X. Courtois, N. Bion, P. Marecot, D. Duprez, Applied Catalysis B: Environmental 80 (2008) 62.

[242] E.C. Corbos, S. Elbouazzaoui, X. Courtois, N. Bion, P. Marecot, D. Duprez, Topics in Catalysis 42-43 (2007) 9.

[243] N. Le Phuc, E.C. Corbos, X. Courtois, F. Can, P. Marecot, D. Duprez, Applied Catalysis B: Environmental 93 (2009) 12.

[244] L.F. Liotta, A. Macaluso, G.E. Arena, M. Livi, G. Centi, G. Deganello, Catalysis Today 75 (2002) 439.

[245] S.M. Andonova, G.S. Senturk, E. Kayhan, E. Ozensoy, The Journal of Physical Chemistry C 113 (2009) 11014.

[246] G. Centi, G. Fornasari, C. Gobbi, M. Livi, F. Trifirò, A. Vaccari, Catalysis Today 73 (2002) 287.

[247] F. Basile, G. Fornasari, M. Livi, F. Tinti, F. Trifirò, A. Vaccari, Topics in Catalysis 30/31 (2004) 223.

[248] G. Fornasari, R. Glöckler, M. Livi, A. Vaccari, Applied Clay Science 29 (2005) 258.

[249] S. Morandi, F. Prinetto, G. Ghiotti, M. Livi, A. Vaccari, Microporous and Mesoporous Materials 107 (2008) 31.

[250] J.J. Yu, Z. Jiang, L. Zhu, Z.P. Hao, Z.P. Xu, The Journal of Physical Chemistry. B 110 (2006) 4291.

[251] L.D. Li, J.J. Yu, Z.P. Hao, Z.P. Xu, Journal of Physical Chemistry C 111 (2007) 10552.

[252] J.J. Yu, J. Cheng, C.Y. Ma, H.L. Wang, L.D. Li, Z.P. Hao, Z.P. Xu, Journal of Colloid and Interface Science 333 (2009) 423.

[253] a. E. Palomares, a. Uzcátegui, a. Corma, Catalysis Today 137 (2008) 261.

[254] X. Li, J. Chen, P. Lin, M. Meng, Y. Fu, J. Tu, Q. Li, Catalysis Communications 5 (2004) 25.

[255] Y. Zhu, D. Wang, F. Yuan, G. Zhang, H. Fu, Applied Catalysis B: Environmental 82 (2008) 255.

[256] A. Ueda, Y. Yamada, M. Katsuki, T. Kiyobayashi, Q. Xu, N. Kuriyama, Catalysis Communications 11 (2009) 34.

[257] H. Xian, X. Zhang, X. Li, L. Li, H. Zou, M. Meng, Q. Li, Y. Tan, N. Tsubaki, The Journal of Physical Chemistry C 114 (2010) 11844.

[258] J. Li, W. Li, L. Wei, R.T. Yang, Catalysis Letters 129 (2009) 104.

[259] L. Wei, J. Li, X. Tang, Catalysis Letters 127 (2008) 107.

[260] J. Goscianska, P. Bazin, O. Marie, M. Daturi, I. Sobczak, M. Ziolek, Catalysis Today 119 (2007) 78.

[261] M.A. Gómez-García, V. Pitchon, A. Kiennemann, Catalysis Today 107-108 (2005) 60.

[262] M. Machida, D. Kurogi, T. Kijima, Catalysis Today 84 (2003) 201.

[263] U. Bentrup, A. Brückner, M. Richter, R. Fricke, Applied Catalysis B: Environmental 32 (2001) 229.

[264] K. Eguchi, T. Kondo, T. Hayashi, H. Arai, Applied Catalysis B: Environmental 16 (1998) 69.

[265] M. Labaki, M. Issa, S. Smeekens, S. Heylen, C.E. a. Kirschhock, K. Villani, M. Jeguirim, D. Habermacher, J.F. Brilhac, J. a. Martens, Applied Catalysis B: Environmental 97 (2010) 13.

[266] H. Lin, C. Wu, Y. Chen, C. Lee, Industrial & Engineering Chemistry Research 45 (2006) 134.

[267] Y. Ji, T.J. Toops, M. Crocker, Catalysis Letters 127 (2008) 55.

[268] V. Easterling, Y. Ji, M. Crocker, J. Ura, J.R. Theis, R.W. McCabe, Catalysis Today 151 (2010) 338.

[269] K. Yamazaki, T. Suzuki, N. Takahashi, K. Yokota, M. Sugiura, Applied Catalysis B: Environmental 30 (2001) 459.

[270] G.E. Arena, A. Bianchini, G. Centi, F. Vazzana, Topics in Catalysis 16/17 (2001) 157.

[271] S. Hammache, L.R. Evans, E.N. Coker, J.E. Miller, Applied Catalysis B: Environmental 78 (2008) 315.

[272] R.J. Hendershot, R. Vijay, C.M. Snively, J. Lauterbach, Chemical Engineering Science 61 (2006) 3907.

[273] P.N. Lê, E.C. Corbos, X. Courtois, F. Can, S. Royer, P. Marecot, D. Duprez, Topics in Catalysis 52 (2009) 1771.

[274] E. Kayhan, S.M. Andonova, G.S. Senturk, C.C. Chusuei, E. Ozensoy, The Journal of Physical Chemistry C 114 (2010) 357.

[275] J.-Y. Luo, M. Meng, Y.-Q. Zha, Y.-N. Xie, T.-D. Hu, J. Zhang, T. Liu, Applied Catalysis B: Environmental 78 (2008) 38.

[276] J. Dawody, M. Skoglundh, E. Fridell, Journal of Molecular Catalysis A: Chemical 209 (2004) 215.

[277] J. Xiao, X. Li, S. Deng, F. Wang, L. Wang, Catalysis Communications 9 (2008) 563.

[278] S. Deng, X. Li, J. Xiao, F. Wang, L. Wang, Journal of Natural Gas Chemistry 16 (2007) 213.

[279] J. Kašpar, P. Fornasiero, N. Hickey, Catalysis Today 77 (2003) 419.

[280] M. Shelef, R.. McCabe, Catalysis Today 62 (2000) 35.

[281] H. Gandhi, Journal of Catalysis 216 (2003) 433.

[282] O. Guralp, G. Qi, W. Li, P. Najt, (2011-01-0307), Society of Automotive Engineers (SAE) (2011).

[283] L. Xu, R.W. McCabe, Catalysis Today 184 (2012) 83.

[284] T. V Johnson, International Journal of Engine Research 10 (2009) 275.

[285] N. Miyoshi, S. Matsumoto, K. Katoh, T. Tanaka, J. Harada, N. Takahashi, K. Yokota, M. Sugiura, K. Kasahara, (950809), Society of Automotive Engineers (SAE) (1995).

[286] L. Cumaranatunge, S. Mulla, a Yezerets, N. Currier, W. Delgass, F. Ribeiro, Journal of Catalysis 246 (2007) 29.

[287] Y. Ji, T.J. Toops, J.A. Pihl, M. Crocker, Applied Catalysis B: Environmental 91 (2009) 329.

[288] J.-Y. Luo, W.S. Epling, Applied Catalysis B: Environmental 97 (2010) 236.

[289] I. Nova, L. Lietti, P. Forzatti, F. Frola, F. Prinetto, G. Ghiotti, Topics in Catalysis 52 (2009) 1757.

[290] P. Forzatti, L. Lietti, I. Nova, S. Morandi, F. Prinetto, G. Ghiotti, Journal of Catalysis 274 (2010) 163.

[291] D. Lorimer, A.T. Bell, Journal of Catalysis 59 (1979) 223.

[292] W.C. Hecker, A.T. Bell, Journal of Catalysis 85 (1984) 389.

[293] B.K. Cho, B.H. Shanks, J.E. Bailey, Journal of Catalysis 115 (1989) 486.

[294] R. Krishnamurthy, S.S.C. Chuang, M.W. Balakos, Journal of Catalysis 157 (1995) 512.

[295] P. Granger, C. Dujardin, J.-F. Paul, G. Leclercq, Journal of Molecular Catalysis A: Chemical 228 (2005) 241.

[296] D.K. Captain, K.L. Roberts, M.D. Amiridis, Catalysis Today 42 (1998) 93.

[297] F.C. Meunier, J.P. Breen, V. Zuzaniuk, M. Olsson, J.R.H. Ross, Journal of Catalysis 187 (1999) 493.

[298] D.K. Captain, M.D. Amiridis, Journal of Catalysis 184 (1999) 377.

[299] D.K. Captain, M.D. Amiridis, Journal of Catalysis 194 (2000) 222.

[300] D.K. Captain, C. Mihut, J.A. Dumesic, M.D. Amiridis, Catalysis Letters 83 (2002) 109.

[301] N. Macleod, R.M. Lambert, Applied Catalysis B: Environmental 46 (2003) 483.

[302] N. Bion, J. Saussey, M. Haneda, M. Daturi, Journal of Catalysis 217 (2003) 47.

[303] N.W. Cant, D.C. Chambers, I.O.Y. Liu, Applied Catalysis B: Environmental 46 (2003) 551.

[304] F. Thibault-Starzyk, E. Seguin, S. Thomas, M. Daturi, H. Arnolds, D. a King, Science 324 (2009) 1048.

[305] R. Dümpelmann, N.W. Cant, A.D. Cowan, Studies in Surface Science and Catalysis 101 (1996) 1175.

[306] J.E. Benson, M. Boudart, Journal of Catalysis 4 (1965) 704.

[307] D.J. O'Rear, D.G. Loffler, M. Boudart, Journal of Catalysis 121 (1990) 131.

[308] S.S. Chaugule, A. Yezerets, N.W. Currier, F.H. Ribeiro, W.N. Delgass, Catalysis Today 151 (2010) 291.

[309] Y. Saito, K. Shimizu, T. Nobukawa, A. Satsuma, Topics in Catalysis 53 (2010) 584.

[310] M. Primet, J.M. Basset, M.V. Mathieu, M. Prettre, Journal of Catalysis 29 (1973) 213.

[311] H. Steininger, S. Lehwald, H. Ibach, Surface Science 123 (1982) 264.

[312] S.H. Cho, J.S. Park, S.H. Choi, S.K. Lee, S.H. Kim, Catalysis Letters 103 (2005) 257.

[313] C.K. Costello, M.C. Kung, H.-S. Oh, Y. Wand, H.H. Kung, Applied Catalysis A: General 232 (2002) 168.

[314] F. Solymosi, L. Volgyesi, J. Sarkany, Journal of Catalysis 54 (1978) 336.

[315] H. Arai, H. Tominaga, Journal of Catalysis 43 (1976) 131.

[316] M.L. Unland, The Journal of Physical Chemistry 79 (1975) 610.

[317] F. Acke, B. Westerberg, M. Skoglundh, Journal of Catalysis 179 (1998) 528.

[318] D. Kondarides, Journal of Catalysis 193 (2000) 303.

[319] C. Scholz, V. Gangwal, M. Decroon, J. Schouten, Applied Catalysis B: Environmental 71 (2007) 143.

[320] C.M.L. Scholz, V.R. Gangwal, J.H.B.J. Hoebink, J.C. Schouten, Applied Catalysis B: Environmental 70 (2007) 226.

[321] P.L.T. Gabrielsson, Topics in Catalysis 28 (2004) 177.

[322] J.R. Theis, E. Gulari, (2006-01-0210), Society of Automotive Engineers (SAE) (2006).

[323] R. Snow, D. Dobson, R. Hammerle, S. Katare, (2007-01-0469), Society of Automotive Engineers (SAE) (2007).

[324] L. Xu, R. Mccabe, W. Ruona, G. Cavataio, (2009-01-0285), Society of Automotive Engineers (SAE) (2009).

[325] L. Xu, R. Mccabe, M. Dearth, W. Ruona, (2010-01-0305), Society of Automotive Engineers (SAE) (2010).

[326] H. Shinjoh, N. Takahashi, K. Yokota, Topics in Catalysis 42-43 (2007) 215.

[327] T. Nakatsuji, M. Matsubara, J. Rouistenmäki, N. Sato, H. Ohno, Applied Catalysis B: Environmental 77 (2007) 190.

[328] E. Corbos, M. Haneda, X. Courtois, P. Marecot, D. Duprez, H. Hamada, Catalysis Communications 10 (2008) 137.

[329] P. Forzatti, L. Lietti, I. Nova, E. Tronconi, Catalysis Today 151 (2010) 202.

[330] R. Bonzi, L. Lietti, L. Castoldi, P. Forzatti, Catalysis Today 151 (2010) 376.

[331] P. Forzatti, L. Lietti, Catalysis Today 155 (2010) 131.

[332] L. Castoldi, R. Bonzi, L. Lietti, P. Forzatti, S. Morandi, G. Ghiotti, S. Dzwigaj, Journal of Catalysis 282 (2011) 128.

[333] Y. Liu, M.P. Harold, D. Luss, Applied Catalysis B: Environmental 121-122 (2012) 239.

[334] J. Wang, Y. Ji, Z. He, M. Crocker, M. Dearth, R.W. McCabe, Applied Catalysis B: Environmental 111-112 (2012) 562.

[335] J. Wang, M. Crocker, Catalysis Letters 142 (2012) 1167.

[336] H.S. Gandhi, J.V. Cavataio, R.H. Hammerle, Y. Cheng., U.S.P. 7332135, (2002).

[337] H.S. Gandhi, J.V. Cavataio, R.H. Hammerle, Y. Cheng, U.S.P. 7485273, (2009).

[338] A. Lindholm, H. Sjövall, L. Olsson, Applied Catalysis B: Environmental 98 (2010) 112.

[339] C.D. DiGiulio, V.G. Komvokis, M.D. Amiridis, Catalysis Today 184 (2012) 8.

[340] Y. Ren, M.P. Harold, ACS Catalysis 1 (2011) 969.

[341] A. Grossale, I. Nova, E. Tronconi, Catalysis Today 136 (2008) 18.

[342] S.J. Schmieg, S.H. Oh, C.H. Kim, D.B. Brown, J.H. Lee, C.H.F. Peden, D.H. Kim, Catalysis Today 184 (2012) 252.

[343] J. Baik, S. Yim, I. Nam, Y. Mok, J. Lee, B. Cho, S. Oh, Topics in Catalysis 30/31 (2004) 37.

[344] J.H. Kwak, D. Tran, S.D. Burton, J. Szanyi, J.H. Lee, C.H.F. Peden, Journal of Catalysis 287 (2012) 203.

[345] Http://www.cleers.org/ (2012).

[346] J.-S. Choi, W.P. Partridge, J.A. Pihl, M.-Y. Kim, P. Kočí, C.S. Daw, Catalysis Today 184 (2012) 20.

[347] W. Li, General Motors “Personal Communication” (2012).

[348] W.S. Epling, A. Yezerets, N.W. Currier, Applied Catalysis B: Environmental 74 (2007) 117.

[349] U. Elizundia, D. Duraiswami, B. Pereda-Ayo, R. López-Fonseca, J.R. González-Velasco, Catalysis Today 176 (2011) 324.

[350] R.D. Clayton, M.P. Harold, V. Balakotaiah, Applied Catalysis B: Environmental 81 (2008) 161.

[351] J.A. Pihl, J.E. Parks, C.S. Daw, T.W. Root, (2006-01-3441), Society of Automotive Engineers (SAE) (2006).

[352] B. Pereda-Ayo, J.R. González-Velasco, R. Burch, C. Hardacre, S. Chansai, Journal of Catalysis 285 (2012) 177.

[353] J.P. Breen, C. Rioche, R. Burch, C. Hardacre, F.C. Meunier, Applied Catalysis B: Environmental 72 (2007) 178.

[354] M. AL-Harbi, W.S. Epling, Catalysis Today 151 (2010) 347.

[355] C. Resini, L. Arrighi, M. Concepcionherreradelgado, M. Angeleslarrubiavargas, L. Alemany, P. Riani, S. Berardinelli, R. Marazza, G. Busca, International Journal of Hydrogen Energy 31 (2006) 13.

[356] J. Wang, Y. Ji, V. Easterling, M. Crocker, M. Dearth, R.W. McCabe, Catalysis Today 175 (2011) 83.

[357] W. Li, K.L. Perry, K. Narayanaswamy, C.H. Kim, P. Najt, (2010-01-0366), Society of Automotive Engineers (SAE) (2010).

[358] C.H. Kim, K. Perry, M. Viola, W. Li, K. Narayanaswamy, (2011-01-0306), Society of Automotive Engineers (SAE) (2011).

[359] T. Johnson, Platinum Metals Review 52 (2008) 23.

[360] S. Brandenberger, O. Kröcher, A. Tissler, R. Althoff, The State of the Art in Selective Catalytic Reduction of NO x by Ammonia Using Metal□Exchanged Zeolite Catalysts, 2008.

[361] C.L. Marshall, M.K. Neylon, US Patent 7220692, (2007).

[362] K. Ramanathan, C.S. Sharma, C.H. Kim, Industrial & Engineering Chemistry Research 51 (2012) 1198.

[363] S.K. Rao, R. Imam, K. Ramanathan, S. Pushpavanam, Industrial & Engineering Chemistry Research 48 (2009) 3779.

[364] K. Ramanathan, C.S. Sharma, Industrial & Engineering Chemistry Research 50 (2011) 9960.

[365] K. Okumura, T. Motohiro, Y. Sakamoto, H. Shinjoh, Surface Science 603 (2009) 2544.

[366] M. Takei, H. Matsuda, Y. Itaya, S. Deguchi, K. Nakano, K. Nagahashi, M. Yoshino, J. Shibata, M. Hasatani, Fuel 77 (1998) 1027.

[367] H.J. Kwon, J. Hyun Baik, Y. Tak Kwon, I.-S. Nam, S.H. Oh, Chemical Engineering Science 62 (2007) 5042.

[368] S.H. Cadle, P.A. Mulawa, Environmental Science & Technology 14 (1980) 718.

[369] R.C. Shores, J.T. Walker Jr., L.G. Jones, M.O. Rodgers, J.R. Pearson, R.B. McCulloch, (2001-01-3538), Society of Automotive Engineers (SAE) (2001).

[370] T.D. Durbin, R.D. Wilson, J.M. Norbeck, J.W. Miller, T. Huai, S.H. Rhee, Atmospheric Environment 36 (2002) 1475.

[371] N. V. Heeb, A.-M. Forss, S. Brühlmann, R. Lüscher, C.J. Saxer, P. Hug, Atmospheric Environment 40 (2006) 5986.

[372] N. V. Heeb, C.J. Saxer, A.-M. Forss, S. Brühlmann, Atmospheric Environment 42 (2008) 2543.

[373] W.R. Pierson, W.W. Brachaczek, Environmental Science & Technology 17 (1983) 757.

[374] M. a. Moeckli, M. Fierz, M.W. Sigrist, Environmental Science & Technology 30 (1996) 2864.

[375] M.P. Fraser, G.R. Cass, Environmental Science & Technology 32 (1998) 1053.

[376] C.D. DiGiulio, J.A. Pihl, J.-S. Choi, M. Lance, J.E. Parks II, M.D. Amiridis, T.J. Toops., (Submitted), Applied Catalysis B: Environmental XX (n.d.) XX.

[377] J.E. Parks II, V. Prikhodko, W. Partridge, J.-S. Choi, K. Norman, S. Huff, P. Chambon., (2010-01-2267), Society of Automotive Engineers (SAE) (2010).

[378] S. Tagliaferri, R.A. Koppel, A. Baiker, Applied Catalysis B: Environmental 15 (1998) 159.

[379] K.C. Taylor, Catalysis Reviews: Science and Engineering 35 (1993) 457.

[380] N. Macleod, J. Isaac, R.M. Lambert, Applied Catalysis B: Environmental 33 (2001) 335.

[381] S.H. Oh, Journal of Catalysis 124 (1990) 477.

[382] T.P. Kobylinski, B.W. Taylor, Journal of Catalysis 33 (1974) 376.

[383] J. Kaspar, M. Graziani, P. Fornasiero, Handbook on the Physics of Rare Earths 29 (2000) 159.

[384] T. Maunula, J. Ahola, T. Salmi, H. Haario, M. Harkonen, M. Luoma, V.J. Pohjola, Applied Catalysis B: Environmental 12 (1997) 287.

[385] R. Dumpelmann, N.W. Cant, D.L. Trimm, Studies in Surface Science and Catalysis 96 (1995) 123.

[386] J.T. Kummer, The Journal of Physical Chemistry 90 (1986) 4747.

[387] M. Shelef, G.W. Graham, Catalysis Reviews: Science and Engineering 36 (1994) 433.

[388] G. Pirug, H.P. Bonzel, Journal of Catalysis 50 (1977) 64.

[389] A. Obuchi, S. Naito, T. Onishi, K. Tamaru, Surface Science 122 (1982) 235.

[390] A. Obuchi, S. Naito, T. Onishi, K. Tamaru, Surface Science 130 (1983) 29.

[391] B.J. Savatsky, A.T. Bell, ACS Symposium Series (1982) 105.

[392] M. Shelef, H.S. Gandhi, Industrial & Engineering Chemistry Product Research and Development 11 (1972) 393.

[393] T.E. Hoost, K. Otto, Applied Catalysis A: General 92 (1992) 39.

[394] L.S.F. Feio, C.E. Hori, S. Damyanova, F.B. Noronha, W.H. Cassinelli, C.M.P. Marques, J.M.C. Bueno, Applied Catalysis A: General 316 (2007) 107.

[395] N. a. Ottinger, T.J. Toops, J.A. Pihl, J.T. Roop, J.-S. Choi, W.P. Partridge, Applied Catalysis B: Environmental 117-118 (2012) 167.

[396] T. Regina Oliveira de Souza, S. Modesto de Oliveira Brito, H. Martins Carvalho Andrade, Applied Catalysis A: General 178 (1999) 7.

[397] W. Liu, M. Flytzani-Stephanopoulos, Journal of Catalysis 153 (1995) 304.

[398] Y.-F.Y. Yao, Journal of Catalysis 87 (1984) 152.

[399] A. Amirnazmi, J. Benson, M. Boudart, Journal of Catalysis 30 (1973) 55.

[400] R. Burch, A. Shestov, J. Sullivan, Journal of Catalysis 188 (1999) 69.

[401] R.G. Sharpe, M. Bowker, Surface Science 360 (1996) 21.

[402] A. Desikusumastuti, M. Happel, Z. Qin, T. Staudt, Y. Lykhach, M. Laurin, S. Shaikhutdinov, F. Rohr, J. Libuda, The Journal of Physical Chemistry C 113 (2009) 9755.

[403] T. Bánsági, T.S. Zakar, F. Solymosi, Applied Catalysis B: Environmental 66 (2006) 147.

[404] E. Roedel, A. Urakawa, S. Kureti, A. Baiker, Physical Chemistry Chemical Physics : PCCP 10 (2008) 6190.

[405] A. Scotti, I. Nova, E. Tronconi, L. Castoldi, L. Lietti, P. Forzatti, Industrial & Engineering Chemistry Research 43 (2004) 4522.

APPENDICES

A.1 PRELIMINARY *IN SITU* FTIR RESULTS COLLECTED OVER Al_2O_3, Pt/Al_2O_3, Ba/Al_2O_3 AND $Pt/Ba/Al_2O_3$

A.1.1 EXPERIMENTAL METHODS

MATERIALS AND PREPARATION

All catalysts were prepared by incipient wetness impregnation using aqueous solutions of barium acetate (Alfa Aesar) and tetraammineplatinum (II) nitrate (Sigma-Aldrich), as summarized in Table A1. Prior to impregnation, Catalox® SBa-200 γ-Al_2O_3 (Sasol) was calcined for 24 hr at 600 °C. Ba was deposited first, dried for 24 hr at R.T., dried for 12 hr at 120 °C and calcined in air for 12 hr at 600 °C. Then, Pt was deposited, dried for 24 hr at R.T., dried for 12 hrs at 120 °C and calcined in air for 5 hr at 500 °C.

Table A1. List of catalysts prepared for the preliminary *in situ* FTIR investigation.

Catalyst	Pt (wt %)	Ba (wt %)	Al_2O_3 (wt %)
Al_2O_3	-	-	Bal.
Pt/Al_2O_3	1.0	-	Bal.
Ba/Al_2O_3	-	17.0	Bal.
$Pt/Ba/Al_2O_3$	1.0	17.0	Bal.

FOURIER TRANSFORM INFRARED SPECTROSCOPY (FTIR)

Spectra were collected on a Nexus 470 FTIR spectrometer operated in transmission mode with 2 cm^{-1} resolution, where 30 scans per spectra were collected for storage experiments (30 s collection time) and 19 scans per spectra were collected for cycling experiments (20 s collection time). The catalysts were pressed into self supported wafers (≈ 15-20 mg cm^{-2}) using a die from International Crystal Laboratories. Analysis was performed in a homemade cell consisting of a stainless steel tube (1.5" ID X 4.5" L) with cooling water flanges welded to each end. The flanges were machined to accommodate polished windows (NaCl 32mm x 3mm – Alfa Aesar) that were held in place by Viton gaskets. Cooling water was passed through the flanges to keep the Viton gasket temperature below 100 °C. The cell was wrapped in a 400 W, 4 ft heating cord (Glas-Col), which allowed heating up to 400 °C. A thermocouple was placed in close proximity to the sample for determination of catalyst temperature. A gas manifold with five mass flow controllers (Brooks 5890E – CO, Tylan – NO, NO_2, O_2, He, H_2, C_3H_6) and two needle valves (Swagelok – He) delivered the mixed gas to the cell, where appropriate gases were purified by high capacity water and moisture traps (Restek). Certified gas mixtures were purchased from National Welders and included: 1% NO in He, 1% H_2 in He, 1% NO_2 in He, 1% C_3H_6 in He, 3% CO in He, 10% O_2 in He, pure H_2 and pure He. Flow through the cell was maintained at 100 cm^3 min^{-1} throughout all experiments.

Two types of experiments were performed (conditions shown in Table A2). First, the catalysts were characterized by adsorption of NO, NO_2, NO+O_2 or CO at RT or 350 °C for 20 min. These experiments are referred to as "storage experiments" and were used to compare storage capacity and assign peaks. Then, samples were investigated under more realistic cycling conditions in order to observe intermediate species. Cycling was performed using 2 min. lean

phases (Table A2), followed by a 2 min He flush to remove all O_2 and lastly, a 2 min rich phase (Table A2). Reductants were investigated separately (i.e., Rich CO refers to cycling with CO as the reductant and Rich H_2 refer to cycling with H_2 as the reductant). Prior to experiments, samples were reduced for 30 min. in H_2 at 400 °C, flushed for 15 min in He, oxidized for 5 hr in 10% O_2 in He at 400 °C, flushed for 1 hr in He at 400 °C and cooled to either RT or 350 °C for experiments. The same sample was used to complete one set of data. Fresh samples underwent additional pretreatment to remove stable carbonates species, where the catalyst was treated in 0.5% NO, 5% O_2 in He mixture at 400 °C for 5 hr, reduced in pure H_2 for 1 hour, and subsequently treated as described above. After all pretreatments, a background spectra was collected and used for subtractions.

Table A2. Gas concentrations (mole %) during storage and cycling Experiments.

Storage

Experiment	NO (%)	NO_2 (%)	CO (%)	H_2 (%)	C_3H_6 (%)	O_2 (%)	He (%)
NO	0.1	-	-	-	-	-	Bal.
NO + O_2	0.1	-	-	-	-	5.0	Bal.
NO_2	-	0.1	-	-	-	-	Bal.
CO	-	-	0.1	-	-	-	Bal.

Cycling

Experiment							
Lean	0.1	-	-	-	-	5.0	Bal.
Rich CO	-	-	0.9	-	-	-	Bal.
Rich H_2	-	-	-	0.9	-	-	Bal.
Rich C_3H_6	-	-	-	-	0.1	-	Bal.

A.1.2 *IN SITU* FTIR STORAGE EXPERIMENTS

Storage of NO, NO + O_2, NO_2 and CO at room temperature (RT) and 350 °C was investigated by *in situ* FTIR spectroscopy on pre-oxidized Al_2O_3, Pt/Al_2O_3, Ba/Al_2O_3 and $Pt/Ba/Al_2O_3$ samples in order to confirm observations and mechanisms presented in the literature [21,22,24,27,31,33,34,37,38,41,43,112,179]. While RT spectra were included, a higher emphasis was placed on spectra collected at 350 °C since this represents a relevant storage temperature. Many bands assignments should be considered tentative since overlapping bands from a variety of possible nitrite and nitrate species makes definitive assignments difficult, if not impossible [50–52,402].

NO

Exposure of pre-oxidized Al_2O_3 catalyst to NO at RT resulted in the formation of low intensity bands at 1650, 1581, 1463, 1322, 1232 and 1080 cm^{-1} (Fig. A1). The bands at 1650 and 1581 cm^{-1} were assigned to nitrates, where a bridging bidentate nitrate, monodentate nitrate or chelating bidentate nitrate could all account for bands in this region of the spectra [22,31,33,34]. The band at 1463 cm^{-1} was assigned to a linear nitrite, while the bands at 1322 and 1232 cm^{-1} were assigned to a bridged bidentate nitrite. Similarly, exposure of pre-oxidized Pt/Al_2O_3 to NO at RT resulted in formation of low intensity bands at 1783, 1652, 1582, 1465, 1322, 1232 and 1078 cm^{-1}. The band at 1783 cm^{-1} was consistent with a Pt mononitrosyl, where the other bands correspond to previously assigned nitrogen oxide species adsorbed on Al_2O_3.

Exposure of Ba/Al_2O_3 to NO at RT resulted in formation of bands at 1647, 1560, 1448 and 1390 cm^{-1}. Assignment of these bands was difficult and it was unclear if bands at 1647, 1560 and 1448 cm^{-1} were associated with the Al_2O_3 and/or $BaO\text{-}BaCO_3$ storage component. It is

worth mentioning that the relative intensity between the 1650 and 1582 cm^{-1} changes when Ba is added to the Al_2O_3 support. This may infer storage to be occurring on Ba or Ba may occupy sites previously accessible to NO_X on the bare alumina support. The band at 1390 cm^{-1} was not assigned, as it was only observed for the Ba/Al_2O_3 sample during exposure to NO in the absence of O_2.

Addition of Pt to the Ba/Al_2O_3 sample completely changed the spectra and bands at 1541, 1443, 1417, 1373, 1314, 1209 cm^{-1} were observed after exposure to NO at RT. The band at 1541 cm^{-1} was most likely associated with a monodentate nitrate or bidentate nitrate on Ba, while bands at 1443, 1417, 1373 and 1314 cm^{-1} could be assigned to monodentate nitrates, monodentate nitrites, linear nitrites, or hyponitrites on Ba [22,31,33,34]. Additionally, these bands could be associated with NO_X species adsorbed on Al_2O_3 or on sites in close proximity to Ba, where definitive assignments is difficult because a large number of NO_X species adsorbed on both Ba and Al_2O_3 at room temperature. The band at 1209 cm^{-1} was assigned to a bridging bidentate nitrite on Ba.

Assignment of NO_X species adsorbed on Al_2O_3, Pt/Al_2O_3, Ba/Al_2O_3 and $Pt/Ba/Al_2O_3$ at 350 °C was more straightforward as seen in Fig. A2. Exposure of Al_2O_3 to NO at 350 °C resulted in very weak bands at 1312 and 1229 cm^{-1}, which were assigned to bridged bidentate nitrites (Fig. A2). For Pt/Al_2O_3, a band at 1555 cm^{-1} was observed in addition to bands 1297 and 1234 cm^{-1}.

The band at 1234 cm^{-1} was assigned to bidentate nitrites, while the band at 1555 cm^{-1} was most likely associated with bridging bidentate nitrates, chelating nitrates or monodentate nitrates, with another vibration occurring around 1297 cm^{-1}. The nitrate peak was centered at 1555 cm^{-1}, but contained shoulders at higher and lower wavenumbers. Storage of NO on Pt/Al_2O_3 at

elevated temperatures probably included a combination of bridging bidentate nitrates, chelating nitrates and monodentate nitrates, which would account for the shoulders. Exposure of Ba/Al_2O_3 to NO at 350 °C resulted in formation of a band at 1211 cm^{-1}, which was previously assigned to a bridging bidentate nitrite on Ba. While storage of NO_X was observed for Ba/Al_2O_3, the storage capacity was low and occurred mainly in the form of nitrites.

Exposure of $Pt/Ba/Al_2O_3$ to NO at 350 °C resulted in formation of a band at 1213 cm^{-1}, which was assigned to a bridged nitrite on Ba (Fig. A2). With increased time of exposure, bands at 1742, 1418 and 1306 cm^{-1} also formed and grew in intensity. Furthermore, the $Pt/Ba/Al_2O_3$ catalyst was the only catalyst tested to show appreciable storage when exposed to NO in the absence of O_2. Fanson et al. [43] also observed significant storage of NO on $Pt/Ba/Al_2O_3$ catalysts, but their results were obtained at RT . In our case, significant storage was only observed at elevated temperatures.

The band at 1742 cm^{-1} was assigned to a NO_X species coordinated on Pt, where the shift to lower wavenumbers could be explained by elevated temperatures, the state of Pt or the chemical environment of Pt (i.e., Pt deposited on Ba may have different electronic properties) [37]. The bands at 1418 and 1306 cm^{-1} were assigned to "bulk-like" ionic nitrates on Ba [21,24,34,40,187,188,191].

This data corroborates well with other results, where Pt increases storage capacity and catalyzes the transition from nitrites to nitrates [22,86]. It also supports the mechanism involving nitrites as intermediate species in the formation of nitrates [21,22,31,34,39]. However, an alternative mechanism, as previously suggested by Fanson et al. [43], where NO directly interacts with the Ba and the main role of Pt is to provide atomic oxygen, possibly though NO decomposition, cannot be ruled out.

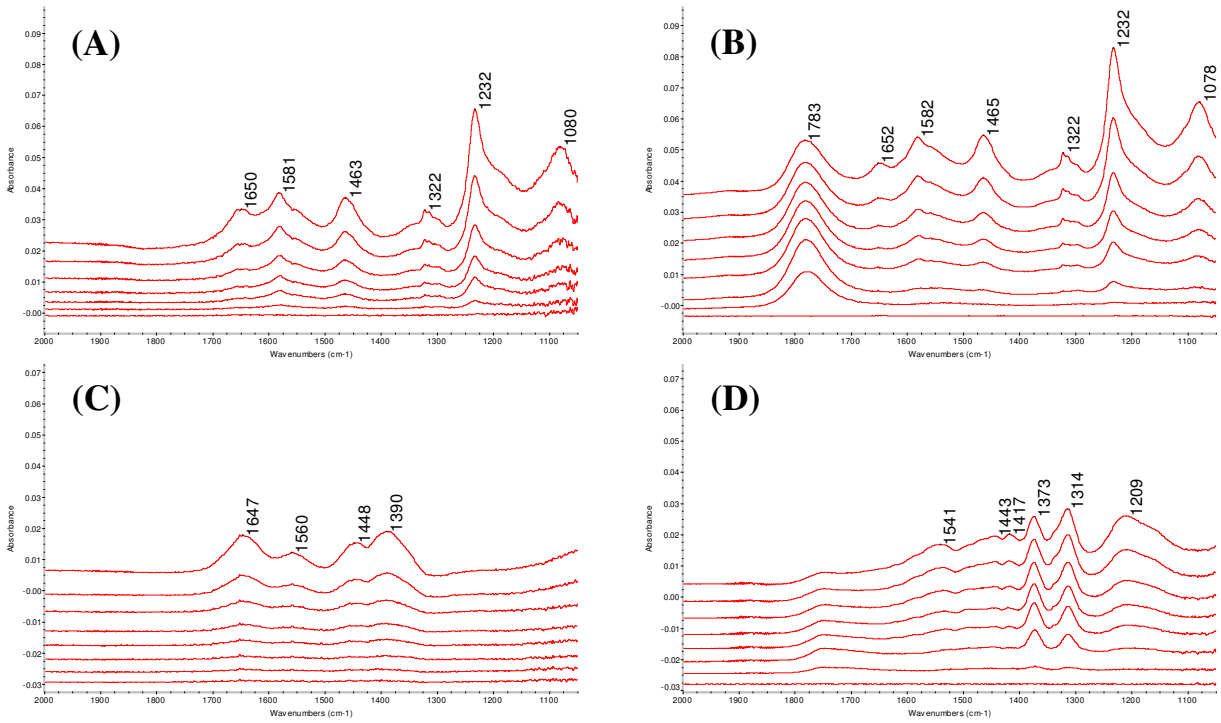

Figure A1. Adsorption of 1000 ppm NO in He at RT on (A) Al_2O_3, (B) Pt/Al_2O_3, (C) Ba/Al_2O_3, (D) $Pt/Ba/Al_2O_3$. Spectra shown after 0, 0.5, 1, 2, 3, 5, 10 & 20 min., respectively.

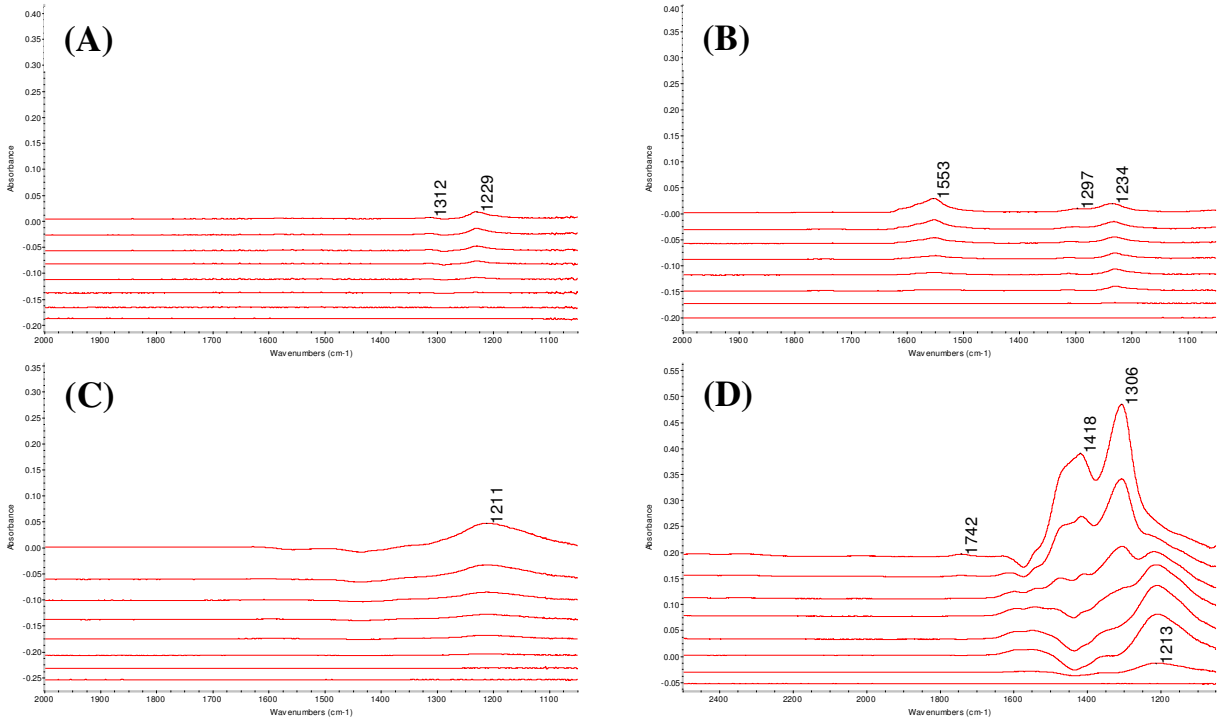

Figure A2. Adsorption of 1000 ppm NO in He at 350 °C on (A) Al_2O_3, (B) Pt/Al_2O_3, (C) Ba/Al_2O_3, (D) $Pt/Ba/Al_2O_3$. Spectra shown after 0, 0.5, 1, 2, 3, 5, 10 & 20 min., respectively.

NO + O_2

Addition of oxygen to the feed drastically increased the concentration of nitrite and nitrate species for all of the catalysts investigated both at RT and 350 °C, as shown in Figs. A3 and A4. Fridell et al. and others previously established the beneficial role O_2 plays in NO_X storage [22,62]. Admission of NO+ O_2 over Al_2O_3 and Pt/Al_2O_3 at RT resulted in formation of bands at 1792, 1585, 1548, 1466, 1316, 1230 and 1077 cm^{-1} (Fig. A3). The band at 1792 cm^{-1} was previously assigned to mononitrosyls on Pt and bands at 1585, 1548, 1466, 1316, and 1230 cm^{-1} were assigned to monodentate or chelating nitrates, linear nitrites, and bridging nitrites, respectively. The band previously observed at 1650 cm^{-1} was no longer resolved, but seemed to be present as a shoulder on the 1585 cm^{-1} band. The strong band at 1077 cm^{-1} could be assigned to a bridged N-coordinated nitrite, a chelating bidentate nitrate or a bridged bidentate nitrate.

Exposure of Ba/Al_2O_3 to NO + O_2 at RT resulted in formation of bands at 1549, 1478, 1347, and 1212 cm^{-1}. It is worth noting the large differences observed between NO and NO + O_2 exposure, as shown in Fig. A1 and A3, respectively. In the presence on O_2, storage occurred mainly as a bridged bidentate nitrite species, while in the absence of O_2 a series of bands at 1647, 1560, 1448 and 1390 cm^{-1} were observed. In this case, the bands at 1549, 1478 and 1347 cm^{-1} in Fig. A3 were assigned to monodentate nitrates/nitrites on Ba or Al, linear nitrites on Ba or Al or hyponitrites on Ba or Al.

Exposure of $Pt/Ba/Al_2O_3$ to NO + O_2 at RT resulted in formation of bands at 1543, 1420, 1331 and 1212 cm^{-1} (Fig. A3). While the primary feature was the bidentate nitrite species at 1212 cm^{-1}, formation of ionic nitrate species at 1310 and 1420 cm^{-1} and bidentate nitrate species at 1543 cm^{-1} indicated the transition from surface nitrites to surface and bulk nitrates with increasing time even at RT and demonstrated the influential role of Pt.

At 350 °C, exposure of Al_2O_3 to NO + O_2 resulted in formation of low intensity bands at 1552 and 1231 cm^{-1}, where the band at 1552 cm^{-1} was consistent with a bridged bidentate nitrate, chelating nitrate or monodentate nitrate and the band at 1231 cm^{-1} was consistent with a bidentate nitrite. Interestingly, nitrate formation was observed over Al_2O_3 even in the absence of a precious metal. Significantly higher storage was observed for Pt/Al_2O_3 exposed to NO + O_2 at 350 °C (Fig. A4). Bands at 1574, 1296 and 1245 cm^{-1} were consistent with nitrate features, where storage most likely occurred as a bridging bidentate nitrate or chelating bidentate nitrates. Monodentate nitrates were also possible, but lack of a band in the 1400-1300 cm^{-1} region inferred storage in this form to be unlikely. Additionally, storage of NO_X as a bidentate nitrite was only observed at shorter times. With increased time of exposure, the band at 1230 cm^{-1} disappeared. This further demonstrated the critical role of Pt, where nitrites stored on the surface were not observed because Pt catalyzed rapid conversion from nitrites to nitrates either by providing atomic oxygen or oxidizing NO to NO_2, which could further oxidize the nitrites to nitrates.

Exposure of Ba/Al_2O_3 to NO + O_2 at 350 °C demonstrated a similar trend as Al_2O_3, where storage occurred primarily as nitrites with formation of nitrates at increased times of exposure (Fig. A4). The primary band at 1208 cm^{-1} was assigned to bidentate nitrites, while less intense bands at 1300 and 1415 cm^{-1} were assigned to ionic nitrates. A band also appeared between 1600 -1500 cm^{-1}, but it was masked by a negative band at 1560 cm^{-1} associated with decomposition of $BaCO_3$. It is worth mentioning that exposure of Ba/Al_2O_3 to NO at 350 °C resulted solely in the formation of nitrites (1210 cm^{-1}). Therefore, the presence of oxygen facilitated storage as nitrates and conversion from nitrites to nitrates, but total storage capacity remained low in comparison to $Pt/Ba/Al_2O_3$ catalysts.

Exposure of $Pt/Ba/Al_2O_3$ to NO + O_2 at 350 °C resulted in significant storage of NO_X, as demonstrated by Fig. A4. Intense bands at 1744, 1547, 1418 and 1306 cm^{-1} were observed and corresponded to nitrosyls on Pt, bidentate nitrates, and ionic nitrates (1418 and 1306 cm^{-1}) on Ba, respectively. Initially, a band at 1223 cm^{-1}, assigned to a nitrite on Ba, was observed. However, this peak was no longer evident at longer times. It is possible that the nitrite was still present, but its vibration was masked by the much larger band at 1306 cm^{-1}. In conclusion, $Pt/Ba/Al_2O_3$ exposed to NO + O_2 at 350 °C stored significantly more NO_X than Al_2O_3, Pt/Al_2O_3 and Ba/Al_2O_3, where storage occurred primarily as ionic nitrates. Conversion from nitrites to nitrates was observed at shorter times (<30 sec), but nitrites were no longer observed at longer times, which provided further evidence for a nitrite to nitrate storage mechanism.

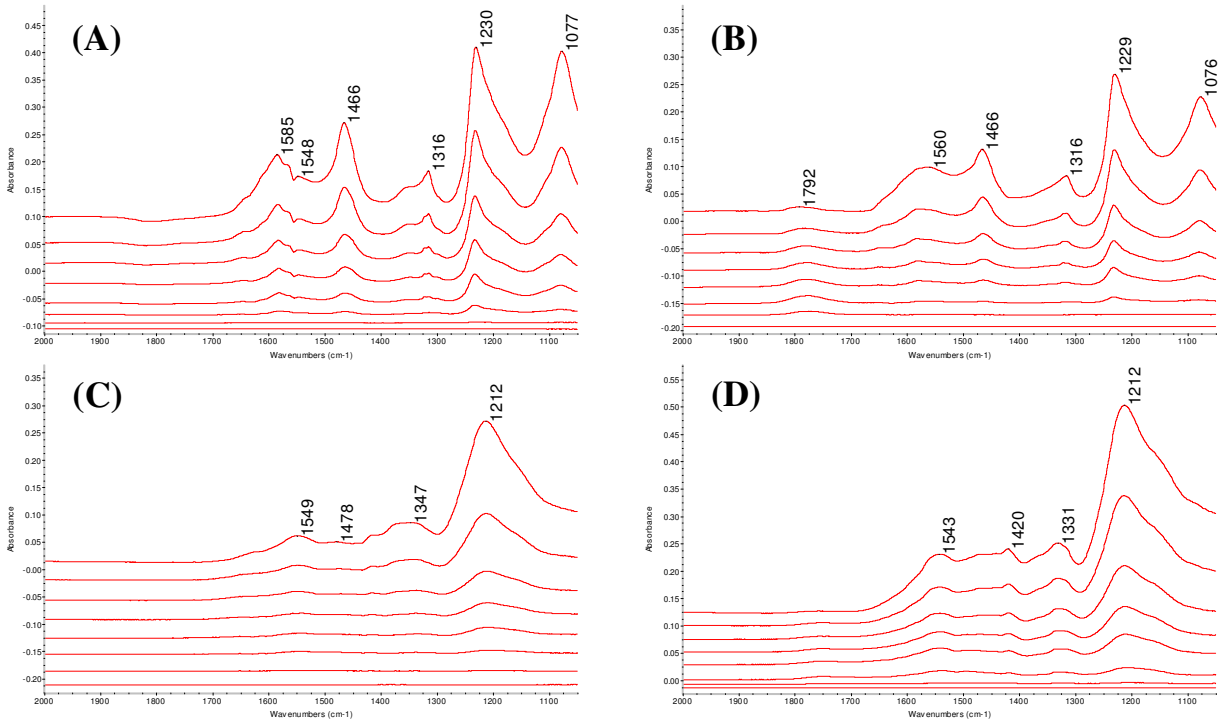

Figure A3. Adsorption of 1000 ppm NO + 5% O_2 in He at RT on (A) Al_2O_3, (B) Pt/Al_2O_3, (C) Ba/Al_2O_3, (D) $Pt/Ba/Al_2O_3$. Spectra shown after 0, 0.5, 1, 2, 3, 5, 10 & 20 min., respectively.

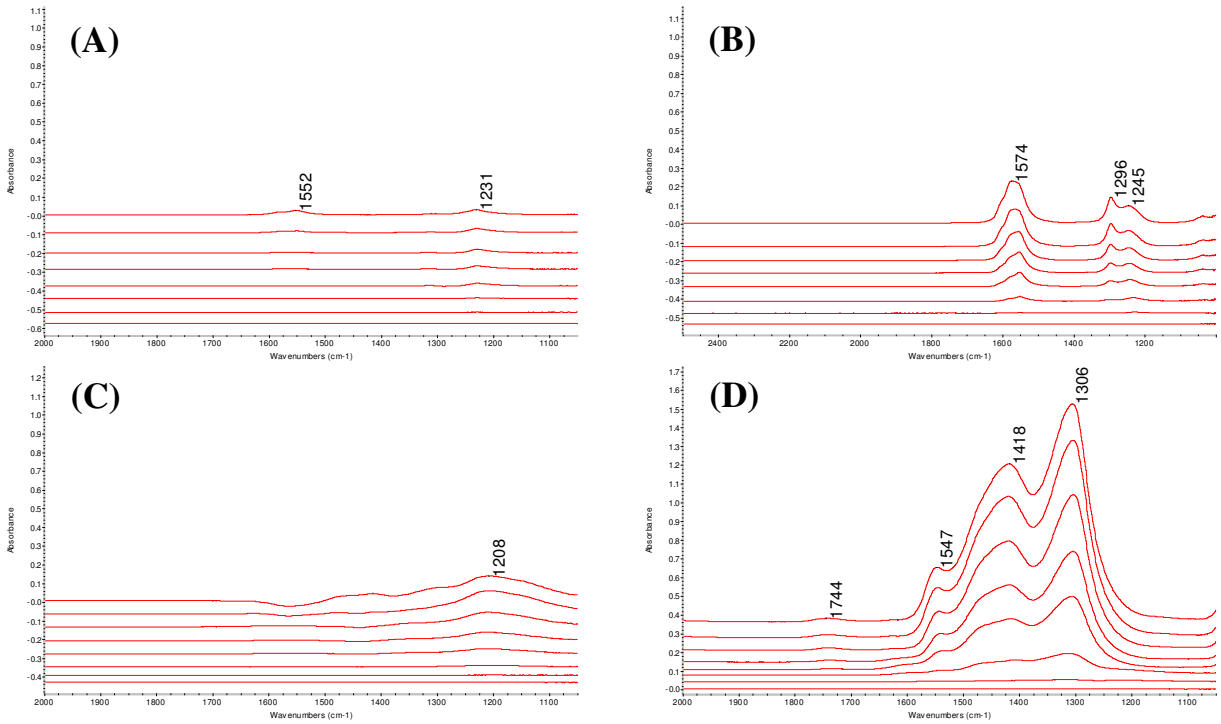

Figure A4. Adsorption of 1000 ppm NO + 5% O_2 in He at 350 °C on (A) Al_2O_3, (B) Pt/Al_2O_3, (C) Ba/Al_2O_3, (D) $Pt/Ba/Al_2O_3$. Spectra shown after 0, 0.5, 1, 2, 3, 5, 10 & 20 min., respectively.

NO_2

Exposure of Al_2O_3, Pt/Al_2O_3, Ba/Al_2O_3 and $Pt/Ba/Al_2O_3$ to NO_2 was also performed. It is worth noting that exposure to NO_2 instead of NO or NO + O_2 effectively negates the beneficial role of Pt, where the main role of Pt is to adsorb and oxidize NO to NO_2. Additionally, many groups have stressed the importance of the Pt/BaO interface in NO_X storage, where Pt acts like a bridge for NO_X to adsorb and spillover onto the Ba component where storage ultimately occurs [8,21,29,46,66,69,73,74]. Sakamoto et al. [71] suggested storage and reduction of NO_X to occur within a few micrometers of the Pt particle and mentioned that preferential adsorption and reduction of NO_X occurring in close vicinity to Pt particles could explain why only 20% of the deposited Ba participates in storage [72]. Therefore if NO_2 is selected as the NO_X source, all storage sites essentially become equivalent because oxidation of NO to NO_2 is no longer the rate determining step for storage and nitrate formation should be facile according to the

disproportionation mechanism presented by Prinetto et al. [40] and others [38,41,42], where disproportionation proceeds through oxidation of BaO to BaO_2 by gas phase NO_2 which subsequently adsorbs two molecules of NO_2 to form $Ba(NO_3)_2$.

Figs. A5 and A6 demonstrate exposure of NO_2 at RT and 350 °C, respectively for Al_2O_3, Pt/Al_2O_3, Ba/Al_2O_3 and $Pt/Ba/Al_2O_3$. In all cases, formation of intense bands assigned to nitrates on Al_2O_3 or Ba were observed. Initially, nitrites were observed, but they were rapidly oxidized to nitrates. Prinetto et al. [34] and Nova et al. [21] previously reported that exposure of NSR catalysts to NO_2 only yielded nitrates. However, Sedlmair et al. [31] observed nitrite species when $Pt/Ba/Al_2O_3$ catalysts were exposed to NO_2.

While nitrites were observed, storage occurred mainly as nitrates on Al_2O_3 or BaO. For Al_2O_3 and Pt/Al_2O_3, bands at 1600 – 1500 and 1300 – 1200 cm^{-1} were assigned to bridged bidentate nitrates, monodentate or chelating bidentate nitrates on Al_2O_3. For Ba/Al_2O_3 and $Pt/Ba/Al_2O_3$, bands at 1552, 1420 and 1310 cm^{-1} were assigned to bridging nitrates on Ba and ionic nitrates on Ba, respectively. It is worth noting that adsorption of NO_2 was qualitatively very similar to adsorption of NO + O_2, but yielded higher intensity bands at equivalent storage times, which was expected since the Pt/BaO interface was no longer important. Additionally, since nitrites were observed during exposure of NO_2, a mechanism involving a nitrite to nitrate route could not be excluded even though NO_2 was used as the NO_X source.

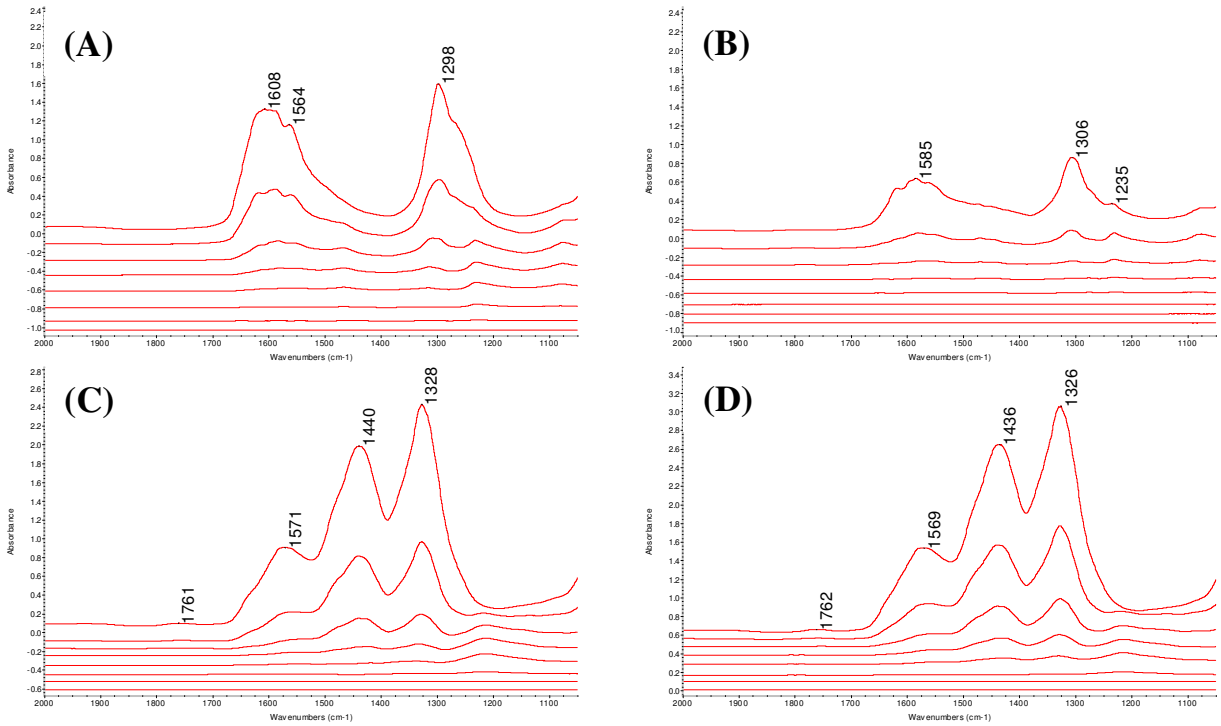

Figure A5. Adsorption of 1000 ppm NO_2 in He at RT on (A) Al_2O_3, (B) Pt/Al_2O_3, (C) Ba/Al_2O_3, (D) $Pt/Ba/Al_2O_3$. Spectra shown after 0, 0.5, 1, 2, 3, 5, 10 & 20 min., respectively.

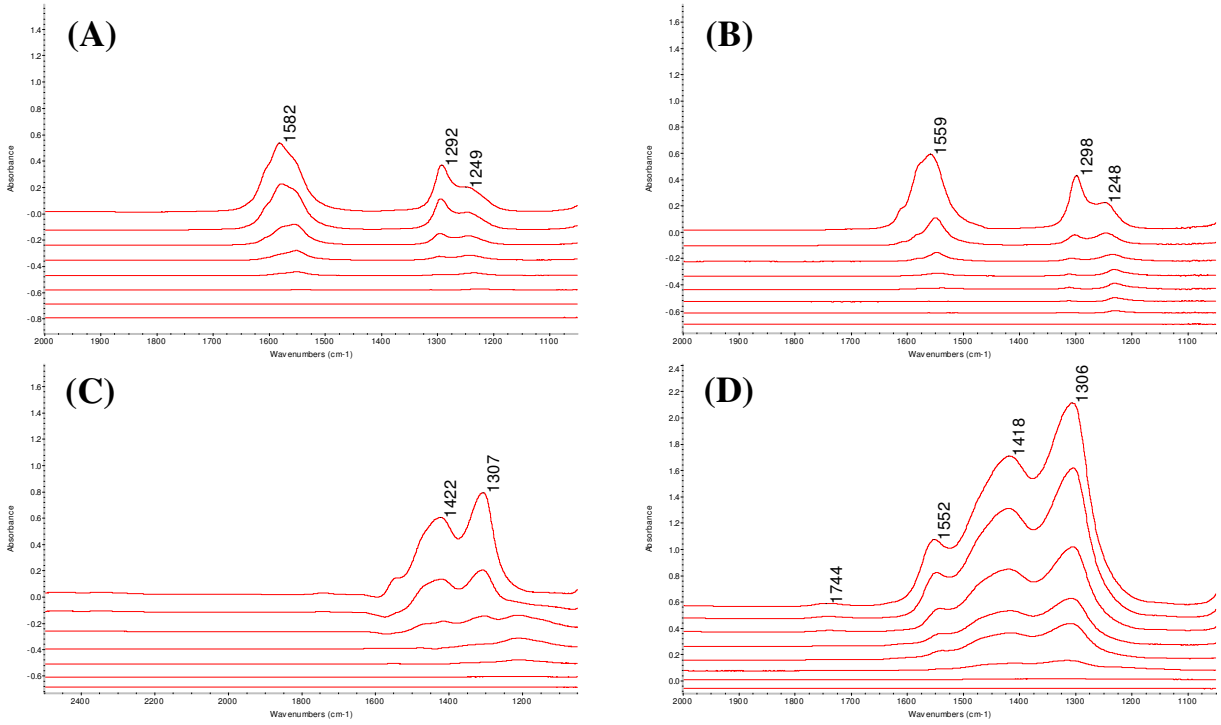

Figure A6. Adsorption of 1000 ppm NO_2 in He at 350 °C on (A) Al_2O_3, (B) Pt/Al_2O_3, (C) Ba/Al_2O_3, (D) $Pt/Ba/Al_2O_3$. Spectra shown after 0, 0.5, 1, 2, 3, 5, 10 & 20 min., respectively.

CO

Exposure of pre-oxidized samples to CO was performed because nitrates/nitrites absorb infrared light in the same region as carbonates, carboxylates and formates and band assignments can be even more difficult when carbon containing species were present in the gas mixtures.

Exposure of Al_2O_3 and Pt/Al_2O_3 to 1000 ppm CO in He at RT resulted in formation of low intensity bands at 2092, 1653, 1470, 1436, 1266 and 1230 cm^{-1} (Figs. A7 and A8). The band at 2092 cm^{-1} was assigned to a CO carbonyl on Pt. Bands at 1653, 1470, 1436, 1266 and 1230 cm^{-1} were most likely associated with bidentate carbonates and unidentate carbonates [37,179]. Detailed bands assignments were not attempted since the bands were insignificant at 350 °C, a relevant storage temperature. Exposure of Ba/Al_2O_3 and $Pt/Ba/Al_2O_3$ to 1000 ppm CO at RT resulted in formation of bands at 2087, 1656, 1567, 1379, 1321 and 1230 cm^{-1}, which could similarly be assigned to Pt carbonyls and bidentate carbonates and unidentate carbonates respectively.

Exposure of Al_2O_3 and Pt/Al_2O_3 to 1000 ppm CO at 350 °C resulted in formation of low intensity bands at 1585, 1515, 1521, 1441, 1392 and 1296 cm^{-1} and were assigned to weakly bound carbonate species on Al_2O_3 (Fig. A8). Notice that storage of CO occurred negligibly at 350 °C on Al_2O_3. These results were in agreement with storage of 1000 ppm NO, in absence of O_2, at 350 °C (Fig. A2). The more intense band at 2049 cm^{-1} was assigned to linearly bound CO carbonyl on reduced Pt.

Exposure of Ba/Al_2O_3 and $Pt/Ba/Al_2O_3$ to 1000 ppm CO resulted in formation of much more intense bands at 1570 and 1335 cm^{-1}, which were assigned to bidentate carbonates [37,179]. A band at 1450 cm^{-1} was not observed in the absence of H_2O and O_2, where the band at 1450 cm^{-1} was previously assigned to bulk $BaCO_3$. This indicated that under the conditions of

the experiment only surface carbonates were formed. Formation of a band at 1450 cm^{-1} would likely indicate deterioration of NSR ability since bulk-like $BaCO_3$ is highly stable and is believed to be inactive for NO_X storage. The band at 2016 cm^{-1} was assigned to a carbonyl on Pt and bands at 2230 and 2162 cm^{-1} were assigned to isocyanate species bound to Al_2O_3 and BaO, respectively [24]. The formation of NCO species even in the absence of NO_X indicated that the Ba storage component contained some residual NO_X stored on the surface even though a high-temperature reduction using H_2 was performed.

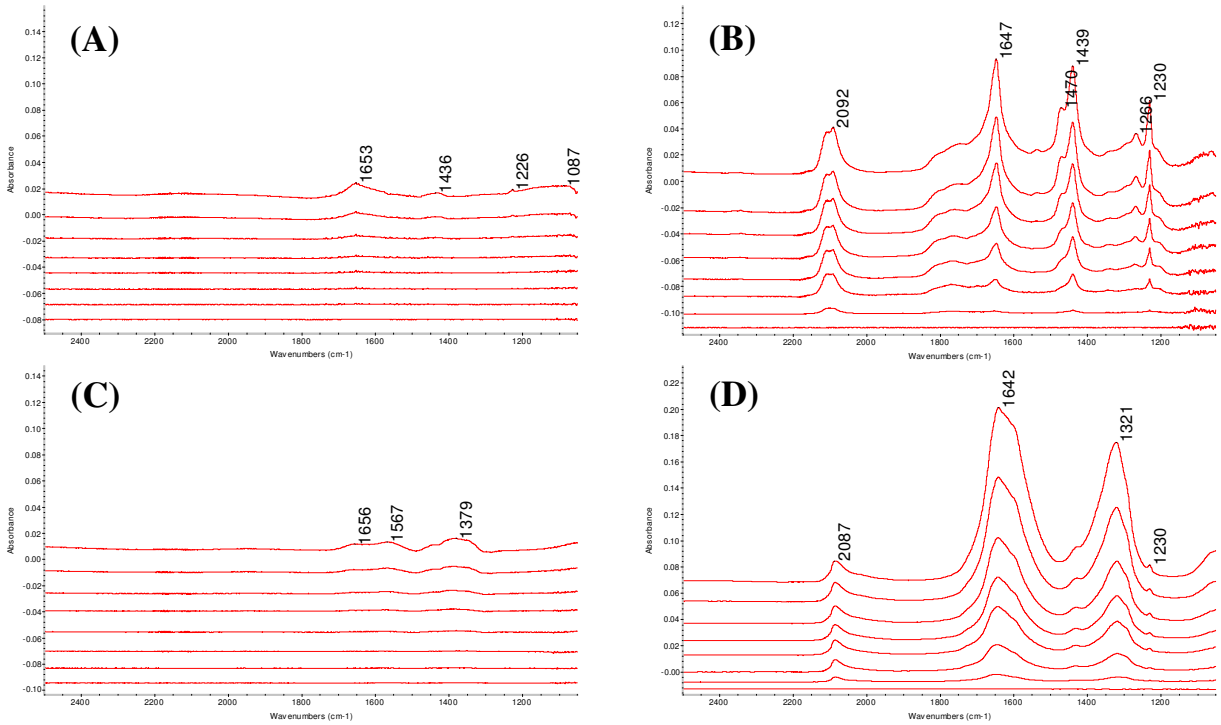

Figure A7. Adsorption of 1000 ppm CO in He at RT on (A) Al_2O_3, (B) Pt/Al_2O_3, (C) Ba/Al_2O_3, (D) $Pt/Ba/Al_2O_3$. Spectra shown after 0, 0.5, 1, 2, 3, 5, 10 & 20 min., respectively.

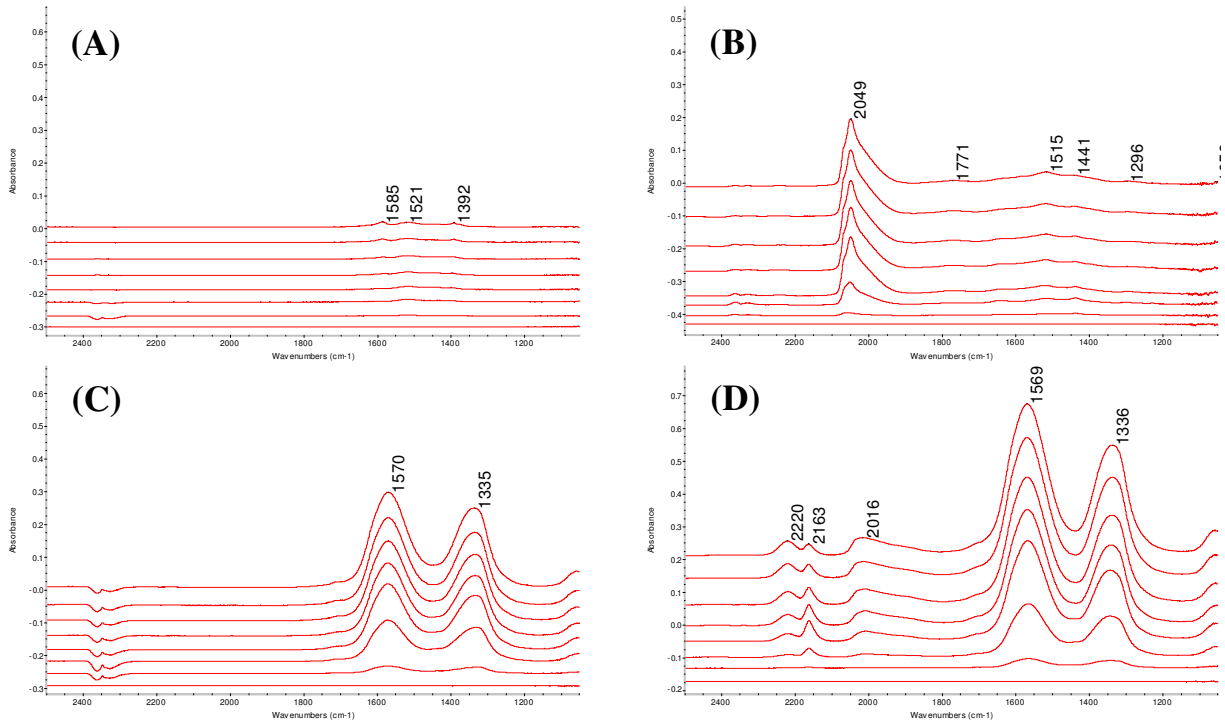

Figure A8. Adsorption of 1000 ppm CO in He at 350 °C on (A) Al_2O_3, (B) Pt/Al_2O_3, (C) Ba/Al_2O_3, (D) $Pt/Ba/Al_2O_3$. Spectra shown after 0, 0.5, 1, 2, 3, 5, 10 & 20 min., respectively.

A.1.3 *IN SITU* FTIR CYCLING EXPERIMENTS

In situ cycling experiments were performed using model NO_X storage and reduction conditions, where the lean period contained 1000 ppm NO + 5 % O_2 and the rich period contained 9000 ppm H_2, 9000 ppm CO or 1000 ppm C_3H_6 in He. The duration of the periods lasted 2 min with a 2 min He flush in between the lean and rich period. The He flush was used to ensure complete removal of O_2 from the IR cell before introduction of the reductant. Spectra were collected in 20 s intervals for 3 complete NO_X storage and reduction cycles. The following sections present results from Pt/Al_2O_3, Ba/Al_2O_3 and $Pt/Ba/Al_2O_3$ samples. The extensive storage characterization experiments presented in Section A.1.2 aided in interpretation of the results because numerous bands were observed during cycling experiments and assignment of these bands would have been difficult without the storage experiments.

PT/AL$_2$O$_3$

In situ cycling using H_2 as a reductant on a Pt/Al_2O_3 catalyst yielded bands at 1551, 1295 and 1241 cm^{-1} during the first lean period, as shown in Fig. A9. These bands were previously assigned to bridging or chelating bidentate nitrates on Al_2O_3 and they continued to grow in intensity for the duration of the lean period. Removal of NO and O_2 during the subsequent He flush destabilized these species and a slow decrease in intensity of the 1551, 1296 and 1241 cm^{-1} bands was observed. Notice the clear maximum obtained for the 1551 cm^{-1} band in Fig. A9. Introduction of 9000 ppm H_2 during the rich periods caused rapid removal of the nitrate bands, where spectra collected during rich periods were nearly flat. This indicated that the reduction period effectively returned the catalyst to its clean "pre-cycled" state. Since effluent gases from the IR cell were not analyzed, it was not possible to determine if the species were reacting on the surface or merely desorbing into the gas phase, but Fridell et al. [62] performed similar experiments over a $Pt\text{-}Rh/Al_2O_3$ catalyst and complete reduction of NO_X was observed during rich periods.

Similarly, cycling using CO and C_3H_6 as reductants on a Pt/Al_2O_3 catalyst yielded bands assigned to bridging or chelating bidentate nitrates on Al_2O_3 during the first storage period, as shown in Figs. A10 and A11. However when CO or C_3H_6 were used as reductants, bands in the region of 1600 – 1200 cm^{-1} appeared. These bands were previously assigned to carbonates on Al_2O_3. Careful inspection of the spectra collected during reduction demonstrated that nitrate species were either reacting or desorbing while CO_X type species were adsorbing on the Al_2O_3. The nitrate feature at 1551 cm^{-1} decreased in intensity while a band assigned to a broad CO_X peak appeared in the 1650 – 1360 cm^{-1} region and grew in intensity. Similarly, the nitrate bands

at 1295 and 1241 cm^{-1} decreased in intensity, while a CO_X band appeared at 1285 cm^{-1} and grew in intensity.

Reduction by CO also resulted in formation of intense bands at 2230 and 2041 cm^{-1}. The band at 2230 cm^{-1} was assigned to an isocyanate (NCO) on Al_2O_3 and the band at 2041 cm^{-1} was assigned to a CO-carbonyl on Pt. Cycling using C_3H_6 as the reductant also resulted in formation of a band around 2020 cm^{-1}. The nature of this band appeared to be quite complex and might involve transience of the oxidation state of Pt or an adsorbed CO_X type species on Pt. Initially this band was centered at 2028 cm^{-1} with a shoulder at 2090 cm^{-1}. Increased time of exposure caused the band to grow in intensity and shift to 2022 cm^{-1}. Further exposure resulted in decreased intensity and a shift to 2005 $cm^{-1,}$ then 1993 cm^{-1}. The shoulder at 2090 cm^{-1} was always observed. The mobility and intensity of this peak has not been discussed in the literature and was only observed for Pt/Al_2O_3 and it is not clear if multiple species are responsible for this behavior. A more detailed investigation regarding this phenomenon was not conducted, as it was not immediately relevant to NSR catalysts.

In summary, Pt/Al_2O_3 catalysts exhibited minor storage of NO_X as nitrates on Al_2O_3 during lean periods and the stored nitrates demonstrated limited stability in He at 350 °C. Removal of nitrates during rich periods occurred rapidly for H_2, CO and C_3H_6 and resulted in formation of CO_X type adspecies when CO and C_3H_6 were used as reductants.

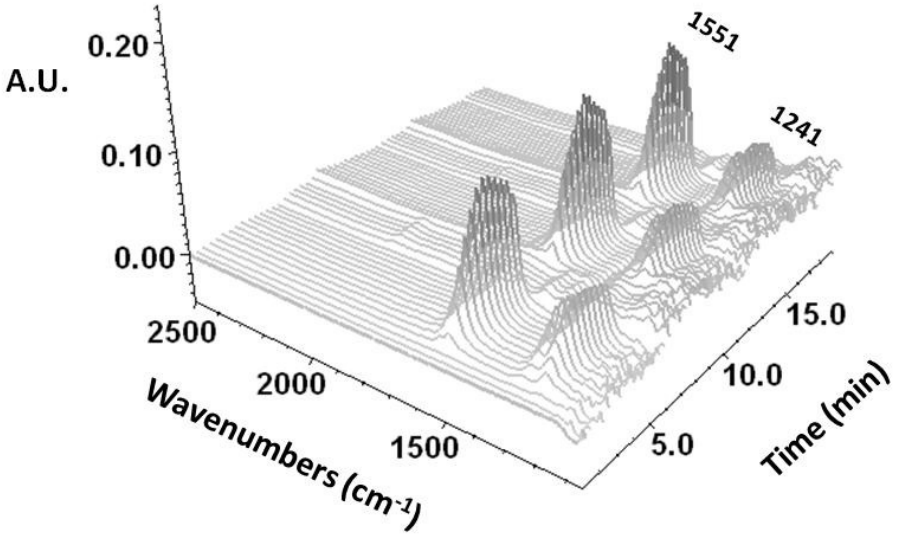

Figure A9. *In situ* cycling over Pt/Al_2O_3 at 350 °C using 9000 ppm H_2 as the reductant.

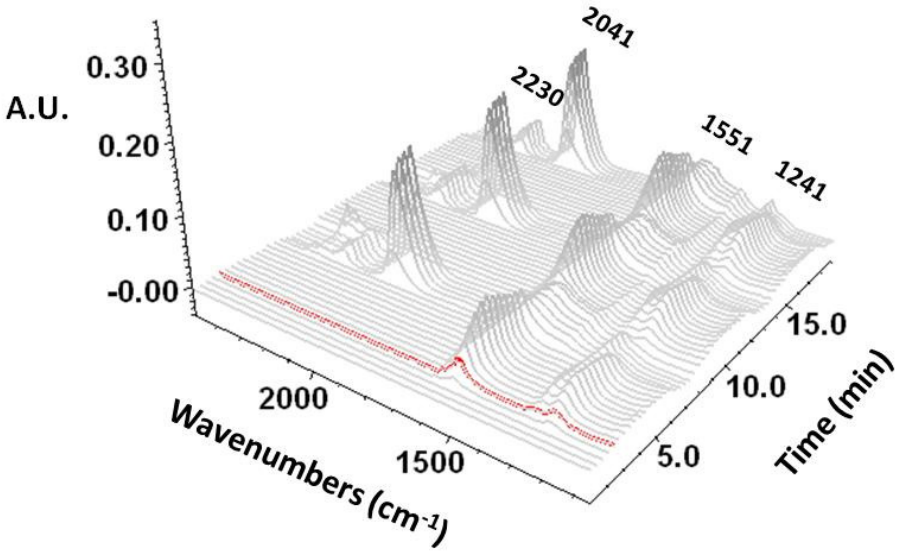

Figure A10. *In situ* cycling over Pt/Al_2O_3 at 350 °C using 9000 ppm CO as the reductant.

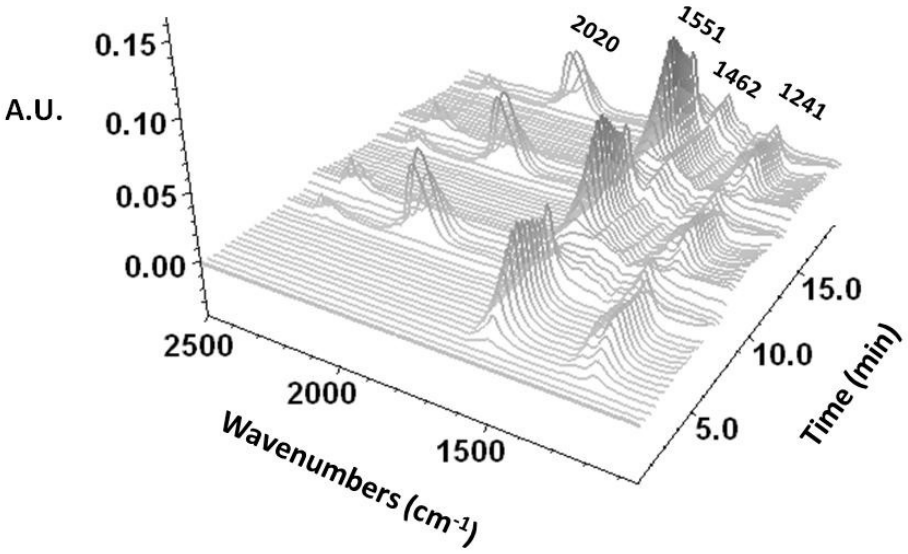

Figure A11. *In situ* cycling over Pt/Al_2O_3 at 350 °C using 1000 ppm C_3H_6 as the reductant.

<u>Ba/Al$_2$O$_3$</u>

In situ cycling using H_2 as the reductant on a Ba/Al_2O_3 catalyst yielded a band at 1206 cm^{-1} during the first lean period, which was previously assigned to bridging bidentate nitrite on Ba (Fig. A12). The intensity of this band remained constant during the subsequent He flush, which demonstrated the increased stability of nitrites formed on Ba in comparison nitrates/nitrites formed on Al_2O_3. Interestingly, exposure of the nitrated Ba/Al_2O_3 catalyst to 9000 ppm of H_2 did not result in removal of the stored NO_X species. Instead, the band at 1206 cm^{-1} continued to grow slowly during each subsequent lean period throughout the experiment. This implied that Ba/Al_2O_3 was inactive during reduction. Fig. A12(B) more clearly demonstrates this concept, where the band at 1206 cm^{-1} remained stable even after exposure to H_2 for 2 min. For Pt/Al_2O_3, the nitrate bands were removed completely during rich periods.

In situ cycling using CO and C_3H_6 as the reductants yielded similar results to cycling using H_2, where nitrites were initially formed and stable in He. However, exposure to CO or

C_3H_6 resulted in the formation of carbonates, as shown in Figs A13 and A14. Notice how the bands at 1560 and 1350 or 1335 cm^{-1} grew rapidly during the first rich period. During the following lean period, CO_X adspecies were desorbed in favor of nitrite formation. This type of behavior was expected since both NO_X and CO_X are acidic species and compete for the same adsorption sites on the basic BaO. Fridell et al. [41] previously demonstrated the poor storage and reduction properties of Ba/Al_2O_3 catalysts, where transient reactor measurements demonstrated insignificant storage and conversion of NO_X to N_2. Nova et al. [63] observed conversion of NO_X using NH_3 as the reductant for a Ba/Al_2O_3 catalyst beginning at 320 °C. Conversion of NO on a $Pt/Ba/Al_2O_3$ began around 100 °C when NH_3 was used a reductant and around 60 °C when H_2 was used as reductant. The considerably lower NO_X conversion temperature demonstrated the advantage of adding Pt to Ba/Al_2O_3.

Fig. A13 appears to demonstrate higher stability of nitrites in comparison to carbonates, where bands 1562 and 1338 cm^{-1} decreased when CO was removed during lean periods, but the nitrite bands at 1210 cm^{-1} appeared to grow with each lean period, as observed for H_2 cycling. Weak bands at 2224 and 2164 cm^{-1} were also observed, as seen in Fig. A13(B). These bands were assigned to NCO species on Al_2O_3 and Ba, respectively [24]. Formation of isocyanates in the absence of Pt was unexpected because these species have been reported to form only on the surface of precious metals [403]. So, the presence of NCO species indirectly implied that minimal reduction was occurring even in the absence of Pt.

Figure A14 demonstrates that when C_3H_6 was used, lower intensities of CO_X adspecies were formed. Additionally, no isocyanate species were observed. These results implied that C_3H_6 was less effective than CO, which was in agreement with results reported by other groups [27].

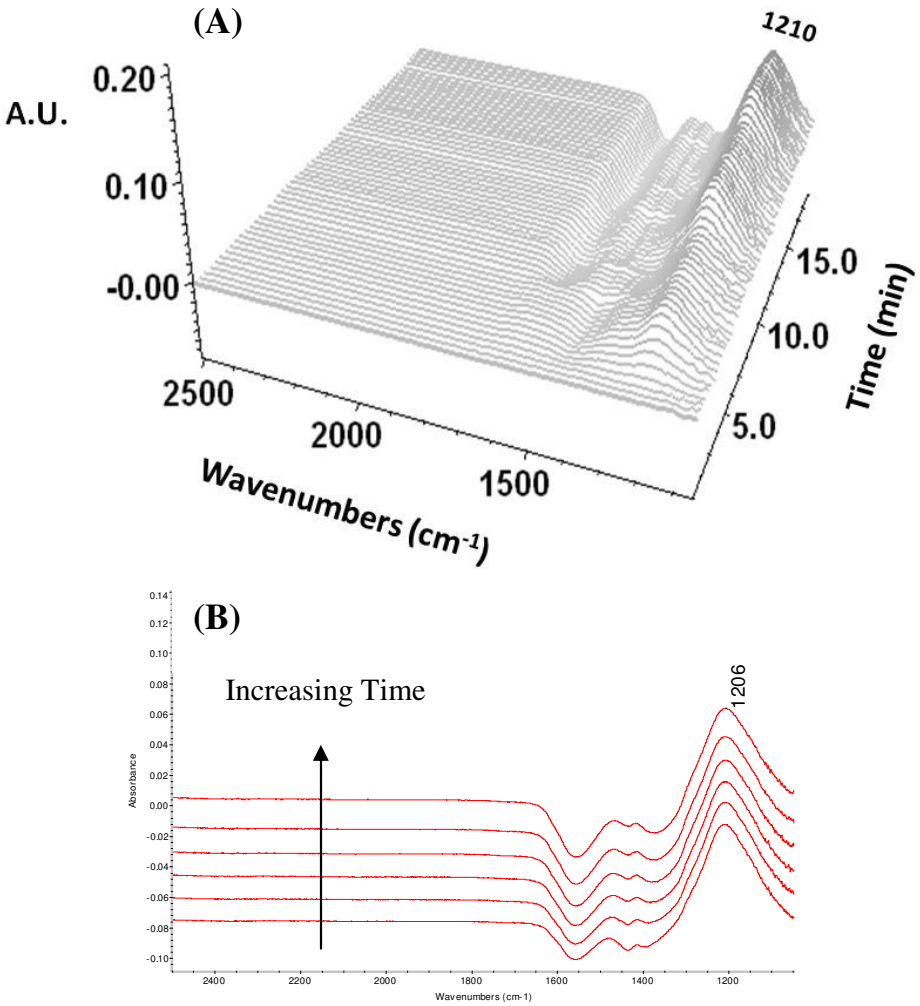

Figure A12. *In situ* cycling on Ba/Al_2O_3 at 350 °C using 9000 ppm H_2 as the reductant. (A) The 3D representation showing all 56 spectra collected during the cycling experiment and (B) Depicts spectra collected during the 2nd rich period.

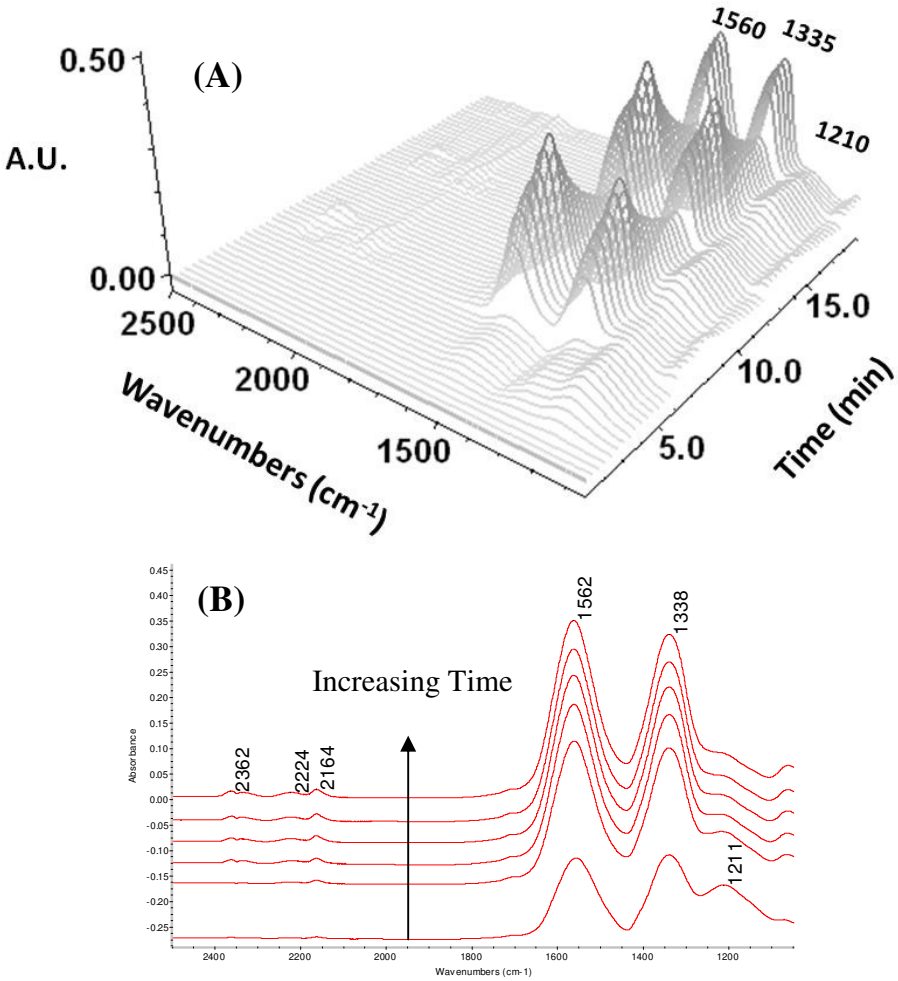

Figure A13. *In situ* cycling on Ba/Al_2O_3 at 350 °C using 9000 ppm CO as the reductant. (A) The 3D representation showing all 56 spectra collected during the cycling experiment and (B) Depicts spectra collected during the 2nd rich period.

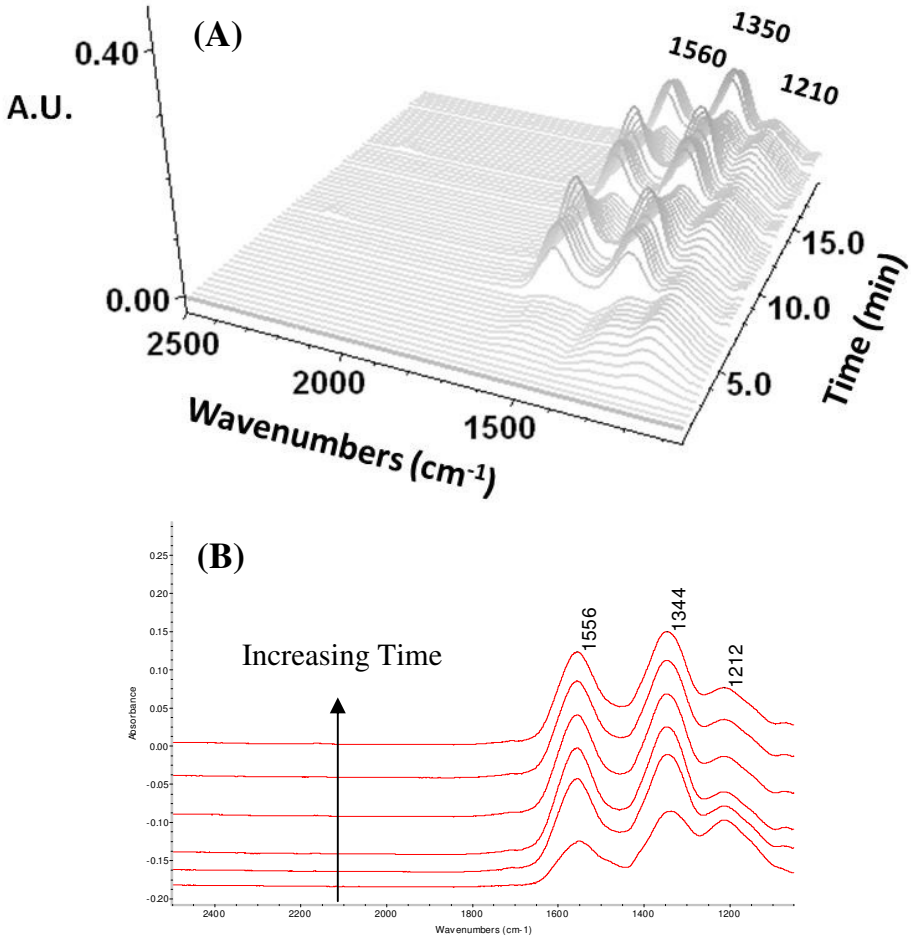

Figure A14. *In situ* cycling on Ba/Al_2O_3 at 350 °C using 1000 ppm C_3H_6 as the reductant. (A) The 3D representation showing all 56 spectra collected during the cycling experiment and (B) Depicts spectra collected during the 2nd rich period.

PT/BA/AL$_2$O$_3$

In situ cycling over Pt/Ba/Al_2O_3 catalyst resulted in 3 distinct regions in the FTIR spectra, as shown in Fig. A15. During the first lean period, bands at 1420 and 1310 cm^{-1} formed and grew rapidly. These bands were previously assigned to ionic nitrates on Ba and were stable in He at 350 °C. Admission of H_2 to IR cell resulted in rapid removal of these nitrate species. Fig. A15 (B) demonstrates the reduction process for H_2, where nitrates were completely removed after 80 s in H_2. The negative bands at 1526 and 1370 cm^{-1} were difficult to assign. They could represent decomposition of $BaCO_3$, but previous CO + O_2 adsorption experiments (omitted for brevity) yielded bands at 1570 and 1335 cm^{-1}. Another possibility could be partial reduction of the BaO surface. Roedel et al. [404] demonstrated that BaO exhibits bands at 1693, 1467 and 1370 cm^{-1} if studied by DRIFTS and bands at 1641 and 1433 cm^{-1} if studied by transmission IR. Later cycling experiments (Fig. A16 and A17) exhibited bands at 1562 and 1350 cm^{-1} for reduction of NO_X by CO and bands at 1556 and 1367 cm^{-1} for reduction of NO_X by C_3H_6.

While some aspects remain unclear, the synergistic effect of incorporating both a precious metal and storage component was clear. The cycling experiments on Pt/Al_2O_3 showed poor storage, but implied complete reduction. The cycling experiments on Ba/Al_2O_3 showed both poor storage and poor reduction. Combining Pt and Ba on Al_2O_3 demonstrated much higher storage capacity and implied complete reduction during rich periods. Since operando methods were not employed, it was not possible to determine the cycle averaged NO_X conversion or selectivity to N_2, but effective removal of nitrates during rich periods at 350 °C was clearly established.

In situ cycling using CO as the reductant yielded a more complex picture than cycling in H_2, as seen in Figure A16. This was due to simultaneous formation of CO_X adspecies as nitrates

were removed/reduced. Interestingly, the bidentate carbonates formed during reduction were more completely removed in subsequent lean periods over $Pt/Ba/Al_2O_3$ catalysts than Ba/Al_2O_3 catalysts. Careful examination of the bands at 1565 and 1310 cm^{-1} demonstrates this phenomenon, where the band at 1565 corresponds to CO_X adspecies and the band at 1310 represents ionic nitrates.

The second major difference between cycling in H_2 and cycling in CO was the formation of intense bands at 2220 and 2162 cm^{-1}. These bands were previously assigned to isocyanate species on Al_2O_3 and Ba, respectively. The presence of these bands and their intensity has led many groups to the conclusion that isocyanate species are intermediates in the reduction on nitrates to N_2 [16,24,27,64,289,290]. While this is one possibility, researchers investigating NO_X reduction mechanisms on three-way catalysts concluded that reaction through isocyanate intermediates only accounted for 5% of the total NO_X conversion observed [2]. However, the conditions and catalysts used for NSR applications are different than those used for TWCs and general conclusions made for these systems do not necessarily extend to NSR catalysts. Fig. A16 (B) depicts the 2^{nd} reduction period, where nitrates were removed/reduced and carbonates/formates and isocyanate species formed. A band at 2020 cm^{-1} also appeared and was assigned to a CO carbonyl on Pt. The isocyanate species and carbonyls were removed almost immediately in subsequent lean periods.

Fig. A17 demonstrates *in situ* cycling when C_3H_6 was used as the reductant. The results were very similar to cycling in CO, but less carbonate/formate species were formed and lower concentrations of isocyanate species were observed. In fact, the band at 2220 was no longer observed.

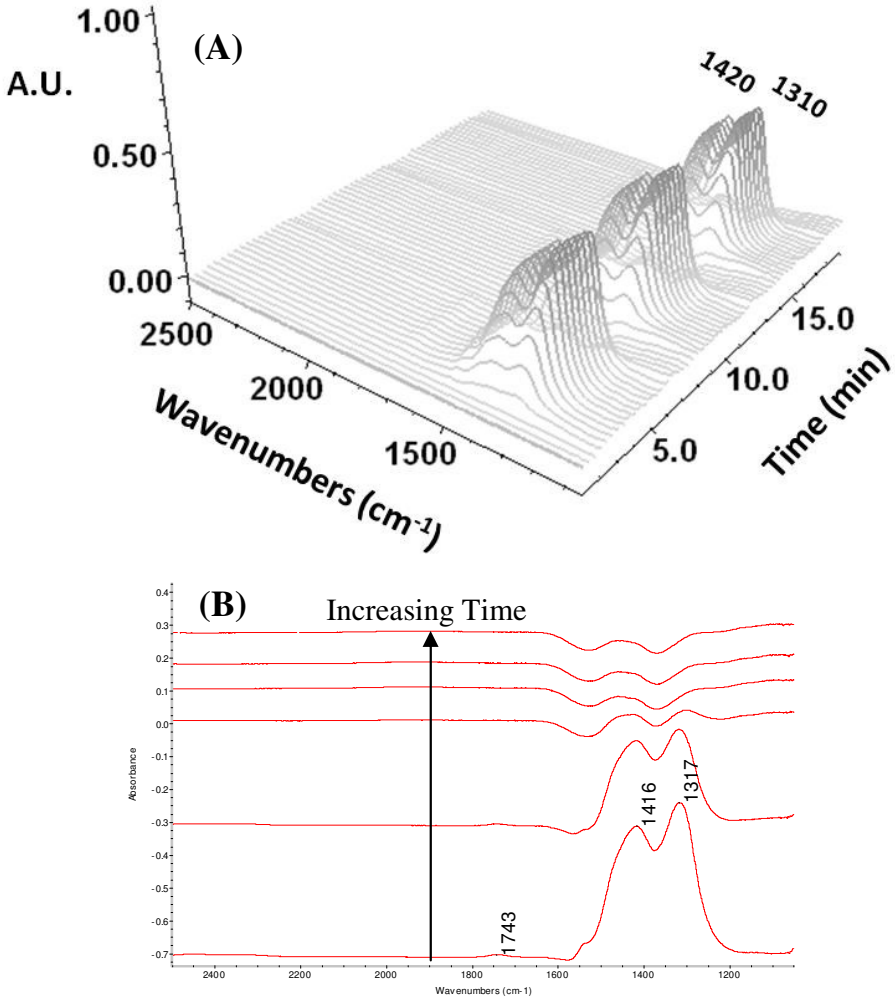

Figure A15. *In situ* cycling on $Pt/Ba/Al_2O_3$ at 350 °C using 9000 ppm H_2 as the reductant. (A) The 3D representation showing all 56 spectra collected during the cycling experiment and (B) Depicts spectra collected during the 2nd rich period.

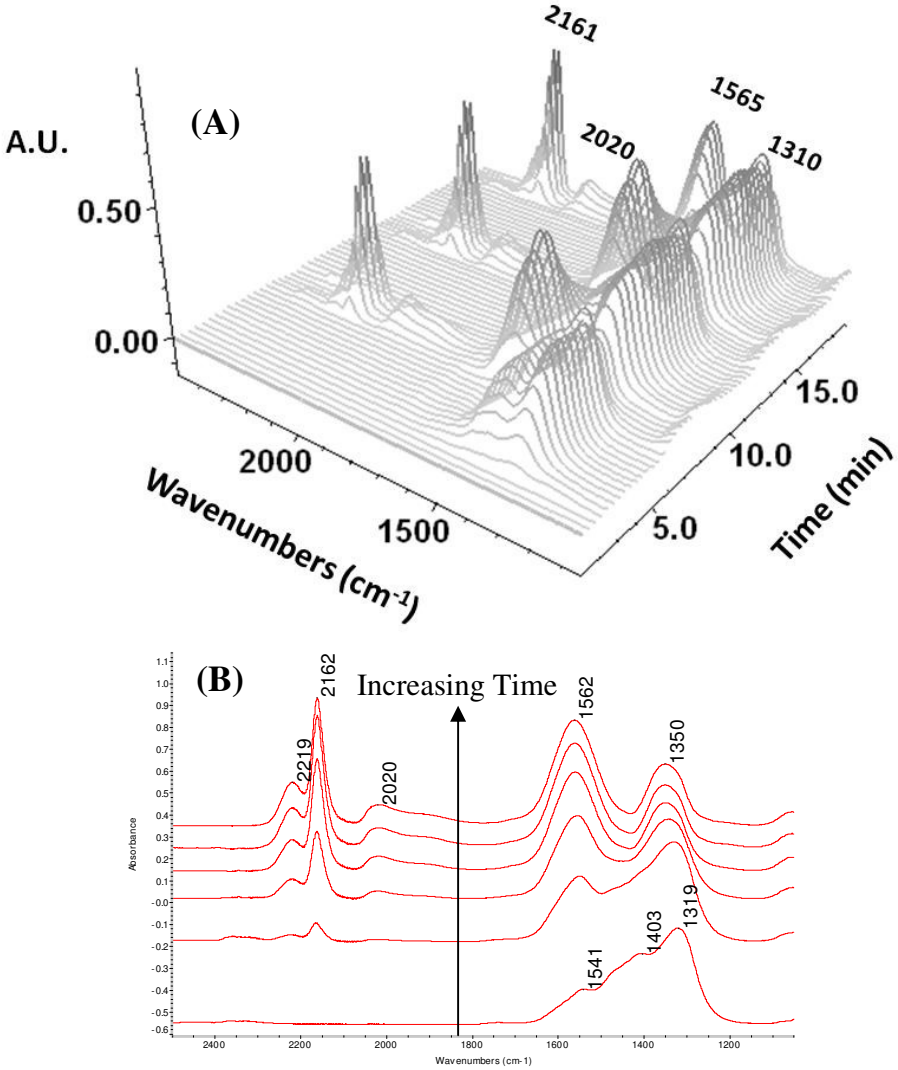

Figure A16. *In situ* cycling on $Pt/Ba/Al_2O_3$ at 350 °C using 9000 ppm CO as the reductant. (A) The 3D representation showing all 56 spectra collected during the cycling experiment and (B) Depicts spectra collected during the 2nd rich period.

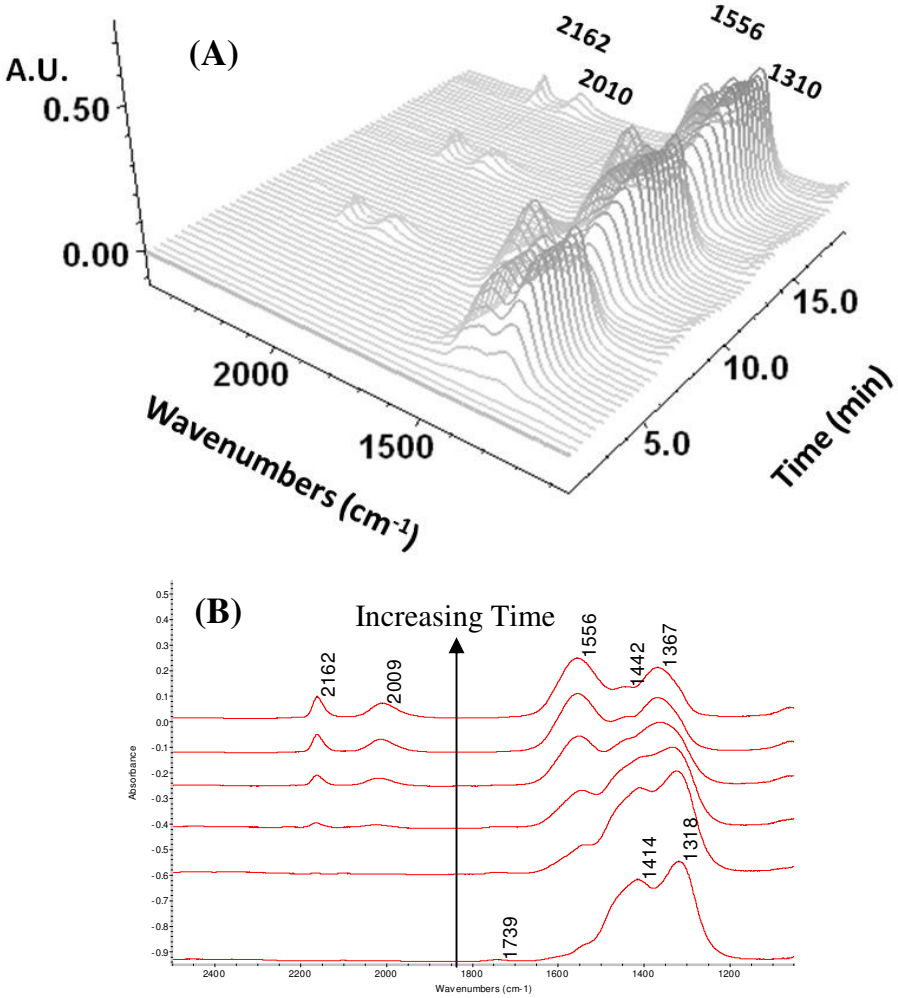

Figure A17. *In situ* cycling on $Pt/Ba/Al_2O_3$ at 350 °C using 1000 ppm C_3H_6 as the reductant. (A) The 3D representation showing all 56 spectra collected during the cycling experiment and (B) Depicts spectra collected during the 2nd rich period.

A.1.4 CONCLUSIONS

Exposure of pre-oxidized Al_2O_3, Pt/Al_2O_3, Ba/Al_2O_3 and $Pt/Ba/Al_2O_3$ to NO, NO + O_2 or NO_2 at RT or 350 °C resulted in formation of nitrites and/or nitrates for all catalysts investigated. The relative concentration between nitrates and nitrites, the total concentration of NO_X adspecies and the coordination of NO_X to Al_2O_3 or Ba was dependent on the storage temperature, the NO_X source (e.g. NO, NO_2 or NO + O_2), addition of Pt to Al_2O_3, addition of Ba to Al_2O_3, and addition of Pt and Ba to Al_2O_3. Storage of NO + O_2 at 350 °C on the $Pt/Ba/Al_2O_3$ catalyst occurred as ionic nitrates on Ba, with bands at 1420 and 1310 cm^{-1}, and as a bridging nitrate on Ba with a band around 1560 cm^{-1}. At short times, a bridging nitrite coordinated to Ba was observed for the $Pt/Ba/Al_2O_3$ catalyst, where Pt catalyzed conversion from nitrites to nitrates. In the absence of O_2, storage as nitrates was observed for the $Pt/Ba/Al_2O_3$ catalyst at 350 °C, but the transition from storage as nitrites to storage as nitrates occurred at longer times. O_2 increased storage capacity and facilitated conversion from nitrites to nitrates. Similarly, exposure of pre-oxidized Al_2O_3, Pt/Al_2O_3, Ba/Al_2O_3 and $Pt/Ba/Al_2O_3$ to CO at RT and 350 °C resulted in formation of CO_X adspecies for all catalysts investigated. Exposure of the $Pt/Ba/Al_2O_3$ catalyst to CO at 350 resulted in formation of bidentate carbonates with bands at 1560 and 1335 cm^{-1}. Storage experiments of both NO_X and CO_X demonstrated numerous bands, where overlap between bands corresponding to NO_X species on Al_2O_3 and Ba and CO_X species on Al_2O_3 and Ba greatly complicated definitive band assignments.

In situ cycling at 350 °C on Pt/Al_2O_3, Ba/Al_2O_3 and $Pt/Ba/Al_2O_3$ catalysts clearly demonstrated the synergistic effect of adding both Pt and Ba to NSR catalysts. Cycling on Pt/Al_2O_3 yielded low storage of NO_X and the nitrites/nitrates exhibited poor thermal stability. However, complete removal of nitrite/nitrate features was observed during rich phases when

employing H_2, CO or C_3H_6 as the reductant. Cycling on Ba/Al_2O_3 also yielded low storage, but the nitrites/nitrates were thermally stable. However, insignificant removal of stored nitrites/nitrates was observed during rich periods. Cycling on $Pt/Ba/Al_2O_3$ yielded appreciable storage of NO_X, high thermal stability of the nitrates/nitrites and rapid removal of nitrates/nitrites during reduction. Comparison of the cycling results on Pt/Al_2O_3, Ba/Al_2O_3 and $Pt/Ba/Al_2O_3$ led to the conclusion that Ba provided high storage capacity of NO_X as thermally stable nitrites/nitrates and Pt catalyzed both the storage and reduction period, where poor activity of the Ba/Al_2O_3 catalysts inferred precious metals to be an integral component of NSR catalysts. Reduction of stored nitrites/nitrates using CO and C_3H_6 led to the formation of isocyanate species, especially for Pt/Al_2O_3 and $Pt/Ba/Al_2O_3$. This again inferred Pt to play an influential role during reduction, as discussed at length in Chapter 2.

A.2 REVIEW: THE ROLE OF ISOCYANATE (NCO) INTERMEDIATES IN THE REDUCTION OF NO_X BY CO

A.2.1 PREFACE

Recently, there has been considerable interest regarding NO_X reduction mechanisms occurring on noble metal supported lean NO_X traps (LNT) or NO_X storage and reduction (NSR) catalysts. It is generally accepted that storage on these catalysts is preceded by oxidation of NO to NO_2 on metal sites, followed by spillover and storage on $BaO/BaCO_3$. However, much less is known about the reduction mechanism. The generally accepted mechanism for reduction by H_2 proceeds through an NH_3 intermediate, where NH_3 is ultimately responsible for the reduction of stored NO_X. Similarly, the mechanism for reduction by CO and hydrocarbons (HCs) reportedly proceeds through an isocyanate intermediate, which can be oxidized to N_2 and CO_2 or undergo hydrolysis to produce NH_3. The NH_3 could then further react, as observed for H_2, and ultimately form N_2. While this mechanism for CO and HCs seems reasonable, considerable skepticism has been expressed in past regarding this route. This review summarizes the current mechanisms proposed for reduction of NO_X over NSR catalysts when CO and C_3H_6 are used as reductants and discusses why isocyanate intermediates could potentially play more of a role than previously reported for other lean NO_X reduction catalysts.

A.2.2 REDUCTION OF NO_X BY CO AND HCS ON NSR CATALYSTS

Investigation of the rich period occurring on NSR catalysts is an inherently difficult process. Firstly, the reduction period is very short, which makes it very difficult to obtain accurate information regarding the state of catalytic sites during operation and *in situ* or

operando techniques with good temporal resolution are required. For example, understanding how the oxidation state of the metal changes during reduction may infer some mechanisms to be more likely than others, but collection of *in situ* XPS data during reaction may not be feasible due to the small time increments required. XPS spectra could be obtained by briefly exposing the catalyst to pulses of reductant, followed by subsequent evacuation and scanning, but it is unclear how this process would affect the surface chemistry and stability of species observed at ambient pressures. Experiments of this nature would be of great importance though because NO_X slip, an undesirable process describing the release of NO_X that exits the catalytic converter before reduction can occur, has been attributed to the inability of oxidized precious metals to reduce NO_X [38,72]. Olsson and Fridell [56] reported formation of Pt oxides on Pt/Al_2O_3 and $Pt/Ba/Al_2O_3$ catalysts after exposure to $NO + O_2$. Higher amounts of Pt oxides were formed on $Pt/Ba/Al_2O_3$ catalysts, which the authors attributed to the basic nature of BaO. So, if Pt supported on Ba/Al_2O_3 is especially susceptible to oxide formation and reduction of NO_X on oxidized Pt is slow or negligible, the length of the reduction period becomes very important because short reduction periods (≈1 -2 s) may be dominated by a metallic state not favorable for NO_X reduction.

Second, and more importantly, there are two processes occurring simultaneously during reduction that affect the net behavior observed. They include: 1.) release of NO_X from the storage sites and 2.) reduction of the released NO_X to N_2. Unfortunately, it is not possible to study these separately, which drastically complicates efforts in understanding the reduction mechanisms occurring on NO_X storage catalysts. Figure A18 is a general overview of the reduction of stored NO_X by CO and C_3H_6. Both the water gas shift (WGS) reaction and NH_3

formation were excluded for clarity. NH_3 is also a possible product, especially in the presence of water, as discussed in the following sections [290].

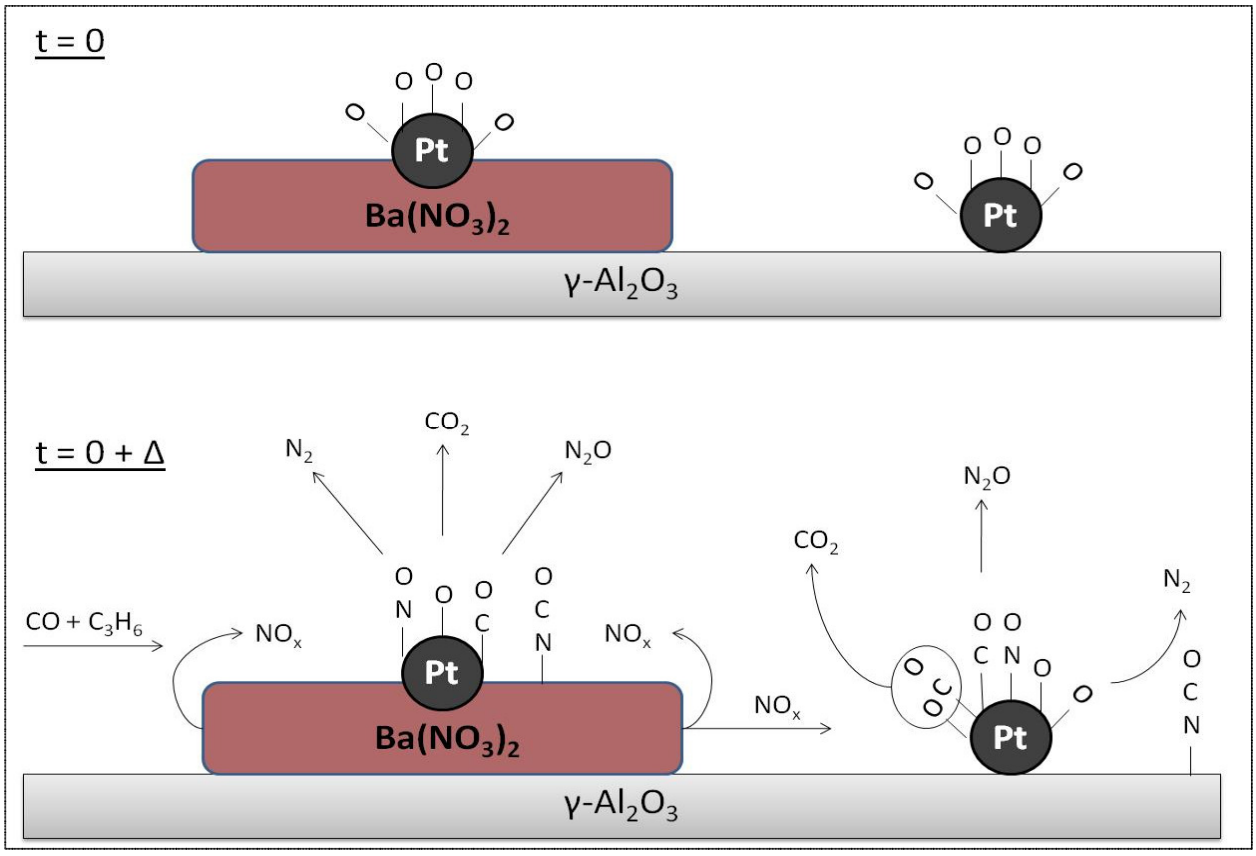

FigureA18. Overview of NO_X reduction (t=0 + Δ) on a $Pt/Ba/Al_2O_3$ catalyst after the storage period has ended (t=0). This figure is intended for clarification purposes only and should not be referenced as an actual representation of the real processes occurring during operation. These subtleties are still unclear and are the topic of this paper. *Note: The role of NH_3 as a product and intermediate was excluded for clarity.*

A.2.3 Release Mechanisms

Understanding the release mechanism of stored NO_X is critical because it determines the chemical nature of the NO_X that interacts with the reductants (i.e., NO vs. NO_2) and where the reduction actually initiates (i.e. on the surface of the support, storage material or metal). Several possibilities have emerged in the literature and include: 1.) thermal release due to heat evolved from oxidation of reductants during the switch from lean to rich conditions, 2.) destabilization of

stored NO_X due to removal of O_2 from the feed, 3.) destabilization of stored NO_X due to establishment of a net reducing environment, 4.) spillover of NO_2 from BaO to Pt and subsequent reduction, 5.) competition between NO_2, CO_2 and H_2O for the same storage sites, and lastly 6.) direct reaction of NO_X with the reductant on the surface of the storage component [59–61].

Kabin et al. [61] demonstrated that a significant exotherm can be generated by introduction of the reductant to lean exhausts. Although the authors were attempting to perform the experiment at 300 °C, the heat generated during oxidation of the reductant increased the average temperature to over 350 °C, with sharp spikes up to approximately 500 °C when the reductant was introduced, as shown in Figure A19.

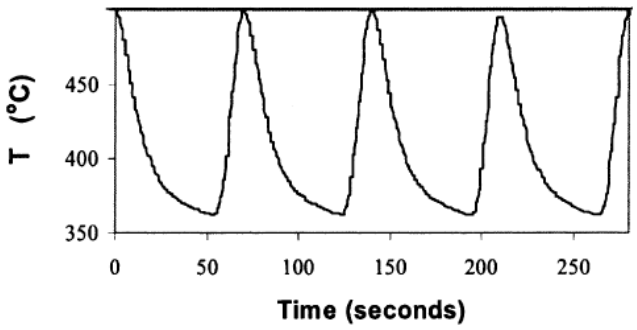

Figure A19. Temperature profile of the catalyst bed during 60 s lean, 10 s rich periods over 2.2%Pt/16.3%BaO/Al_2O_3 (w/w), where lean: 500 ppm NO, 5% O_2, 1000 ppm C_3H_6 and rich: 500 ppm NO, 5% O_2, 1.4% C_3H_6. Reprinted from Kabin et al., 2004 [18].

Additionally, Scotti et al. [405] performed temperature programmed desorption (TPD) of NO_2 stored at 350 °C, a relevant storage temperature, and determined that thermal evolution of NO_2 reached a maximum around 460 °C and thermal evolution of NO reached a maximum around 550 °C on Ba/Al_2O_3, as shown in Fig. A20. NO_2-TPD performed on Pt/Ba/Al_2O_3 catalyst resulted in the release of mainly NO at temperatures slightly lower than 460 °C, where evolution as NO instead of NO_2 for Pt containing samples was explained by reduction

of NO_2 to NO over Pt. A decrease in the thermal stability of Ba nitrates due to addition of precious metals was also reported by Prinetto et al. [34].

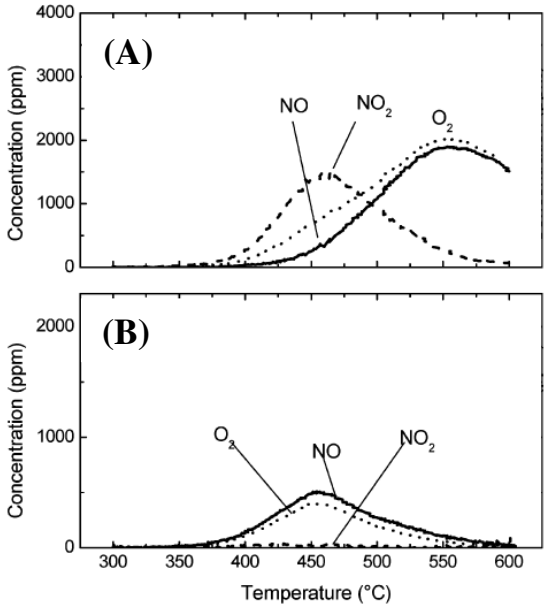

Figure A20. TPD profiles of **(A)** 20%Ba/Al_2O_3 (w/w) and **(B)** 1%$Pt/20\%Ba/Al_2O_3$ (w/w) after exposure to 1000 ppm NO_2 in He at 350 °C, Scotti et al. [405].

Since Kabin et al. [61] routinely observed temperatures above 500 °C for cycling and Scotti et al. [405] reported that thermal evolution began below 500 °C, one could argue that thermal evolution of NO_X from Ba is a reasonable release mechanism. However, Nova et al. tested the validity of a thermal release mechanism by performing temperature programmed surface reaction (TPSR) measurements on Ba/Al_2O_3 and $Pt/Ba/Al_2O_3$ (20/100 and 1/20/100 w/w, respectively) catalysts under near-isothermal conditions [60]. Both catalysts were saturated using NO + O_2 or NO_2 mixtures at 350 °C, flushed with He, cooled to room temperature, and then ramped at 15 °C/min in 2000 ppm H_2. If thermal evolution of NO_X was crucial for reduction to occur, reaction of the stored nitrates would not be expected to begin until approximately 350 °C. This was indeed the case for Ba/Al_2O_3, as consumption of hydrogen did not begin until approximately 350 °C. As a side note, establishment a net reducing environment

did not seem to dramatically change the thermal stability of the stored nitrates (≈ a 20 °C shift to lower temperatures). However, it did affect the product distribution, most likely through Reactions A1 and A2. Ba/Al_2O_3 unexpectedly catalyzed this reaction, but it was unclear how. In the absence of a catalyst, consumption of H_2 in NO_2 (g) was not observed even when the temperature was increased to 500 °C. The authors speculated that stored NO_X may have played a role.

$$NO_2 + H_2 \rightarrow NO + H_2O \quad \text{(A1)}$$

$$NO + H_2 \rightarrow \frac{1}{2}N_2 + H_2O \quad \text{(A2)}$$

Alternatively, consumption of hydrogen during H_2-TPSR on the $Pt/Ba/Al_2O_3$ sample began at 150 °C, which was significantly lower than the temperature required for thermal release. Several mechanisms were proposed that could explain this behavior including: 1.) adsorption and activation of hydrogen on metal sites, where hydrogen could then spill over onto to the support and destabilize stored NO_X, 2.) direct reduction of NO_X by activated hydrogen on the support, or lastly, 3.) NO_2 released from the storage component could diffuse to the metal, where reduction by hydrogen could occur. The role of the reactions occurring directly on the support is unclear, but Forzatti et al. [290] observed formation of weak bands assigned to isocyanates adsorbed Ba and Al on a Ba/Al_2O_3 catalysts, which essentially proved that reaction on the support was possible even without the presence of a precious metal to activate reductants. Figure A21 depicts the dramatic changes observed between H_2-TPSR on Ba/Al_2O_3 and $Pt/Ba/Al_2O_3$ catalysts.

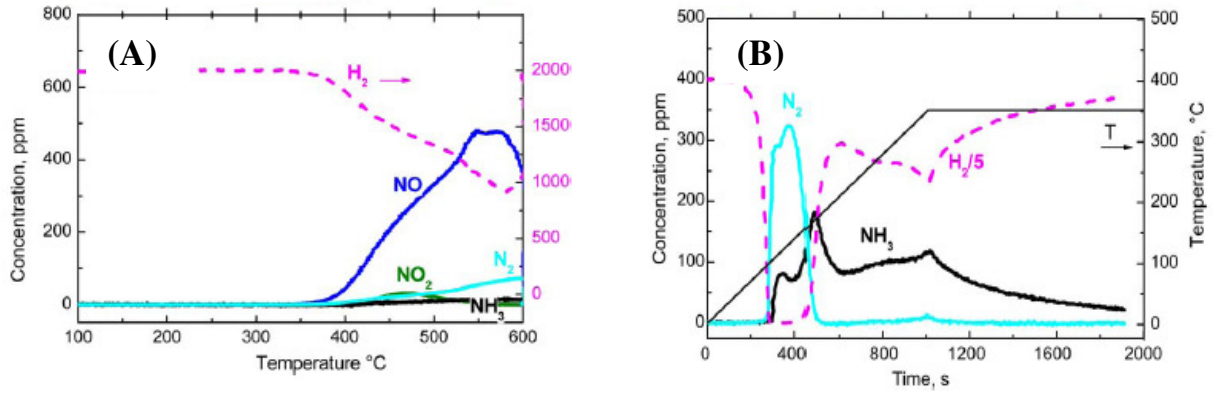

Figure A21. TPSR profiles of **(A)** 20%Ba/Al_2O_3 (w/w) and **(B)** 1%Pt/20%Ba/Al_2O_3 (w/w) after exposure to NO_X in He at 350 °C, cooled to RT, and then ramped at 15 °C/min in 2000 ppm H_2, Nova et al. [60].

The first two release mechanisms proposed by Nova et al. [60] are easily visualized, while the latter is harder to grasp. Liu and Anderson [59] explained this mechanism more clearly and argued that the release of NO_X was based on the law of microreversibility. In other words, equilibrium is established between the NO_X stored on the Ba at the Pt/Ba interface. When hydrogen is introduced, it reacts with the NO_X on Pt, which then desorbs and essentially opens the gate and allows more NO_X to pour onto the Pt surface where it can react with additional hydrogen. This process would continue until the supply of hydrogen was exhausted or all the NO_X stored on the surface was consumed.

NO_X release due to removal of oxygen from the gas phase was also suggested as a release mechanism, according to Reactions 3 and 4 [59]. However, this is very unlikely since NO_X species adsorbed on the surface survived evacuation even at 500 °C [34]. Su and Amiridis [22] reported similar results regarding the stability of stored nitrite/nitrate species in He at 350 °C.

$$(NO_3^-)_2 \Leftrightarrow O^{2-} + \frac{1}{2}O_2 + 2NO_2 \qquad \text{(A3)}$$

$$(NO_3^-)_2 \Leftrightarrow O^{2-} + \frac{1}{2}O_2 + NO \quad \text{(A4)}$$

The last NO_X release mechanism worth mentioning involves competitive adsorption between CO_2, NO_2, H_2O and SO_2. Generally, $BaSO_4 >> BaCO_3 \geq Ba(NO_3)_2$ in terms of thermodynamic stability [44,105]. Therefore, if $Ba(NO_3)_2$ was exposed to CO_2 in the absence of NO_X, you would expect exchange between $Ba(NO_3)_2$ in favor of $BaCO_3$ and the rate of exchange would depend on the concentration of CO_2 and the temperature. Similarly if $BaCO_3$ was exposed to NO_X in the absence of CO_2, you would expect to exchange $BaCO_3$ for $Ba(NO_3)_2$. In reality, this is exactly what you observe experimentally and this type of methodology is used to remove bulk-like $BaCO_3$ from samples for FTIR measurements because $BaCO_3$ strongly absorbs infrared light at 1450 cm^{-1} [179,290]. SO_2, on the other hand, essentially irreversibly binds to BaO under the temperatures and conditions present during typical NSR operation. This leads to deactivation of the catalyst, where the degree of deactivation was observed to be directly proportional to the amount sulfur to which the catalyst has been exposed and harsh regeneration treatments must by employed to recover activity [105,197]. While competitive adsorption is almost certainly occurring, it is probably not the most dominant release mechanism for stored NO_X. Instead, it is more likely that the working capacity (defined here as the total number of sites available for NO_X storage) of the catalyst decreases, which impairs performance as observed by Epling et al. [181] when CO_2 and water were included in the reaction mixture.

In conclusion, the most likely mechanisms for release of NO_X are as follows: (1) adsorption and activation of reductant molecules on metal sites, which then spill over onto to the support and destabilize stored NO_X, 2.) direct reduction of NO_X on the support by activated reductant molecules and lastly, 3.) spillover of NO_2 from BaO to Pt, according to the law of

microreversibility, and subsequent reduction on precious metal sites. Thermal release due to heat evolved during oxidation of reductants and competitive adsorption of CO_2 could aid in the release of NO_X, but these mechanisms are not expected to be the driving force behind the release of stored NO_X. Release due to removal of O_2 or NO from the feed are expected to contribute very little (or not at all) to the total amount of NO_X released during storage.

A.2.4 Reduction Mechanisms

A considerable amount of effort was donated to the mechanism of NO_X release because the NO_X reduction mechanism is intimately tied to NO_X release. For example, a reduction mechanism that proceeds through a reductant that is activated over a precious metal that subsequently spills onto the support and reacts with stored NO_X is much different than a reduction mechanism that proceeds through NO_2 migration from the storage sites to the metal and subsequent reduction over the metal. While the differences between these two processes seems obscure, elucidation of the release and reduction mechanism will not only provide fundamental understanding of the chemistry occurring on these materials; it will allow researchers to target specific areas for improvement during systematic design of new catalysts better suited to carry out this chemistry (i.e. stabilization of activated hydrocarbon adspecies on the support may facilitate reduction if the process mainly proceeds though reactions taking place on the support). The following sections focus on NO_X reduction mechanisms for deNO_X catalysts and NSR catalysts.

A.2.4.1 Reduction Mechanisms on de-NO_X Catalysts

Removal of NO_X from both stationary and mobile sources has generated an immense amount of research activity because NO_X release can lead to acid rain, smog, and destruction of

ozone layer [1–3,5,7]. Therefore, regulations were introduced to control the release of NO_X into the environment and a vast array of catalysts have been proposed and tested for activity in the reduction of NO_X under an assortment of operating conditions including: NH_3-SCR on base oxides (e.g. V_2O_5 and Cr_2O_3), NH_3-SCR on metal zeolites (e.g. Cu-ZSM5), HC-SCR on precious metals and zeolites (e.g. Ag/Al_2O_3, Pt/Al_2O_3, Cu-ZSM5), reduction of NO in the presence of H_2, CO or HCs (TWCs) on supported metals (e.g. Cu_2O/Al_2O_3, Pt/Al_2O_3, Pd/Al_2O_3, Rh/Al_2O_3, Ir/Al_2O_3 and Ru/Al_2O_3) and lastly, direct decomposition of NO (e.g. Cu-Zeolites) [1–3,5,7].

This section briefly highlights mechanistic details for reduction of NO_X by CO and HCs on the catalysts relevant to this review. Many details were omitted for brevity since a complete review of all $deNO_X$ catalysts is out of the scope of this paper.

REDUCTION MECHANISMS OCCURRING ON HC-SCR CATALYSTS

Reaction 5 describes the desirable reaction products after a lean NO_X mixture has been treated using a HC-SCR catalyst, where zeolite based, non-zeolitic oxide-based and noble metal based catalysts have all been investigated for their potential use in this application [2,3,5].

$$NO\ (g) + O_2(g) + HC \xrightarrow[HC-SCR\ Catalyst]{} N_2 + CO_2 + H_2O \quad (5)$$

Zeolite based catalysts are generally composed of Cu supported/exchanged on mordenite or ZSM5 and can only achieve high activity (conversion of 66%) in a narrow temperature range (150-230 °C) and are highly susceptible to deactivation by water [3]. Therefore, application in automotive exhaust systems is unlikely and these catalysts will not be discussed further.

Non-zeolitic oxide-based catalysts are generally composed of Co, Ni, Cu, Fe, Sn, Ga, In, or Ag supported on Al_2O_3, TiO_2, ZrO_2 or MgO [5]. Of these, Ag/Al_2O_3 has generated the most

interest because it offers the highest activity and selectivity [5]. While the reduction mechanism occurring on these catalysts is still unclear, several observations have been reached regarding the activity of these materials and include: 1.) The ability of the material to form adsorbed NO_X species, which is most likely preceded by oxidation of NO to NO_2 and subsequent spillover, 2.) The ability of the material to form partially oxidized hydrocarbon adspecies, and 3.) The ability of adsorbed NO_X and hydrocarbon species to react with one another to form organo-nitrogen intermediates, where decomposition leads to cyanides, isocyanates, NH_3 and activated NH_3 (-NH_2), which can then further react with other adsorbed NO_X species, or gas phase NO [3,5]. When NO_2 was used instead of NO as the NO_X source, the rate increased and implied that NO_2 may play a critical role in the overall mechanism. Additionally, reaction of NO_X with oxygen containing HC species (e.g. alcohols instead of propylene) increased the rate, which suggested that adsorbed, partially oxidized hydrocarbon intermediates may also be an important intermediate. Lastly, isocyanate and cyanide species were observed spectroscopically, which supported their role as intermediates. Fig. A22 summarizes this mechanistic scheme. Thibault-Starzyk et al. [304] also recently reported that the transition from a cyanide to isocyanate intermediate was an integral step in this reduction mechanism [26]. Fig. A23 summarizes the updated mechanism based on their results.

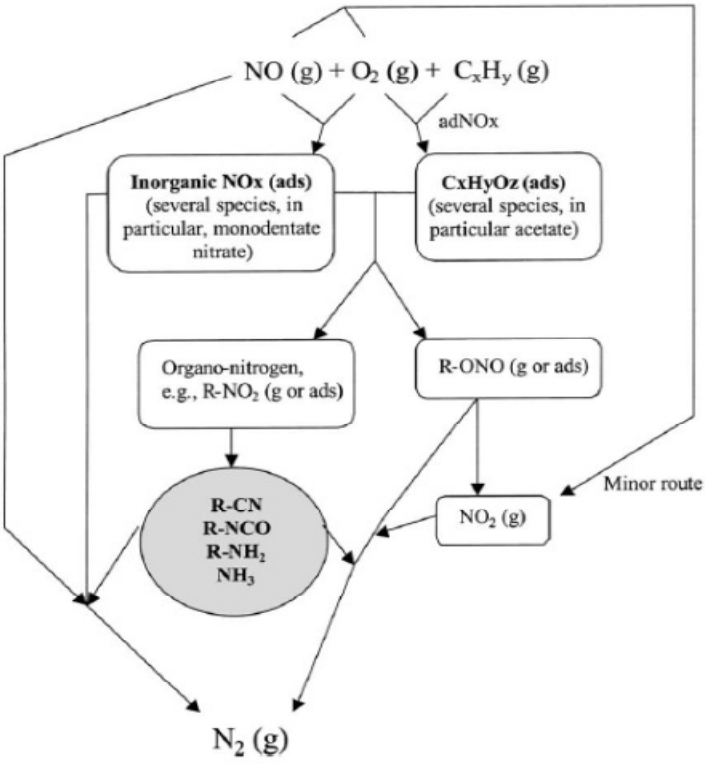

Figure A22. Possible reaction scheme of HC-SCR of NO occurring on Ag/Al_2O_3 catalysts, Burch et al. [5].

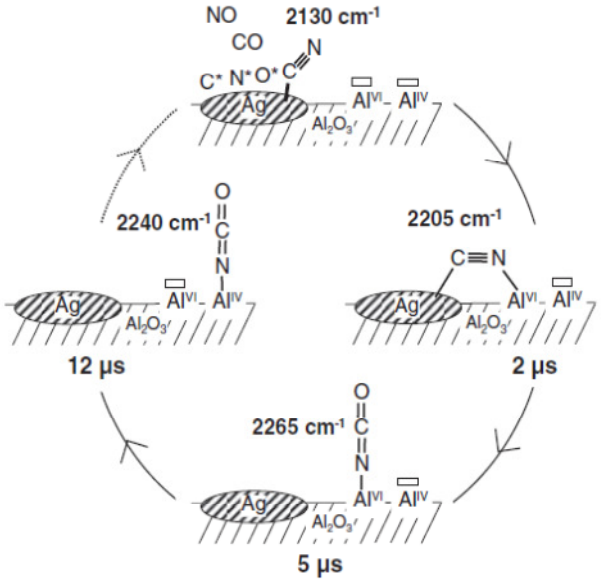

Figure A23. Updated HC-SCR of NO reaction mechanism occurring on Ag/Al_2O_3 when CO was used as the reductant molecule, Thibault-Starzyk et al., 2009 [26].

Noble metal based catalysts were also investigated for activity in the HC-SCR reaction, where Ir and Pt supported catalysts seemed to be most active [2,3,5]. Three possible NO_X reduction mechanisms emerged for noble metal based HC-SCR catalysts including: 1.) a reduction of NO_X mainly through formation of cyanides or isocyanates, 2.) reduction through the formation of organo-nitrogen intermediates, or 3.) reduction through decomposition of NO on the surface of precious metals.

As opposed to previous investigations on Ag/Al_2O_3 catalysts, researchers have been much more reticent to propose that the main route for NO_X reduction on Pt/Al_2O_3 catalysts proceeds through cyanide, isocyanate or organo-nitrogen intermediates and controversy on the importance of these mechanisms persists. Both of these routes were proposed based on species observed spectroscopically (FTIR and XPS), but as Breen et al. point out, differentiation between spectator species and true reaction intermediates can be difficult [5]. Generally, the lack of kinetic data tied to cyanide, isocyanate and organo-nitrogen concentrations makes elucidation of their role in the reduction of NO_X difficult. However, these species cannot be excluded as potential reaction intermediates and the presence of water may greatly alter their relative importance since –NCO species can readily react with water. Reactions involving NCO adspecies can be described as follows [5]:

$$-NCO + NO \rightarrow N_2 + CO_2 \quad \text{(A6)}$$

$$-NCO + NO \rightarrow N_2O + CO \quad \text{(A7)}$$

$$-NCO + NO_2 \rightarrow N_2O + CO_2 \quad \text{(A8)}$$

$$-NCO + NO_2 \rightarrow N_2 + CO + O_2 \quad \text{(A9)}$$

$$-NCO + [O] \rightarrow N_2 + CO_2 \quad \text{(A10)}$$

$$-NCO + H_2O \rightarrow NH_3 + CO_2 + O_2 \quad \text{(A11)}$$

The last mechanism proposed for HC-SCR on platinum group metal involves reduction of the oxidized metal surface by hydrocarbons, followed by adsorption and decomposition of NO, where N(ads) combines with another N(ads) species to form N_2 [2,3,5]. Fig. A24 demonstrates this pathway. In conclusion, a variety of mechanisms have been proposed for HC-SCR of NO_X and the true mechanism is still unknown. Ag based systems are usually represented by mechanisms where isocyanate/organo-nitrogen intermediates dominate, but platinum group metal systems are preferentially described by NO decomposition mechanisms. In reality, some or all of these mechanisms may be operating simultaneously, where the relative contribution of each pathway is dependent on the temperature, concentration of NO/NO_2, concentration of reductant, concentration on O_2, particle size and the inherent properties of the metal and the support. In fact Meunier et al. [297] predicted drastically different behavior for Ag particles of varying sizes, where small particles oxidize NO to NO_2 and large particles dissociate NO. Fig. A25 depicts this behavior. Notice how the NO decomposition and reaction through isocyanate/organo-nitrogen intermediates mechanisms are both occurring simultaneously, but the Ag particle size selectively activates one process over another.

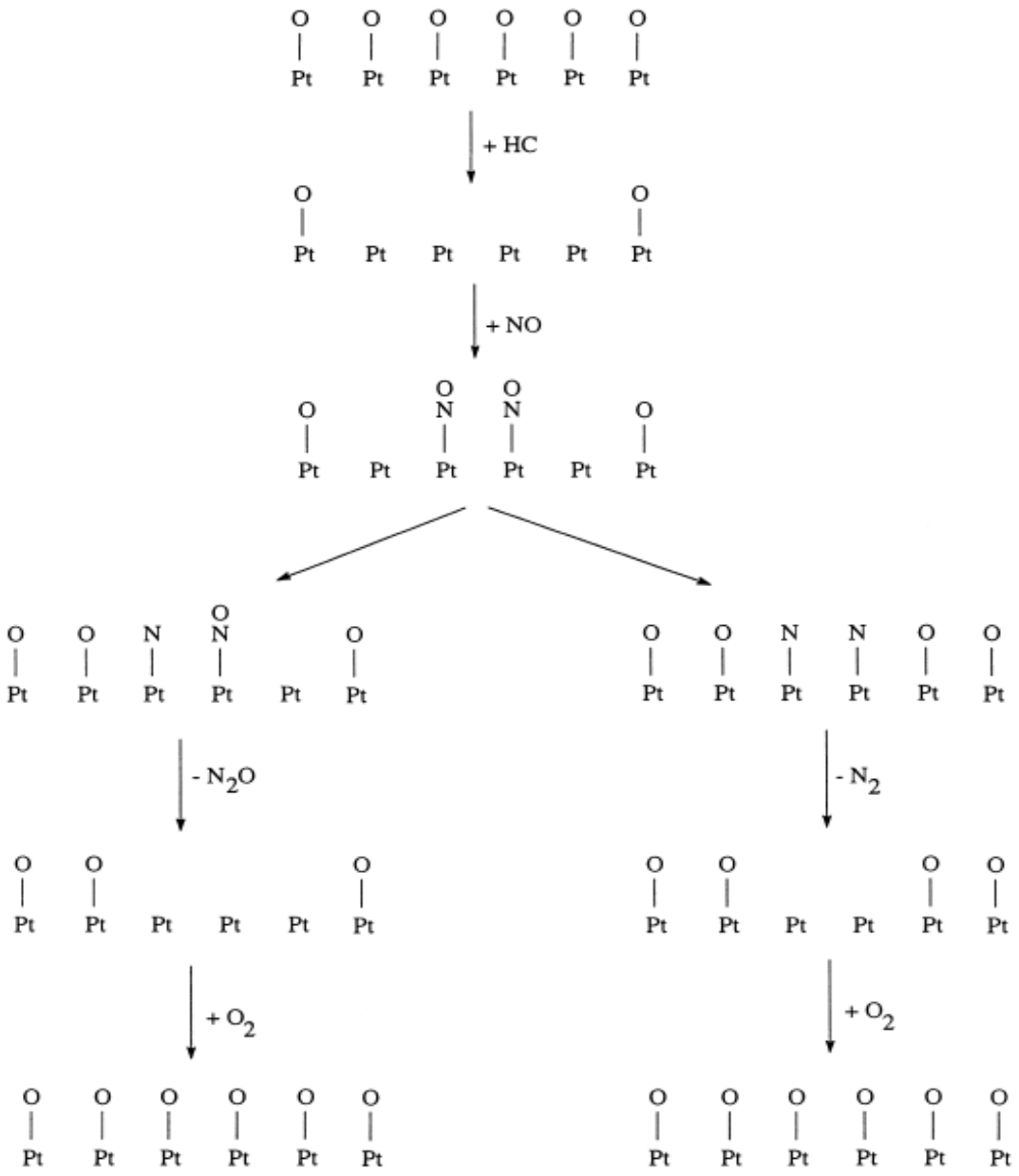

Figure A24. NO decomposition mechanism for HC-SCR of NO_X on platinum group metal supported catalysts, where the main role of the reductant is to remove adsorbed oxygen that can come from either adsorption of oxygen from the gas phase or decomposition of NO, Parvulescu et al. [2].

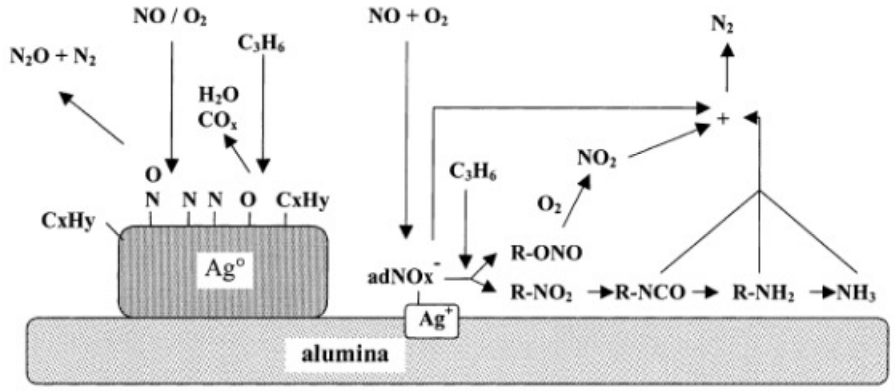

Figure A25. Example of how Ag particle size could activate one mechanism over another. Notice that large Ag particles can participate in NO decomposition, where the role of adsorbed HC species is to scavenge O(ads) from the metal surface. Small particles are reported to exist in an oxidized state and can only oxidize NO to NO_2. These site are responsible for catalyzing the NCO/organo-nitrogen route, Meunier et al. [297].

REDUCTION MECHANISMS BY CO AND HCS ON TWCS

The reduction of NO_X under conditions where the concentration of NO_X and available reductants is very close to the stoichiometric equivalent (i.e., TWCs) is generally accepted to proceed through decomposition of NO on the surface of a platinum group metal [2,3,5]. These catalysts are almost exclusively formulated using Pt or Pd supported on Al_2O_3, and promoted using Rh and/or ceria. Rh and Ru are thought to be highly active metals since they selectively decompose NO to N(ads) and O(ads). Ruthenium, while active, is poisoned by small amounts of gas phase O_2 and is therefore not relevant for TWCs or NSR catalysts [2]. Ir on the other hand has been reported to decompose NO even in the presence of large amounts of gas phase oxygen and may be interesting for future study [2,132]. Reactions A12 – A15 describe reduction of NO by CO on TWCs [2].

$$CO + M \rightarrow M - CO \quad \text{(A12)}$$

$$NO + M \rightarrow M - NO \quad \text{(A13)}$$

$$M + M - NO \rightarrow M - N + M - O \quad \text{(A14)}$$

$$M - N + M - N \rightarrow N_2 + 2M \quad \text{(A15)}$$

$$M - N + M - NO \rightarrow N_2O + 2M \quad \text{(A16)}$$

$$M - N + NO \rightarrow N_2O + M \quad \text{(A17)}$$

$$M - O + CO \rightarrow CO_2 + M \quad \text{(A18)}$$

$$M - N + CO \leftrightarrow M - NCO \quad \text{(A19)}$$

Notice that Reaction 19 also describes the formation of isocyanate species, where M-NCO could further react as described previously in Reactions A6-A11. Parvalescu et al. suggested that formation of these species, while observed spectroscopically, constituted only 5% of the overall N_2 production [2]. However, in a more recent review, Burch [3,5] suggests that this mechanism may be responsible for more N_2 production than initially thought. In summary, the mechanisms occurring on TWCs are pretty much identical to mechanisms presented for HC-SCR catalysts.

REDUCTION MECHANISMS BY CO AND HCS ON NSR CATALYSTS

Early reports on NSR catalysts mention the formation of isocyanates during reduction with carbon containing compounds, but their role in the reduction mechanism was not discussed [62]. Later, Fanson et al. [43] observed formation of strong bands at 2163 cm^{-1}, which they assigned to isocyanates on Ba. The intensity of the bands correlated well with the NO_X storage

capacity of the catalysts, which was suggested to imply their role as intermediates. However, if –NCO adspecies are spectators and account for only 5% of the total N_2 produced, as suggested by Parvalescu et al. [2], it is logical that increasing or decreasing the amount of NO_X stored on the catalysts would directly influence the concentration of isocyanate species as shown in Reaction A20.

$$[-NCO] = \varphi\,[Ba(NO_3)_2] \tag{A20}$$

Reaction A20 is meant for instructional clarification only and demonstrates the case where isocyanate species are formed via a side-route mechanism not responsible for production of N_2, where φ is the fraction of $Ba(NO_3)_2$ that participates in this reaction (φ=0.05 if you assume Parvalescu is correct). While the true value for φ is unknown, use of this Reaction infers that the concentration of isocyanate species should be directly proportional to the amount of NO_X stored by the catalyst, as observed by Fanson et al [43]. However, this does not establish these species as intermediates. It only infers that their relative concentration is dependent on the amount of total NO_X stored. To more conclusively assign these species as intermediates, the intensity of isocyanate species needs to be tied to the concentration of N_2 or other reduction products observed in the gas phase.

Lesage et al. [145] attempted to compare the formation of isocyanate species to evolution of N_2 by studying the NSR process on a Pt-Rh/Ba/Al_2O_3 catalyst using *operando* FTIR spectroscopy. Isocyanate species were observed, even in the presence of water, but their intensity was much lower in comparison to experiments conducted under dry conditions. Additionally, their formation was not convincingly tied to production of N_2. Figure A26 (A) depicts the formation of isocyanates during rich conditions and their removal during the subsequent lean period. Figure A26 (B) depicts the associated chemigrams and mass

spectrometer data. Notice that production of N_2 occurs mainly during the first few seconds of the rich periods (shown in grey) and drops off as the isocyanate species intensity increases. This led the authors to imply that isocyanates poisoned the catalyst and led to deactivation during reduction. Lesage et al. [145,146] reported that formation of isocyanate species was undesirable and suggested development of catalytic formulations to minimize formation of these species.

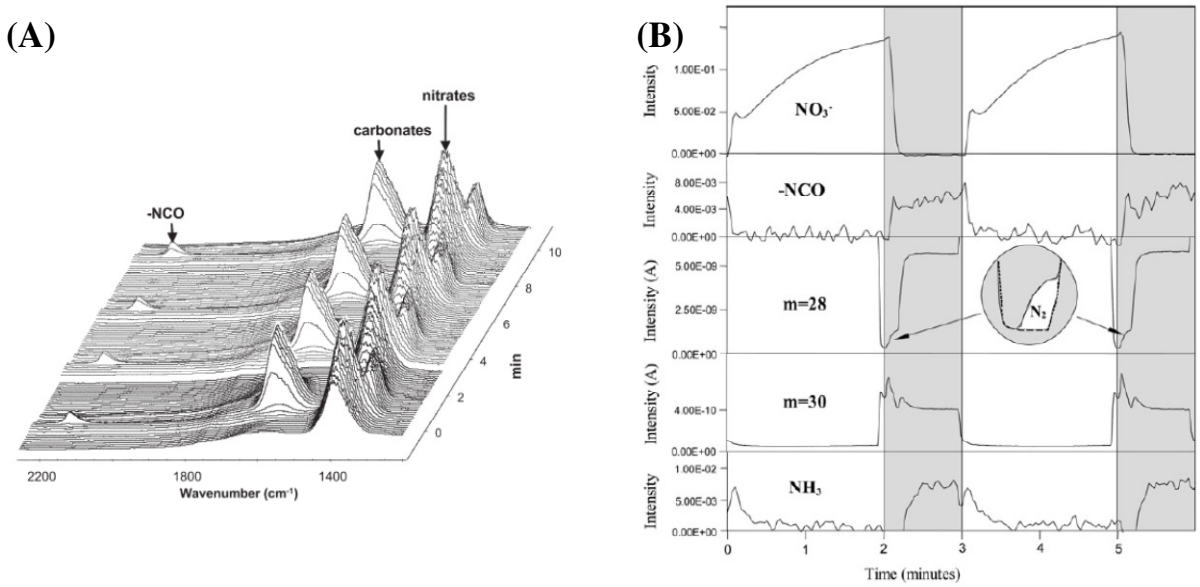

Figure A26. NSR mechanism on Pt-Rh/Ba/Al_2O_3 studied by *operando* FTIR spectrometry. (A) FTIR spectra demonstrating the formation of nitrates, carbonates and isocyanates during periodic lean/rich operations (Lean: 500 ppm NO, 10% O_2, 10% CO_2, 2% H_2O; Rich: 2% CO, 1% H_2, 10% CO_2, 2% H_2O). (B) Chemigrams and mass spectra data corresponding to (A), where m=28 corresponds to N_2 and m=30 corresponds to NO, Lesage et al. [145].

In a later work, Lesage et al. [146] compared the Pt-Rh/Ba/Al_2O_3 to their newly formulated Pt/K/CeO_2-Al_2O_3 catalyst and suggested that higher stability of nitrates on K resulted in a shift to longer times regarding formation of isocyanates. Figure A27 represents this shift. While nitrates on K are generally thought to be more stable, increased consumption of reductants due to the oxygen storage capacity of ceria could also be used to explain the shift to longer times [151,164]. Generally, Lesage et al. [145,146] seem to favor the route of NO decomposition leading to production of N_2, where formation and reaction of isocyanates could either poison the

catalyst or provide a supplementary route to N_2. Either way, isocyanate intermediates were not suggested as the main route to production of N_2.

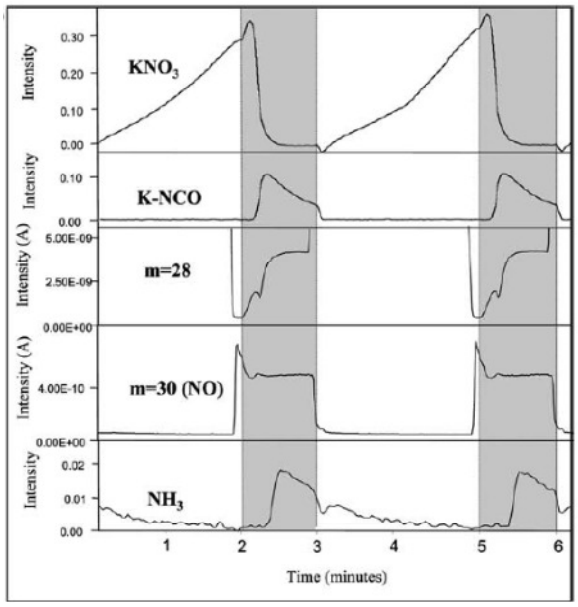

Figure A27. Chemigrams and mass spectra during periodic lean/rich cycling (Lean: 500 ppm NO, 10% O_2, 10% CO_2, 2% H_2O; Rich: 2% CO, 1% H_2, 10% CO_2, 2% H_2O) performed on a $Pt/K/CeO_2$-Al_2O_3 catalyst, where m=28 corresponds to N_2 and m=30 corresponds to NO. Reprinted from Lesage et al. [146].

In the absence of water, Abdulhamid et al. [27] observed formation of strong IR bands at 2220 and 2162 cm^{-1} on $M/Ba/Al_2O_3$ (M=Pt, Pd, or Rh) catalysts using both CO and C_3H_6 as reductants. These peaks have been confidently assigned to isocyanate species on Al and Ba, respectively [24,27]]. Since NCOs were observed during cycling using CO and C_3H_6, Abdulhamid et al. [27] concluded similar mechanistic pathways must operating for both reductants, but were reticent to suggest a reduction mechanism based on their data. Deterioration of Pt based catalysts was observed and was attributed to the formation of carbonyls on Pt or isocyanates on Al (2230-2220cm^{-1}) or Ba (2162 cm^{-1}). Interestingly, this behavior was not observed on Pd or Rh based catalysts.

Szailer et al. [24] on the other hand, proposed a fairly detailed mechanism based on their results using Pt/Al_2O_3 and $Pt/Ba/Al_2O_3$ catalysts. At low temperatures, decomposition of NO and reaction of N(ads) with CO to form NCO(ads) was active, but production of N_2 was low (<473 K). At higher temperatures (>573 K), NCO(ads) could react with stored NO_X to produce N_2. Addition of water drastically increased production of N_2. The following mechanism was proposed to explain these observations:

$$Pt - O + H_2 \rightarrow Pt^* + H_2O \quad \text{(A21)}$$

$$2Pt - N \rightarrow 2Pt^* + N_2 \quad \text{(A22)}$$

$$(x+1)Pt^* + NO_X \rightarrow xPt - O + Pt - N \quad \text{(A23)}$$

$$Pt - N + Pt - H \rightarrow Pt - NH_X + Pt - H \rightarrow NH_3 \quad \text{(A24)}$$

$$Pt - N + Pt - CO \rightarrow Pt^* + Pt - NCO \quad \text{(A25)}$$

$$Pt - O + CO \rightarrow Pt^* + CO_2 \quad \text{(A26)}$$

$$NCO(ads) + NO_X \rightarrow N_2 + CO_2 \quad \text{(A27)}$$

$$NCO(ads) + H_2O \rightarrow NH_2(ads) + OH(ads) \quad \text{(A28)}$$

$$NH_3 + NO_X + H_2O \rightarrow [NH_4NO_X] \rightarrow N_2 + H_2O \quad \text{(A29)}$$

Note: Pt^* represent a free Pt site and X(ads) represent a molecule adsorbed on a nondescript site

Reactions A21-A24 describe reduction by H_2 and were included to demonstrate that reduction of NO_X by H_2 or CO is preceded by decomposition of NO (Reaction A23). For H_2, the N adatom can either combine with another N adatom to form N_2 (Reaction A22) or react with H_2

to form ammonia (Reaction A24), where NH_3 can desorb un-reacted or selectively reduce NO_X (Reaction A29). Similarly for CO, the decomposed N adatom can either combine with another N adatom or react with CO(ads) to form isocyanates (Reaction A25). The authors admitted that reaction of two N adatoms cannot be excluded as a pathway for production of N_2 when CO is used as a reductant, but suggested that the main route proceeded through formation of isocyanates that react with water, oxygen or stored NO_X to ultimately form N_2. This claim is based on the observation that adding water and CO to the reactor during reduction increased production of N_2.

Two particularly important subtleties of this mechanism are worth mentioning. First, NO must decompose to an N adatom before it can react with CO to form an isocyanate. Therefore, both NO reduction mechanism share NO decomposition as a primary step. Second, isocyanate species were not observed on metal surfaces, but on the support – both Ba (2162 cm^{-1}) and Al_2O_3 (2220-2250 cm^{-1}) [24,27,43,62,64,145,146,289,290]. So, were isocyanate species reacting on the support with stored NO_X, or must they diffuse back to the surface of the metal to undergo reaction?

Recently, Breen et al. [16] reported reactor data consistent with the mechanism presented by Szailer et al., where a series of catalyst were tested in a fast transient reactor capable of 200 ms time resolution. This allowed the NO_X reduction process to be studied under realistic operating conditions (e.g., 60 s lean and 1.2 s rich). In this case, N_2 evolved in two distinct periods during reduction, the first occurred immediately after the switch from lean to rich and the second occurred immediately after the switch back to lean conditions. Fig. A28 describes this behavior for a series of typical NSR catalysts, where the precious metal loading and type of precious metal greatly affected the behavior observed.

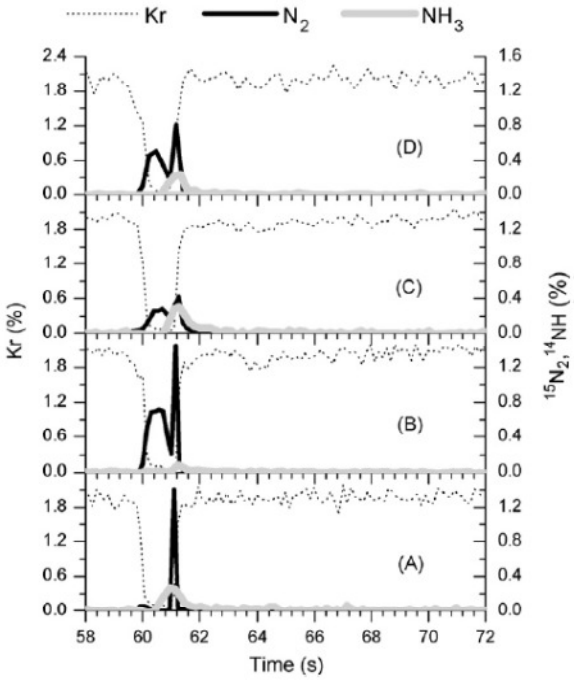

Figure A28. Evolution of reaction products during a rich event (CO + H_2 + H_2O + CO2) at 350 °C on a series of NSR catalysts formulated from commonly used precious metals including: (A) 0.5% Pt, (B) 1.6% Pt, (C) 1.1% Rh and (D) 0.5% Pt-0.8% Rh supported on 17%Ba/Al_2O_3 (w/w), Breen et al. [16].

Figure A29 demonstrates how changing the reductant affected N_2 evolution. Notice the large N_2 spike when CO was used as a reductant in the absence of H_2, where approximately 90% of the total N_2 evolved on this catalyst came from the 2nd N_2 evolution period. This suggested that isocyanates were formed on the catalyst during rich periods and were quickly oxidized to N_2 or hydrolyzed to NH_3 during subsequent lean periods. Breen et al. concluded that the first N_2 peak was formed by rapid reduction of NO_X on the surface of reduced Pt or Rh and the second N_2 peak was formed by reaction of stored NH_3 with stored NO_X from by hydrolysis of isocyanates. The authors omitted the possibility of oxidation of stored NH_3 to produce N_2 and reaction of isocyanates with NO/O_2 to form N_2 as another route to N_2 production. However, storage of NH_3 at elevated temperatures is very unlikely, as recently shown by Bahrami et al. [175]. Lastly, Breen et al. [16] used fairly high concentrations of reductants, which could also

alter the reduction mechanism. For example, a high concentration of CO in the gas phase may facilitate isocyanate intermediates because the probability of an N adatom reacting with an adsorbed CO species before it can react with another N adatom may increase if the concentration of CO on the surface increases proportionally to the concentration of CO in the gas phase.

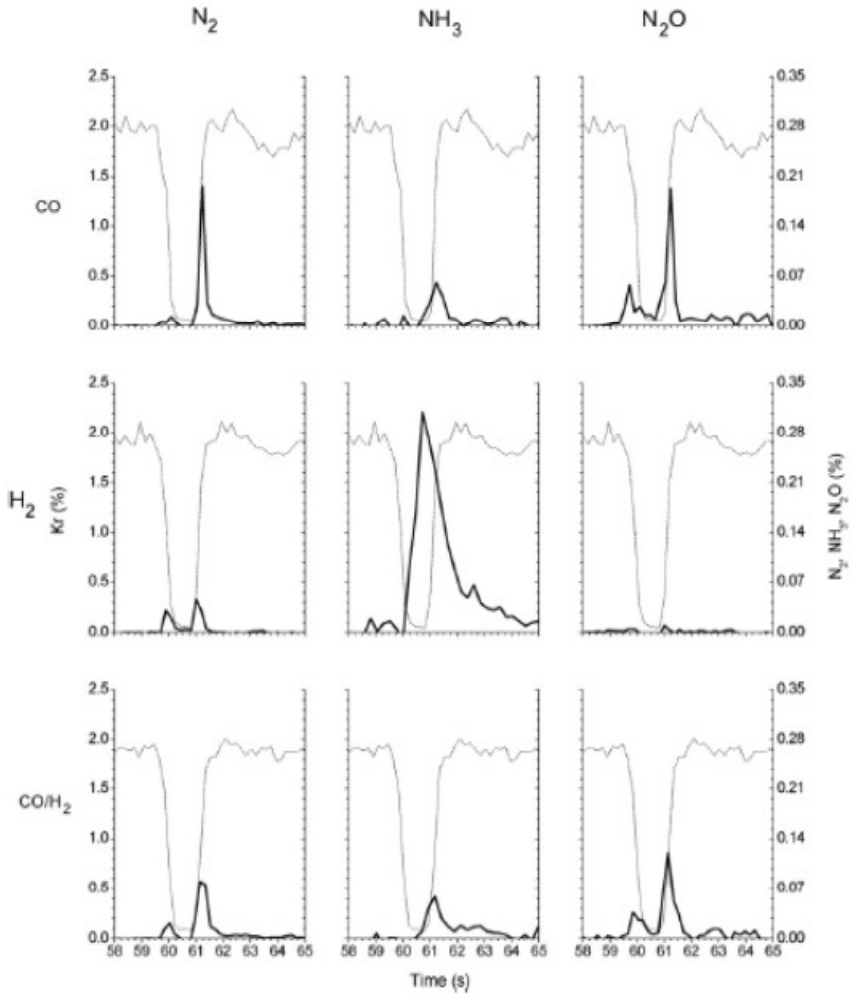

Figure A29. Reaction products during a rich event over a 0.5%Pt-0.8%Rh/17%Ba/Al_2O_3 (w/w) NSR catalyst at 250 °C, where the rich phase contained 6% CO, 6%H_2 or 1.5% H_2 and 4.5% CO, Breen et al. [16].

Nova et al. [64,289] also proposed that the reduction of NO_X could proceed through isocyanate intermediates, but pointed out that the water gas shift reaction (Reaction A30) could also create large amounts of H_2 from CO in the presence of water. When a Pt/Ba/Al_2O_3 catalyst

was exposed to CO and H_2O, the light-off temperature for the WGS reaction occurred slightly above 200 °C. Above 300 °C, H_2 and CO_2 were the only products observed, as shown in Fig. A30. Scholz et al. [28,319,320] have also mentioned the WGS reaction as a potentially important reaction occurring on NSR catalysts. This conclusion was reached because CO and H_2 were equally effective reductants in the presence of water, but H_2 was much better than CO in the absence of water.

$$CO + H_2O \rightarrow H_2 + CO_2 \quad \text{(A30)}$$

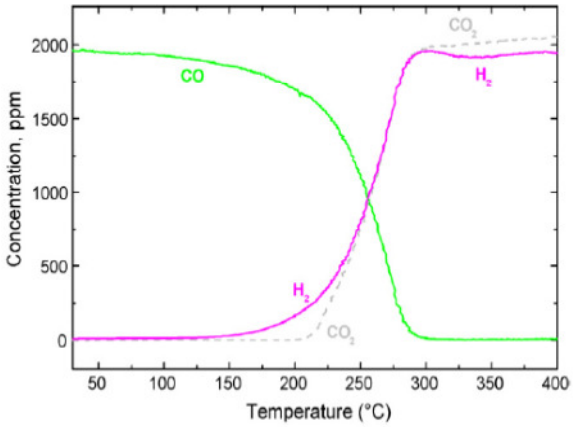

Figure A30. Temperature programmed surface reaction (TPSR) of 2000 ppm CO + 1% (v/v) H_2O over a 1%Pt/20%Ba/Al_2O_3 (w/w) NSR catalyst, Nova et al. [64,289].

Forzatti et al. also suggested that formation of N_2 proceeds through formation of isocyanate intermediates, where the isocyanates could then react with adsorbed NO_X species, NO, O_2 or H_2O as shown in Fig. A31 [290]. However, an alternative mechanism for reduction of surface nitrates with CO in the absence of water was also proposed. Reactions A31 – A35 highlight this mechanism.

$$-Ba-ONO_2+Pt-CO \rightarrow -Ba-ONO+CO_2+Pt^* \quad (31)$$

$$-Ba-ONO+Pt-CO \rightarrow -Ba-OCONO+Pt^* \quad (32)$$

$$-Ba-OCONO+Pt-CO \rightarrow -Ba-OCNO+CO_2+Pt^* \quad (33)$$

$$-Ba-OCNO+Pt-CO \rightarrow -Ba-NCO+CO_2+Pt^* \quad (34)$$

$$-Ba-NCO+Ba-ONO \rightarrow -Ba-O-Ba- \ +N_2+CO_2 \quad (35)$$

The first step involves decomposition of barium nitrate to nitrite. Next, CO spills over from Pt onto Ba and inserts itself into barium nitrite forming an organo-nitrogen-like compound. Reaction with another CO molecule reduces this complex ultimately forming an NCO adspecies on Ba. This species can then undergo reactions A6-A11, A27-A28, or reaction A35 to produce N_2.

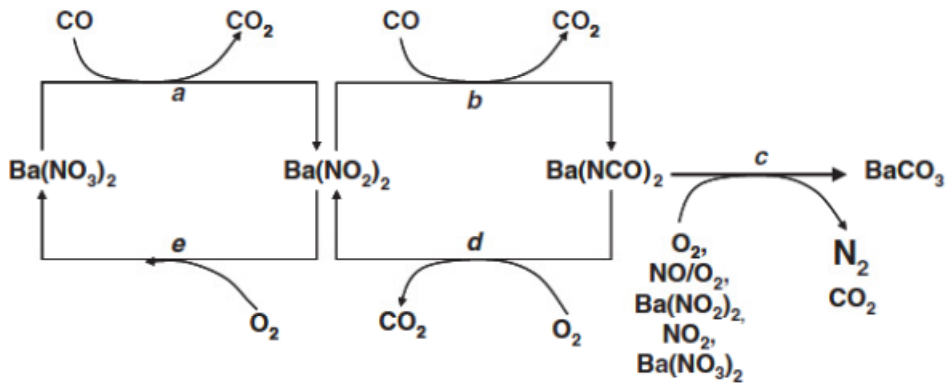

Figure A31. Proposed reaction network for reduction of $Ba(NO_3)_2$ by CO in the absence of water. Reprinted from Forzatti et al., 2010 [15].

In summary, reduction of NO_X by CO and C_3H_6 has many potential reaction pathways and the overall reduction mechanism operating on these catalysts remains elusive. Additionally, the role of isocyanate intermediates is still unclear. While a considerable number of investigations have observed isocyanate species in FTIR spectra, evidence tying their presence to

the production of N_2 is still lacking, where parallel reactions like WGS greatly complicate understanding. In the presence of H_2O production of H_2 from CO and H_2O could dramatically change the reduction mechanism and could favor the currently proposed reduction mechanism for H_2, which involves NH_3 an intermediate [60,286,346].

A.2.5 CONCLUSIONS

NO_X storage and reduction catalysts are very promising for use in lean-burn engine exhausts because they are capable of converting high amounts of harmful NO_X to N_2 and have already been implemented in Japan. Since their inception, many advances have been made and the current materials are more thermally resistant and sulfur tolerant than their predecessors. However, the reduction mechanisms occurring on these catalysts are still unclear. Since these catalysts are often limited by their inability to completely reduce NO_X stored during the short times necessary for these systems to operate, better understanding of the reduction mechanism is crucial for optimization of this aspect of the catalyst.

While the specific reduction mechanism is still unclear, this review has exposed some of the more significant conclusions available in the literature. Mainly, release of stored NO_X most likely proceeds through adsorption of reductant molecules that either react with NO_X on the metal surface or spillover onto the support and destabilize/react with adsorbed NO_X. Reduction by CO or hydrocarbons most likely proceeds through NO decomposition to N adatoms that react with other N adatoms to form N_2 or react with adsorbed to form isocyanates, where isocyanates could then react with NO, O_2, H_2O or stored NO_X to produce N_2, N_2O or NH_3, where NH_3 is an excellent molecule for SCR of NO_X. Additionally, the role of the WGS reaction cannot be

excluded and CO may react with water to produce H_2, which has long been considered a better reductant than CO or C_3H_6. The role of C_3H_6 in the reduction of stored NO_X is still unclear.